Functional Metal Oxide Surfaces:
Photocatalytic, Self-Cleaning and Micro-/Nanostructuring Applications

Dissertation

submitted to obtain the degree of
Doctor of Engineering (Dr.-Ing.)
at the
Faculty of Engineering, Institute for Material Science,
Kiel University

SALIH VEZIROGLU

Kiel, Germany
March 2021

1st Examiner: **Prof. Dr. Franz Faupel**
Chair for Multicomponent Materials
Faculty of Engineering, Kiel University

2nd Examiner: **Prof. Dr. Lorenz Kienle**
Chair for Synthesis and Real Structures
Faculty of Engineering, Kiel University

3rd Examiner: **Prof. Dr. Jost Adam**
Department of Mechanical and Electrical Engineering
Faculty of Engineering, University of Southern Denmark

Examination Committee Chair: **Prof. Dr. Stephan Wulfinghoff**
Computational Materials Science
Faculty of Engineering, Kiel University

Date of Disputation: **December 10, 2020**

…this thesis is dedicated to my wife “Pınar” and son “Bilge Kağan” and whole family…

Acknowledgement

To accomplish the research studies presented in this PhD dissertation would not have been possible without the encouragement and support of various people. Therefore, I would like to thank the people at the Institute for Material Science at Faculty of Engineering-Kiel University. I would particularly like to thank:

Firstly, I would like to express my deepest gratitude to my supervisor Prof. Dr. Franz Faupel for allowing me to join his exciting research group (Chair for Multicomponent Materials). He believed in me right from the start. I am thankful for his guidance in all time of my research and his patience, motivation, and immense knowledge. I also appreciate a lot his help in my personal life. Without his supervision, it wouldn't have been possible to accomplish this PhD dissertation. I have had a great experience in the last three years, and it is an honor for me to be a part of his research group.

Likewise, I thank my second supervisor Prof. Dr. Oral Cenk Aktas for his dedicated support on my PhD study and related all research. His guidance helped me all the time in science, research, and writing scientific papers as well as this thesis. His broad vision, deep knowledge, and insightful comments developed my foresight to let me grow as a researcher. I would also like to thank him for his friendship, understanding, and a great sense of humor in my daily life as well as scientific research. Without his dedication and motivation, it wouldn't have been possible to achieve most of the publications, which were partially presented in this dissertation, in a very short time.

A special thanks to Prof. Dr. Klaus Rätzke and Dr. Thomas Strunskus for their encouragements, deep knowledge in physic and chemistry and fruitful suggestions to improve the quality of my scientific research. I thank Dipl.-Ing. Stefan Rehders for providing technical support and assistance whatever equipment and experiments were needed.

I would like to acknowledge my PhD fellows (in the first year) and friends Muhammed Zubair Ghori (from Fraunhofer Institute ISIT) and Josiah Ngenev Shondo. It was a great pleasure for me to discuss with them and share ideas for improving our results. Also, here, thanks go to my office colleagues Brook Shurtleff and Ron-Marco Friedrich for their friendship as well as theoretical discussions and coffee breaks.

I would like to thank Assoc. Prof. Dr. Jacek Fiutowski and Assoc. Prof. Dr. Jost Adam (from the Mads Clausen Institute, NanoSYD, University of Southern Denmark-SDU) for great collaborative works with our research group. They performed the Helium ion microscopy (HIM) analysis, specific electrochemical, and optical simulations which were used in this dissertation. Similarly, I would like to thank Prof. Dr. Yahya Açil and Assoc. Prof. Dr. Aydin Gülses (from Department of Oral and Maxillofacial Surgery, University Hospital of Schleswig-Holstein) for great collaborative works on biomedical investigations.

I sincerely thanks to Anna-Lena Obermann, Katharina Röder, Majid Hussain, Marie Ullrich, Jaeho Hwang, Lynn Schwaeke, Dominik Stefan, Ayse Sunbul, Afrin Jahan Shara, Kevin Rogall and Tim Tjardts for their support in my experimental work. I wish them all the best for their life and professional career.

I am enormously thankful to my recent and former colleagues in the Chair of Multicomponent Materials (Alexander Vahl, Oleksandr Polonskyi, Stefan Schröder, Christian Ohrt, Jonas Drewes, Wiebke Reichstein, Igor Barg, Niko Carstens, Maximilian Heiko Burk, Torge Hartig, Benjamin Spetzler and others) for their contributions, supports and fruitful discussions about our research.

Especially, I would like to acknowledge the Graduate Center and Federal State Funding at Kiel University for providing funding for my doctoral study.

Finally, from the bottom of my heart, I would like to say big thanks to my wife, parents, sister, and brother for providing me with unfailing support and continuous encouragement throughout all my research career as well as support writing this thesis.

Abstract

Photocatalysis is the most applicable approach to decompose various organic pollutants due to its high efficiency, low-cost, and eco-friendly nature. Heterogeneous photocatalysis has become a hot topic in the field of green chemistry. Titanium (IV) oxide (TiO_2) photocatalyst has been widely investigated in comparison to other metal oxide semiconductors due to its high activity, low cost, and high chemical and physical stability. On the other hand, TiO_2 is also preferable materials in some specific applications such as self-cleaning (indoor and outdoor applications). This dissertation covers the development of TiO_2 based functional metal oxide surfaces for photocatalytic and self-cleaning applications as well as micro-/nanostructuring of gold (Au) and silver (Ag).

This thesis is composed of **14 Chapters**: Following Introduction (**Chapter 1**) and Theoretical Background (**Chapter 2**), Method and Characterization processes are described in **Chapter 3**. The Results and Discussion, which are originally based on peer-reviewed nine publications, are presented in corresponding nine chapters (**Chapters 4**, **5**, **6**, **7**, **8**, **9**, **10**, **11**, and **12**). Afterward, Summary & Conclusion and Outlook are presented in **Chapter 13** and **Chapter 14**, respectively.

Chapter 4 (reprinted version of **Publication 1**) covers extremely high catalytic activity with Au/ZnO-CeO_2 hybrid structure in the presence of sodium borohydride ($NaBH_4$), via electron relay process. Systematic studies were carried out to find the optimum ratio between CeO_2 and ZnO which yields a high surface area, stable support for Au loading, and a dynamic Ce^{3+}/Ce^{4+} conversion. We demonstrated that the continuous fluctuation of Ce^{3+}/Ce^{4+} and the metallic character of Au nanoparticles residing on ZnO-CeO_2 structures form an effective electron relay system that yields high catalytic degradation rates.

Chapter 5 (reprinted version of **Publication 2**) covers a facile method to synthesize hierarchical Au needle clusters (HAuNCs) on highly active TiO_2 thin film. The systematic studies were carried out to control the size and the geometry of deposited HAuNCs by simply altering the photocatalytic activity of the TiO_2 target, UV light intensity, and irradiation time. Also, the photocatalytic deposition approach was used for positioning and patterning of HAuNCs on the TiO_2 target without using any surfactant or stabilizer.

Chapter 6 (based on **Publication 3**) covers an effective way of preparing a highly active Au nanocluster (NC) decorated TiO_2 thin film by a novel photodeposition method. Here, the solvent types were altered as well as the illumination time to control the surface coverage of the Au NCS, which has a direct effect on the photocatalytic activity. Au NCs (at low surface coverage) seem to significantly enhance the optical absorption of TiO_2 at UV wavelengths and therefore lead to higher photocatalytic performance.

Chapter 7 (reprinted version of **Publication 4**) covers plasmonic and non-plasmonic contributions of Au nanoparticles (NPs) on the overall photocatalytic activity of the Au-TiO_2 hybrid structure. The systematic studies were conducted on the different ratio of the visible (Vis) and ultra-violet (UV) light (Vis/UV) to

investigate plasmonic and non-plasmonic enhancements. Here, it is shown that a gradual increase of Vis/UV led to a steady enhancement of the photocatalytic performance of the Au-TiO_2 hybrid structure.

Chapter 8 (reprinted version of **Publication 5**) covers the photocatalytic deposition of Ag NPs on reactive sputtered columnar TiO_2 structures. Here, the morphology and surface coverage of deposited Ag NPs were controlled by altering the UV exposure time. We have demonstrated that optimum surface coverage led to a significant increase in the photocatalytic activity of the Ag-TiO_2 hybrid structure.

Chapter 9 (reprinted version of **Publication 6**) covers a facile method, combining sputtering and gas aggregation techniques (GAS), to prepare a photocatalytic TiO_2 thin film decorated with stable plasmonic aluminum (Al) NPs. Here, Al NPs show a localized surface plasmon resonance (LSPR) effect on TiO_2 photocatalysis under UV irradiation. We have presented the negative and positive influences of LSPR on UV photocatalysis by irradiating Al-TiO_2 hybrid structures at two different UV wavelengths: both at and above the plasmonic absorption of Al NPs.

Chapter 10 (reprinted version of **Publication 7**) covers a magnetron sputtering and GAS approaches were combined for the preparation of columnar TiO_2 structures decorated with PdO NPs. Here, a totally solvent-free synthesis approach was presented for good control of surface coverage, size, morphology, and stoichiometry of PdO NPs in comparison to wet-chemical synthesis methods. We have revealed that a steady equilibrium between PdO and PdO_2 phases under UV irradiation seems to provide an efficient electron-hole pair separation, which improves the overall photocatalytic activity of PdO-TiO_2 hybrid structure.

Chapter 11 (reprinted version of **Publication 8)** covers a facile approach to synthesize cauliflower-like CeO_2–TiO_2 hybrid structures by magnetron reactive sputtering, exhibiting an extremely high photocatalytic activity. We have demonstrated that heating and air-quenching of the sputter-deposited TiO_2 thin film (first layer) triggered the formation of a nanocrack network, the second heat-treatment led to the transformation of the CeO_2 film (second layer) into CeO_2 nanoclusters (NCs). Here, dynamic shifting of Ce^{3+}/Ce^{4+}, where at the CeO_2-TiO_2 interface, enhances the photocatalytic activity as well as self-cleaning properties in air.

Chapter 12 (reprinted version of **Publication 9**) covers a combination of hard-templating and infiltration processes. Here, the micro-and nanoscale topography were tuned by the 2D assembling of TiO_2 nanoparticles on the surface. This overall process can be easily extended to the 3D TiO_2 structure. Initiated chemical vapor deposition (iCVD) method was used to deposit an ultrathin and highly conformal polytetrafluoroethylene (PTFE) layer on bulk material (3D PTFE/TiO_2). After coating a thin layer of PTFE, 3D TiO_2 showed an extraordinary superhydrophobicity.

Chapter 13 covers overall Summary & Conclusion for all presented researches in this thesis.

Finally, an Outlook (**Chapter 14**) is provided for future research activities.

Kurzfassung

Photokatalyse is die effektivste Art der Zersetzung von unterschiedlichsten organischen Verunreinigungen aufgrund der hohen Effizienz, ihrer niedrigen Kosten und ihres umweltschonenden Verhaltens. Heterogene Photokatalyse ist ein hoch aktuelles Thema im Kontext der nachhaltigen grünen Chemie. Titan (IV) oxid (TiO_2) Photokatalysatoren wurden, im Vergleich zu anderen Metalloxiden, besonders weitgehend untersucht, aufgrund ihrer hohen Aktivität, niedrigen Kosten und hoher chemischer und physikalischer Stabilität. Ebenfalls ist TiO_2 auch bevorzugtes Material für einige spezielle Anwendungen wie z.B. selbstreinigende Oberflächen (im Indoor- bzw. Outdoorbereich). Diese Dissertaton behandelt die Herstellung von funktionalen Metalloxidoberflächen für photokatalytische und selbstreinigende Anwendungen sowie der Mikro- und Nanostrukturierung von Gold (Au) und Silber (Ag).

Diese Thesis besteht aus 14 Kapiteln: Nach einer Einleitung (**Kapitel 1**) und der Behandlung der theoretischen Grundlagen (**Chapter 2**) werden Methoden und Charakterisierungsprozesse erklärt (**Kapitel 3**). Daraufhin werden die Ergebnisse auf Grundlage von 9 wissenschaftlich begutachteten (Engl.: Peer-reviewed) Publikationen diskutiert und jeweils in den damit assozierten Kapiteln aufgezeigt (**Kapitel 4-12**). Im Anschluss werden die Ergebnisse zusammengefasst, es wird ein Fazit dieser Arbeit gezogen und es werden Zukunftsperspektiven aufgezeigt (**Kapitel 13 und 14**).

Kapitel 4 (nachgedruckte Version von **Publikation 1**) behandelt extrem hohe katalytische Aktivitäten mittels Au/ZnO-CeO_2 Hybridstrukturen unter der Anwesenheit von Natriumborhydrid ($NaBH_4$), welche durch einen Elektronenrelaisprozess ermöglicht werden. Systematische Studien wurden durchgeführt, um ein optimales Verhältnis von CeO_2 und ZnO zu finden, welches zu einer großen Oberfläche führt, sowie einen stabilen mechanischen Halt für Au, und eine dynamische Ce^{3+}/Ce^{4+} conversion aufweist. Wir demonstrieren, dass eine kontinuierliche Fluktuation von Ce^{3+}/Ce^{4+} und der metallische Charakter von Au-Nanopartikeln auf den ZnO-CeO_2 Stukturen einen effektiven Elektronenrelaisprozess ergeben, welcher eine hohe katalytische Zersetzungsrate aufweist.

Kapitel 5 (nachgedruckte Version von **Publikation 2**) behandelt ein einfache Methode zur Synthese von hierarchischen Au-Nadelclustern (HAuNCs) auf hochaktiven TiO_2 Dünnschichten. Systematische Studien wurden durchgeführt, um die Größe und Geometry der HAuNCs kontrollieren zu können mittels der Veränderung der photokatalytischen Aktivität der TiO_2 Oberfläche, UV-Licht Intensitäten und der Bestrahlungszeit. Der photokatalytische Depositionsansatz wurde genutzt für die Positionierung und Stukturierung von HAuNCs auf der TiO_2 Oberfläche ohne Benutzung von grenzflächenaktiven Substanzen oder Stabilisatoren.

Kapitel 6 (nachgedruckte Version von **Publikation 3**) behandelt eine effektive Möglichkeit zur Präparation von hochaktiven Au-Nanoclustern (NC) auf TiO_2 Dünnschichten mittels einer neuen Photodepositions-

methode. Hier werden die Lösungsmittel sowie die Beleuchtungszeit variiert, um die Oberflächenbedeckung von Au NCs zu kontrollieren, welche einen direkten Effekt auf die photokatalytische Aktivität hat. Au NCs (bei niedriger Oberflächenbedeckung) scheinen eine signifikante Verstärkung der optischen Absorption von TiO_2 im UV-Bereich hervorzurufen, welche somit zu einer höheren photokatalytischen Performance führen.

Kapitel 7 (nachgedruckte Version von **Publikation 4**) behandelt plasmonische und nicht-plasmonische Einflüsse von Au-Nanopartikeln (NPs) auf die photokatalytische Aktivität der Au-TiO_2 Hybridstrukturen. Systematische Studien wurden durchgeführt, um den Einfluss unterschiedlicher Verhältnisse von sichtbarem (Vis) und Ultraviolettem-Licht (UV) auf die plasmonischen bzw. nicht-plasmonischen Eigenschaften zu untersuchen. Hier zeigen wir, dass ein gradueller Anstieg des Verhätnisses Vis/UV zu einer stetigen Verbesserung der photokatalytischen Performance der Au-TiO_2 Hybridstruktur führt.

Kapitel 8 (nachgedruckte Version von **Publikation 5**) behandelt die photokatalytische Deposition von Ag NPs auf reaktiv gesputterte TiO_2 Säulenstrukturen. Hier wurde die Morphologie und Oberflächenbedeckung von deponierten Ag NPs kontrolliert durch Änderung der UV-Beleuchtungszeit. Wir haben gezeigt, dass die optimale Oberflächenbedeckung zu einer signifikanten Erhöhung der photokatalytischen Aktivität der Ag-TiO_2 Hybridstruktur führt.

Kapitel 9 (nachgedruckte Version von **Publikation 6**) behandelt eine einfache Methode, bestehend aus der Nutzung einer Kombination von Sputtern und Gasaggregationstechniken (GAS), um photokatalytische TiO_2 Dünnschichten mit stabilen plasmonischen Aluminium (Al) NPs herzustelllen. Wir zeigen hier, dass die lokalisierten Oberflächenplasmonresonanzen (LSPR) der Al NPs einen Effekt auf die TiO_2 photokatalytischen Eigenschaften unter UV-Beleuchtung haben. Wir päsentieren die negativen sowie positiven Einflüsse von LSPR auf die UV Photokatalyse durch Beleuchtung der Al-TiO_2 Hybridstrukturen bei zwei unterschiedlichen UV Wellenlängen: Beide bei und über der plasmonischen Absorption von Al NPs.

Kapitel 10 (nachgedruckte Version von **Publikation 7**) behandelt einen Präparationsansatz von TiO_2 Säulenstrukturen dekoriert mit PdO NPs mittels Magnetronsputtern und GAS. Eine lösungsmittelfreie Synthese wird präsentiert für Kontrolle der Oberflächenbedeckung, Größe, Morphologie und Stöchiometrie der PdO NPs im Vergleich zu nasschemischen Synthesemethoden. Wir zeigen, dass ein stetiges Equilibrium zwischen PdO und PdO_2 Phasen unter UV-Beleuchtung anscheinend eine effiziente Elektron-Loch Paar Separation hervorruft, welche die photokatalytische Aktivität von PdO-TiO_2 Hybridstrukturen verbessert.

Kapitel 11 (nachgedruckte Version von **Publikation 8**) behandelt eine einfache Methode zur Synthetisierung von blumenkohlartigen CeO_2-TiO_2 Hybridstrukturen durch reaktives Magnetronsputtern, welche eine extrem hohe photokatalytische Aktivität aufweist. Wir demonstrieren, dass Heizen und

Abschrecken der gesputterten TiO_2 Dünnschicht (erste Schicht) zu der Formation eines Netzwerks von Nanocracks führt. Eine zweite Wärmebehandlung führt zur Transformation der CeO_2 Schicht (zweite Schicht) in CeO_2 Nanocluster (NCs). Hier sorgt der Wandel von Ce^{3+}/Ce^{4+} an der Grenzfläche von CeO_2-TiO_2 zur Verstärkung der photokatalytischen Aktivität bzw. der selbstreinigenden Eigenschaften der Strukturen.

Kapitel 12 (nachgedruckte Version von **Publikation 9**) behandelt eine Kombination von Hard-Templating und Infiltrationsprozessen. Hierbei wird die mikro- und nanoskalige Topographie gezielt verändert durch 2D Anhäufung von TiO_2 Nanopartikeln auf der Oberfläche. Dieser Prozess kann einfach auf 3D TiO_2 Strukturen erweitert werden. Initiierte chemische Gasphasenabscheibung (iCVD) wurde genutzt, um eine ultradrünne und konforme Polytetrafluorethylenschicht (PTFE) auf Bulk Material (3D PTFE/TiO_2) abzuscheiden. Nach der Abscheidung zeigte das 3D TiO_2 ein superhydrophobes Verhalten.

Kapitel 13 behandelt eine Zusammenfassung und ein Fazit für alle präsentierten Untersuchungen in dieser Thesis.

Zu guter Letzt wird ein Ausblick (**Kapitel 14**) gegeben für zukünftliche wissenschaftliche Aktivitäten.

Declaration of Authenticity

I, Salih Veziroglu, hereby declare that this thesis and the respective research was independently composed and authored by myself.

This work complies with the DFG recommendations for safeguarding good scientific practice. All content and ideas drawn directly or indirectly from external sources are clearly indicated.

This thesis has not been published or been submitted to any other examining body and all related research items that have been composed and published in peer-review journals are clearly indicated as such.

Publication 1. Ultra-fast degradation of methylene blue by $Au/ZnO\text{-}CeO_2$ nano-hybrid catalyst, ***Materials Letters*** 209 (2017) 486–491.

Publication 2. Photocatalytic Growth of Hierarchical Au Needle Clusters on Highly Active TiO_2 Thin Film, ***Advanced Materials Interfaces*** 5 (2018) 1800465.

Publication 3. Photo-deposition of Au Nanoclusters for Enhanced Photocatalytic Dye Degradation over TiO_2 Thin Film, ***ACS Applied Materials and Interfaces*** 12, (2020) 14983.

Publication 4. Plasmonic and non-plasmonic contributions on photocatalytic activity of $Au\text{-}TiO_2$ thin film under mixed UV-Visible light, ***Surface & Coatings Technology*** 389, (2020) 125613.

Publication 5. Ag Nanoparticles Decorated TiO_2 Thin Films with Enhanced Photocatalytic Activity, ***Physica Status Solidi (A) - Applications and Materials Science*** (2019) 1800898.

Publication 6. Role of UV Plasmonics in the Photocatalytic Performance of TiO_2 Decorated with Aluminum Nanoparticles, ***ACS Applied Nano Materials*** 1 (2018) 3760–3764.

Publication 7. PdO Nanoparticles Decorated TiO_2 Film with Enhanced Photocatalytic and Self-Cleaning Properties, ***Materials Today Chemistry*** 16 (2020) 100251.

Publication 8. Cauliflower-like $CeO_2\text{-}TiO_2$ hybrid nanostructures with extreme photocatalytic and self-cleaning properties, ***Nanoscale.*** 11 (2019) 9840–9844.

Publication 9. Superhydrophobic 3D Porous $PTFE/TiO_2$ Hybrid Structures, ***Advanced Materials Interfaces*** 6 (2019) 1801967.

I declare that no academic degree has been withdrawn from me.

Signature:

Place and date: Kiel, den 11 August 2020

Publications in the Context of this Dissertation

in chronological order, first or equally contributing authors are underlined.

[1] **S. Veziroglu,** M. Kuru, M.Z. Ghori, F.K. Dokan, A.M. Hinz, T. Strunskus, F. Faupel, O.C. Aktas, Ultra-fast degradation of methylene blue by Au/ZnO-CeO_2 nano-hybrid catalyst, ***Mater. Lett.*** 209 (2017) 486–491.

[2] **S. Veziroglu,** M.Z. Ghori, M. Kamp, L. Kienle, H.G. Rubahn, T. Strunskus, J. Fiutowski, J. Adam, F. Faupel, O.C. Aktas, Photocatalytic Growth of Hierarchical Au Needle Clusters on Highly Active TiO_2 Thin Film, ***Adv. Mater. Interfaces.*** 5 (2018) 1800465. **(FRONTISPIECE)**

[3] M.Z. Ghori, **S. Veziroglu,** A. Hinz, B.B. Shurtleff, O. Polonskyi, T. Strunskus, J. Adam, F. Faupel, O.C. Aktas, Role of UV Plasmonics in the Photocatalytic Performance of TiO_2 Decorated with Aluminum Nanoparticles, ***ACS Appl. Nano Mater.*** 1 (2018) 3760–3764. **(FRONT COVER)**

[4] **S. Veziroglu,** M.Z. Ghori, A.L. Obermann, K. Röder, O. Polonskyi, T. Strunskus, F. Faupel, O.C. Aktas, Ag Nanoparticles Decorated TiO_2 Thin Films with Enhanced Photocatalytic Activity, ***Phys. Status Solidi Appl. Mater. Sci.*** (2019) 1800898. **(FRONT COVER)**

[5] O.C. Aktas, S. Schröder, **S. Veziroglu,** M.Z. Ghori, A. Haidar, O. Polonskyi, T. Strunskus, K. Gleason, F. Faupel, Superhydrophobic 3D Porous PTFE/TiO_2 Hybrid Structures, ***Adv. Mater. Interfaces.*** 6 (2019) 1801967. **(INSIDE BACK COVER)**

[6] **S. Veziroglu,** K. Röder, O. Gronenberg, A. Vahl, O. Polonskyi, T. Strunskus, H.-G. Rubahn, L. Kienle, J. Adam, J. Fiutowski, F. Faupel, O.C. Aktas, Cauliflower-like CeO_2 –TiO_2 hybrid nanostructures with extreme photocatalytic and self-cleaning properties, ***Nanoscale.*** 11 (2019) 9840–9844. **(INSIDE BACK COVER)**

[7] **S. Veziroglu,** J.Hwang, J. Drewes, J. Shondo, T. Strunskus, O. Polonskyi, F. Faupel, and O. C. Aktas, PdO Nanoparticles Decorated TiO_2 Film with Enhanced Photocatalytic and Self-Cleaning Properties, ***Materials Today Chemistry.*** 16 (2020) 100251.

[8] **S. Veziroglu,** A.-L. Obermann, M. Ullrich, M. Hussein, M. Kamp, L. Kienle, T. Leißner, H.-G. Rubahn, O. Polonskyi, T. Strunskus, J. Fiutowski, M. Es-Sounid, J. Adam, F. Faupel, O. C. Aktas, Photo-deposition of Au Nanoclusters for Enhanced Photocatalytic Dye Degradation over TiO_2 Thin Film, ***ACS Applied Materials and Interfaces.*** 12, (2020) 14983.

[9] **S. Veziroglu,** M. Ullrich, M. Hussain, J. Drewes, J. Shondo, T. Strunskus, J. Adam, F. Faupel, O. C. Aktas, Plasmonic and non-plasmonic contributions on photocatalytic activity of Au-TiO_2 thin film under mixed UV-Visible light, ***Surface & Coatings Tech.*** 389, (2020) 125613.

Further Publications within PhD Period

Collaborative projects and interdisciplinary studies, in chronological order, first or equally contributing authors are underlined.

[10] M.Z. Ghori, **S. Veziroglu,** B. Henkel, A. Vahl, O. Polonskyi, T. Strunskus, F. Faupel, O.C. Aktas, A comparative study of photocatalysis on highly active columnar TiO_2 nanostructures in-air and in-solution, ***Sol. Energy Mater. Sol. Cells.*** 178 (2018) 170–178.

[11] A. Vahl, J. Dittmann, J. Jetter, **S. Veziroglu,** S. Shree, N. Ababii, O. Lupan, O.C. Aktas, T. Strunskus, E. Quandt, R. Adelung, S.K. Sharma, F. Faupel, The impact of O_2 /Ar ratio on morphology and functional properties in reactive sputtering of metal oxide thin films, ***Nanotechnology.*** 30 (2019) 235603.

[12] A. Vahl, **S. Veziroglu,** B. Henkel, T. Strunskus, O. Polonskyi, O.C. Aktas, F. Faupel, Pathways to Tailor Photocatalytic Performance of TiO_2 Thin Films Deposited by Reactive Magnetron Sputtering, ***Materials (Basel).*** 12 (2019) 2840.

[13] A. Haidar, A.A. Ali, **S. Veziroglu,** J. Fiutowski, H. Eichler, I. Müller, K. Kiefer, F. Faupel, M. Bischoff, M. Veith, O.C. Aktas, H. Abdul-Khaliq, PTFEP–Al_2O_3 hybrid nanowires reducing thrombosis and biofouling, ***Nanoscale Adv.*** 1 (2019) 4659–4664. **(INSIDE FRONT COVER)**

[14] H. Yetgin, **S. Veziroglu,** O.C. Aktas, T. Yalçinkaya, Enhancing thermal conductivity of epoxy with a binary filler system of h-BN platelets and Al_2O_3 nanoparticles, ***Int. J. Adhes. Adhes.*** 98 (2020) 102540.

[15] S. Sayin, T. Kohlhaas, **S. Veziroglu,** E. Sukran Okudan, M. Naz, S. Schröder, I. Saygili, Y. Acil, F. Faupel, J. Wiltfang, O. C. Aktas, A. Gülses, Marine Algae-PLA Composites as De Novo Alternative to Porcine Derived Collagen Membranes, ***Material Today Chemistry.*** 17 (2020) 100276.

[16] S. Kalantzis, **S. Veziroglu**, T. Kohlhaas, C. Flörke, Y. K. Mishra, J. Wiltfang, Y. Acil, F. Faupel, O. C. Aktas, A. Gülses, Early Stage Osteoblastic Activity on TiO_2 Thin Film Decorated with Flower-like Hierarchical Au Structures, ***RSC Advances.*** 10 (2020) 28935-28940.

[17] J. Shondo, **S. Veziroglu**, D. Stefan, Y. K. Mishra, T. Strunskus, F. Faupel, and O.C. Aktas, Tuning Wettability of TiO_2 Thin Film by Photocatalytic Deposition of 3D Flower- and Hedgehog-like Au Micro- and Nanostructures, ***Applied Surfaces Science.*** 537 (2021) 147795

[18] W. Reichstein, L. Sommer, **S. Veziroglu**, S. Sayin, S. Schröder, I. Saygili, Y. Acil, J. Wiltfang, F. Faupel, A. Gülses, O. C. Aktas, Functionalization of Polylactic Acid-Algae Composite Membrane by initiated Chemical Vapor Deposition for Enhanced Osteoblast Proliferation, ***Polymers*** 13 (2021) 186

[19] **S. Veziroglu**, M. Ayna, T. Kohlhaas, S. Sayin, J. Fiutowski, Y. K. Mishra, F. Karayurek, H. Naujokat, I. Saygili, Y. Acil, J. Wiltfang, F. Faupel, O. C. Aktas, A. Gülses, Bi-functional Polylactide Acid-Algae Composite Patch Enables Proliferation of Human Osteoblast Cells and Suppression of Human Osteosarcoma Cells, ***Polymers*** (2021), Under consideration.

[20] P. Ansari, **S. Veziroglu,** Y. K. Mishra, O. C. Aktas, M. U. Salamci, Selective Laser Melting based Additive Manufacturing in Stainless Steel: Detailed Process Understanding using Multi-Physics Simulation and Experimental, ***Materials Today Communications*** (2021), Under consideration.

[21] J. Shondo, **S. Veziroglu**, T. Tjardts, J. Fiutowski, S. Schröder, Y. K. Mishra, T. Strunskus, F. Faupel, and O. C. Aktas, iCVD coated Ag Flower-like Microstructures on TiO_2 Thin Films with Enhanced Oil/Water Separation and Self-Cleaning Properties, (2021) In preparation

[22] R. Gupta, P. Kharia, R. Saini, V. K. Kudapa, A. Mondal, **S. Veziroglu**, O. C. Aktas, F. Faupel, D. K. Avasthi, M. Agarwal, A. Biswas, Y. K. Mishra, Challenges and Opportunities in Fabrication of Corrosion Resistant Super Hydrophobic Coating: A Critical Review, (2021) In preparation

Other Scientific Contributions within PhD period

in chronological order (from latest to earliest), presenter is underlined.

Conference Presentations

[1] **S. Veziroglu**, J. Shondo, T. Tjardts, T. Strunskus, F. Faupel, O. C. Aktas, Enhancing Photocatalytic Performance of TiO2 Thin Films by Metallic and Oxide Nanostructures, 5th German-Czech Workshop on Nanomaterials, Dresden/Germany, 2020

[2] **S. Veziroglu**, J. Shondo, D. Stefan, A. Sunbul, K. Rogall, T. Tjardts, T. Strunskus, F. Faupel, O. C. Aktas, Patterning of TiO_2 Thin Films with 3D Flower- and Hedgehog-like Au Micro- and Nanostructures for Photocatalytic and Self-Cleaning Applications, Materials Science and Engineering Congress (MSE)-2020, Virtual, 2020.

[3] **S. Veziroglu**, J. Shondo, D. Stefan, T. Strunskus, F. Faupel, O. C. Aktas, Photocatalytic Deposition Method as Unconventional Approach for Preparing of Micro- and Nanostructures on TiO_2 Thin Films, NanoTR-15, Antalya/Turkey, 2019.

[4] **S. Veziroglu**, M. Hussain, M. Ullrich, J. Hwang, A. Vahl, T. Strunskus, F. Faupel, O. C. Aktas, Nanostructured Photocatalytic Thin Films and Their Functional Applications, E-MRS 2018 Fall Meeting, Warsaw/Poland, 2019.

[5] **S. Veziroglu**, M. Hussain, M. Ullrich, L. Schwaeke, J. Hwang, T. Strunskus, F. Faupel, O. C. Aktas, Photocatalytic Deposition Method: A Novel Strategy for Preparing Au Micro-Nanostructures on Metal Oxide Thin Films, E-MRS 2018 Fall Meeting, Warsaw/Poland, 2019.

[6] **S. Veziroglu**, J. Ngenev Shondo, A. Vahl, O. Polonskyi, T. Strunskus, F. Faupel, O. C. Aktas, Enhancing Photocatalytic Performance of TiO_2 Thin Films by Metallic Nanoparticles and Hybrid Oxide Nanostructures, 9th International Workshop on Polymer Metal NanoComposites, Helsinki/Finland, 2019.

[7] **S. Veziroglu**, M. Hussain, M. Ullrich, J. Hwang, J. Shondo, T. Strunskus, F. Faupel, O. C. Aktas, Nanostructured Thin Films with Enhanced Self-Cleaning and Photocatalytic Properties, NanoTech Poland 2019 – NIBS, Poznan/Poland, 2019.

[8] **S. Veziroglu**, M. Z. Ghori, K. Röder, M. Ullrich, J. Shondo, T. Strunskus, F. Faupel, O. C. Aktas, Nanostructured Mixed Oxide Thin Films with Enhanced Photocatalytic and Self-Cleaning Properties, E-MRS Spring 2019, Nice/France, 2019.

[9] **S. Veziroglu**, M. Z. Ghori, K. Röder, T. Strunskus, F. Faupel, O. C. Aktas, Synthesis and Characterization of Photocatalytic TiO_2 Thin Films Decorated with Ag Nanoparticles, E-MRS Fall 2018, Warsaw/Poland, 2018.

[10] **S. Veziroglu**, M. Z. Ghori, M. Kuru, F. Faupel, O. C. Aktas, Effect of Au Concentration on Degradation of Methylene Blue using Au/ZnO Catalyst, E-MRS Spring 2018, Warsaw/Poland, 2018.

Conference Posters

[11] **S. Veziroglu**, J. Ngenev Shondo, A. Vahl, O. Polonskyi, T. Strunskus, F. Faupel, O. C. Aktas, Enhancing Photocatalytic Performance of TiO_2 Thin Films by Metallic Nanoparticles and Hybrid Oxide Nanostructures, Advanced Materials Summer School, Palanga/Lithuania 2019.

[12] J. Bläsi, L. Senne, A. Vahl, **S. Veziroglu**, N. Carstens, F. Faupel, C. Aktas, M. Gerken, Photocatalytic gold layer growth on thin and structured TiO_2 substrates, Color Line Workshop, Kiel/Germany, 2019.

[13] **S. Veziroglu**, M. Z. Ghori, K. Röder, M. Ullrich, J. Shondo, T. Strunskus, F. Faupel, O. C. Aktas, Shape-Controlled Gold Nanoarchitectures on Highly Active TiO_2 Thin Film: Synthesis and Functional Applications, E-MRS Spring 2019, Nice/France, 2019.

Supervised / Co-supervised Theses

Bachelor theses:

[1] **Anna-Lena Obermann**

Au Nanoparticle Architecture on TiO_2 Thin Films

[2] **Christian Finke**

Functional Photocatalytic Thin Films

[3] **Lynn Schwaeke**

Photocatalytic Deposition of Pt and Au Metallic /Au-Pt Bimetallic Structures on TiO_2

[4] **Kevin Rogall**

Controlled Photocatalytic Deposition of Gold Micro- and Nanostructures on TiO_2 Thin Films Using Reducing Agents

[5] **Kassem Ganem**

Potential Use and Economic Impact of Photocatalytic TiO_2 For Air Purification and Anti-Bacterial/Viral (Covid-19) Applications

[6] **Christian Bruhn**

Preparation of Photo-Deposited Ag Nanoparticles on TiO_2 Under Alcoholic Media

Master theses:

[7] **Katherina Röder**

Preparation and Characterization of TiO_2/CeO_2 Bilayers for Functional Applications

[8] **Marie Ullrich**

Contribution of Plasmonic Effects to the Photocatalytic Activity of Titanium Dioxide Thin Films decorated with Gold Nanoparticles

[9] **Jaeho Hwang**

Gas Phase Synthesis of Nanoparticles for Functional Applications

Table of Contents

1 Introduction

Photocatalysis is the most effective approach to decompose various organic pollutants due to its high efficiency, eco-friendly nature and low-cost.[1] Heterogeneous photocatalysis has become a hot topic in the field of green chemistry (**Figure** 1.1). Currently, several types of metal oxide semiconductors such as titanium dioxide (TiO_2), tungsten oxide (WO_3), cerium oxide (CeO_2), zinc oxide (ZnO), and combinations of them have been used as photocatalysts.[2] TiO_2 became the most popular metal oxide photocatalyst after the pioneering study of Fujishama and Honda, which demonstrated superior catalytic properties of TiO_2.[3] Without any doubt TiO_2 photocatalyst has been widely investigated in comparison to other metal oxide semiconductors.

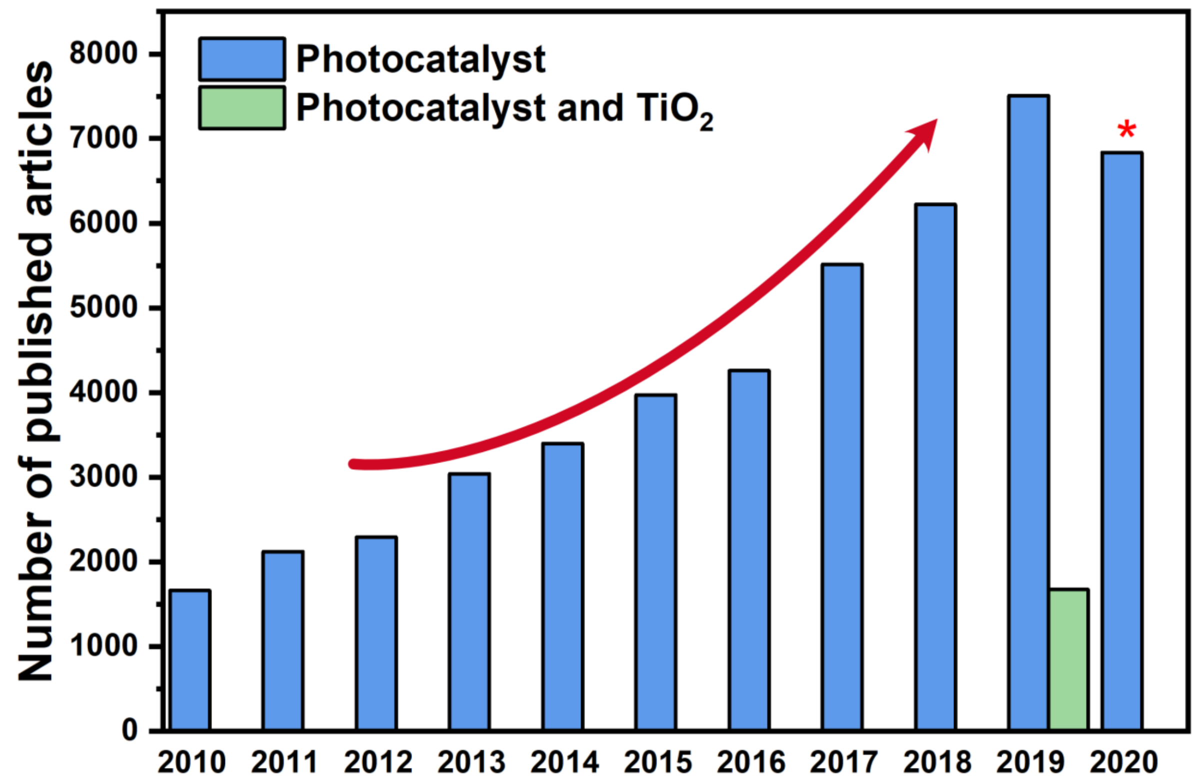

Figure 1.1. The number of published articles on "photocatalyst" and "photocatalyst and TiO2" in last ten years (searching "photocatalyst" and "photocatalyst and TiO2" terms in all fields from www.sciencedirect.com in June 2020). (* represents already accepted articles in 2020)

As seen in **Figure** 1.1, the interest in photocatalyst has been exponentially increasing and almost 25% of studies on photocatalysts are directly related to TiO_2. However, the use of TiO_2 photocatalyst in extensive applications is limited due to the fast recombination of electron-hole pairs [4] and its wide bandgap (3.0 eV for rutile and 3.2 eV for anatase).[5] TiO_2 is photoactivated by only UV irradiation which accounts for only ~5% of the full solar spectrum (**Figure** 1.2).

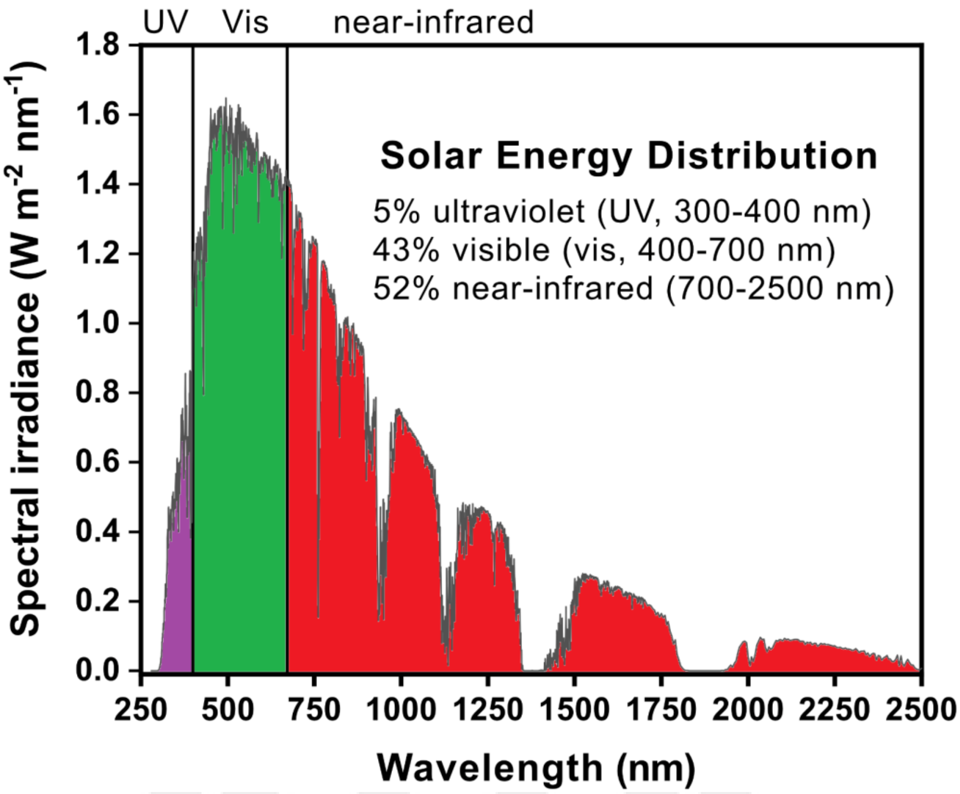

Figure 1.2. Solar radiation spectrum. (Modified from [6])

In order to improve the photocatalytic performance of TiO_2 some strategies have been reported in the literature.[7] Followings are the most preferred approaches:

- Tailoring morphology and the crystal structure of TiO_2
- Decorating TiO_2 with metals (aluminum, copper, etc.) and noble metals (gold, silver, and platinum)
- Coupling other metal oxide semiconductors (ZnO, CeO_2, etc.) with TiO_2

Particle size plays a significant role in the photocatalytic performance of TiO_2. Decreasing the particle size to the nanoscale (increasing active surface area) leads to a higher photocatalytic activity.[8] However, the use of nanoparticles for photocatalytic applications in continuous flow systems (such as water treatment) has some practical limitations (**Publication 1**). In such systems, it is difficult to separate and recycle nano-scaled photocatalysts from the water. Therefore, the use of photocatalysts as a robust and stable thin film is more suitable for functional applications.[9]

Several methods have been explored in the literature to prepare a robust and stable TiO_2 thin film. Most common methods are as sol-gel [10], thermal evaporation [9], chemical vapor deposition (CVD) [11], physical vapor deposition (PVD) [12] and pulsed laser deposition (PLD) [13]. The sol-gel approach is the most preferred one due to its ease of application and low cost (no need for costly equipment). However, preparing homogenous and reproducible thin films are a challenge as well as large-area sample preparation. The PVD is a favorable approach to prepare reproducible TiO_2 thin films and it is easily scalable to roll-to-roll systems compare to other deposition methods. The hundreds of meters homogenous TiO_2 thin films can easily prepare by this prospect.

The magnetron sputtering technique is the most promising approach among other PVD techniques because it allows a good control of compositional and structural properties of the prepared thin films by simply altering deposition parameters. Recently, Chair for Multicomponent Materials at Faculty of Engineering-Kiel University showed how the surface area, morphology, crystal structure, defect density, and crack network of the prepared TiO_2 thin films are crucial variables to achieve a high photocatalytic activity.[9,14] A systematic analysis has been conducted to reveal the influence of oxygen partial pressure (during the deposition) on the morphology, the mechanism behind the crack formation (network of nanoscale cracks) and crystal structure transformation (from amorph to anatase/rutile) by the heat-treatment. The results showed that all the varieties individually affect the photocatalytic performance of the prepared TiO_2 thin films.[15]

Decorating TiO_2 with plasmonic metal nanoparticles (NPs) such as gold (Au), silver (Ag) and aluminum (Al) is an effective strategy to improve photocatalytic activity of TiO_2 as well as to tailor its morphology aforementioned before.[16] (**Publication 2, Publication 3**, **Publication 5** and **Publication 6)**. For instance, Au NPs deposited on the TiO_2 surface increase the lifetime of electron-hole pairs and extend the bandgap absorption (UV to visible regions of the solar spectrum).[16] Au NPs leads to a strong absorption in the visible wavelengths due to the Localized Surface Plasmon Resonance (LSPR). Plasmonic Au NPs in-contact with TiO_2 forms a Schottky Barrier (SB) and this fosters the injection of hot electrons into the conduction band of the TiO_2 (**Publication 4**). This phenomenon improves the electron-hole separation, yielding a high photocatalytic activity.[17]

Alternatively, combining TiO_2 with rare-earth elements (cerium etc.) and their oxides has been demonstrated to be an effective way to enhance the photocatalytic activity of TiO_2, too. Especially mixed oxides are of great interest owing to the synergetic effect leading to extraordinary photocatalytic and self-cleaning properties.[18] Recently, cerium (IV) oxide (CeO_2) has gained much attention because of its special electron orbital structure, high thermal stability, oxygen storage capability, unique catalytic, and optical properties.[19] Fluctuating of oxidation states between Ce^{3+} and Ce^{4+}play a major role on catalytic and optical properties of cerium oxide.[18,20] Moreover, the heterojunction at TiO_2 and CeO_2 interface promotes the charge separation and increases the lifetime of electron-hole pairs.[21] (**Publication 8**) Similar to the TiO_2-CeO_2 hybrid structure, PdO can also be used to form heterojunction with TiO_2.[22] Here, a steady equilibrium between PdO and PdO_2 enhances the effective charge carrier (electron-hole pair) separation, which improves the photocatalytic activity, to degrade organic contaminants (**Publication 7**).

The photocatalytic activity can be monitored by two common approaches: degradation in an aqueous and non-aqueous medium.[23] In the aqueous system, the bleaching of methylene blue (MB) solution, in the presence of photocatalytic thin film, is monitored by the change in its absorption. However, in the non-aqueous system, which has been demonstrated by Chair for Multicomponent Materials at Faculty of

Engineering-Kiel University, first a MB layer (dry film) is deposited on the photocatalytic thin film and afterwards the change in its transmission and absorption is monitored.[23] Beside monitoring the change in the optical absorption (aqueous and non-aqueous systems), the change in the wetting angle can be also used as an alternative way to investigate the photocatalytic activity of thin films. Here, a thin layer of oleic acid is coated on the surface and the dynamic change in wetting angle is monitored under UV/Vis light illumination. This is a strong supplementary for exploring self-cleaning properties of the photocatalytic thin films (**Publication 7** and **Publication 8**).

Besides specific strategies demonstrated to improve the photocatalytic and self-cleaning activity, a novel micro and nano-structuring method based on photocatalytic reduction is also proposed in this thesis. A systematic study was conducted on photocatalytic reduction to investigate the formation of globular and hierarchical needle-like structures by altering solvent type, dielectric constant of the solvent, deposition time, light intensity, and photocatalytic activity of thin film. The finite element modeling (collaboration with the University of Southern Denmark) was used to reveal the mechanism of 1D growth (Au needle-like structures) during the photocatalytic deposition (**Publication 2** and **Publication 3**). Proposed photocatalytic deposition technique can be easily modified to deposit multicomponent metallic structures such as Pt-Au, Au-Ag, etc. micro- and nanoclusters as well as depositing individual metallic structures.

In this thesis, we highlighted some specific publications on functional metal oxide surfaces for photocatalytic, self-cleaning, and micro-/nanostructuring applications (**Publication 2** and **Publication 3**). However, the concepts developed in this thesis has led to some additional publications, too. Although these interdisciplinary studies are indirectly related to the proposed doctoral research; they are not included in the thesis in order not to disturb the overall content integrity.

2 Theoretical Background

This chapter provides the theoretical background for metal oxide semiconductors and explains photocatalysis mechanism. This includes a brief review of the bandgap (direct and indirect) phenomenon. Furthermore, as the most common photocatalyst structural and catalytic properties of TiO_2 are discussed by emphasizing some promising approaches (plasmonic, non-plasmonic, and heterojunction enhancement) to improve its photocatalytic activity. In addition to the photocatalytic activity, the self-cleaning properties of metal oxides is explained by considering both passive and active mechanisms. The last part describes the patterning of TiO_2 with micro-nanoscale metallic structures by photocatalytic deposition as unconventional surface modification.

2.1 Transition Metal Oxides

Transition metal oxides form an interesting class of materials owing to their extraordinary structural, electronic and catalytic properties.[24] In general metal oxides have attracted the attention for several decades because of their unique properties which involve ferromagnetic, photoluminescence, ferroelectric, and semiconducting characteristics. Therefore, they are preferred as main building blocks for various applications including, photovoltaic, lithium-ion batteries, photocatalysis, gas sensing, cleaning, biomedical, and so on.[25] In transition metal oxides, the nature of metal-oxygen bonding can vary between nearly ionic to highly covalent or metallic character.[24] The partially filled d subshell in such transition oxides opens up a wide range of magnetic and electronic properties.[24] Furthermore, the physicochemical properties of metal oxides depend on their preparation route and operating conditions. Especially, the electronic structure (bandgap) of these materials can be controlled by tuning their size and dimension. This allows a precise design of band gap (band gap engineering) and corresponding properties for specific applications.[26] Recent studies on metal oxides have been concentrated on some specific materials such as titanium oxide (TiO_2), tungsten oxide (WO_3), zinc oxide (ZnO), copper oxide (Cu_2O), tin oxide (SnO_2), and cadmium oxide (CdO) due to their tunable electrical, magnetic and catalytic etc. properties (by altering their size, shape, doping elements/amount and combining each other).

2.2 Semiconductors and Photocatalysis

In general, the light absorption by a semiconductor is a phenomenon that happens under an oscillated electromagnetic field, where several types of energy transfer proceed. A representative absorption spectrum of a semiconductor in the wide range of wavelength is demonstrated in **Figure** 2.1. For atoms and molecules, the electron excitation happens between specific energy levels of narrow width to provide relatively sharp spectra. However, the energy levels of electrons are extremely wide in semiconductor materials. Therefore, photons with energy more than the bandgap of semiconductor are absorbed in a remarkably wide range in the spectrum.

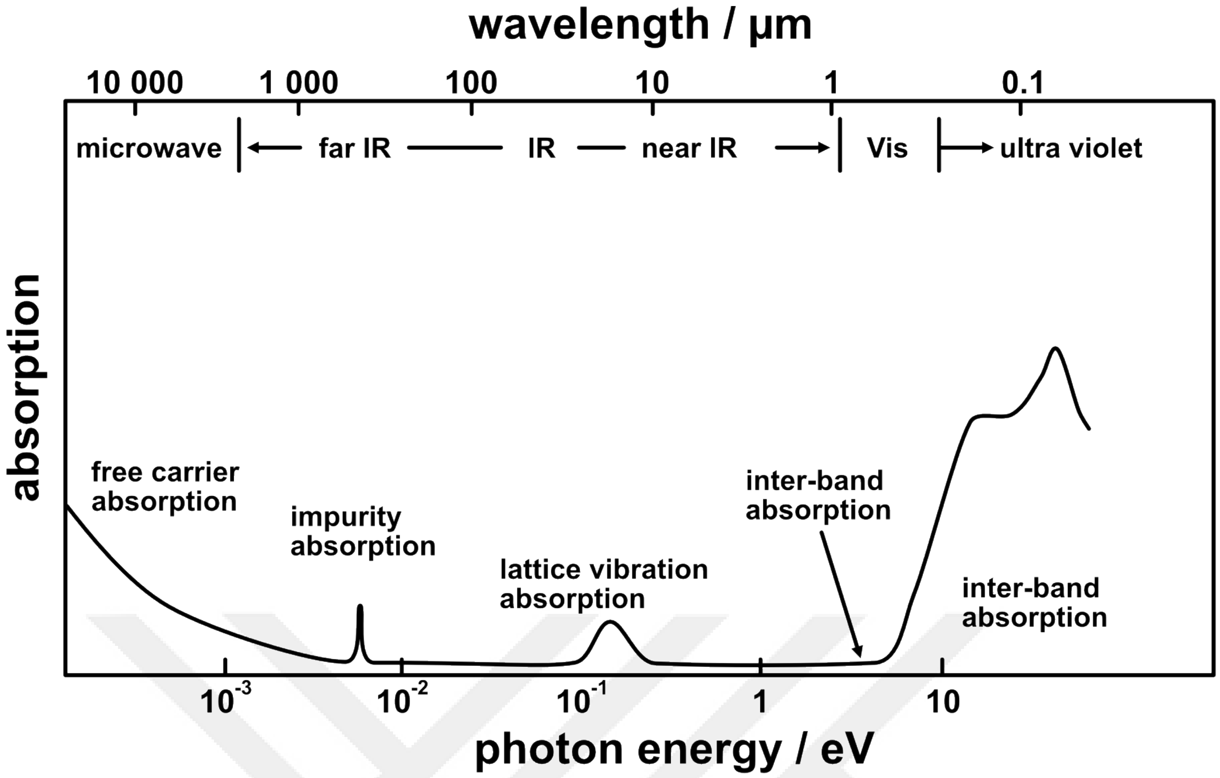

Figure 2.1. The representative absorption spectrum of a semiconductor. (Modified from [27])

Here, inter-band absorption can be classified into two types as a direct and indirect transition as schematically shown in **Figure** 2.2. The direct electron transfer occurs when the electron is excited from the maximum energy state (top) of the valance band to the minimum energy state (bottom) of the conduction band at the same wave vector ($\vec{k}$). Such a semiconductor is called a direct bandgap semiconductor. However, in some cases including Si and Ge, the maximum energy state of the valence band is not always the minimum energy state of the conduction band with the same $\vec{k}$. The electronic excitation from the top of the valance band to the bottom of the conduction band cannot occur, because the wave vector should be changed ($\Delta k \neq 0$). In this case, the light absorption happens along with the vibrational excitation of the crystal lattice ($\Delta k = 0$). The wave vector is changed by the excitation of phonon during the absorption process. Therefore, this case is called as indirect electron transfer and they are called as indirect bandgap semiconductors. Here, the absorption edge of the indirect bandgap semiconductor becomes gentle as compared to that of the direct bandgap semiconductor.

The optical properties of the semiconductor are determined by the bandgap. For example, if the semiconductor absorbs the photons which have more energy (E) than its bandgap (E_g), the electrons are promoted from the valance band to the conduction band. This phenomenon (promotion of the electrons) creates holes in the valance band. The electrons and holes generated in the photo-absorption process are called photoinduced charge carriers.

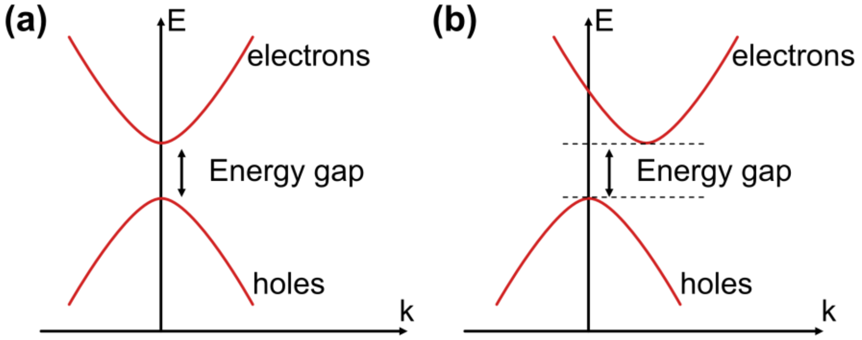

Figure 2.2. Band diagram illustration of (a) direct bandgap semiconductors and (b) indirect bandgap semiconductors. (Modified from [28])

The energy of these electrons and holes can be calculated by (Eq. 2-1) and (Eq. 2-2) equations according to energy levels of the upper edge of the valence band (E_V) and the bottom of the conduction band (E_C) at around k =0.

$$E_V(k) = -\frac{\hbar^2 k^2}{2m_h^*} \quad \text{Eq. 2-1}$$

$$E_C(k) = E_g + \frac{\hbar^2 k^2}{2m_e^*} \quad \text{Eq. 2-2}$$

Here, k is wave vector, $\hbar$ is the reduced Plank's constant, m_h^* and, m_e^* are the effective masses of the valence band hole and the conduction band electron, respectively. In general, at the absorption edge of the transition between bands, the absorption coefficient α is calculated by the equation (Eq. 2-3) below,

$$\alpha \propto \frac{(hv - E_g)^n}{hv} \quad \text{Eq. 2-3}$$

where hv is the energy of photons. Here, for allowed the direct and indirect transition from E_V to E_C, n should be 1/2 and 2, respectively. As can be seen, the electron transfer from E_V to E_C highly depends on the type (electronic state) of the semiconductor. Similarly, the recombination behavior of charge carriers (from E_C to E_V) is also influenced by the electronic state of the semiconductor as schematically shown in **Figure** 2.3.

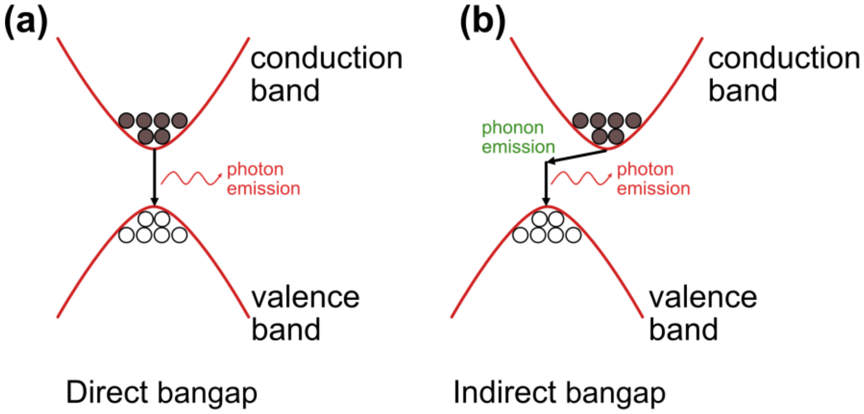

Figure 2.3. Schematic illustration of charge carrier's recombination mechanism in the **(a)** direct and **(b)** indirect bandgap semiconductors. (Modified from [29])

In the direct bandgap semiconductors, the recombination energy is emitted only in the form of the photon emission as schematically shown in **Figure** 2.3a. However, the recombination energy is released as a photon and a phonon caused by the difference in electron momentum in the indirect bandgap semiconductor (**Figure** 2.3b). Therefore, the lifetime of the charge carriers increases in indirect transitions and they exist at longer periods for possible chemical reactions.

The bandgap energy of semiconductors also depends on its physical dimensions. For example, nanoscale semiconductors have higher bandgap energy than bulk semiconductors (**Figure** 2.4). Here, the energy levels in the band become separate and they shift due to the limitation of the carriers in the particle when the size of the semiconductor becomes extremely small. This phenomenon is called the quantum size effect. In the case of a single atom or molecule (also identified as quantum dots) discrete energy levels exist. So, the nanoscale semiconductors (compared to bulk) have the absorption spectrum shifting to lower wavelengths which is also described as the "blue shift". The electronic structure (bandgap) of semiconductor materials can be tuned by controlling their size and dimension as aforementioned. The possibility of tuning properties increases the use of such materials in numerous applications, especially in photocatalysis. Various semiconductors have been examined as potential photocatalysts.

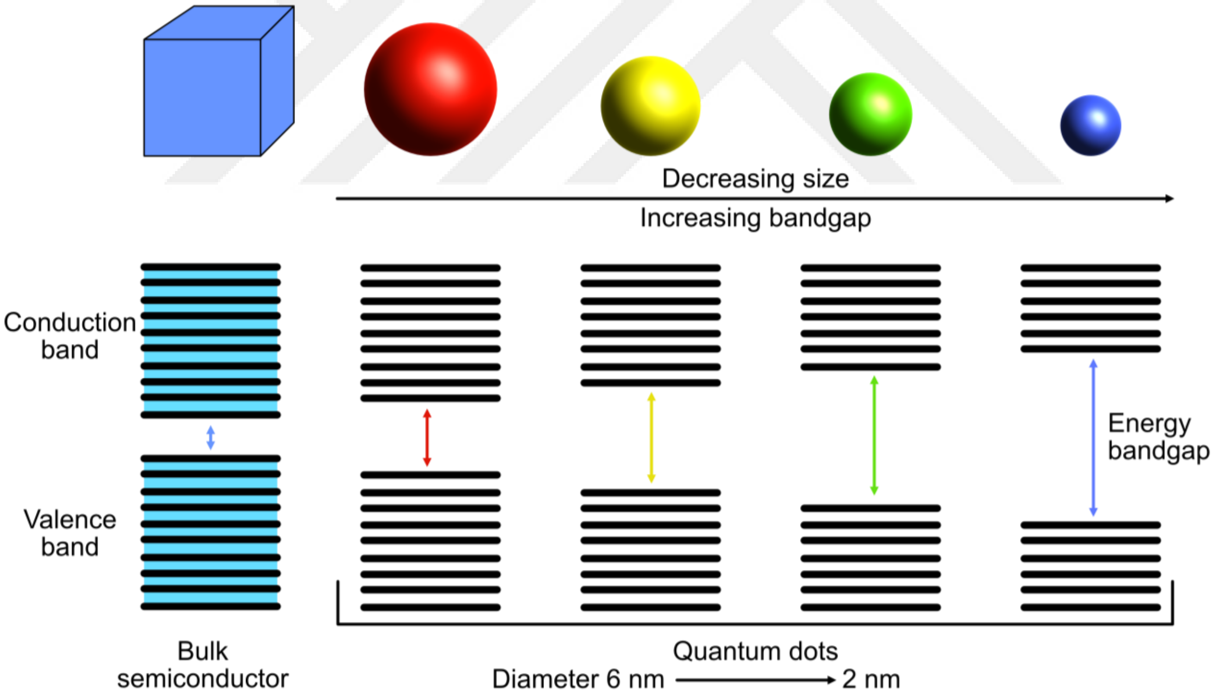

Figure 2.4. Energy band variation in quantum dots as the size is varied. (Modified from [30])

Photocatalysis, which directly converts solar (light) energy into chemical energy, is considered as one of the most encouraging approaches for energy resource and environmental degradation problems. This approach has several benefits, including high efficiency, low-cost and environmental protection, the entire degradation of pollutants, without any secondary pollution. Commonly, a metal-oxide semiconductor photocatalyst is composed of light-harvesting, exiting electrons to form charge carrier (electron-hole pairs), charge separation and transfer, and surface oxidation and reduction reactions as schematically shown in **Figure** 2.5.

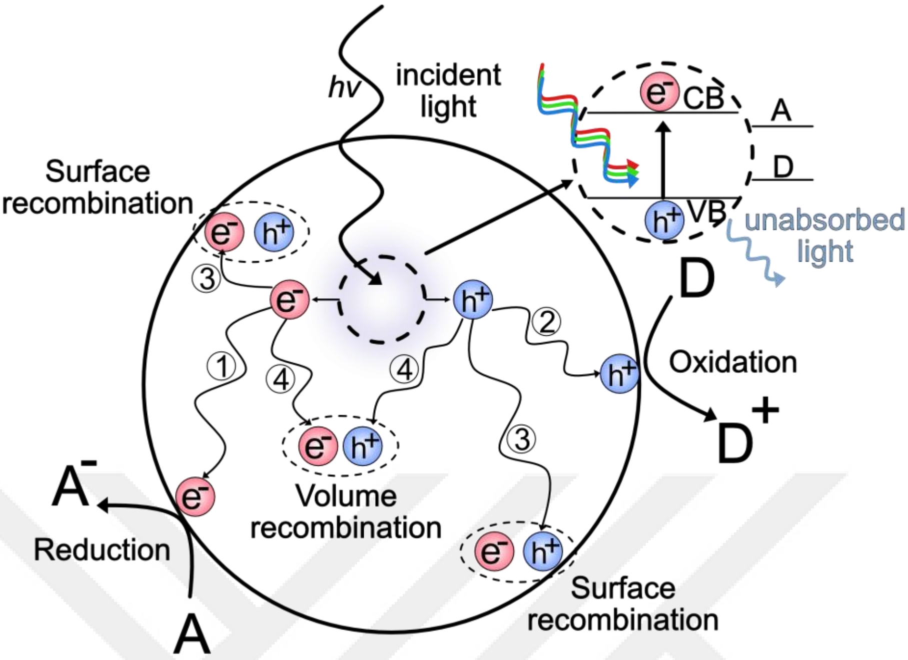

Figure 2.5. Overall photoexcitation and charge transferring pathway of photocatalyst in nanoparticle form (A: Acceptor and D: Donor). (Modified from [31])

When the energy of the incident light is larger than the bandgap energy of the semiconductor, the electrons in the valance band of the semiconductor are excited to the conduction band by photons, and the corresponding holes are generated in the valence band. Basically, photogenerated electrons and holes (charge carriers) move to the outer surface of the semiconductor. The photogenerated electrons have strong reducing properties and they reduce the substances (like organic compound) adsorbed on the surface of the semiconductor. However, photogenerated holes oxidize the substance absorbed on the surface.

Photocatalysis is the most effective approach to decompose various organic pollutants owing to its high efficiency, eco-friendly nature, and low-cost.[1] Heterogeneous photocatalysis has become a hot topic in the field of green chemistry. Currently, several types of metal oxide semiconductors materials for instance TiO_2, ZnO, WO_3, and combinations of them have been used as photocatalysts.[2]

2.3 TiO_2 Photocatalyst

As early as in the 1960s, many research groups investigated the photoinduced phenomena under UV illumination using a semiconductor such as TiO_2 and ZnO. They found that some molecules such as O_2 and H_2O are absorbed and desorbed by the semiconductor surface during UV irradiation, respectively. This phenomenon is a clear consequence of photogenerated charge carriers and their migration to outer surface.[32] Similarly, Kato et al. reported the oxidation reaction of tetralin in the liquid phase using TiO_2 photocatalyst during the UV illumination.[33] This study can be considered as one of the first reports in the literature for the photocatalytic use of TiO_2 under UV illumination. TiO_2 became the most popular metal oxide photocatalyst after the pioneering study of Fujishama and Honda in 1972.[3]

TiO_2 is the most studied photocatalyst owing to its low cost, high stability, and activity. It has three different crystal structures: anatase, rutile, and brookite (**Figure** 2.6). The ore of rutile is usually gained as a reddish-brown crystal. The name of "rutil" is "red" in the Greek language. However, pure TiO_2 is colorless in all crystalline forms. The origin of the "anatase" is "upward tension" in the Greek language due to its long crystalline form. Brookite was named after an English mineralogist "H. J. Brook". Rutile is a thermodynamically more stable phase than the others. This means that all TiO_2 is transformed to the rutile phase at a higher temperature. Brookite is a highly unstable form compared the rutile and anatase and it is difficult to obtain as a pure crystal form. Rutile is commonly used for a pigment while anatase is widely used for photocatalytic applications.[27]

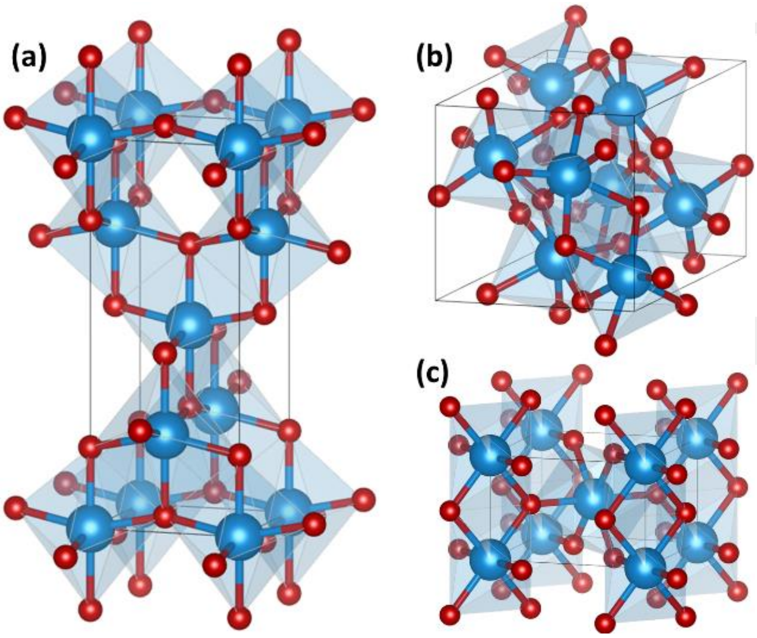

Figure 2.6. Crystal structures of **(a)** anatase, **(b)** rutile, and **(c)** brookite.

In general, the photocatalytic performance of anatase is higher than that of rutile. One of the main reasons might be the difference between their bandgap.[34] The bandgap of anatase is around 3.2 eV (restricts its activity limit to UV light) and it is 0.2 eV higher than that of rutile. However, an indirect bandgap structure rather than direct helps minimizing the electron-hole recombination during the photocatalytic reaction. This difference in the band gap structure between anatase and rutile has more impact on the photocatalytic activity of TiO_2.[35] Moreover, in case of anatase, the excited electrons ($E = -0.66$ eV vs. SHE) have enough energy for the reduction of H^+ to hydrogen, while holes ($E = 2.54$ eV vs. SHE) oxides water to oxygen. Both reactions help degrading many organic pollutants for overall photocatalytic effect.

The absorption of light (photons) by TiO_2 causes the photocatalytic reaction at its surface which allows the degradation of organic compounds and dissociation of water molecule (water splitting). Although the detailed mechanism of photocatalytic reactions vary depending on the type of the organic pollutant, briefly photogenerated charge carriers play the major role for photocatalysis (**Figure** 2.7).

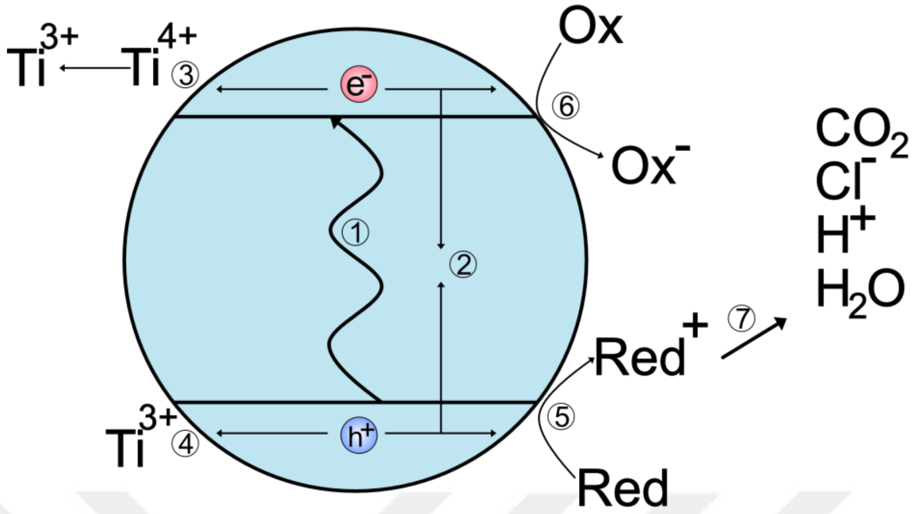

Figure 2.7. Photocatalytic reaction mechanism of TiO_2 photocatalyst under UV illumination. (Modified from [2])

Primary steps in the photocatalytic degradation are classified as following steps: (1) generation of charge carriers (electron-hole pairs) by photon absorption; (2) recombination of charge carriers; (3) trapping of electrons at conduction band (Ti^{4+} site to yield Ti^{3+}); (4) trapping of electrons at valence band; (5) oxidative reaction pathway by holes at valence band; (6) reductive reaction pathway by electrons at conduction band; and (7) further thermal and photocatalytic reaction to produce mineralization products.

2.4 Enhancing the Photocatalytic Activity

TiO_2 has been widely used photocatalyst in the literature in comparison to other transition metal oxide semiconductors as mentioned before. However, one of the major challenges in TiO_2 photocatalyst is insufficient sunlight utilization. TiO_2 is only photoactivated by UV irradiation which accounts for ~5% of the full solar spectrum. Furthermore, the TiO_2 also suffers from the inefficient photogenerated charge (electrons and holes) separation and the correspondingly poor quantum efficiency. Some strategies including the tuning of optical properties to achieve a broad-band absorption, the optimization of charge (electron and holes) separation/recombination by heterojunctions, and the use of cocatalysts have been proposed to enhance the photocatalytic performance of TiO_2.

2.4.1 Plasmonic Enhancement of Photocatalytic Performance

The heterojunction structure by coupling plasmonic materials (such as gold, silver, aluminum etc.) with TiO_2 can significantly enhance photocatalytic activity due to localized surface plasmon resonance (LSPR), which promotes the photoexcitation of electrons-holes pairs (charge carriers) in TiO_2.[36] Plasmonic energy transfer can be categorized to three major mechanism as light scattering/trapping, hot electron injection and plasmon-induced resonance energy transfer (PIRET) (schematically shown in **Figure** 2.8).

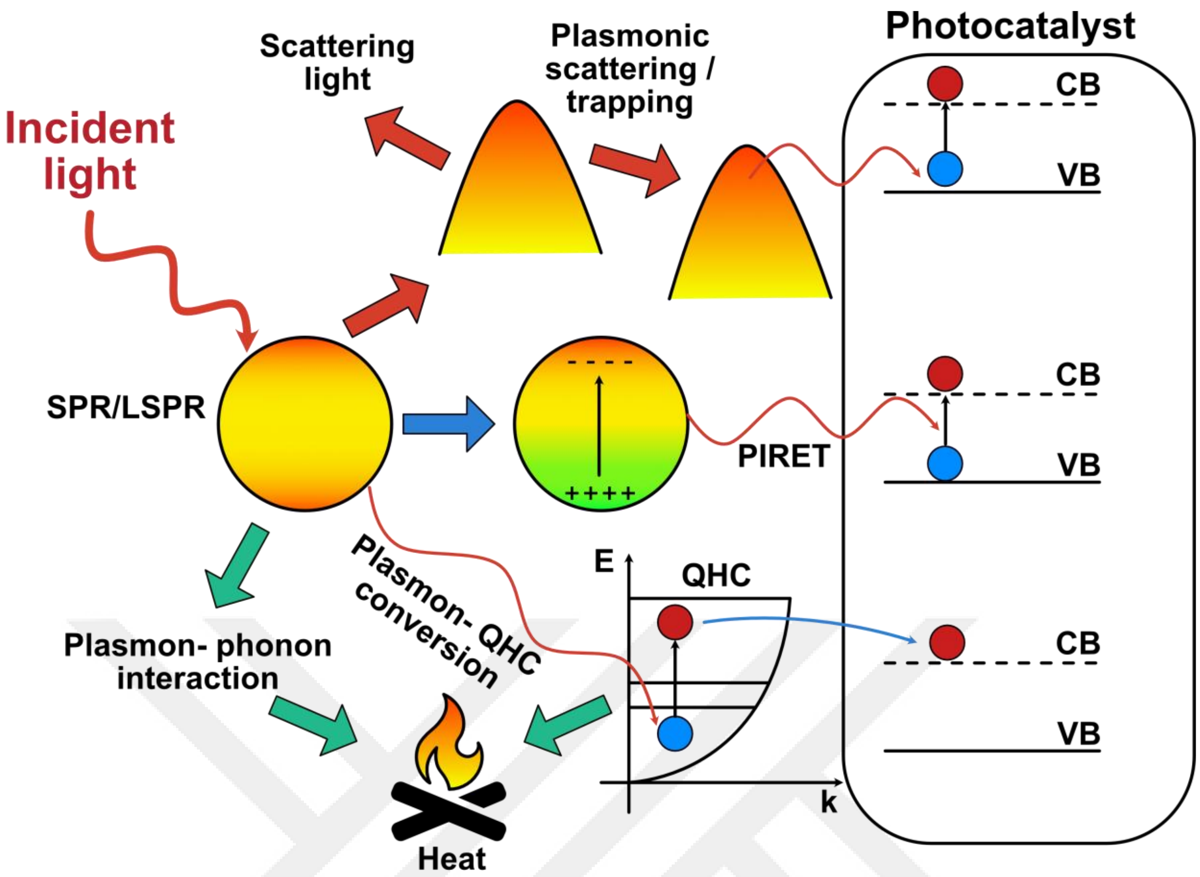

Figure 2.8. Different types of energy transformation by plasmonic contribution in the photocatalytic reactions. QHC: Quantum hot carriers (Modified from [40])

Interest in plasmonic photocatalysis was reported first in the mid-2000s (especially after the study reported by Awazu et al.) and these materials have been getting increasing interest during the last 10 years.[37] Mainly, the two critical issues (in all published studies) are addressed to achieve an efficient plasmonic (visible-light-driven) photocatalyst. These are (1) reducing the absorption energy below 3 eV (photocatalytic reaction can take place under UV illumination) and (2) improving the separation of photogenerated charge carriers (electrons and holes) for reduction and/or oxidation reaction before their recombination.

The plasmonic photocatalyst generally consists of noble metal nanoparticles and the semiconductor photocatalyst where such particles are decorated.[38,39] When the noble metal and the semiconductor connect each other, the specific interface is formed, which is called as Schottky barrier. The Schottky barrier causes the transferring the hot electrons, in the metal, to the conduction band of the TiO_2. This phenomenon improves the electron-hole separation, yielding a high photocatalytic efficiency.[17] Such a Schottky barrier fosters hot electron transfer which requires an energy level of 1 eV to 4 eV. Aside from the hot-electron transfer, plasmon-induced resonance energy transfer also affects the enhancement of the photocatalytic efficiency.

In a photocatalytic system, plasmon can induce different effects as shown in **Figure** 2.9. These effects alter the key chemical and physical process in TiO_2 such as charge separation/recombination, and light absorption. The plasmon can be tuned by altering the material type, shape, size, and interspacing of nanoparticles to be used.[41] For instance, the plasmon resonance of Au can be shifted from the visible wavelengths range into the infrared wavelengths range by decreasing the size of the nanoparticles. Similarly, it is also possible to change the plasmon resonance of Ag from UV to the visible wavelengths range by reducing their size down to ~10 nm.[42]

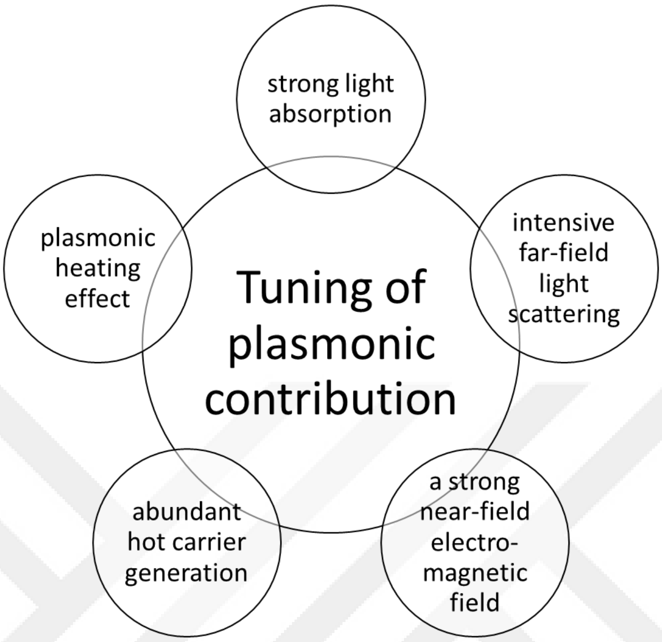

Figure 2.9. Tuning of plasmonic contribution in the photocatalytic reaction by various strategies.[40]

2.4.2 Non-plasmonic Enhancement of the Photocatalytic Performance

In addition to plasmonic enhancement, metal-semiconductor (TiO_2) hybrid structures can also be used to enhance photo/catalytic efficiency, which is called as a non-plasmonic enhancement. As mentioned before, a semiconductor like TiO_2 has low photocatalytic activity because of the high recombination rate of the electrons and holes. However, many studies have reported that noble metal (Au, Ag, etc.) loaded TiO_2 structures enhance the photocatalytic activity upon UV illumination.[43] In such a system, the photogenerated electrons, at the TiO_2 surface, are moved to Au nanostructures functioning as highly charge separation and strongly promote the redox reactions. **Figure** 2.10 shows the main difference in the mechanism of non-plasmonic and plasmonic enhancement. The metal nanoparticles trap the photoexcited electrons and they act as electron sink centers as shown in **Figure** 2.10a. Reduction and oxidation reactions happen at the semiconductor and metal surfaces, respectively.[44] Here, non-plasmonic enhancement can be also combined with plasmonic enhancement to increase the overall performance by using different light sources. This process is also called as **synergistic effect of photocatalysis,** which is an alternative to plasmon-enhanced photocatalysis.

As the mechanism is shown in **Figure** 2.10, where TiO_2 in combination with Au nanoparticles improves the photocatalytic efficiency under UV (**Figure** 2.10a) and as well as visible (**Figure** 2.10b) irradiation. Recently, Yan et al. reported that the photocatalytic activity of Au/TiO_2 hybrid structure under UV and visible irradiation. The photocatalytic performance, under such a mix irradiation (both UV and visible), was significantly higher than that only under UV irradiation. They reported that the synergetic effect of using mix light (both UV and visible) could be the reason for the improvement of the overall performance.[45] However, Lin et al. showed that when visible irradiation energy increases (under constant UV irradiation intensity), more hot electrons exist on the surface of the Au nanoparticles as a result of the LSPR absorption. This reduces photocatalytic efficiency by suppressing the electron transferring from TiO_2 to the Au nanoparticles.[43] Therefore, the ratio between UV and visible irradiation is an important parameter to control the efficiency of the overall photocatalytic reaction.

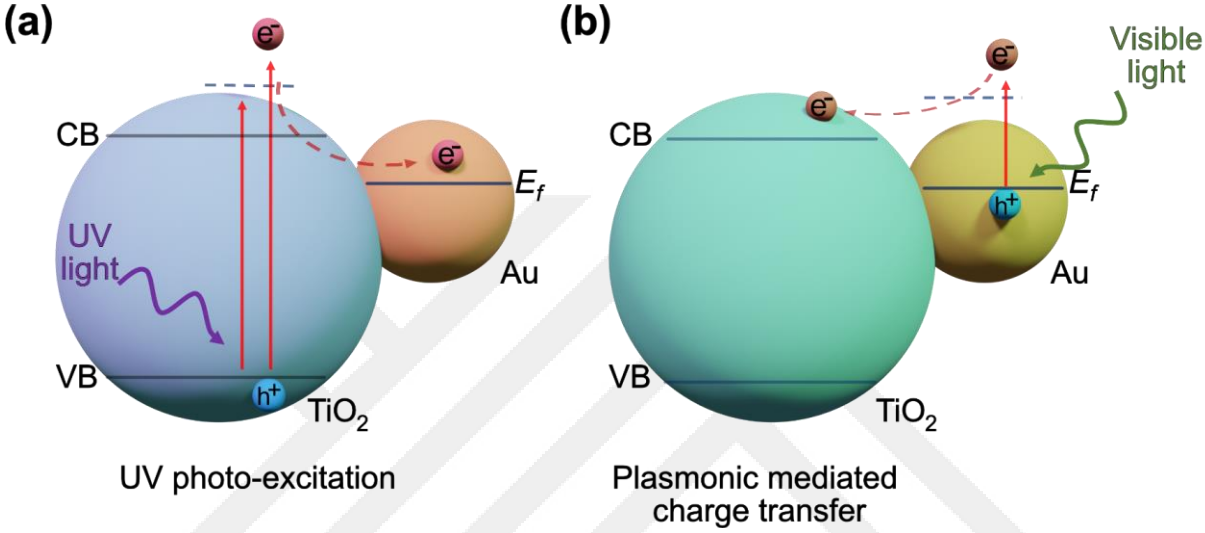

Figure 2.10. The schematic description of (a) non-plasmonic and (b) plasmonic enhancement in the photocatalytic reaction. (Modified from [43])

The size and distribution of metallic nanoparticles on metal oxides are also crucial for enhancing the photocatalytic efficiency. These nanoparticles are ideal candidates for photocatalytic applications, compared to a bulk metal which is mostly inert in various chemical reactions.[46] Synthesis of Au particles on the nanoscale brings some difficulties such as the agglomeration and instability of the particles which decrease the photocatalytic efficiency enormously. Therefore, it is essential to control the size, shape, and formation of stable plasmonic and non-plasmonic nanoparticles.[47]

2.4.3 Coupling Metal-Oxides (heterojunction) for Enhancement of Photocatalytic Performance

The coupling of TiO_2 with other metal oxide semiconductors (ZnO, CeO_2, and PdO) improves the photocatalytic efficiency of TiO_2 via enhancing the charge separations and broadening the absorption of the solar spectrum.[48] Among these metal oxide semiconductors, CeO_2 has gained much attention because of its special electron orbital structure, high thermal stability, oxygen storage capability, unique catalytic, and optical properties. The fluctuating of oxidation states between Ce^{3+} and Ce^{4+} plays a major role on the catalytic and optical properties cerium oxide.[20] There are various research studies on the synthesis of mixed oxides composed of TiO_2 and CeO_2 for their functional use in photocatalytic and catalytic applications.[49–51]

TiO_2 and CeO_2 are photoactive under the UV region of the solar spectrum. During the UV irradiation, electrons (at conduction band) and holes (at valance band) react with oxygen and water molecules to generate radicals which decompose organic materials, respectively. Moreover, the heterojunction at TiO_2 and CeO_2 interface promotes the charge separation and increases the lifetime of the charge carriers (electrons and holes) (**Figure** 2.11). This enhances the photocatalytic efficiency of the TiO_2-CeO_2 hybrid structures compared to those of individual TiO_2 or CeO_2.[21]

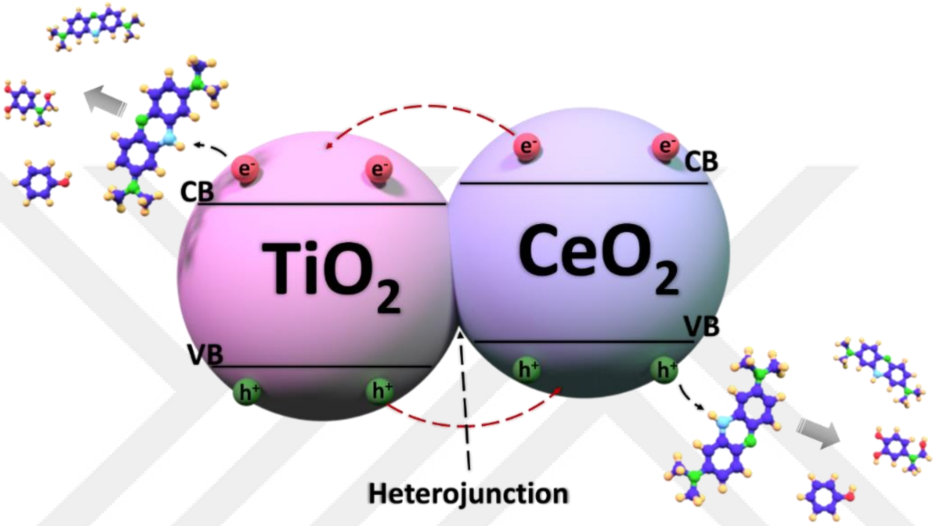

Figure 2.11. Photocatalytic reaction mechanism of TiO_2-CeO_2 photocatalyst under UV irradiation. (Modified from [52])

Similar to TiO_2-CeO_2 hybrid structure, Pd and PdO can also be used to form heterojunction on TiO_2.[22] Zhou et al. reported that PdO-TiO_2 nanobelts showed high photocatalytic activity toward the degradation of methylene blue (MB) and rhodamine B (RhB) under UV and Visible illumination.[53] A steady equilibrium between PdO and PdO_2 phases seems to provide an efficient charge carrier (electron-hole pair) separation.

As it was mentioned previously, decorating plasmonic and non-plasmonic nanoparticles on TiO_2 enhances the photocatalytic activity of TiO_2 under UV and visible irradiation. Similarly, such an approach can be used to enhance the photocatalytic activity of the TiO_2-CeO_2 hybrid photocatalyst. Zhu et al. reported that Au/CeO_2-TiO_2 nanoparticles showed higher photocatalytic efficiency in comparison to CeO_2-TiO_2, Au/CeO_2, and Au/TiO_2 under UV and visible light illumination.[54] The authors showed that the molar ratio between TiO_2 and CeO_2 was a crucial parameter to achieve high photocatalytic efficiency.

Both coupling metal oxides (hybrid oxide structure) together and decorating such metal oxides with plasmonic and non-plasmonic nanoparticles strongly improve the photocatalytic and catalytic efficiency. These hybrid structures show significant catalytic performance, but it is difficult to recycle these particles from the solution. Therefore, it is necessary to produce a robust thin film for photocatalytic and catalytic applications.

2.5 Self-cleaning Effect Induced by Metal Oxides

Self-cleaning surfaces have been getting a great deal of interest for both their unique properties and practical applications for a variety of technology especially in energy and environmental areas. Generally, self-cleaning surfaces are divided into two categories according to their contact angles (CAs) as: (a) superhydrophilic surfaces and (b) superhydrophobic surfaces.[55] In this context, it is important to attain surfaces with CAs < 10° and/or CAs > 150° for self-cleaning applications. Although a wide range of practical applications and commercial products including fabrics, skyscraper windows, furnishing materials, glass, cement, paints, car mirrors, and solar panels exist further studies are needed to increase the efficiency and utilities of photocatalytic self-cleaning materials.[56] These materials/products can easily be cleaned by a stream of natural water such as rain, which reduces the maintenance cost. The fabrication of multifunctional photocatalytic materials, for self-cleaning applications, by integrating biologically inspired structures (micro- or nanoscale topography) would be favorable for environmental concerns.

2.5.1. Passive Self-Cleaning Effect

It is well known that when water drops roll off the lotus leaves, the dirt or dust particles are removed from the surface. This phenomenon is commonly known as the "Lotus effect".[57] During the spreading of a water drop, the contaminants on the surface are easily washed away due to the water repellent and low adhesive properties of hydrophobic surfaces (**Figure** 2.12).

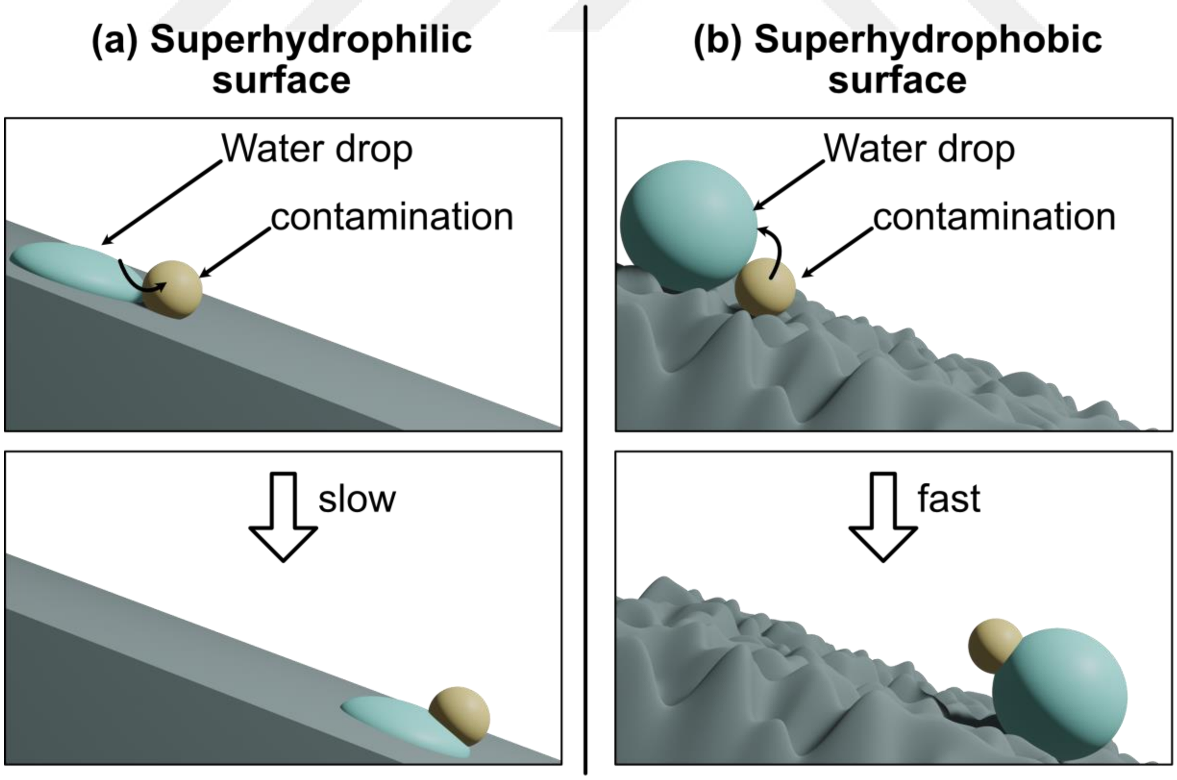

Figure 2.12. Schematic illustration of passive self-cleaning mechanism on (a) a superhydrophilic and (b) a superhydrophobic surface. (Modified from [58])

The passive self-cleaning effect depends on both physical and chemical topography of materials surface.[59] Here, a water drop can easily slide from the sample surface and clean the contamination is illustrated in **Figure** 2.12. The surface roughness is an important parameter for the passive self-cleaning surfaces. For example, surface roughness makes a hydrophobic surface even more hydrophobic (superhydrophobic- low surface energy) and a hydrophilic surface even more hydrophilic (superhydrophilic-high surface energy). Therefore, the adhesion of the contamination on the superhydrophobic surfaces is several times lower than on the superhydrophilic surfaces. The water drops can easily roll off the superhydrophobic surface by the help of surface energy and gravity (slightly titled) while cleaning the contamination from the surface.

2.5.2. Active Self-Cleaning Effect

One can mention an active self-cleaning concept which covers both photocatalytic degradation of organic contaminants and photo-induced hydrophilicity under the UV light. Photo induced hydrophilicity is one of the most studied mechanisms in semiconductor oxides. Among the various metal oxide semiconductors, TiO_2 has been widely investigated due to its photocatalytic and photoinduced hydrophilic properties.[55] Furthermore, TiO_2 is considered to be an ideal choice for self-cleaning applications because of its good transparency in the visible light spectrum. In the self-cleaning mechanism, first, TiO_2 degrades the organic contaminants under UV illumination and second photoinduced hydrophilicity decreases the water contact angle and therefore removes the contaminant from the TiO_2 surface by rainfall.

Numerous mechanisms have been demonstrated to account for the photoinduced hydrophilicity showed by TiO_2 containing [60];

- generation of photo-induced surface (especially oxygen) vacancies
- light-induced formation of surface OH^- groups
- photoinduced removal of contaminants from TiO_2 surfaces exposed to air or/and water

In photoinduced hydrophilicity, some electrons interact with the surface trapped electrons sites while some of the holes react with lattice oxygen creating oxygen vacancies during the UV illumination (photocatalytic reaction mechanism was explained in detail at Section 2.3). Therefore, the binding energy between titanium and oxygen atoms decreases. After UV illumination, the surface becomes more suitable for the absorption of hydroxyl groups due to the creation of oxygen vacancies (**Figure** 2.13). However, in the dark environment, the TiO_2 surface has reversible wettability which is an additional advantage in comparison to other materials.[61]

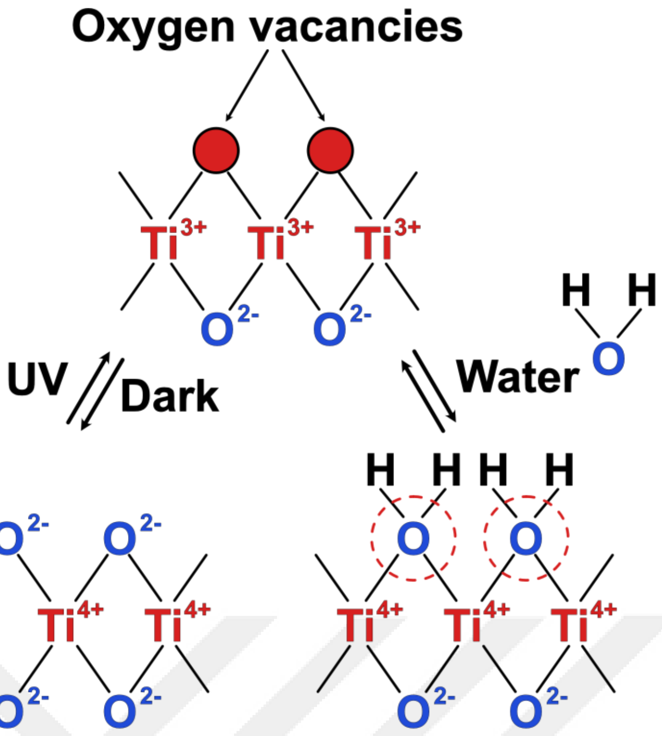

Figure 2.13. Schematic representation of photo-induced hydrophilicity. (Modified from [58])

Here, the replacement of the absorbed OH- groups by oxygen mainly causes the conversion from superhydrophilic to superhydrophobic states. Oxygen bridging sites also play a significant role in the surface wettability conversions. After TiO_2 has a metastable state during the UV illumination, this state recovers quickly after UV illumination is completed. However, the hydrophilic properties of TiO_2 depend on the relative humidity and oxygen content in the environment beside the photocatalytic properties.[62]

2.5.3. Combination of Passive and Active Self-Cleaning Effect

Numerous approaches have been reported by several groups to enhance the photocatalytic performance and active self-cleaning effect of TiO_2-based materials. Here, the contact area between TiO_2 and contaminations is highly important to degrade the organic contaminants by the photocatalytic reaction. That is why for an active self-cleaning effect one needs high wettability (hydrophilic) on the surface. However, due to high contact interaction, contaminations (dust, etc.) can adhere to the TiO_2 surface and increase the surface roughness, which may lead to a hydrophobic behavior. This may malfunction the self-cleaning effect of the TiO_2 surface.[63]

The active self-cleaning effect can be used in combination with the passive self-cleaning effect to improve the cleaning efficiency of the surface (by overcoming adhesion of organics on the surface). Surface modification, for instance inducing surface roughness, might be a favorable way to improve the self-cleaning performance. Recently, the coupling of TiO_2 with other materials (plasmonic, non-plasmonic metals, and metal oxides) enhances the charge separation (electron and hole pairs) to increase the photocatalytic and self-cleaning activity. Furthermore, the surface roughness in combination with the heterostructure formation can be used to fabricate superior photocatalytic/self-cleaning materials.

2.6 Unconventional Surface Patterning by Photodeposition

In the literature, various studies were published about the synthesis of noble (Au, Ag, Pt, etc.) nanostructures with different shapes and sizes.[64] However, it is still a challenge to achieve good adhesion between these nanoparticles and metal oxide surfaces. Therefore, some approaches (seed-mediated growth and electrodeposition methods) have been proposed to enhance the adhesion of nanoparticles on metal oxide by using some binder molecules (thiols and silanes etc.).[65] Mostly organic molecules are used for binding nanoparticles with a solid substrate. However, these may decrease the surface conductivity and affect the catalytic activity of the deposited particles.[66] Electrodeposition methods can also be considered to prepare plasmonic and non-plasmonic nanoparticles on solid substrates. But, the electrodeposition process works only on the conductive substrate such as indium tin oxide (ITO).[65] Therefore, there is a need to prepare stable plasmonic and non-plasmonic nanoparticles on metal oxide thin films without using any organic molecules (binders) or a conductive electrode.

One can deposit various metallic structures on metal oxide semiconductors by photocatalytic reduction regardless from the conductivity of the surface.[67] Such a photocatalytic deposition method allows for controlling the geometry and the size of the micro- and nanostructures to be deposited by simply changing the photocatalytic activity of the metal oxide (used as the substrate), UV light intensity, and irradiation time. Furthermore, the positioning and patterning of micro- and nanostructures on the semiconductor photocatalyst without using any surfactant or stabilizer are also possible for this approach.

3 Methods and Characterization

The methods related to the preparation and characterization of thin films and micro- and nanostructures will be presented in this chapter. Firstly, the process of sputtering and nanocluster formation, using gas aggregation source (GAS), will be explained. Second, a photocatalytic deposition method will be introduced for the synthesis of micro- and nanostructures on sputter-deposited thin film surfaces. Finally, the specific analytical methods, performed for characterization of the prepared hybrid thin films and micro-/and nanostructures will be briefly described. However, specific preparation and characterization methods will be introduced separately in corresponding publications.

3.1 Preparation of Thin Film and Hybrid Structures

3.1.1 Sputtering of Metal and Metal Oxides

A. Relevance to experimental work in thesis

- Preparing of TiO_2 thin films (Publication 2, Publication 3, Publication 4, Publication 5, Publication 6, Publication 7 and Publication 8).
- Depositing of CeO_2 nanoclusters on to TiO_2 thin films (Publication 8).

B. Technical details and theoretical background

Sputter deposition is a widely used physical vapor deposition (PVD) method which allows ejection of the material from a surface 'target', then depositing it onto a 'substrate'. It is a highly preferred approach where stoichiometry, purity, density, and adhesion are essential for the aimed thin film. Generally, the sputter deposition method is extensively used to prepare thin film on semiconductor materials, reflective coatings, magnetic films, and hard coatings (tools, engine parts), etc. This physical sputtering technique is based on the ion bombardment of a target in a vacuum system. Here, an electrically excited gas plasma hits the target surface and physically ejects some atoms from the surface by momentum transfer. These ejected atoms gather on all surfaces including the substrate surface.[68,69]

Beside the sputter deposition method pulsed laser deposition and especially thermal evaporation are usual preferred PVD methods. In sputter deposition, the target is kept at a low temperature by cooling water behind it, and atoms are removed from the target surface by momentum transfer rather than by heat (unlike evaporation method). This is a major difference between sputtering and evaporation techniques, which makes the sputtering films are more compacted and denser than which evaporation method used [70]. In sputter deposition, some process parameters have to be controlled to prepare reproducible films.[71] These are schematically demonstrated in **Figure** 3.1

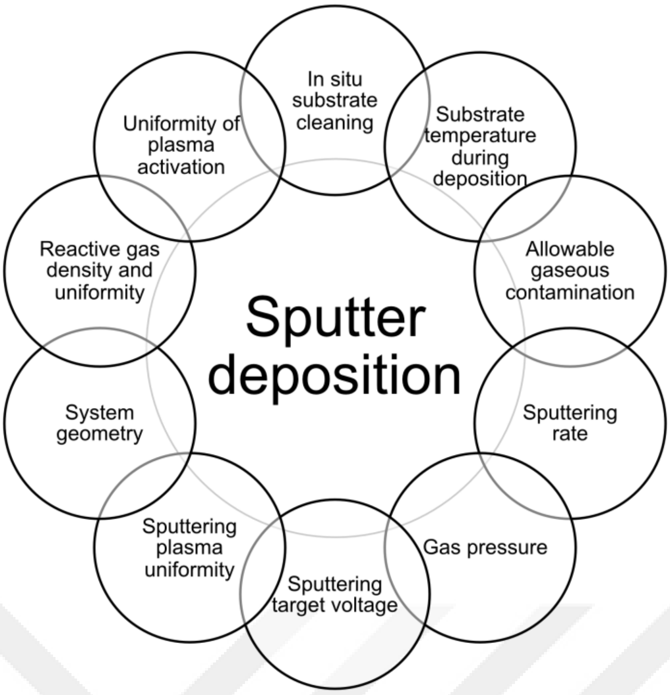

Figure 3.1. The deposition parameters of the sputtering.

The most common approach for the sputter deposition is the use of a magnetron source, which is named as "magnetron sputtering". Here, a magnetic field is applied around the target to energize argon atoms for bombarding the target. This magnetic field traps the electrons around the target. Therefore, higher ionization of argon atoms increases the deposition rate. In magnetron sputtering, the target can be powered in different techniques such as current (DC) for conductive targets and radio frequency (RF) for nonconductive targets.[68]

The first modern planar magnetron was invented by Chapin et al. in 1979. He tried to solve the drawback of diode sputtering, called magnetron sputtering afterward, such as low deposition rates and high thermal load to substrates. The new planar magnetron approach could be used to overcome these problems and suitable for industrial applications.[72] Here, the magnets are attached to the backside of the target to control the electron movement by a generated magnetic field as schematically demonstrated in **Figure** 3.2. Here, a glow discharge is ignited between two electrodes in a vacuum environment when an electrical voltage is applied through the target. Afterward, the bombardment occurs as positively charged ions, which are accelerated to the cathode.

Generally, Ar atoms (buffer gas) and consequent emission of secondary electrons are mainly responsible for the collision between the particles. However, the induced magnetic field line limits the motion of electrons and ejection of target atoms from the target material. The planar magnetron target is cooled by water during the sputtering process.

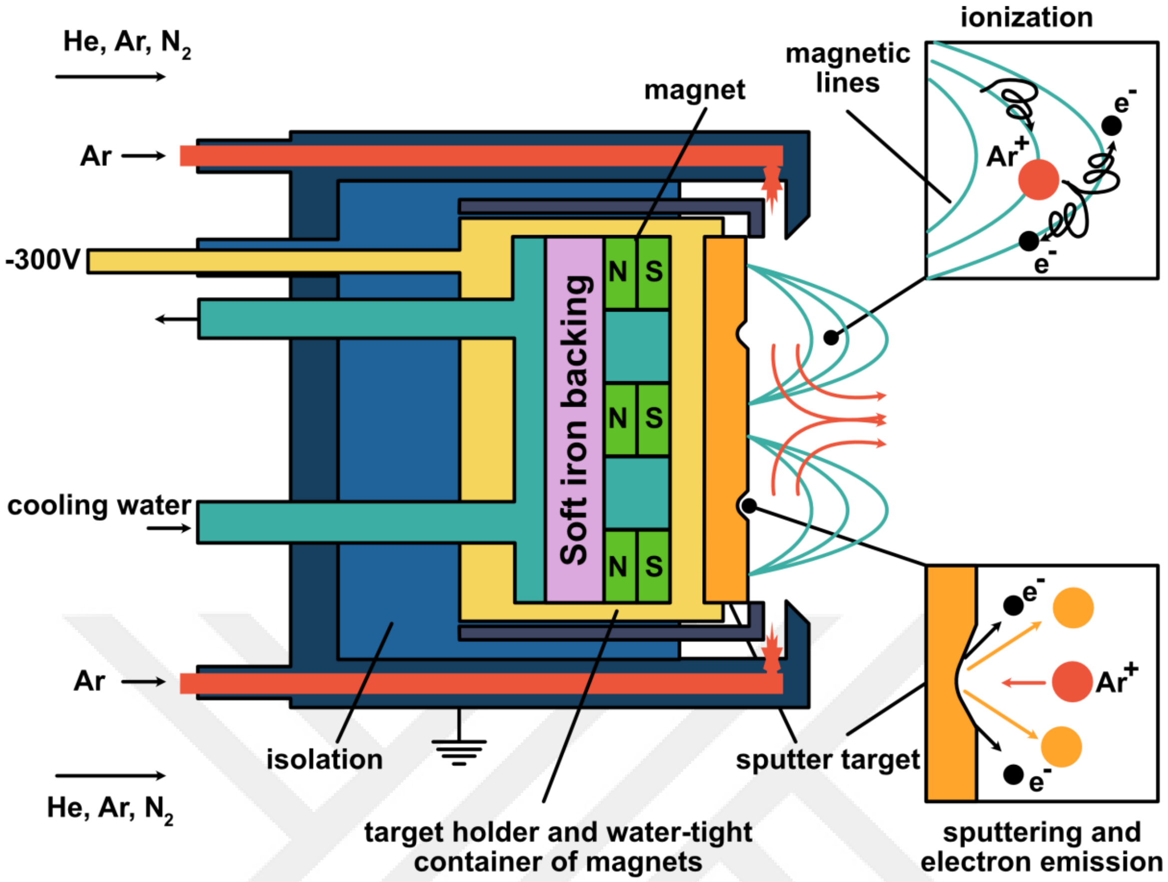

Figure 3.2. The schematic diagram of a magnetron sputter head and electron trapping occurs by the magnetic field. (Modified from [73])

During the magnetron sputtering process, both the electric field and the magnetic field affect the motion of electrons and the force acting on the electron under the electromagnetic field. This phenomenon is determined by the Lorentz Force, determined by the following equation (Eq. 3-1).[74]

$$\boldsymbol{F} = q_e\,(\boldsymbol{E} + \boldsymbol{v} \times \boldsymbol{B}) = m_e\,\boldsymbol{a} \qquad \text{Eq. 3-1}$$

where q_e is the charge of electrons, $\boldsymbol{E}$ and $\boldsymbol{B}$ are an external electric and magnetic field, $\boldsymbol{v}$ is the velocity of electron, m_e is the mass of electron and $\boldsymbol{a}$ is its acceleration. Here, when the electrons enter the magnetic field, they follow the magnetic field line which is parallel to the sputter target. Therefore, the ring-shaped glow and circular groove on the sputter target. However, the Ar^+ ions are free to move in the magnetic field due to their relatively heavy mass than electrons. This leads to a higher concentration of electrons and ionized gas near the sputter target region and increases the possibility of bombardment events causing higher sputtering rates.[75]

3.1.2 Metal and Metal Oxide Cluster by Gas Aggregation Source (GAS)

A. Relevance to experimental work in thesis

- Deposition of Al nanoparticles on to TiO_2 thin films (Publication 6).
- Deposition of PdO nanoparticles on to TiO_2 thin films (Publication 7).

B. Technical details and theoretical background

The concept of a gas aggregation source (GAS) approach was first demonstrated by Sattler et al. [76] and further developed by Haberland et al.[77] They used a planar magnetron as a source to form nanocluster. Here, the planar magnetron source produces charged clusters and nanoparticles, which are dragged by the flow of the carrier gas (especially Ar). Afterward, these clusters and nanoparticles are separated from the source through an orifice into the deposition chamber which has lower pressure as schematically shown in **Figure** 3.3.

Mainly, GAS requires an additional chamber (with a small nozzle at the end of the chamber) compare to the conventional magnetron sputtering approach. This additional chamber is connected to a deposition chamber which is maintained under ultra-high vacuum by the support of the turbomolecular pump system. The pressure gradient between the aggregation and deposition chambers play a crucial role in particle formation due to the small orifice. This pressure difference can be controlled by either the size of the orifice or additional vacuum pump which is directly connected to the GAS chamber. The formed nanoparticles in the aggregation chamber are carried out through output orifice with continuous flowing the inert gas (Ar or He) into the vacuum deposition chamber in the form of a cluster beam. Afterward, formed nanoparticles are finally deposited onto a substrate.

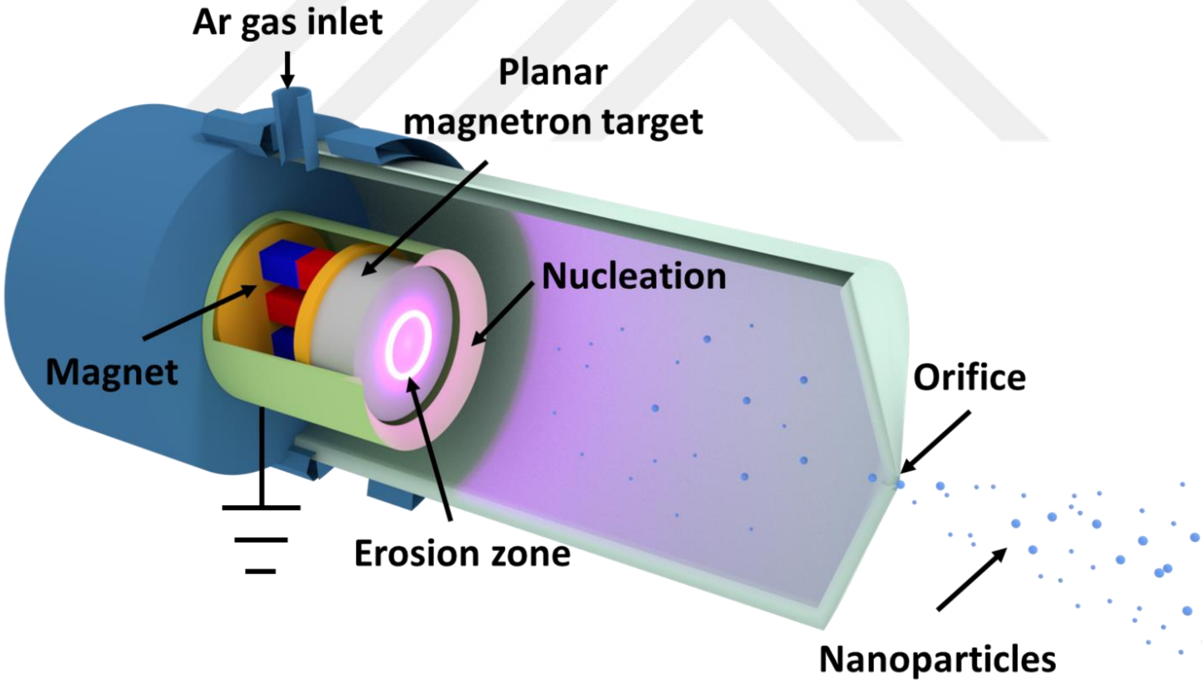

Figure 3.3. Working principle of gas aggregation source (GAS).

The main advantage of the GAS approach is non-dependence on deposition time in terms of morphology. The deposition time only affects the coverage of nanoparticles on the substrate compared to the sputter deposition method.[78] However, the size of the formed nanoparticles highly depends on some operating parameters such as the inert gas (Ar or He) flow, the sputtering discharge power, rate and the aggregation length.[79] Furthermore, to overcome a critical size of nanoparticles, thermodynamics is important for crystal stability. When atoms combine with each other, the free energy (ΔG) of the formed nuclei changes and it affects the formation and stability of the clusters. Therefore, the formation of the clusters can be divided into three different regimes according to the potential changing as shown in **Figure** 3.4.

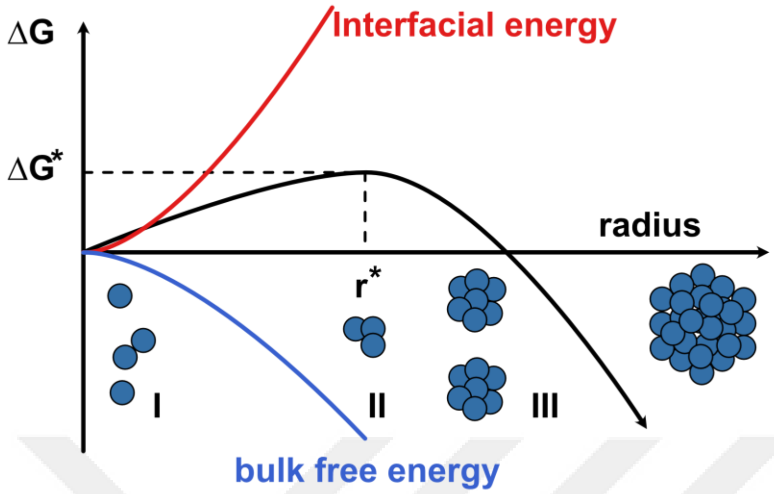

Figure 3.4. The dependence of cluster free energy on the cluster radius according to the classical nucleation theory. (Modified from [73])

These three different regimes can be categorized as follows.

- **I.** Nucleation starts with the formation of small particles.
- **II.** Small particles reach to a critical size.
- **III.** The continuous growth of particles.

The first stable particle can be formed at the free energy maximum where a critical cluster size is achieved. The critical cluster radius can be calculated by the two equations (Eq. 3-2 and Eq. 3-3),

$$r^* = -\frac{2\gamma}{\Delta G_v} \qquad \text{Eq. 3-2}$$

$$\Delta G^* = \frac{16\pi\gamma^3}{3(\Delta G_v)^2} \qquad \text{Eq. 3-3}$$

where, r^* is the critical radius of cluster, γ is the interfacial energy, ΔG_v is the bulk free energy and ΔG^* is the critical free energy.[80]

In the GAS approach, it is possible to produce a metal oxide cluster when reactive gas (especially oxygen) is used with the inert carrier gas (Ar or He). The effect of reactive gas highly depends on the reactivity of the target material. Here, the cluster formation can be investigated in three steps:

- **I.** Introducing reactive gas to the target
- **II.** Cluster nucleation
- **III.** Further cluster growth

Here, if a chemical reaction occurs between the target and the reactive gas, the sputtering rate decreases drastically due to the poising of the target. Therefore, the amount of reactive gas has to be much lower (several orders of magnitude) than the inert process gas (Ar or He). At the nucleation and growth stage, the reactive gas forms the cluster seed and the effect of the binding energy of the cluster due to extra heat energy. Therefore, the mixture of the right amount of reactive gas and inert process gas (Ar or He) is critical (at the nucleation and growth stages) to get successful deposition.

3.1.3 Photodeposition of Metal Clusters

A. Relevance to experimental work in thesis

- Deposition of hierarchical Au needle clusters on to TiO_2 thin films (Publication 2).
- Deposition of Au nanoparticles on to TiO_2 thin films in presence of additional solutions such as iso-propanol, acetone and 1- hexanol (Publication 3).
- Deposition of Au nanoclusters on to TiO_2 thin films (Publication 4).
- Deposition of Ag nanoparticles on to TiO_2 thin films (Publication 5).

B. Technical details and theoretical background

The photocatalytic deposition method was first demonstrated by Clark and Vondjidis in 1965.[81] The authors used the mixture of TiO_2 and silver nitrate ($AgNO_3$) to form the metallic silver after illumination. Afterward, Kraeutler and Bard reported, well-dispersed Pt nanoparticles could be obtained on TiO_2 powder, in 1978. This study sparked interest in photocatalytic deposition.[82] Here, they used a slurry, which contains TiO_2 powder, hexachloroplatinic acid (H_2PtCl_6), hydrochloric acid (HCl), etc. to synthesis Pt nanoparticles on TiO_2 (Anatase) by illumination.

Photocatalytic deposition is centered on photo-induced electrochemistry, and it is also known as photochemical deposition or photoreduction. Here, the general equation for reductive photodeposition of a metal (M) is described by the following equation (Eq. 3-4).

$$M^{n+}_{(aq)} + ne^{-} \rightarrow M_{(s)} \qquad \text{Eq. 3-4}$$

Furthermore, oxidative photodeposition can be described as the formation of metal oxide nanoparticle deposition by following equation (Eq. 3-5)

$$M^{n+}_{(aq)} + nh^{+} + nH_2O \rightarrow MO_{n(s)} + 2nH^{+} \qquad \text{Eq. 3-5}$$

The reductive and oxidative photocatalytic deposition (a special type of photodeposition supported by a catalytic material) methods are schematically demonstrated in **Figure 3.5**.

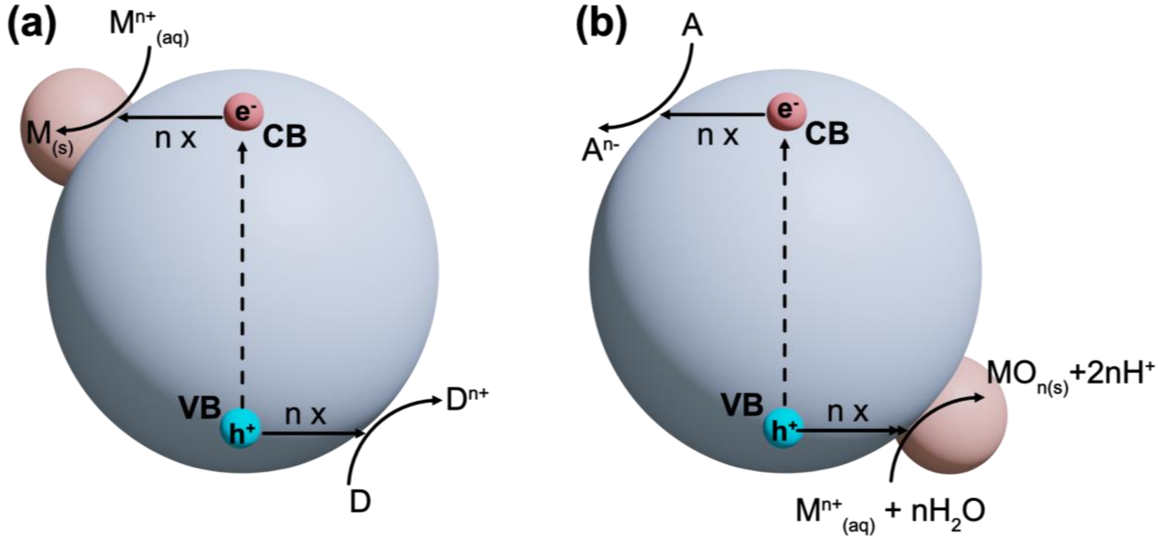

Figure 3.5. Schematic illustration of **(a)** reductive and **(b)** oxidative photocatalytic deposition approaches. (Modified from [83])

The photocatalytic property of the semiconductor material has a huge effect on the photocatalytic deposition method process. However, several conditions or parameters are needed to consider for occurring the photocatalytic deposition reaction as schematically shown in **Figure** 3.6. These parameters highly affect the chemical, structural, and catalytic properties of the deposited materials.

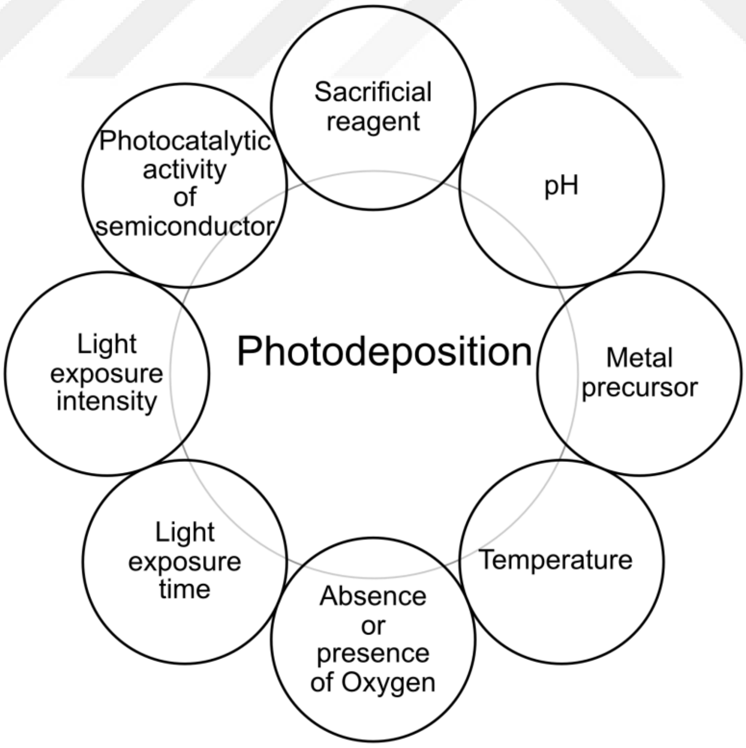

Figure 3.6. The various parameters of the photocatalytic deposition method. (Modified from [83])

First, the energy bandgap of semiconductor should be lower than the photon energy of the exposure light. Because the electron from the valance band (VB) can be excited when the light has a proper energy level to overcome the bandgap of the semiconductor (detailed in section 2.2) . Second, the energy level of the conduction band (CB) of the semiconductor should be more negative than the reduction potential of the metal ion. Examples of the band positions of several semiconductors are given in **Figure** 3.7. Third, the separation and migration of photogenerated charge carriers (electron-hole pairs) have to be more efficient to increase the possibility of the reactions. Finally, the semiconductor should act as a substrate for the deposition of the metal/metal oxide. If all conditions are combined, the synthesis of metal/metal oxide nanostructures on the semiconductor by photocatalytic deposition approach is possible.

Besides photocatalytic deposition, various methods exist to deposit nanoparticles on the semiconductor surface such as chemical reduction [42], atomic-layer deposition (ALD) [84] and electrodeposition [85]. However, the photocatalytic deposition, which is a simple and green approach, does not need additional chemical reagents and any extensive condition rather than a simple light exposure.

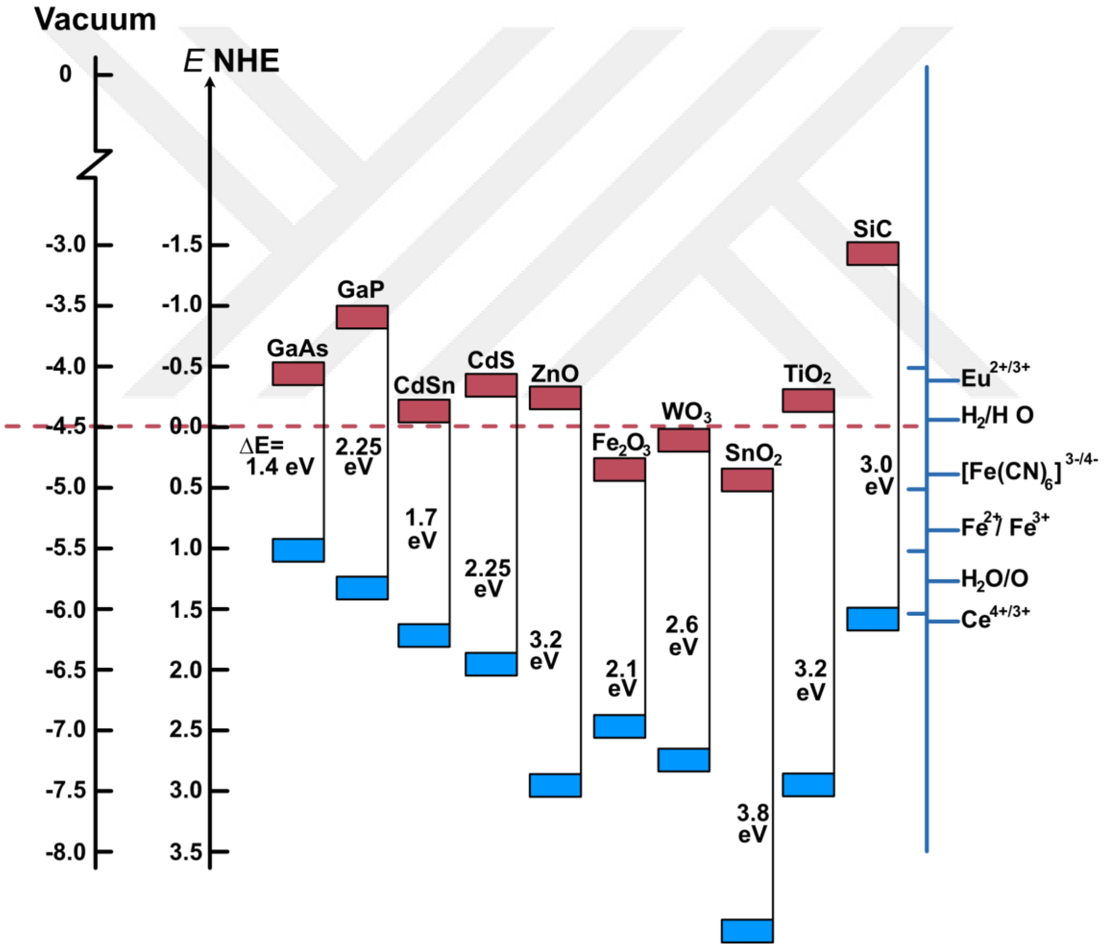

Figure 3.7. The schematic summary of band positions of various semiconductors (Left side: Energy scale in electron volts with reference to the vacuum level with normal hydrogen electrode. Right side: some reduction potential of specific compounds) (Modified from [86])

Photocatalytic deposition of metal/metal oxide nanoparticles on TiO_2 has been carried out by many researchers. The nanoparticles can range from noble metals such as Pt, Ag, and Au to metal oxides such as PdO_2 and RuO_2.[83] The photocatalytic deposition approach is widely used to synthesis core-shell particles [87], bimetallic or trimetallic cocatalysts.[88]

3.2 Material Characterization

3.2.1 Scanning Electron Microscopy (SEM)

A. Relevance to experimental work in thesis

- Surface and morphology characterization of prepared samples (Publication 2, Publication 3, Publication 4, Publication 5, Publication 6, Publication 7, Publication 8 and Publication 9).
- Analysis of particle size distribution by using binary SEM images (Publication 5 and Publication 6).
- Elemental mapping by using Energy Dispersive X-Ray (EDX) detector (Publication 2, Publication 4 and Publication 6).

B. Technical details and theoretical background

Scanning electron microscopy (SEM) is one of the most powerful and versatile instruments to investigate the morphology, microstructure, and chemistry of a range of materials and examine the particle's size at the micro-to nanoscale. The most striking feature of the SEM technique is giving a good topographical impression of the sample. The primary components of the SEM are a source of electrons/electron gun (e.g. tungsten (W) electron filament), electromagnetic lenses to focus electrons, electron detectors, specimen chamber and, computer control system as shown in **Figure** 3.8. The SEM may also include an energy-dispersive x-ray spectrometer (EDX) and a back-scattered electron detector.

Electrons, produced by electron gun (filament), are accelerated downwards where they passed through a combination of lenses and apertures to produce a fine beam of electrons. This electron gun works in a vacuum to avoid scattering of the electrons and is connected from the outside to a high voltage such as (30-40 kV). When electrons start moving toward the anode (positive charge), some of them simply go right through it and directly move to the specimen which is also a positive charge. When the electrons hit the specimen, there are two types of electrons come off from the surface as called secondary and back-scatter electrons.

The secondary electrons (SE) are typically defined as having energies of less than 50 eV and generated by inelastic scattering of the primary electrons. However, the back-scattered electrons (BSE) are primary electron (greater than 50 eV) generated by elastic scattering through an angle greater than 90° and contain deep information about surface morphology. Both SE and BSE electrons are collected by the specific detectors which use the information from those electrons (signals) to form an image on the computer.

The quality of the obtained image highly depends on the distance between gun and specimen, electron beam voltage, type of detectors (SE or BSE), tilt angle and conductivity of the sample. Materials of low conductivity (high resistivity, $>10^{10}\ \Omega$) charge rapidly under the incident electron beam and may cause a dielectric breakdown in the region of the sample. This leads to differences in the surface potentials and causes complex and dynamic image artifacts which commonly described as "charging". The surface charging increases the local potential which disrupts the normal SE emission from the specimen and severely degrades the quality of the image. Applying a conductive layer (such as gold or carbon) on the sample surface helps to reduce the surface charging and minimize the deterioration caused by enhancing electron emission. Additionally, SEM can be used by the EDX detector to investigate the range of elements through the periodic table (boron upwards). The details can be found in [89–92].

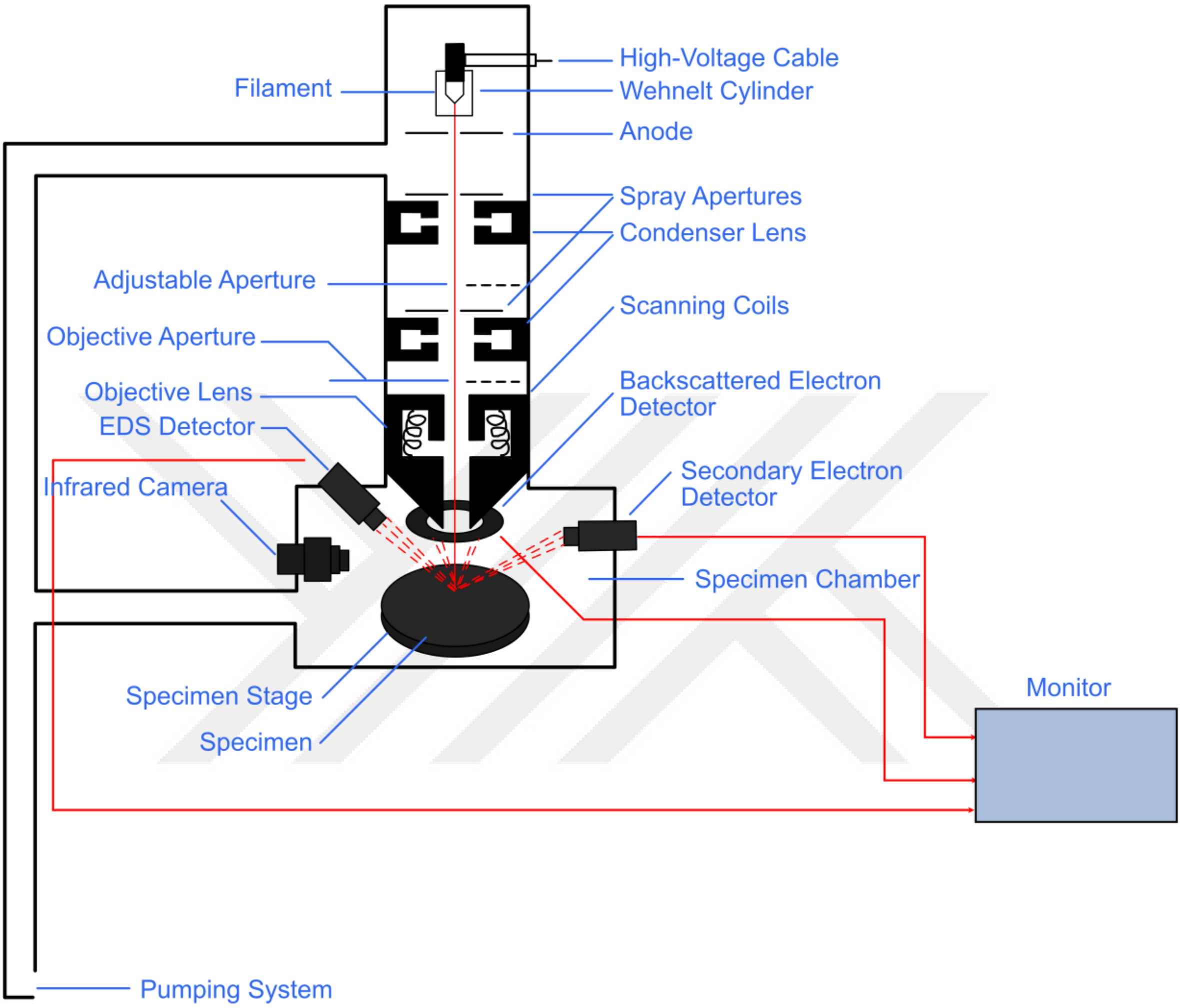

Figure 3.8. The working principle of the conventional SEM.

3.2.2 Helium Ion Microscopy (HIM)

A. Relevance to experimental work in thesis

- Investigating the formation of Au needle-like nanostructures and nanoparticles on TiO_2 thin film without using any additional conductive layer (Au or carbon) coating (Publication 2 and Publication 3).
- Understanding the formation of CeO_2 nanoclusters on TiO_2 thin film without using any additional conductive layer (Au or Carbon) coating (Publication 8).

B. Technical details and theoretical background

The SEM has long been a standard approach in the study of surface morphology and structure of both hard and soft materials. The SEM is mostly used for high-resolution imaging in particular in biology and material science. However, the SEM has encountered some fundamental challenges in the imaging of soft materials at high magnification and surface charging caused by the insulating properties of most of the samples. Also, it can be difficult to define where the edge of the particles at high magnification imaging. The surface charging problem can be solved by depositing some conductive materials, but it can cause the loss of subtle surface features. The helium ion microscope (HIM) is a new type of microscopy technique that uses helium ions for surface imaging and analysis. The HIM works similarly to an SEM, but it uses a focused beam of helium ions instead of electrons (**Figure** 3.9).

In the HIM approach, it is theoretically possible to focus the ion beam into a smaller probe size compared to an electron beam used in the current SEM technique. Because the helium ions have high brightness, very small size (almost one atom size), and the shorter wavelength which highly improves the resolution of particles or surface imaging.

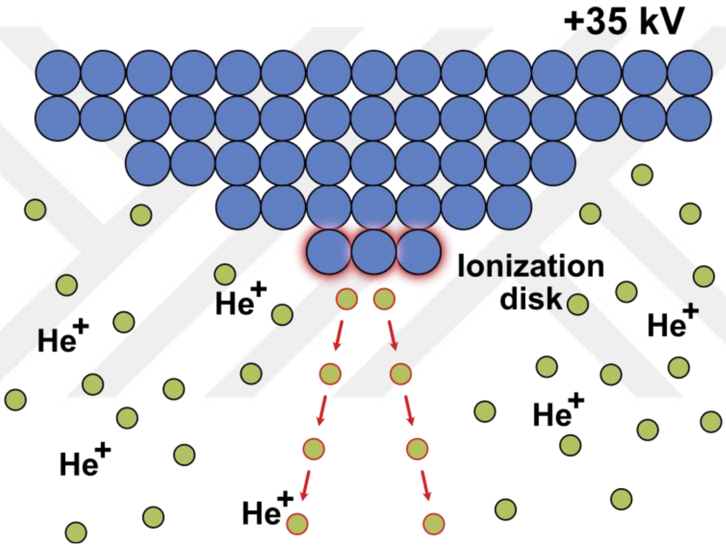

Figure 3.9. Schematic illustration of the ionization in helium ion microscopy.

The working principle of HIM can be divided into 4 different stages as follows:

- Ionization of Helium
- Acceleration of ions
- Formation and control of beam
- Interaction of sample and helium ions

The HIM operates ~ 35kV He ions focused on a small spot with only 3 atoms (referred to as a trimer). The main advantage of HIM is the much larger field of view and a unique capability to image for lower conductivity samples without a deposited conductive layer. The three-atom configuration gives greater stability and subsequently longer operation times compared to a single atom. The HIM also allows a topographic, material and crystallographic investigation of the sample using various detectors similarly to the SEM. The details can be found in [93,94].

3.2.3 Transmission Electron Microscopy (TEM)

A. Relevance to experimental work in thesis

- Structural and morphological analysis (particle shape and size) of CeO_2, ZnO and Au nanoparticles and corresponding SAED pattern (Publication 1).
- Detail analysis of Au needle formation by FIB analysis and corresponding SAED pattern (Publication 2).
- Understanding the Au cluster formation on TiO_2 and elemental mapping (Publication 3).
- Investigating the size and shape of Al nanoparticles and oxide layer (Publication 6).
- Structural and morphological analysis of PdO nanoparticles on TiO_2 before and after heat treatment and corresponding SAED pattern (Publication 7).
- Structural and morphological analysis of CeO_2 clusters on TiO_2 before and after heat treatment and corresponding SAED pattern (Publication 8).

B. Technical details and theoretical background

Transmission electron microscopy (TEM) is a powerful and unique technique to characterize the micro- and crystalline structure, morphology, and elemental information of the materials. It is a microscopy technique in which a high energy beam of electrons is transmitted through a very thin sample and the interaction of electrons with the atoms. The TEM works on the same basic principles as the light microscope but it uses the highly energetic electrons instead of light (**Figure** 3.10). Here, the wavelength of the electrons is much smaller than that of light which is many orders of the magnitude better than a conventional light microscope. Therefore, the TEM can show the finest details of the internal structure of the materials.

The electrons emitted from the electron gun are focused on a small beam by using the condenser lens. Then, the beam hits the specimen and some of the electrons are transmitted (by the electrostatic potential) depending on the thickness and electron transparency of the specimen. These transmitted electrons are focused on the fluorescent screen (a layer of photographic film) to form an image by the objective lens. A TEM sample must be thin enough to transmit enough electrons to form an image with minimum energy loss. Therefore, the preparation of a sample is an important part of the TEM analysis. Furthermore, an improvement to TEM is high-resolution transmission electron microscopy (HRTEM) which provides imaging of the crystallographic structure of a specimen at the nuclear scale. Another great feature of the electron microscope is that an electron diffraction pattern can be obtained. The details can be found in [95,96].

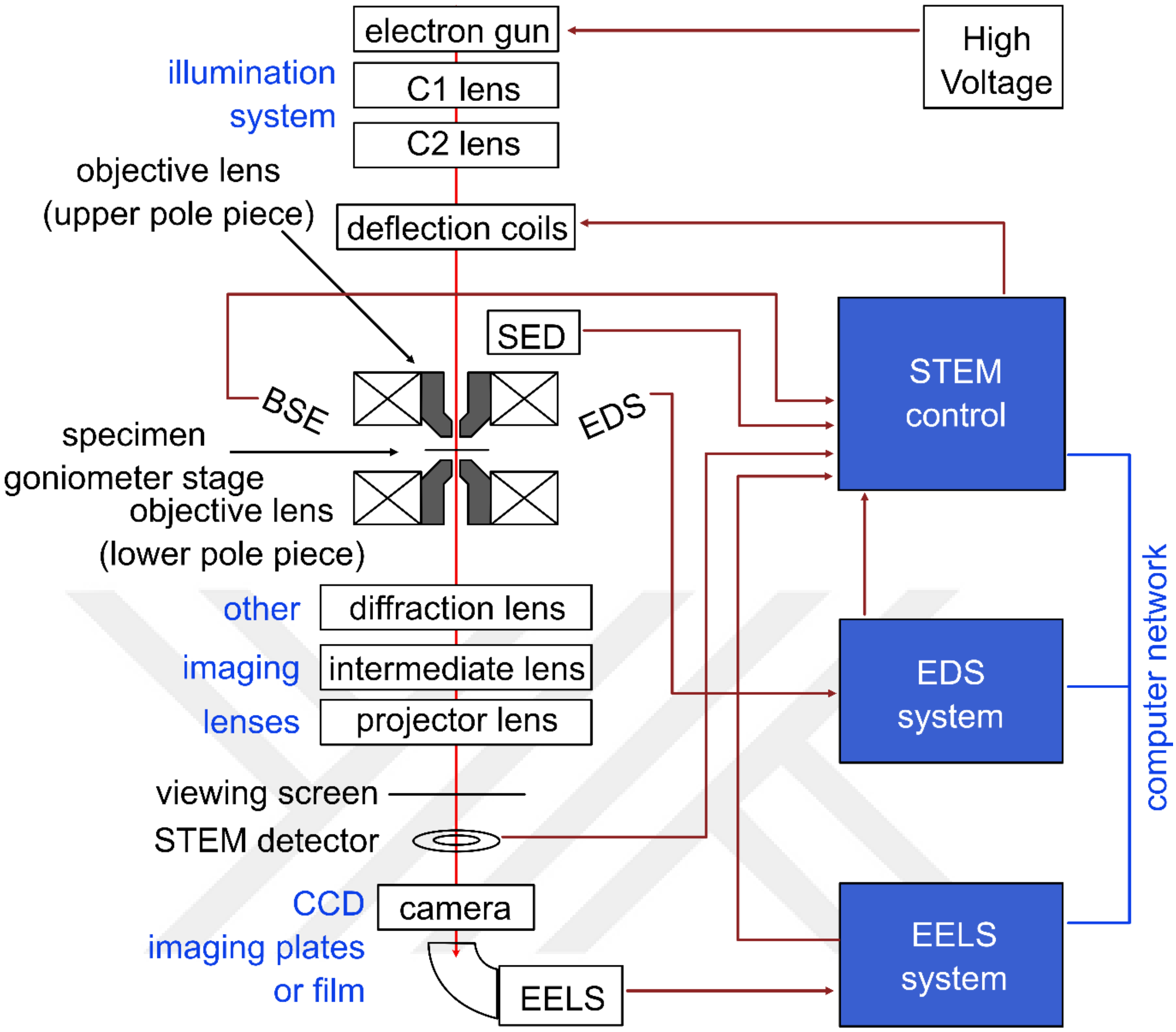

Figure 3.10. The working principle of the conventional TEM.

3.2.4 X-ray Photoelectron Spectroscopy (XPS)

A. Relevance to experimental work in thesis

- Compositional analysis of Au-CeO_2/ZnO hybrid structure (Publication 1).
- Investigating the oxidation state of Au, Ti and O in Au-TiO_2 hybrid structures (Publication 3 and Publication 4).
- Examination of the oxidation state of Ag, Ti and O in Ag-TiO_2 hybrid structure (Publication 5).
- Understanding the oxide shell formation on Al and Al_2O_3 nanoparticles (Publication 6).
- Investigation of the dynamic change between Pd^0 and Pd^{2+} before and after heat treatment (Publication 7).
- Investigation of the dynamic change between Ce^{3+} and Ce^{4+} before and after heat treatment (Publication 8).
- Understanding the PTFE layer formation on TiO_2 surface by iCVD (Publication 9).

B. Technical details and theoretical background

X-ray Photoelectron Spectroscopy (XPS), also known as Electron Spectroscopy for Chemical Analysis (ESCA), is qualitative and/or quantitative surface analysis technique, which is mostly used to determine the elemental composition, element oxidation states and bonding relationships for all kinds of surface elements (except for H and He). It is a surface-sensitive technique, works under a high vacuum (p< 10^{-7} mbar), for analyzing the surface to a depth of approximately 1-10 nm due to the small attenuation length of the created photoelectrons.[97] However, it is a very expensive and slow process. The XPS works by irradiating a specimen with monochromatic X-rays (Al kα, typically 1–3 keV) resulting in photoelectrons to be emitted from the specimen surface.

The electron of the specimen is knocked by an X-ray photon as shown in **Figure** 3.11. This electron with binding energy (E_b), regarding the Fermi level, is emitted from the atom with kinetic energy (E_k) due to the photoelectric effect which was described by Einstein in 1915. The E_b of the electron can be calculated by the following equation (Eq. 3-6).

$$E_b = h\nu - E_k - \phi \qquad \text{Eq. 3-6}$$

Here, h is Planck constant, ν is the frequency of the radiation, E_k is the kinetic energy of the ejected photoelectron and ϕ is the work function. An electron energy analyzer is used to determine the kinetic energy of the emitted photoelectrons. The elemental identity, oxidation state, and quantity of a detected element can be obtained from the intensity of a photoelectron peak and kinetic energy. The details can be found elsewhere [98].

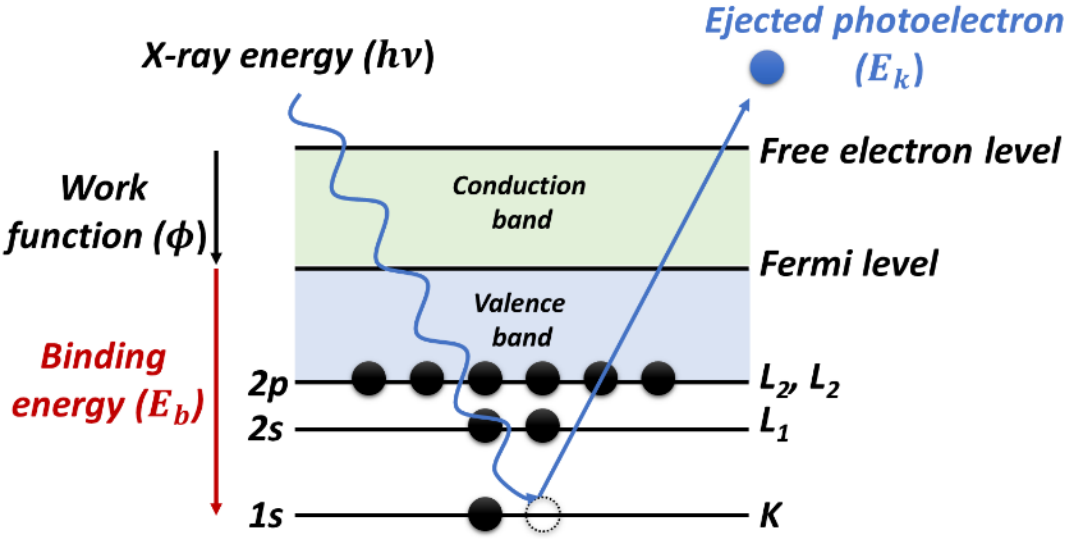

Figure 3.11. The working principle of the XPS.

3.2.5 Raman Spectroscopy

A. Relevance to experimental work in thesis

- Investigation of the crystal structure of Au/ZnO-CeO$_2$ hybrid structure.

- Understanding of the formation of anatase and rutile phases in TiO_2 regarding heat treatment temperature (Publication 2).
- Investigating the formation of PTFE layer deposited by iCVD (Publication 9).

B. Technical details and theoretical background

Raman spectroscopy is a non-destructive method in the field of vibrational spectroscopy for analyzing the crystal structure of the films and particles by the interaction of laser light source. The Raman spectroscopy is based on the phenomenon of the inelastic light scattering process. When a specimen is exposed by a monochromatic light in the visible region, the major portion of the light is transmitted through the specimen. However, the minor part of the light is absorbed and scattered by the specimen. When the electron absorbs energy from the incident photon, and it rises to a virtual state of energy. The energy transferred is given by the formula (Eq. 3-7):

$$E = hv \qquad \text{Eq. 3-7}$$

Here, h is plank constant and v is the frequency of the incident photon. The electron then falls back to an energy level by losing energy. If the energy lost equals the energy of the incident photon (v_s), the electron falls back to its initial vibrational level and in this process emits another photon. Since the energy lost in equivalent to the energy of the incident photon (v_i), the released photon has the same frequency as the incident photon. As the frequency is the same, Rayleigh scattering occurs. However, sometimes electrons when losing energy from the virtual state, can fall back to a different vibrational level. In this case, the energy lost by the electron is different than the energy absorbed from the incident photon. As a result, the photon emitted by the electron has energy, different than the incident photon. This is possible when the frequency of the emitted photon is different than the incident photon. This gives rise to Raman scattering. Depending upon the final energy of the electron or final vibrational level of the electron, Raman scattering can be separated into stokes lines and anti-stokes lines as shown in **Figure** 3.12**.**

If the frequency of the scattered photon (v_s) is less than the frequency of the incident photon (v_i), stokes lines are observed on the Raman spectrum. This happens when the electron absorbs energy. Similarly, when the frequency of the emitted photon (v_s) is greater than the incident photon (v_i), anti-strokes lines are observed. This means that energy is released by the electron. The Raman spectra give the fingerprint and it is different for different crystal structures. By studying the spectra, one can identify the rotational levels and thus a particular crystal structure. This helps in performing qualitative analysis. The details can be found in [99].

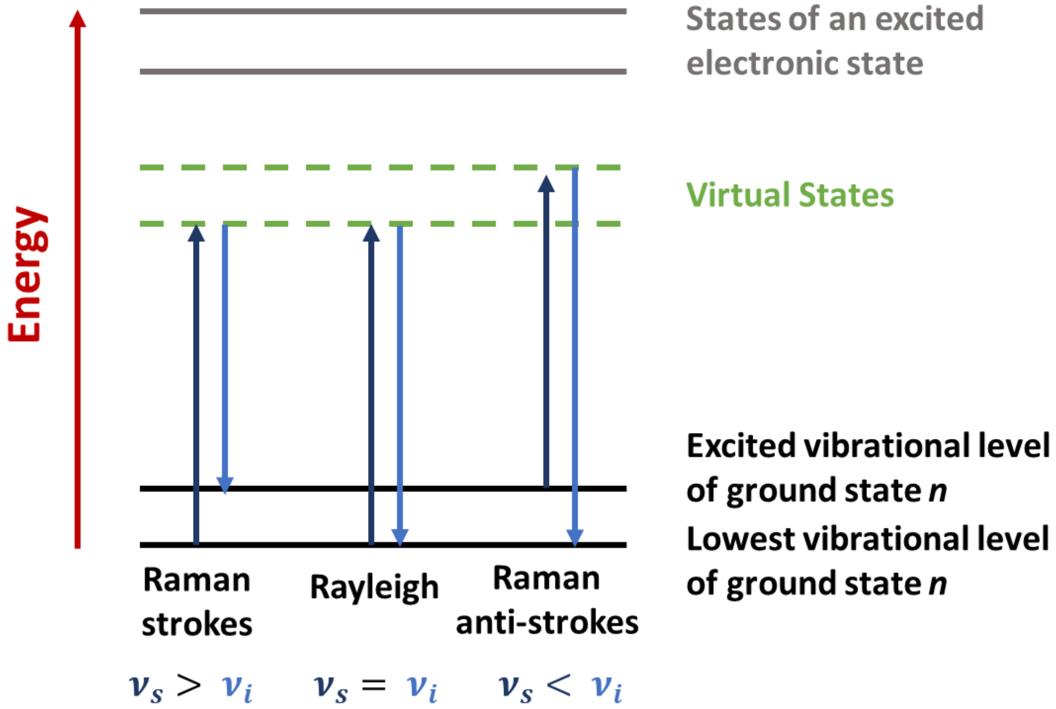

Figure 3.12. Diagram of the Rayleigh and Raman scattering process (Strokes and ani-strokes lines).

3.2.6 Photocatalytic Performance Analysis

A. Relevance to experimental work in thesis

- Analysis of the catalytic activity of Au/CeO_2-ZnO hybrid structure (Publication 1).
- Investigation of the photocatalytic activity of TiO_2 thin films at different heat treatment temperature (Publication 2).
- Testing the photocatalytic performance of prepared samples under UV light source (Publication 3, Publication 5, Publication 6, Publication 7 and Publication 8).
- Testing the photocatalytic performance of prepared samples under UV and Vis light sources (Publication 4).

B. Technical details and theoretical background

The photocatalytic activity is measured by the degradation of the dye molecules in aqueous solution under UV illumination (around λ =365 nm) standardized as ISO 10678:2010 and DIN 52980:2008-10. Methylene blue (MB) is commonly used as a test dye because it exhibits the large solar absorptivity at 664 nm but almost no absorption at 360-380 nm as shown in **Figure** 3.13

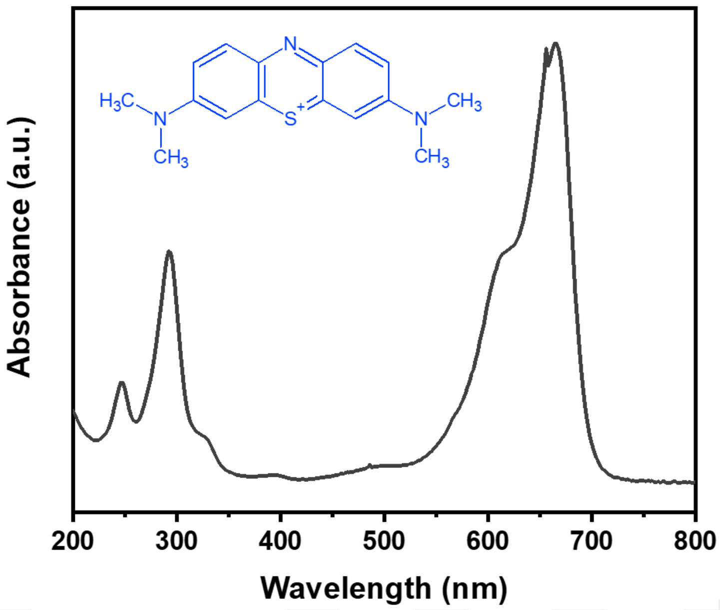

Figure 3.13. Chemical structure and the absorption spectrum of MB in aqueous solution.

In the typical photocatalytic measurement (DIN52980), a thin film sample is dipped into MB aqueous solution (10 µmol L^{-1}) as schematically shown in **Figure** 3.14a. The solution is magnetically stirred and irradiated by UV light (at λ =365 nm) for a certain time (t). The change in the absorption at 664 nm is recorded by the UV-Vis spectrophotometer.

The idealized measurement curve as shown in **Figure** 3.14b is divided into three different phases: **(i)** initial conditioning phase, the surface of the photocatalyst is not irradiated by UV-light, however it adsorbs MB molecules on the surface (shows small changing on the absorption). When the UV illumination starts (t_0), the degradation of MB happens. **(ii)** it is called the linear degradation regime (from t_0 to t). Here, the degradation of MB is limited by charge carrier generation (electrons and holes).

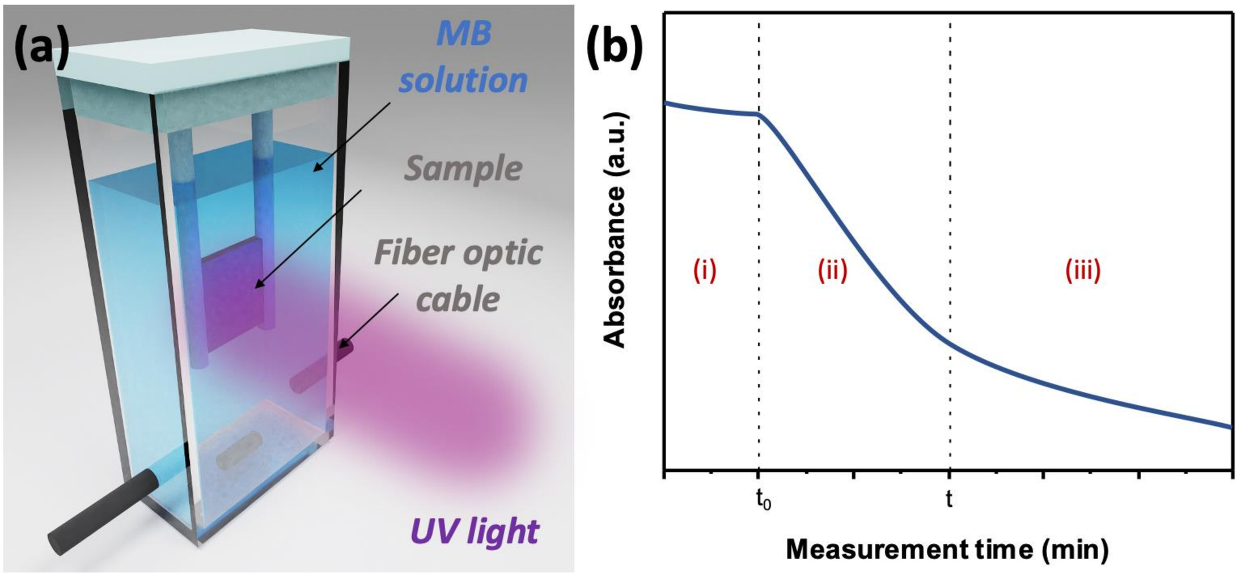

Figure 3.14. **(a)** Schematic representation of the photocatalytic measurement setup and **(b)** Idealized measurement curve for MB degradation.

During the photocatalytic measurement, the concentration of MB necessarily decreases, and it is reached, where no longer the generation of electrons (e^-) and holes (h^+) limits the degradation rate. At this point, the measurement shows **(iii)** the exponential degradation regime, because the degradation reaction rate depends on the availability of MB molecules at the surface of the photocatalyst. Here, the transition from linear to exponential degradation depends on the sample performance, intensity of UV light, and initial concentration of MB.

After the photocatalytic activity test, MB is completely degraded down to the final products such as SO_4^{2-}, CO_2, NH_4^{+}, and NO_3^-. Initially, a solution of MB has a blue color. However, discoloring of MB is occurring after the first degradation step, which is assumed to involve exactly one photon. Thus, the change in absorbance (which relates to the concentration of MB) of the test solution is a direct measure for the degradation of MB molecules and consequentially relates to the photocatalytic performance of the investigated photocatalyst.

3.2.7 Wetting Angle Analysis

A. Relevance to experimental work in thesis

- Investigation of the self-cleaning performance of prepared samples (Publication 7 and Publication 8).
- Analysis of the superhydrophobic properties of PTFE coating (Publication 9).

B. Technical details and theoretical background

Contact angle measurement is performed to determine the hydrophilicity/hydrophobicity (wettability by water), adhesion, and absorption of the surface. It is a key tool for surface characterization and wetting study due to its simplicity and flexibility. The concept of wettability was first described by Thomas Young in 1805. The wettability is the spreading of a liquid over the surface (creating a continuous layer) and it is a physical sign of the interfacial energy between the three components systems. These can be categorized as the liquid-gas interface, the liquid-solid interface, and the solid-gas interface. The contact angle measurement is the most common approach to study the wettability properties of the surface. Here, a small drop of liquid (Volume ≈ 4–5 μL) is used to determine the contract angle between drop and surface as schematically shown in **Figure** 3.15.

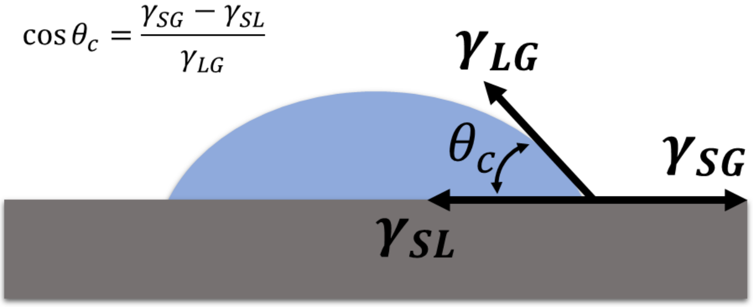

Figure 3.15. The contact angle formed by the liquid spreads over the surface

When the liquid drop touches the surface, the shape has an equilibrium with the horizontal surface. In Young approach, the energy balanced approach to the three equilibrium interfacial tensions and equation is derived as Young's equation (Eq. 3-8)

$$\cos\theta = \frac{\gamma_{SG} - \gamma_{SL}}{\gamma_{LG}} \qquad \text{Eq. 3-8}$$

where θ symbolizes the contact angle, γ_{SG}, γ_{SL}, and γ_{LG} represent the solid-vapor, solid-liquid and liquid-vapor, and interfacial tensions. The Young's equation can be obtained when the surface is flat, nonreactive, inert, homogeneous, insoluble, smooth, and nonporous.

In Young's equation, if the contact angle is greater than 90°, the surface is hydrophobic (**Figure** 3.16). On the other hand, if the contact angle is less than 90°, the surface is hydrophilic. If the contact angle is greater than 150°, the surface is defined as being superhydrophobic. When a water droplet touches the superhydrophobic surfaces it looks like a ball. However, if the contact angle is less than 5°, the surface is defined as being superhydrophilic. Water droplet that touches the superhydrophilic surface, it spread out completely. This is useful for anti-fog coating. If the surface is superhydrophilic, then any water that contacts the surface forms a thin film instead of forming droplets on the surface.

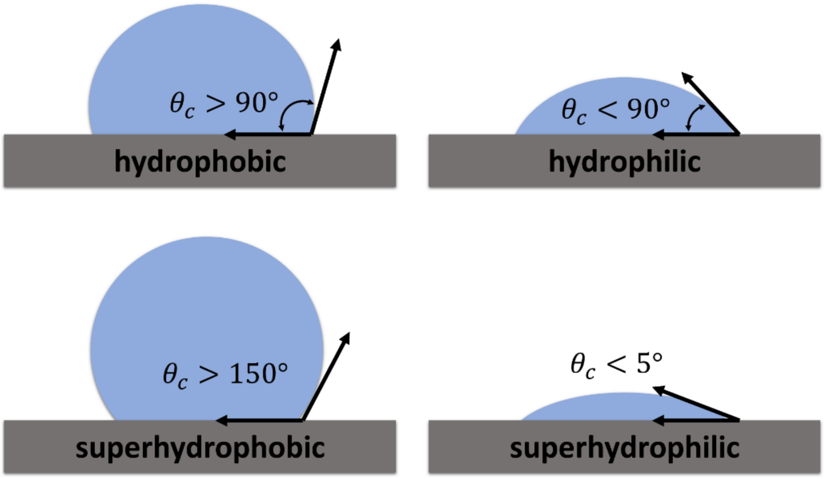

Figure 3.16. Schematic description of the hydrophobic and hydrophilic surfaces.

There are two main factors governing hydrophobicity and hydrophilicity: surface chemistry and roughness. The surface chemistry determines whether the surface has low or high surface energy (which determines the surface is hydrophobic or hydrophilic). Generally, the surface with low surface energy (ex: Teflon, etc.) acts as hydrophobic and the one with high surface energy (ex: metals, etc.) does as hydrophilic. As the second factor, surface roughness makes a hydrophobic surface even more hydrophobic and a hydrophilic surface even more hydrophilic. There are two different models explaining how a water droplet can contact a rough surface. Here, θ_E is the equilibrium contact, which is the contact angle for an ideal flat surface. $\theta^+$is the apparent contact angle, which is the contact angle on a rough surface (**Figure** 3.17).

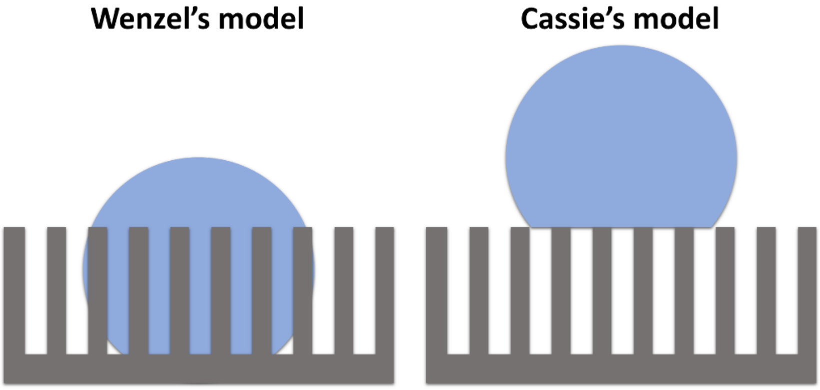

Figure 3.17. The assumption of the Wenzel and Cassie's models.

These two models were developed by Wenzel and Cassie-Baxter. They showed how surface roughness can affect a water droplet's contact angle. In Wenzel's state, there are no air bubbles underneath the droplet and the droplet has complete contact with the surface. The droplet sticks very well to the surface and it is called a pinned droplet. Here, the surface roughness by the formula (Eq. 3-9)

$$r = \frac{A_{real}}{A_{geometrical}} \qquad \text{Eq. 3-9}$$

where A_{real} and $A_{geometrical}$ are the real and geometrical areas of the surface. The Wenzel equation is derived based on the hypothesis that the drop profile is sufficiently bigger compared with the roughness scale of the surface and liquid completely penetrates. The resultant equation was given by Eq. 3-10.

$$\cos\theta_W = r \cdot \cos\theta_Y \qquad \text{Eq. 3-10}$$

where θ_Y a generalization of Young's contact angle, θ_W is the Wenzel contact angle, and r is the average roughness parameter.

If a droplet is in the Cassie-Baxter state, the water droplet sits on top of tiny air bubbles. In this state, the water droplet bounce or roll-off. This is useful for water repellent and self-cleaning surfaces. A surface can be self-cleaning because any water droplet, which contacts with the surface, roll-off and picking up any dirt on the surface. The Cassie-Baxter state occurs on a highly rough surface. It is calculated by the formula (Eq. 3-11).

$$\cos\theta_C = f_1 \cos\theta_1 - f_2 \qquad \text{Eq. 3-11}$$

where θ_C is the Cassie contact angle, f_1 is the fractional surface area with contact angle θ_1, and f_2 is the fractional surface area with contact angle θ_2.

The wetting angle analysis is one of the most versatile methods for understanding the interfacial characteristics between the sample surface and a liquid (commonly water droplet). According to models aforementioned, it is assumed that the surface is clean and contamination-free. Here, there is no any extra interaction between sample surface and liquid. However, the influence of the adsorbed contaminations on the surface has a huge impact on the wettability behavior of the surface. Surface contamination can reduce or increase the wettability drastically due to changing of the surface roughness and charge distribution on the surface.[100] However, this phenomenon can be used to investigate the self-cleaning properties of the surface, which is called as dynamic wetting angle measurement. Here, the contact angle is measured by the degradation of the organic contamination (especially oleic acid) under light exposure. The change in the wettability behavior gives the overall idea about the self-cleaning properties of the surface.

4 Ultra-fast Degradation of Methylene Blue by Au/ZnO-CeO$_2$ Nano-hybrid Catalyst

This chapter is based on an article published in Materials Letters.[18]

Reprinted with permission from Salih Veziroglu, Muhammad Zubair, Mehmet Kuru, Fatma Kilic-Dokan, Thomas Strunskus, Alexander Martin Hinz, Franz Faupel, Oral Cenk Aktas
Materials Letters 209 (2017) 486–491.
The article is available via the internet at https://doi.org/10.1016/j.matlet.2017.08.069

Abstract

Au/ZnO-CeO$_2$ hybrid structure was prepared by in-situ synthesis of 15–20 nm CeO$_2$ particles in aqueous environment, in which ZnO particles (400–500 nm) were dispersed, using surfactant assisted precipitation method. Au was loaded on prepared structures through the reduction of AuCl$_3$ by ascorbic acid. TEM analysis and Raman spectroscopy showed that synthesized hybrid structure is composed of both hexagonal ZnO and cubic CeO$_2$ phases. While methylene blue test solution was degraded totally within 8 min in the presence of Au/ZnO-CeO$_2$ hybrid catalysis, use of Au/ZnO and Au/CeO$_2$ led to a significantly low degradation rate (about 22% and 11%, respectively). As proven by XPS analysis the incorporation of ZnO to CeO$_2$ seem to trigger the formation of Ce^{+3}/Ce^{+4} dynamic equilibria and this enhances the catalytic efficiency enormously.

4.1 Introduction

In recent years the use of metallic nanoparticles (NPs) for heterogeneous catalysis has been increased significantly due to their superior catalytic properties.[101] Especially Au NPs act as perfect catalyst due to their stability against over-oxidation and chemical leaching.[102] These stable Au NPs are extremely effective to degrade organic pollutants in the presence of reducing agents.[103] $NaBH_4$ is a strong reducing agent which can itself reduce various common organic dyes even without using any additional catalyst. On the other hand, such a reduction reaction is kinetically not favourable due to the large redox potential differences between the electron donors and acceptors.[104] It has been shown that Au NPs together with $NaBH_4$ form an effective electron relay system which favours the electron transfer in the reduction of organic dyes.[103]

Various metal oxides have been successfully used to support Au nanocatalyst.[105] Such metal oxides not only enhance the stability of Au NPs against the agglomeration and leaching also increase the catalytic reactivity. Especially CeO_2 is one of the mostly preferred oxides in catalytic applications because of its high oxygen storage capacity and dynamic conversion between $Ce^{3+}$and Ce^{4+} states.[106] ZnO is also an extensively investigated catalytic material due to its high efficiency and low-cost.[106,107] It has been shown ZnO-CeO_2 mixed oxide structure exhibits superior catalytic activity in comparison to pure CeO_2 and ZnO.[108]

Here, we present synthesis of Au NPs loaded ZnO, CeO_2 and ZnO-CeO_2 hybrid structures to reveal the beneficial features of using both mixed oxide structure and metallic NPs for catalytic applications. After characterizing morphology and structural properties of prepared structures, we compared their catalytic efficiencies by monitoring the reduction of methylene blue (MB) solution in the presence of $NaBH_4$.

4.2 Experimental Section

Nanocatalysts were produced by a two-steps process **Figure** 4.5. ZnO particles were used as purchased and CeO_2 particles were synthesized by a block-copolymer surfactant (Pluronic-123) assisted precipitation using $CeCl_3 \cdot 7H_2O$ and a subsequent calcination at 400°C for 6h.[109] Au loading on ZnO, CeO_2 and ZnO-CeO_2 particles was carried out by the reduction of $AuCl_3$ using ascorbic acid.

Raman spectroscopy was used as a fast-analytic tool to reveal and to compare crystal structures of prepared samples. Further structural analysis and morphological characterization were carried out using transmission electron microscope (TEM). X–ray photoelectron spectroscopy (XPS) was used to investigate surface elemental compositions and states.

The catalytic performance of synthesized oxides was monitored by in-situ UV–Vis spectroscopy. For each test around 4 ml catalyst (0.025 mg/ml), 1 ml MB (13 mg/l) and 100 µl freshly prepared $NaBH_4$ (0.2 mol/l) solution was used and the change in the absorption (at 664 nm) of this solution was recorded at every 60 s.

4.3 Result and Discussion

Raman spectroscopy was used as a fast-analytical tool to reveal the formation of Au/ZnO-CeO_2 hybrid structures by simply comparing their spectral analysis with those of Au/ZnO and Au/CeO_2 structures. **Figure** 4.1a shows the typical Raman spectra of these structures excited at 532 nm. The peaks located at 332, 379, and 437 cm^{-1} can be assigned to $2E_2$, A_1, and E_2 (high) vibration modes of wurtzite hexagonal phase of ZnO.[110] The peak observed at 457 cm^{-1} generally corresponds to the F_{2g} Raman active-mode of fluorite cubic structure of CeO_2.[111] Thus, the presence of both bands at 457 and 437 cm^{-1} in Au/ZnO-CeO_2 hybrid structure clearly shows that the synthesized sample is in good crystal quality with both hexagonal ZnO and cubic CeO_2 phases.

A detailed TEM analysis was performed to reveal further structural and morphological properties (particle shape and size) of prepared oxides. It was possible to observe Au loading in pure ZnO and CeO_2, as well as in ZnO-CeO_2 hybrid structures (**Figure** 4.1b–d). Due to the good contrast between Au and ZnO and the clear difference in their particle size one can easily detect the formation of 30–40 nm Au particles on relatively larger ZnO particles (400–500 nm). On the other hand, it was hard to detect Au particles in case of Au/CeO_2 nanocatalyst due to the poor contrast between CeO_2 and Au. Although fine Au NPs formed on larger CeO_2 clusters (agglomerates), one can observe that primary particle size (15–20 nm) of CeO_2 structures are comparable with that of Au NPs.

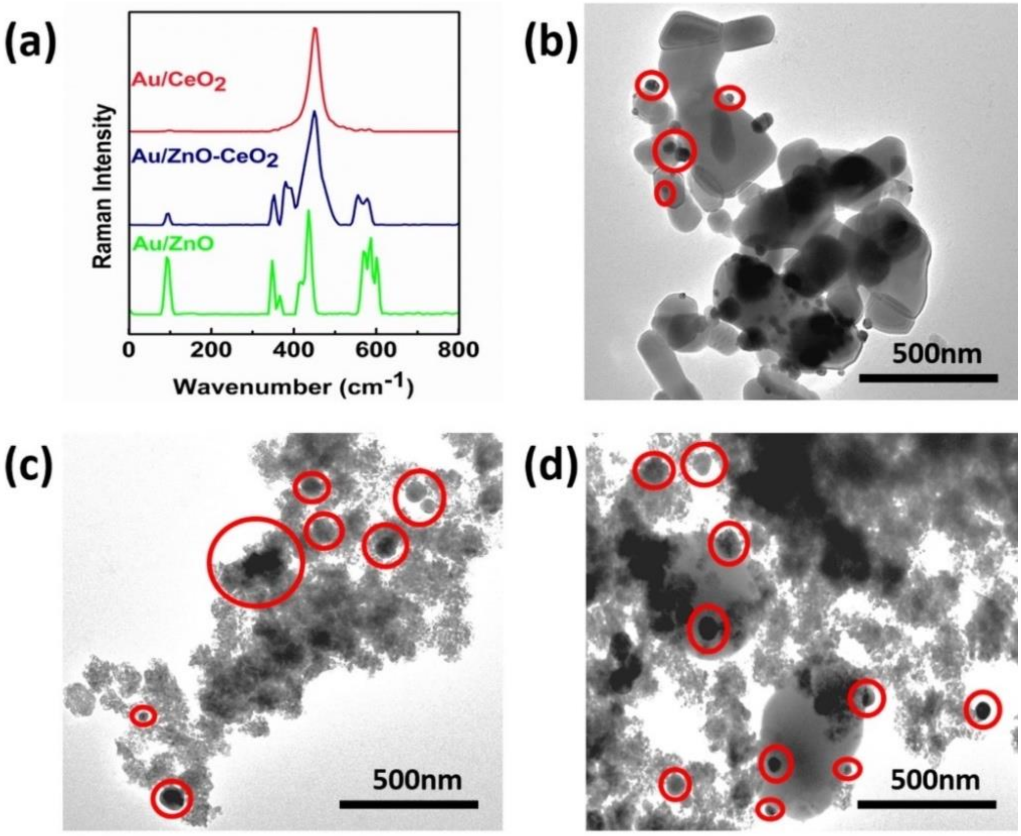

Figure 4.1. **(a)** Raman Spectra of Au/CeO_2, Au/ZnO-CeO_2 and Au/ZnO catalysts and **(b)** TEM images of Au/ZnO **(c)** Au/CeO_2 **(d)** Au/ZnO-CeO_2 catalysts. Red circles indicate Au NPs.

The peaks located at 332, 379, and 437 cm^{-1} can be assigned to 2E$_2$, A$_1$, and E$_2$ (high) vibration modes of wurtzite hexagonal phase of ZnO.[110] The peak observed at 457 cm^{-1} generally corresponds to the F$_{2g}$ Raman active-mode of fluorite cubic structure of CeO$_2$.[111] Thus, the presence of both bands at 457 and 437 cm^{-1} in Au/ZnO-CeO$_2$ hybrid structure clearly shows that the synthesized sample is in good crystal quality with both hexagonal ZnO and cubic CeO$_2$ phases.

A detailed TEM analysis was performed to reveal further structural and morphological properties (particle shape and size) of prepared oxides. It was possible to observe Au loading in pure ZnO and CeO$_2$, as well as in ZnO-CeO$_2$ hybrid structures (**Figure** 4.1b–d). Due to the good contrast between Au and ZnO and the clear difference in their particle size one can easily detect the formation of 30–40 nm Au particles on relatively larger ZnO particles (400–500 nm). On the other hand, it was hard to detect Au particles in case of Au/CeO$_2$ nanocatalyst due to the poor contrast between CeO$_2$ and Au. Although fine Au NPs formed on larger CeO$_2$ clusters (agglomerates), one can observe that primary particle size (15–20 nm) of CeO$_2$ structures are comparable with that of Au NPs.

Elemental mapping images for Au/ZnO-CeO$_2$ hybrid structure is shown in **Figure** 4.2a. The results clearly show that the hybrid structure was composed of Zn, Ce, O and Au; and CeO$_2$ particles were dispersed uniformly on and between larger ZnO structures. Selected-area electron diffraction (SAED) patterns confirm clearly the presence of both ZnO and CeO$_2$ crystals as shown in **Figure** 4.2b. Lattice spacing analysis by TEM (**Figure** 4.2c and d) indicate that the ZnO nanostructures exhibited a hexagonal structure and that CeO$_2$ exhibited a cubic structure [108,112], consistent with SAED (**Figure** 4.2b) and Raman spectroscopy analysis (**Figure** 4.1a).

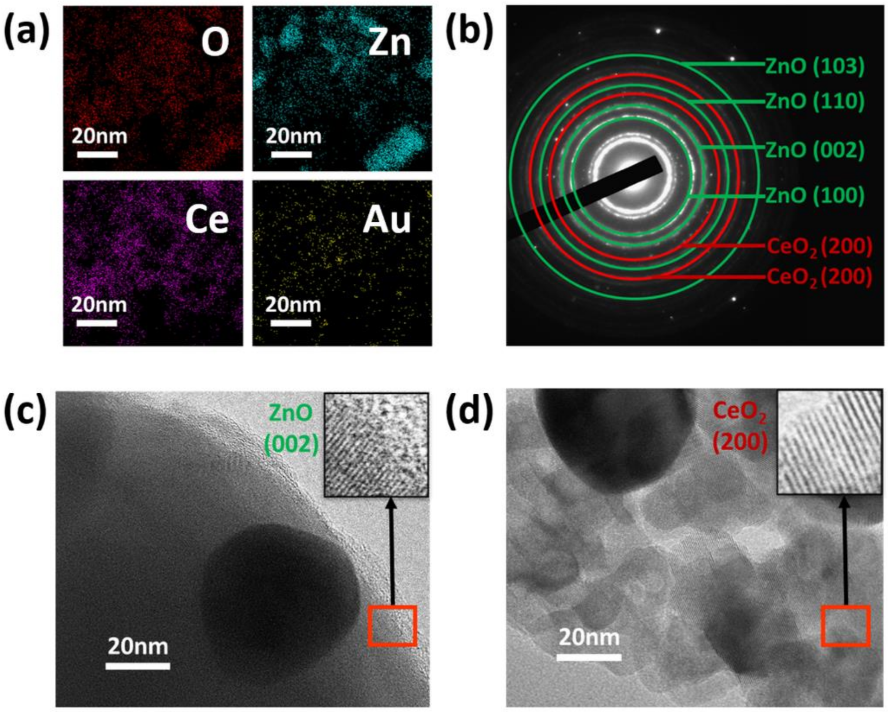

Figure 4.2. **(a)** Elemental mapping of O, Zn, Ce and Au **(b)** SAED pattern of Au/ZnO-CeO$_2$. TEM analysis of Au/ZnO-CeO$_2$ catalyst: **(c)** ZnO rich region and **(d)** CeO$_2$ rich region.

The elemental composition and chemical states of the synthesized Au/ZnO-CeO$_2$ hybrid structure were confirmed by XPS. The XPS survey spectrum showed clearly that hybrid catalyst surface was composed of Zn, Ce, O, C and Au (as shown in **Figure** 4.6). The high resolution XPS spectra of Zn, Ce, O and Au are shown in **Figure** 4.3a–d. According to the fitting procedure given by Rajendran et al. the broad O1s (**Figure** 4.3a) peak seem to consist of four different peaks at binding energies of 532.3, 529.9, 529.1 and 534.1 eV which are attributed to Zn^{2+}, Ce^{3+}, Ce^{4+} and surface hydroxyl groups, respectively.[108]

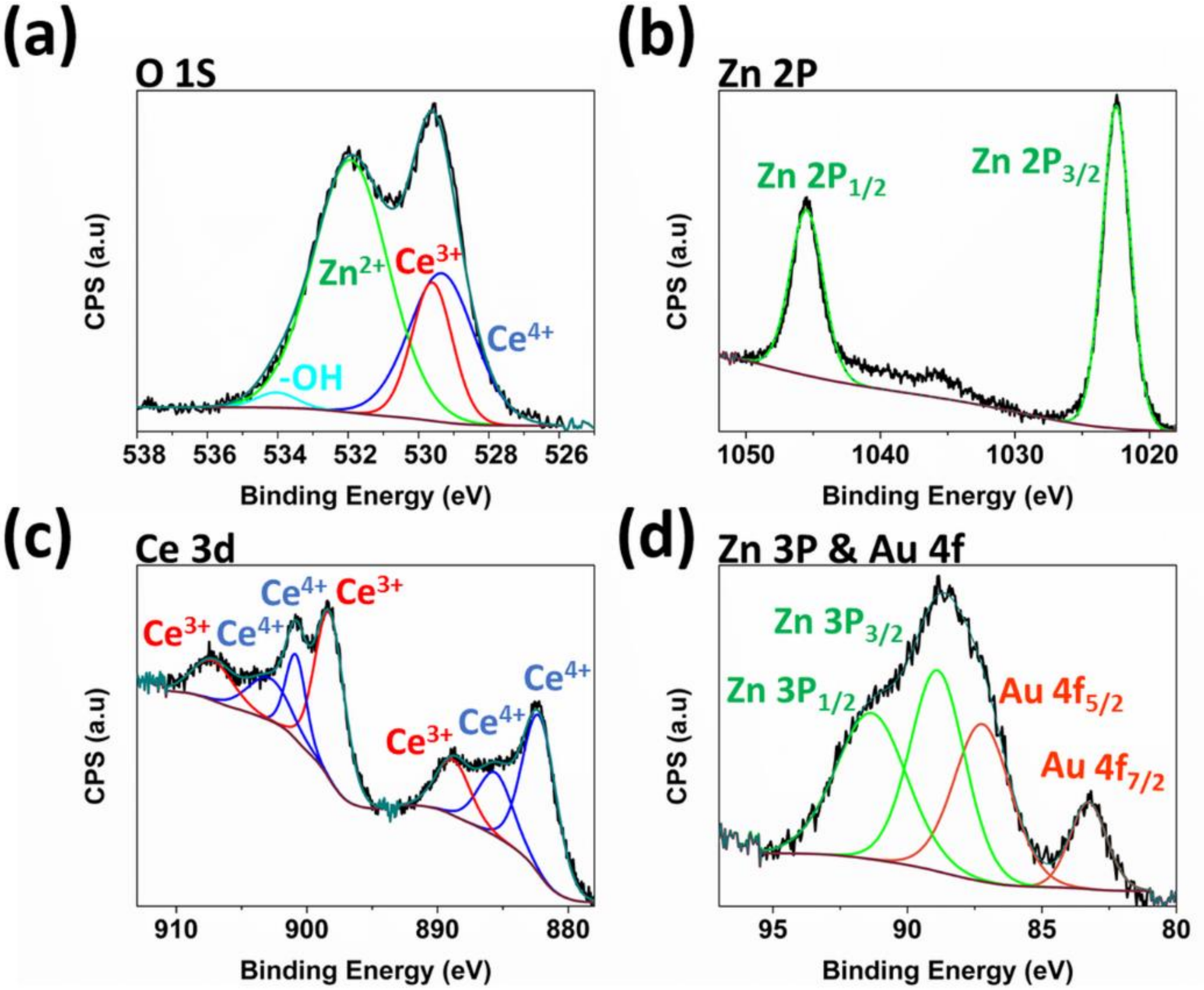

Figure 4.3. High resolution XPS spectra of Au/ZnO-CeO$_2$ catalyst **(a)** O1s, **(b)** Zn2p, **(c)** Ce3d and **(d)** Zn3p and Au4f.

In Zn2p spectrum (**Figure** 4.3b) the binding-energies 1022.8 and 1045.7 eV represent Zn 2p$_{3/2}$ and Zn 2p$_{1/2}$, respectively. Ce3d spectrum presented in **Figure** 4.3c is composed of seven peaks and these were represented as integrated peaks of Ce^{3+} and Ce^{4+} states by Rajendran et al.[108] According to Rajendra et al. the set of peaks at around 882.37, 886.53, 901.65 and 907.80 eV, demonstrates the existence of Ce^{4+}, while the peaks at 888.91 and 898.56, 907.36 eV, confirm the presence of Ce^{3+}. Although a high resolution XPS analysis is needed to quantify Ce^{3+}/Ce^{4+} ratio, the presence of multiple peaks in Ce3d spectrum can be attributed to the co-existence of Ce^{3+} and Ce^{4+} states. **Figure** 4.3d represents the overlapped and integrated

Au 4f spectrum with the Zn 3p spectrum. Binding energies 82.9 and 87.4 eV are attributed to Au $4f_{7/2}$ and Au $4f_{5/2}$, respectively. [112]

As shown in UV–Vis spectroscopy results (**Figure** 4.4a), without any catalyst, the degradation of MB by $NaBH_4$ (**Figure** 4.4b) was extremely slow and this clearly shows the reduction reaction is kinetically not favourable. One can easily see a slight increase in the MB degradation rate after adding Au/ZnO catalyst. The addition of Au/CeO_2 catalyst led to much higher increase in MB degradation rate. In comparison to Au/CeO_2 and Au/ZnO, using Au/CeO_2-ZnO mixed catalyst led to an extremely high degradation rate. The total decolourization took around 8 min and this shows effectiveness of mixed oxide catalyst. Degradation rate constants of corresponding catalysis are given in **Table** 4-1 by comparing their material and structural properties.[104]

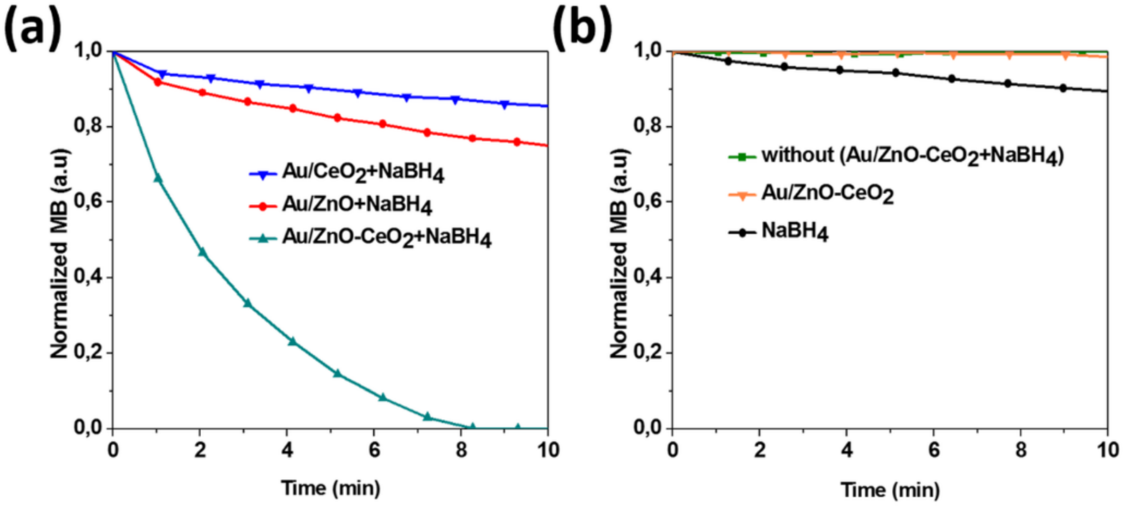

Figure 4.4. **(a)** Comparison of time dependent degradation of MB for Au/ZnO, Au/CeO_2 and Au/ZnO-CeO_2 and **(b)** Comparison of individual effects of catalyst and $NaBH_4$ on the degradation of MB.

Due to much finer size of CeO_2 particles the increase in degradation can be attributed to the increase in the surface area. On the other hand, since Au/CeO_2 catalyst exhibited much slower degradation in comparison to Au/ZnO-CeO_2 hybrid catalyst, extremely high catalytic activity of the hybrid structure cannot be explained only by the surface area contribution. It is believed that the co-existence of Ce^{+3}/Ce^{+4} and the dynamic fluctuation between these two states and moreover presence of Au-NPs induces a synergetic effect to the reduction of MB. It is known that presence of metallic NPs lowers redox potentials to intermediate levels. **Figure** 4.4b clearly indicates that highly reductive $NABH_4$ and Au/ZnO-CeO_2 hybrid catalyst forms an ideal electron relay system. Hybrid catalyst without $NaBH_4$ the is not effective at all (similarly use of $NaBH_4$ without catalyst is also not effective).

4.4 Conclusion

In summary, we presented that Au/ZnO-CeO_2 hybrid catalyst exhibits extremely high catalytic activity in the presence of $NaBH_4$, via electron relay process. Incorporation of ZnO to CeO_2 triggers the formation of Ce^{+3}/Ce^{+4} dynamic equilibria. This continuous fluctuation and the metallic character of Au NPs residing on ZnO-CeO_2 structures form an effective electron relay system which yields high degradation rates. Systematic studies are necessary to find the optimum ratio between ZnO and CeO_2 which yields a high surface area, a stable support for Au loading and a dynamic Ce^{+3}/Ce^{+4} conversion.

Acknowledgements

Authors thank to Dr. Oleksandr Polonskyi for his contributions to XPS analysis.

Supporting Information

CeO_2 was synthesized by Pluronic-123 (P-123) assisted Cerium Chloride ($CeCl_3 .7H_2O$). Firstly, P-123 and $CeCl_3 .7H_2O$ were dissolved in absolute ethanol and the mixture was sonicated at 60°C to evaporate ethanol and transform the solution into the gel. The gel was placed into the oven for 1 day at 70°C to dry it completely. The final product was calcined at 400°C for 6 hours to obtain oxidized CeO_2. To produce ZnO-CeO_2 mixed oxide, ZnO powder was added at the start of CeO_2 synthesis as shown in **Figure** 4.5a. The process to load Au on pure ZnO, CeO_2 and ZnO-CeO_2 hybrid oxides is illustrated in **Figure** 4.5b respectively. A freshly prepared 2wt% Gold Chloride ($AuCl_3$) solution was added into the nano-powder suspension and stirred for 10 minutes. Then freshly prepared Ascorbic Acid solution was added to the sorbent and continuously stirred for 20 minutes. The solution was left for 1 day to complete the Au loading onto the metal oxides. The solution was vacuum filtered, and the obtained catalysts were dried at 70°C for one day.

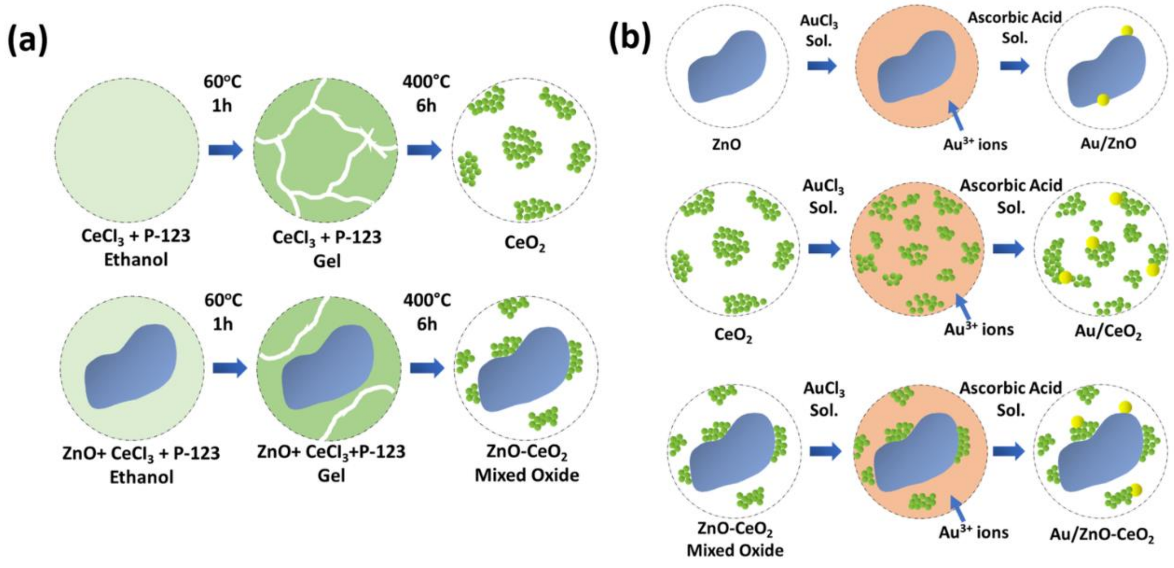

Figure 4.5. Schematic presentation of synthesis processes of **(a)** CeO_2 and CeO_2-ZnO structures and **(b)** Au loading on CeO_2, ZnO and ZnO-CeO_2.

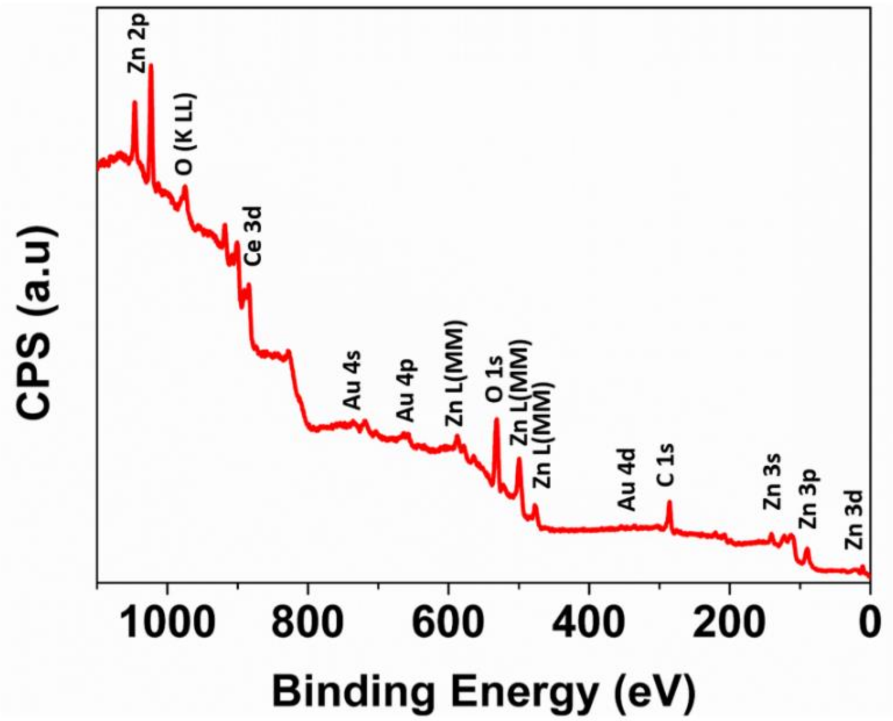

Figure 4.6. XPS survey spectrum of Au/CeO_2-ZnO hybrid nanostructures

In **Figure** 4.7a-c there is no prominent decolorization of MB have been notices by using $NaBH_4$ and Catalyst individually, in contrast by combining $NaBH_4$ and catalyst together an enormous change in MB colour have been recorded in **Figure** 4.7d after first 8 minutes of reaction.

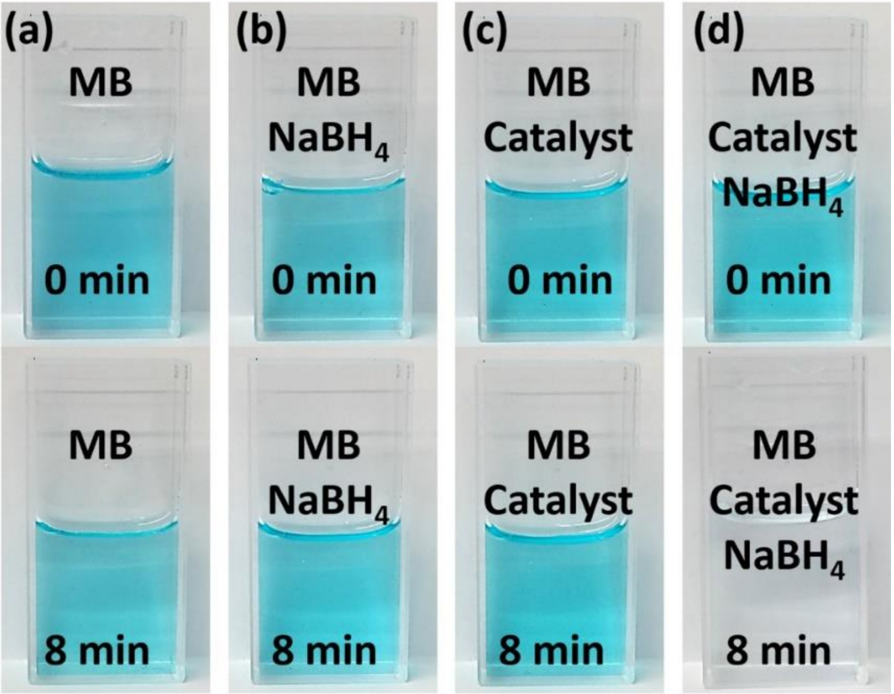

Figure 4.7. Photographs of Methylene Blue (MB) test solution at different time intervals which illustrate the degradation **(a)** without any Au/CeO_2-ZnO catalyst and $NaBH_4$ **(b)** with only $NaBH_4$ **(c)** with only Au/CeO_2-ZnO catalyst and **(d)** with both Au/CeO_2-ZnO catalyst and $NaBH_4$

Table 4-1. Comparison of synthesized catalysis structures

Catalysts	**ZnO / CeO_2 Ratio**	**Au wt. (%)**	**Primary Particle Size (nm)**	**Rate Constant (s^{-1})**
Au/ZnO	1.0/0.0	2	30-40/400-500	0.6×10^{-3}
Au/CeO_2	0.0/1.0	2	30-40/15-20	0.3×10^{-3}
Au/ZnO-CeO_2	0.3/0.7	2	30-40/400-500/20-30	9.2×10^{-3}

*Degradation rate constants were calculated as described elsewhere.[104]

ADVANCED MATERIALS INTERFACES

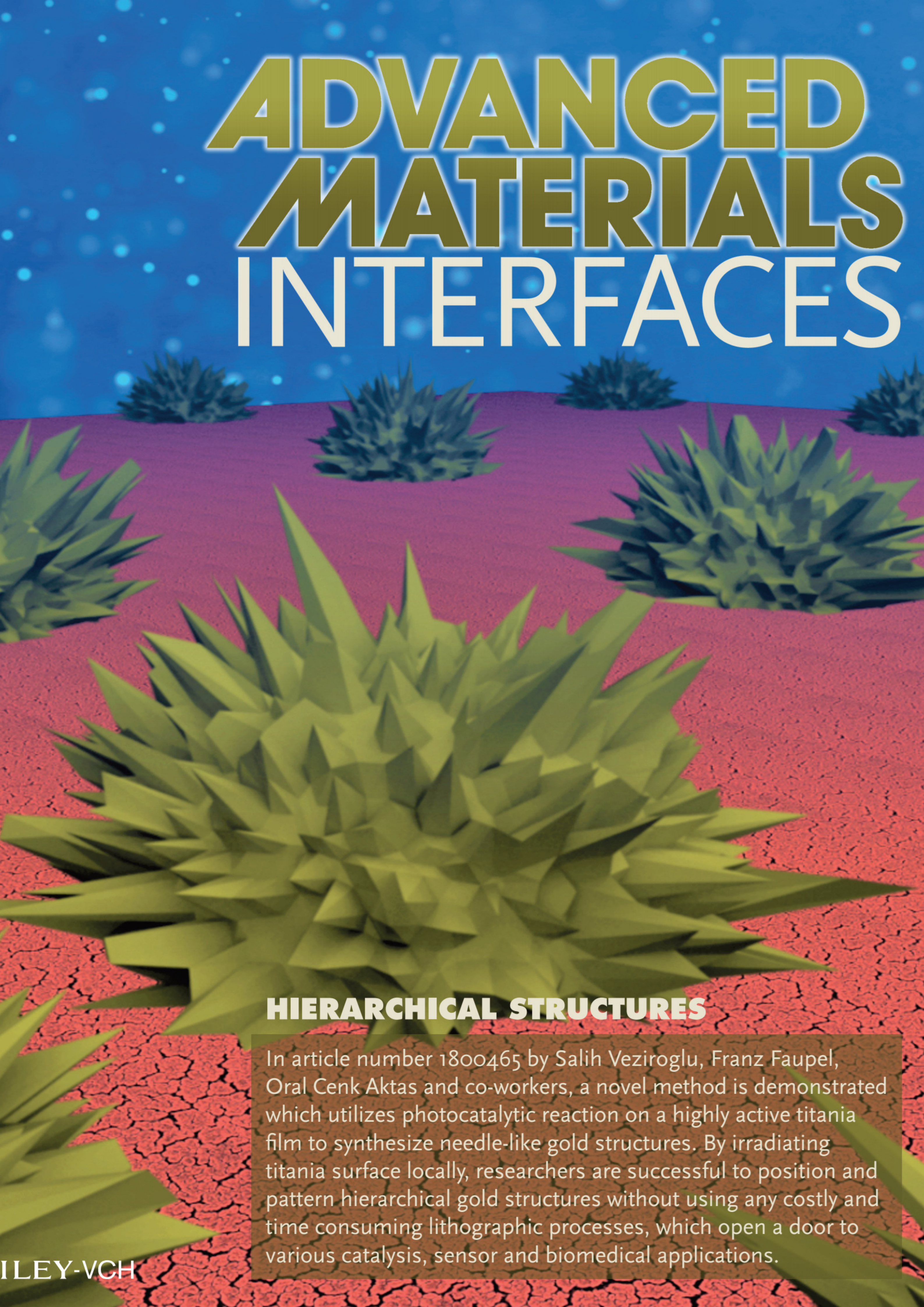

HIERARCHICAL STRUCTURES

In article number 1800465 by Salih Veziroglu, Franz Faupel, Oral Cenk Aktas and co-workers, a novel method is demonstrated which utilizes photocatalytic reaction on a highly active titania film to synthesize needle-like gold structures. By irradiating titania surface locally, researchers are successful to position and pattern hierarchical gold structures without using any costly and time consuming lithographic processes, which open a door to various catalysis, sensor and biomedical applications.

ILEY-VCH

5 Photocatalytic Growth of Hierarchical Au Needle Clusters on Highly Active TiO_2 Thin Film

This chapter is based on an article published in Advanced Materials Interfaces.[113]

Reprinted with permission from Salih Veziroglu, Muhammad Zubair Ghori, Marius Kamp, Lorenz Kienle, Horst-Günter Rubahn, Thomas Strunskus, Jacek Fiutowski, Jost Adam, Franz Faupel, Oral Cenk Aktas ***Adv. Mater. Interfaces*** 2018, 5, 1800465.
The article is available via the internet at https://doi.org/10.1002/admi.201800465

Abstract

Hierarchical gold (Au) structures with sharp edges garner a strong interest for nanoelectronics, nanoenergy harvesting devices, and nano-biomedical applications due the exceptional strong electric field (hot spot) enhancement at their tips. Herein, a facile method to synthesize hierarchical Au needle clusters (HAuNCs) on highly active titanium oxide (TiO_2) thin film is reported. Different from surfactant-directed photochemical-assisted synthesis methods, a photocatalytic deposition approach is demonstrated, which allows positioning and patterning of HAuNCs on TiO_2 target without using any surfactant or stabilizer. This green synthesis approach enables to control the size and the geometry of deposited HAuNCs by simply altering the photocatalytic activity of TiO_2 target, UV light intensity, and irradiation time.

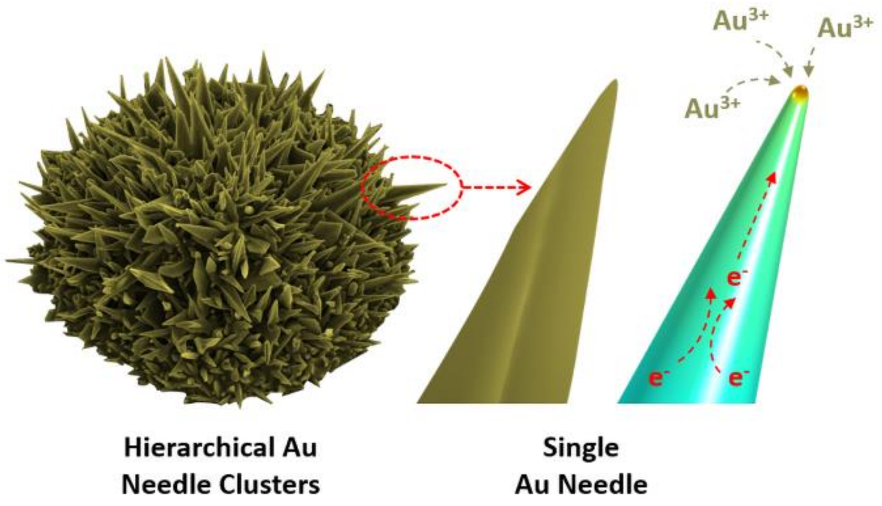

5.1 Introduction

Anisotropic hierarchical gold (Au) nanostructures have received exceptional attention during the last decade, owing to their superior unique structural, optical, electronic and catalytic properties, in comparison to typical spherical Au nanoparticles.[64] Especially branched Au nanostructures (nanostars, nanoplates, nanopyramids etc.)[114–116] with sharp edges garnered a strong interest for nano-electronics, nano-energy harvesting devices and nano-biomedical applications due the exceptional strong electric field (hot spot) enhancement at their tips.[117–119]

Surfactant-directed (seed-mediated) chemical reduction and polyol methods have been frequently used to produce branched and needle-like Au nanostructures.[120] In most of these synthesis methods the geometry and size of such Au nanostructures are basically controlled by the incorporation of an ionic liquid to a reducing agent. [118,121] Unfortunately, some of such ionic surfactants/stabilizers may arise health problems due to their toxic nature.[122] The use of highly active ionic species may also lead to the in-situ contamination (release of ions or reduction/oxidation) during the synthesis of Au nanostructures.

Beside their high throughput, bottom-up techniques which are mostly wet-chemical approaches (synthesis of particles within a solvent) are not relevant for the controlled positioning and patterning of Au nanostructures on a solid target.[123,124] The electrodeposition of Au on pre-patterned conductive electrodes, including indium tin oxide (ITO), Au and similar materials, has been demonstrated as an effective method to control the positioning and local deposition of hierarchical Au nanostructures such as nanospikes, nanoflowers and nanoneedles.[125,126] On the other hand, the high aggressiveness (high pH value) of electrolyte solutions (e.g. $HAuCl_4$) and the prerequisite of having a conductive surface limit the choice of substrate materials. Moreover, the need for structuring of the electrodes through a multi-step lithography process make the electrodeposition a time consuming and an expensive method for patterning of surfaces with Au nanostructures. Alternatively, galvanic replacement (electrodeless) synthesis methods are proposed but these mostly fail in controlling and positioning of Au nanostructures on a solid target.[120,127]

Photochemistry is another convenient method to synthesize anisotropic Au nanostructures.[128] At strong intensities, the incident light promotes the reduction of Au^{3+} ions within an aqueous solution (e.g. $HAuCl_4$), but additionally a cationic surfactant is needed to trigger the anisotropic growth.[120] Photocatalytic reduction of Au^{3+} ions on active surfaces such as TiO_2 (indirect reduction via photogenerated electrons from TiO_2) has been proposed as an alternative to the direct photoreduction of Au^{3+}.[129] While the method allows synthesis of Au structures directly on a photocatalytic surface without using any surfactant, it is challenging to achieve hierarchical and high aspect ratio (AR) Au structures.[130] Huang et al. presented the synthesis of urchin-like Au structures composed of extremely sharp nanoneedles using TiO_x-sol as the base active material.[131] On other hand, the authors observed the accumulation of TiO_2 thin layer on Au nanostructures at the end of the process, which clearly indicates the existence of a bi-phasic TiO_2/Au morphology rather than a stoichiometric Au.

In general, the photocatalytic reduction of Au^{3+} ions on non-stationary TiO_2 micro- and nanoparticles (dispersed within a solvent) cannot be applied for a practically relevant positioning or local (selective) loading of Au nanostructures. In such colloidal systems mostly high light intensities are needed to promote the photocatalytic reduction of Au^{3+} due to the dynamic movement of particles and their interactions.[67] On the other hand, the high light intensity may trigger the direct reduction of Au^{3+} (rather than the photocatalytic reduction by TiO_2) and this lead to uncontrolled formation of Au aggregates.

Here we present a facile method for synthesis of **H**ierarchical **A**u **N**eedle-**C**luster**s** (HAuNCs) on a highly active TiO_2 thin film by applying photocatalytic reduction of Au^{3+} without using any capping agent or surfactant. The use of extremely low UV light intensity prevented the uncontrolled direct reduction of Au^{3+} ions within the solution (proposed reactions are explained in **Figure** 5.10). We also demonstrate patterning of TiO_2 surface by HAuNCs in a controlled way by using a simple and cheap non-contact mask.

5.2 Experimental Section

5.2.1 Preparation of TiO_2 Thin Films

A custom sputtering system equipped with a DC planar magnetron source (Advanced Energy, MDX 500) was used to sputter TiO_2 thin films from a metallic titanium target (Ti-Goodfellow, 99.99 %, 5 cm diameter) using argon (Ar) and oxygen (O_2) as process gas and reactive gas, respectively. Polished silicon (Si) substrates (10 mm x10 mm) were cleaned in the ultrasonic bath using three different solvents (acetone, isopropanol, and water, respectively) and subsequently dried with nitrogen gas. After placing substrates into the vacuum chamber the base pressure was adjusted about 5×10^{-5} Pa by a turbo molecular pump (Pfeiffer Vacuum, HiPace 400) and a rotary pump (Agilent Technologies, SH-110). While DC power (90 W) was pulsed (a rectangular trigger signal with a peak-to-peak amplitude of 5 V was applied) at a frequency of 50 kHz with 55 % duty cycle to reduce the excessive oxidation and the poisoning of the target surface. Ar/O_2 gas mixture with a constant ratio of 250 sccm: 10 sccm was supplied with the help of precise mass-flow-control system (MKS, Multi Gas Controller 647C). During sputtering, substrates were rotated at 30 rpm to assure a homogeneous film deposition. After the sputtering (2h), prepared TiO_2 thin films were heat-treated in the oven (Nabertherm, LE 4/11/R6) at 350-750 °C for 1h and directly quenched in the air.

5.2.2 Characterization of TiO_2 Thin Film:

Scanning Electron Microscope (Supra55VP-Carl Zeiss) was used to characterize the morphology of prepared thin films, with an electron beam of 2-5 kV and a standard aperture size of 30 μm. Raman spectra of prepared TiO_2 thin films were collected using a confocal Raman system (WITec, alpha300AR) equipped with a laser operating at a wavelength of 532 nm to reveal the crystal structure.

5.2.3 Photocatalytic Activity Analysis

In order to measure the performance activity of TiO_2 thin film MB was used a test pollutant. The photocatalytic bleaching of MB was performed in a custom-made light-shielded reactor consists of Teflon® reactor, quartz cuvette and magnetic stirrer. MB powder (Sigma–Aldrich, CAS 7220-79-3) was dissolved in deionized water to a concentration of 10 µmol/l. TiO_2 thin film (deposited on 1 cm^2 Si substrate) was immersed in the 6.5 ml aqueous MB solution (10 µM) and irradiated with the UV light (365 nm). The change in absorption of MB solution was monitored at 664 nm wavelength by UV–vis spectroscopy (StellarNet EPP2000C-SR-50 with SL5-DH light source) [9,23].

5.2.4 Synthesis of HAuNCs on TiO_2 Thin Film:

HAuNCs were deposited on TiO_2 thin film by the photocatalytic reduction of Au^{3+} iosns. We dipped the TiO_2-coated Si substrate in to a quartz cuvette, filled with 6.5 ml of a concentrated (0.8 mM) aqueous $HAuCl_4$ (Alfa Aesar) solution. Afterwards, a UV-LED operating at a wavelength of 365 nm irradiated on the substrate surface through the quartz cuvette. UV light intensity (0.25 mW/cm^2 and 4.5 mW/cm^2) and irradiation time (1-60 min) were changed systematically. For patterning of surfaces with HAuNCs a simple mask was used to irradiate TiO_2 layer selectively. Basically the mask was cut (12 mm x12 mm) from a nylon woven net filter and it was brought closer to the TiO_2 surface with help of Teflon spacers attached at the edge of the substrate (providing a substrate-mask distance of about 1.5 mm). The mask After UV irradiation, the samples were washed with de-ionized (DI) water and dried with nitrogen to remove any residual $HAuCl_4$ solution from the substrate.

5.2.5 Electrochemical Simulation

We performed electrostatic field calculations, based on the finite-element method (FEM), using the commercially available FEM software COMSOL Multiphysics. We applied a constant voltage (1 V) between a top and a bottom electrode (the latter carrying the Au nanostructure) in a capacitor arrangement, filled with the aqueous solution. Without the nanostructure, this leads to a homogeneous electric field, used as a reference for normalizing the LEFE values ($E_0 = 1.33\times10^6$ V/m for a capacitor with a thickness of 300 nm). Based on this, for a better comparability, we calculate the resulting nanostructure-induced electrical field enhancement as the (unit-less) ratio $|E/E_0|$. See **Figure** 5.15 for a more detailed numerical analysis on the influence of AR and needle tip radius on the local electrical field enhancement.

5.2.6 Characterization of HAuNCs

The morphology of the HAuNCs was studied by scanning electron microscopy (Supra55VP-Carl Zeiss) and helium ion microscopy (HIM, Orion NanoFab-Carl Zeiss). SEM was operated at low beam energy of 3 kV. HIM was carried out at 25 keV beam energy with a probe current ranging from 0.1 to 0.4 pA. No conductive coatings were applied to the samples prior to both SEM and HIM analyses in order to preserve the sample surface information. Structural analysis of HAuNCs was characterized via TEM using a Tecnai

F30 STwin microscope (300 kV, field emission gun (FEG) cathode, spherical aberration coefficient Cs = 1.2 mm). The samples for TEM investigations were prepared by focused ion beam (FIB) milling using a lift-out method (which were embedded in a carbon matrix) with a FEI Helios Nanolab system (details of FIB sample preparation is provided in Supporting Information). Afterwards bright field images and selected area electron diffraction (SAED) patterns of prepared samples were recorded to reveal structural properties.

5.3 Result and Discussion

5.3.1 Photocatalytic Deposition of HAuNCs

In a typical experiment we sputter-deposited a 600 nm thick TiO_2 layer onto a silicon wafer according to the method we reported earlier.[9] Subsequently, we vertically dipped the prepared sample into a quartz cuvette filled with the aqueous $HAuCl_4$ solution. We used a UV-LED, operating at a wavelength of 365 nm and a UV light intensity of 4.5 mW/cm^2 to irradiate the sample surface through a UV-transparent quartz cuvette. The scheme given in **Figure** 5.1 shows the basic growth mechanism of a single HAuNC.

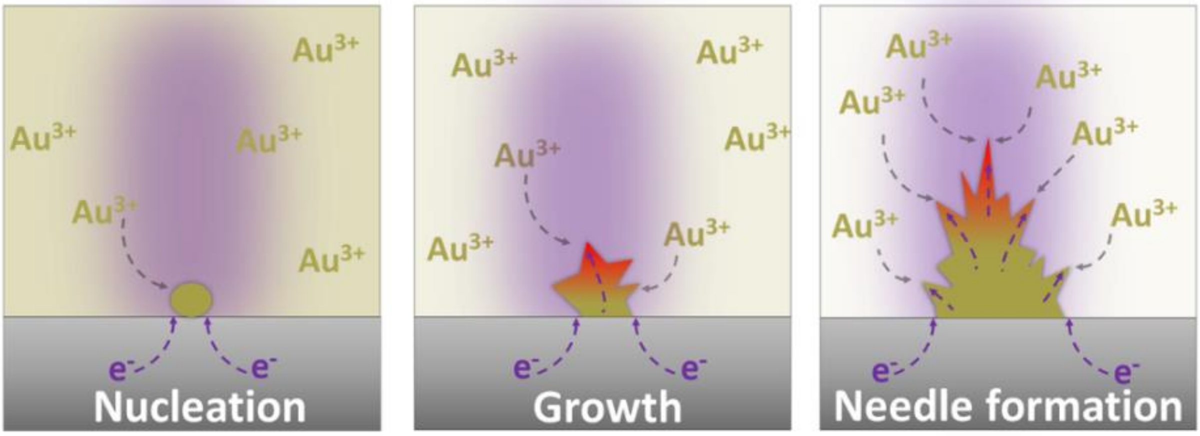

Figure 5.1. Schematic representation of HAuNC growth mechanism.

First, UV irradiation generates electron-hole pairs in TiO_2 film and then Au^{3+} ions (in aqueous solution) are reduced into a stable Au cluster by such densely generated electrons. The relative decrease of Au^{3+} concentration on the surface, where first embryonic Au cluster nucleate, seems to promote the diffusion of more Au^{3+} ions (from higher to lower concentration regions), followed by preferential piling of Au clusters into needle-like structures (HAuCNs shown in **Figure** 5.2). We observed that the sharpness of such needle-like structures (**Figure** 5.12) increased by the irradiation time, which might be attributed to the high electron density at sharp edges (**Figure** 5.13), promoting the preferential reduction of Au^{3+}. As Safei et al. showed the density of electrons was exceptionally high at sharp tips of branched Au nanostructures.[126]

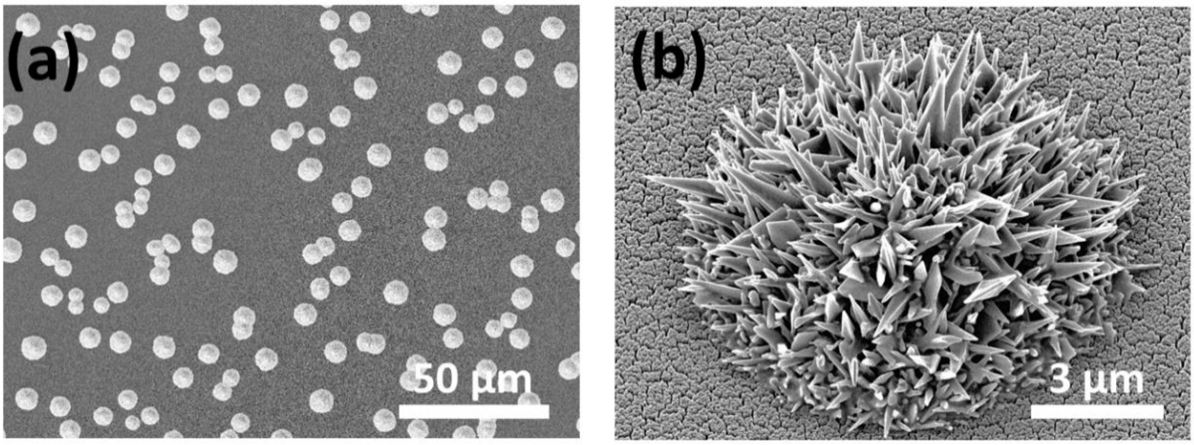

Figure 5.2. **(a)** SEM image of HAuNCs deposited on TiO_2 and **(b)** HIM image of a single HAuNC.

It is known that higher UV light intensities lead to greater density of electron-hole pairs in TiO_2.[9] Therefore, we altered the UV light intensity to understand its influence on the growth of HAuNCs. In order to verify the ability of generating electron-hole pairs in TiO_2 (photocatalytic performance) at different UV light intensities we immersed the prepared TiO_2 samples in an aqueous methylene blue (MB) solution and monitored the change in its absorption (at 664 nm as shown in **Figure** 5.3), as we described in detail previously.[9,23]

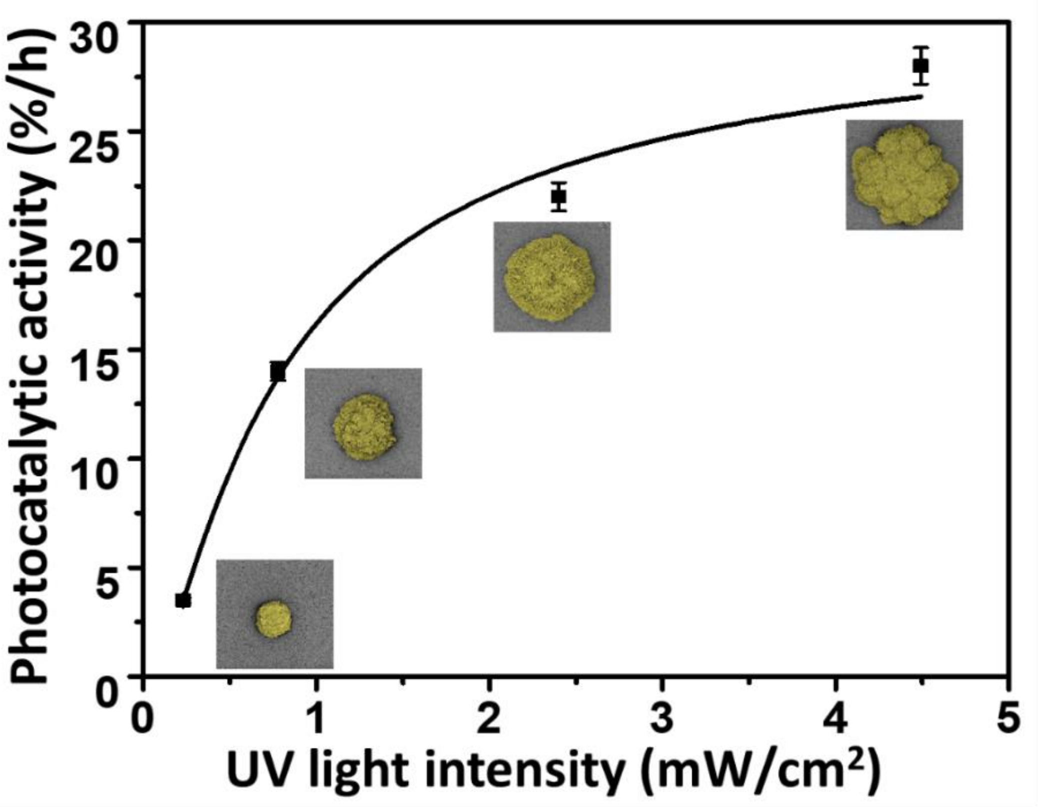

Figure 5.3. Photocatalytic activity analysis (determined by the MB degradation) at different UV light intensities (inset shows SEM images (recolored to achieve contrast) of HAuNCs prepared at corresponding UV light intensities).

Photocatalytic performance (monitored by photocatalytic bleaching of MB) at different light intensities were correlated with the morphology of HAuNCs as shown by insets given in **Figure** 5.3 (achieved at corresponding light intensities). Sharper Au structures were observed at UV light intensities above 2.4 mW/cm^2, where also highest photocatalytic activities were achieved (which correspond to a MB bleaching rate of 23 - 30 % per hour).

We examined the morphology of deposited HAuNCs in detail using **H**elium **I**on **M**icroscopy (HIM), and the corresponding images are presented in **Figure** 5.4. **Figure** 5.4a shows the low magnification HIM image of a single HAuNC, where needle-like structures are apparent with tip radius of 5–20 nm and length of 1-2 μm (**Figure** 5.4b). At high resolution images, (**Figure** 5.4c and **Figure** 5.4d), sharp needle-like Au nanostructures are clearly seen.

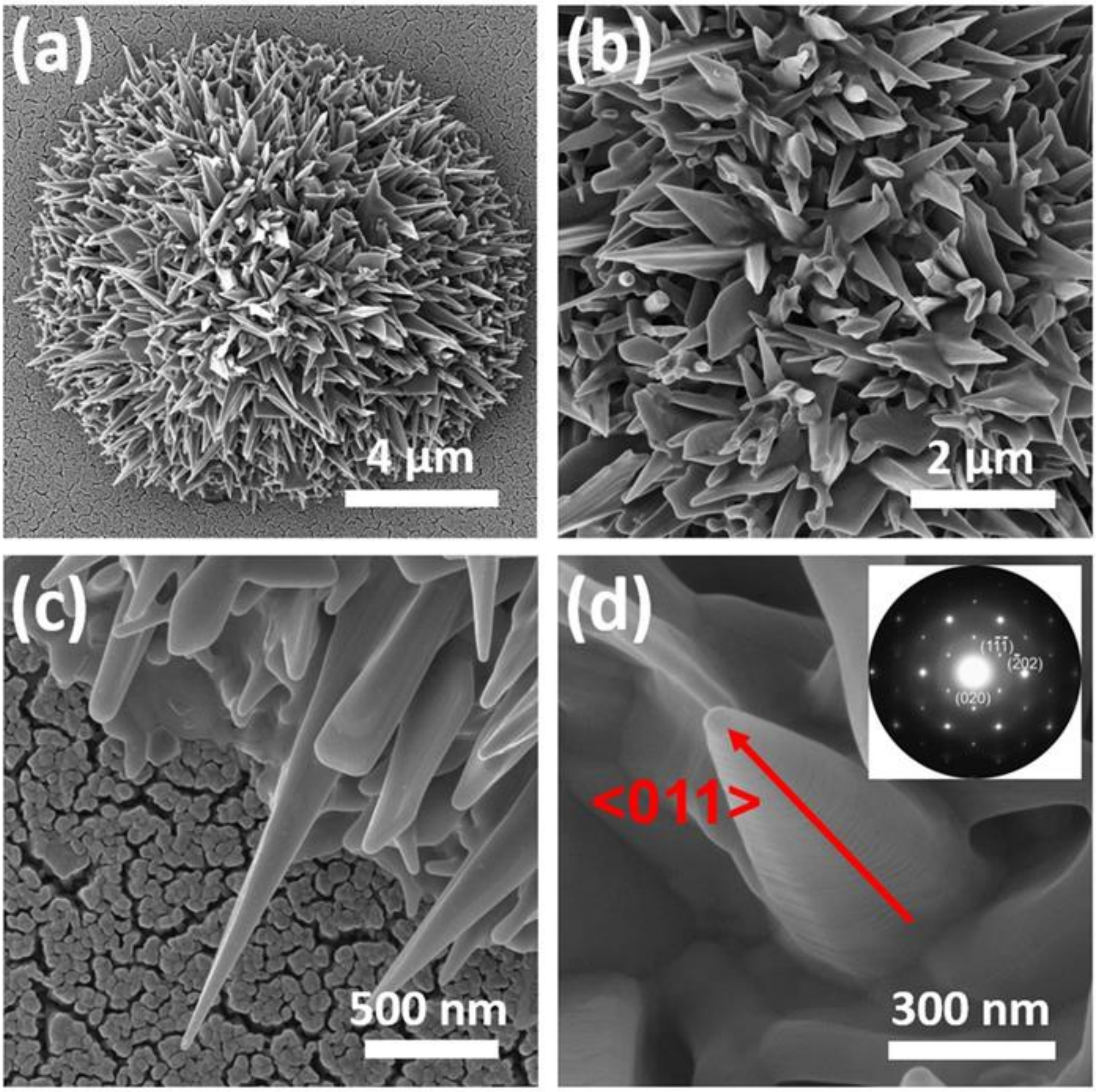

Figure 5.4. HIM images of **(a)** a single HAuNC at low magnification, **(b)** needle-like Au structures which form hedgehog-like microstructure, **(c)** and **(d)** high magnification series showing needle-like Au nanostructures. Inset indicates SAED pattern ([101] zone axis) and the arrow represents the <011> growth direction.

After Focused Ion Beam (FIB) milling, we investigated the crystallinity and the growth direction of a single Au needle (taken from HAuNCs). The <011> growth direction was confirmed by multiple selected area diffraction (SAED) patterns (inset, **Figure** 5.4d) in different zone axis from the depicted needle (see **Figure** 5.14). The single crystallinity was proven by SAED from different positions along the growth direction. Although the sample was prepared in cross section (FIB,) the sample thickness impedes further analysis by HRTEM imaging.

5.3.2 The Influence of UV Light Intensity and Irradiation Time on the Growth of HAuNCs

We systematically altered the UV irradiation time (two different sets of samples exposed to (a) high-4.5 mW/cm² and (b) low-0.25 mW/cm² UV light intensity) to reveal details of the growth mechanism of HAuNCs (corresponding SEM images are given in **Figure** 5.5a and **Figure** 5.5b).

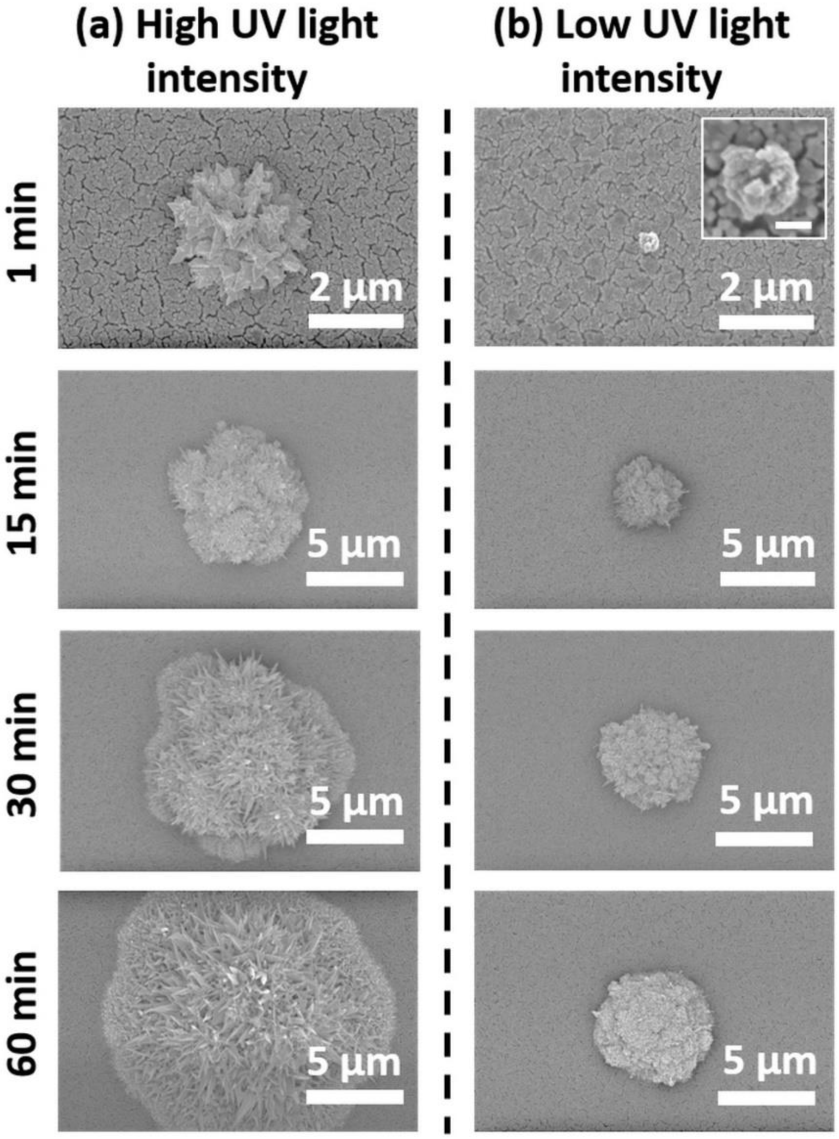

Figure 5.5. SEM images of HAuNCs deposited at different irradiation time intervals (1-60 min) at **(a)** high UV light intensity (4.5 mW/cm²) and **(b)** low UV light intensity (0.25 mW/cm²) (Inset scale bar: 200 nm).

The Au atom concentration increased gradually (by the UV irradiation time) as the Au^{3+} ions got reduced. We have shown that the critical nucleus size of noble metals on dielectric surfaces is as small as a single atom.[132] Thus, already two metal atoms form a stable nucleus if they encounter each other. This is also expected for metal atoms in solution. When the Au atom concentration reached supersaturation they possibly formed aggregates, turning into small clusters through the heterogeneous nucleation (on the TiO_2 thin film). Once formed, these nuclei rapidly grew into larger sized nanocrystals within a short time (**Figure** 5.5a) and finally a hedgehog-like morphology was achieved. UV light intensity played a major role on the final morphology of the deposited Au nanostructures. While the high UV light intensity led to a fast nucleation and high growth rate (led to formation of larger Au nanostructures within a short time as shown **Figure** 5.5a) we observed formation of much smaller Au clusters at low UV light intensity (**Figure** 5.5b). In addition, nucleated clusters got sharper by the time at high UV light intensity whereas less sharp and poorly ordered Au nanostructures formed at low UV light intensity.

In order to reveal the difference in the growth of Au nanostructures at high and low UV light intensities, by simulating the formation of the local electrical field enhancement (LEFE) around such structures at early and final growth stages using an electrochemical model[126] as shown in **Figure** 5.6 (the morphology of Au particles given at **Figure** 5.5 have been taken as structure model prototypes). Structures observed after 1 min irradiation were used to reveal the “early stage growth” mechanism. Whereas, sharper structures observed after 60 min irradiation were taken as models for evaluating the “final stage growth” mechanism. Details are provided in **Figure** 5.11.

Following a fast nucleation (promoted by high density of electron/hole generation) at high UV light intensity, sharp Au structures (**Figure** 5.5a, 1 min) with an AR of 4 lead to a significant LEFE (**Figure** 5.6a, early stage). It is believed that high LEFE ($E = 4.7\ E_0$, where $E_0 = 1.33\text{x}10^6$ V/m is the *reference* electric field magnitude for a 300 nm thick capacitor without any nanostructure present) enhances further accumulation of Au^{3+} ions and the subsequent promotion of the preferential reduction around sharp regions. In contrast, at low UV light intensity, the nucleation was slow (less Au accumulation led much smaller particles) and embryonic clusters seem to exhibit a globular morphology (**Figure** 5.5b, 1 min), which we address to the lower electron/hole generation density. The lack of sharper regions led to a homogenous distribution of an electrical field (**Figure** 5.6b, early stage) rather than a local enhancement limiting the preferential reduction. Clearly AR of sharp structures (final stage) deposited at high UV light intensity is significantly higher than those deposited at low UV light intensity. A more detailed analysis reveals that the tip radius and AR play a major role on the LEFE at needle-like Au structures (**Figure** 5.15).

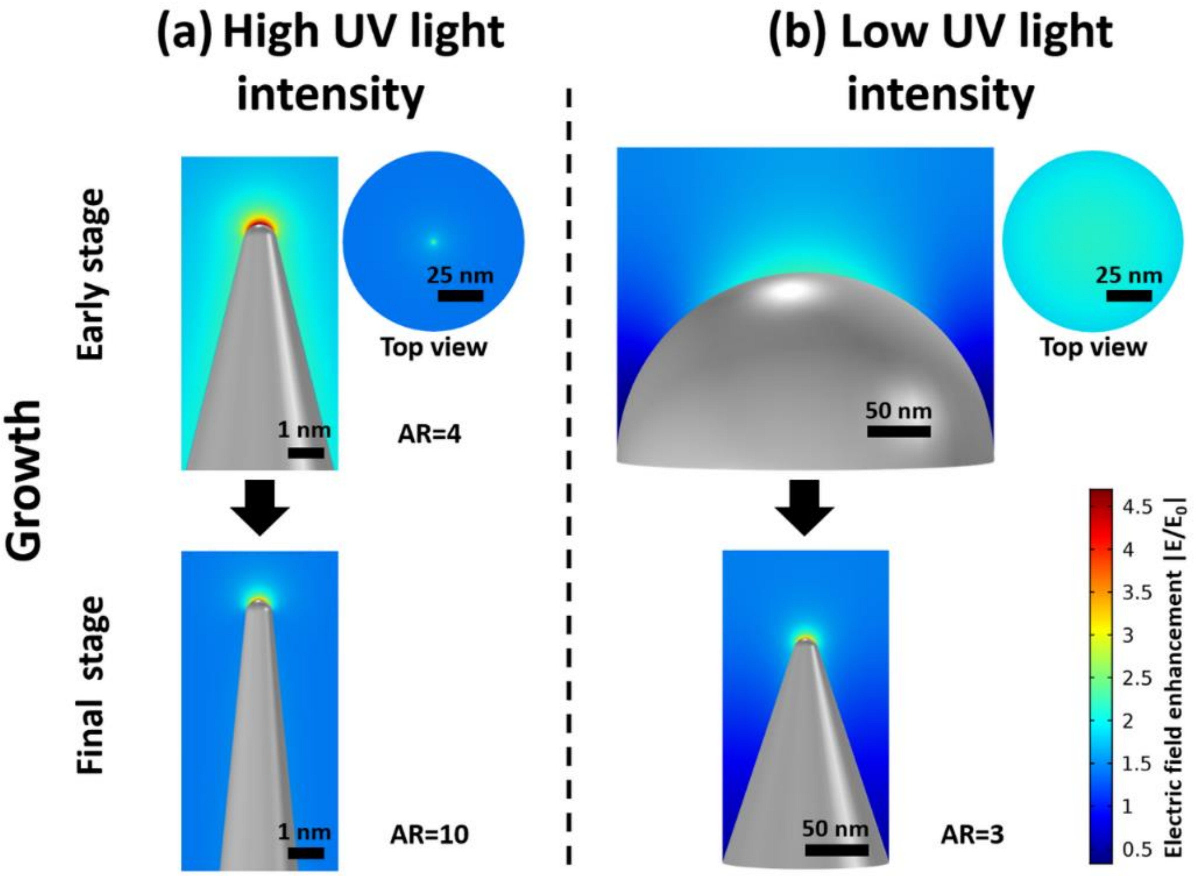

Figure 5.6. Computed local electric field enhancement around deposited Au nanostructures at **(a)** high UV light intensity (magnified images of the tip from a single needle as the model structure for early and final stage growth) and **(b)** low UV light intensity (spherical particle as the model for the early stage growth and needle-like geometry as the model for the final stage growth). In calculations, $E_0 = 1.33 \times 10^6$ V/m and all structures correspond to morphologies visualized by SEM (**Figure** 5.3). Details are provided in **Figure** 5.11.

5.3.3 Influence of Photocatalytic Activity of TiO_2 Target on the Growth of HAuNCs

In photocatalytic reduction studies the crystallinity, which determines the activity of the base material (to be loaded with Au), mostly has not been evaluated in detail and its influence on the growth Au morphology remains undermined. In order to evaluate the effect of the photocatalytic activity of the TiO_2 target on the growth mechanism of HAuNCs, we prepared a series of TiO_2 films which were composed of different crystal structures (heat-treated at different temperatures).

As depicted in **Figure** 5.7a, TiO_2 film heat-treated at 550-650 °C exhibited the highest photocatalytic activity (photocatalytic bleaching of MB). Raman spectra (**Figure** 5.7b) of the deposited layers also showed a good correlation with the photocatalytic activity analysis. The increase in the anatase content led to higher photocatalytic activity (**Figure** 5.7a) and promoted the growth of much sharper and highly ordered Au nanostructures (**Figure** 5.7c). In contrast, we did not observe the formation of any Au nanostructure on amorphous and rutile (containing limited amount of anatase) TiO_2 films (**Figure** 5.7c). Our systematic analysis showed that crystallinity, UV light intensity and irradiation time were the main process parameters to control the size and geometry of deposited HAuNCs.

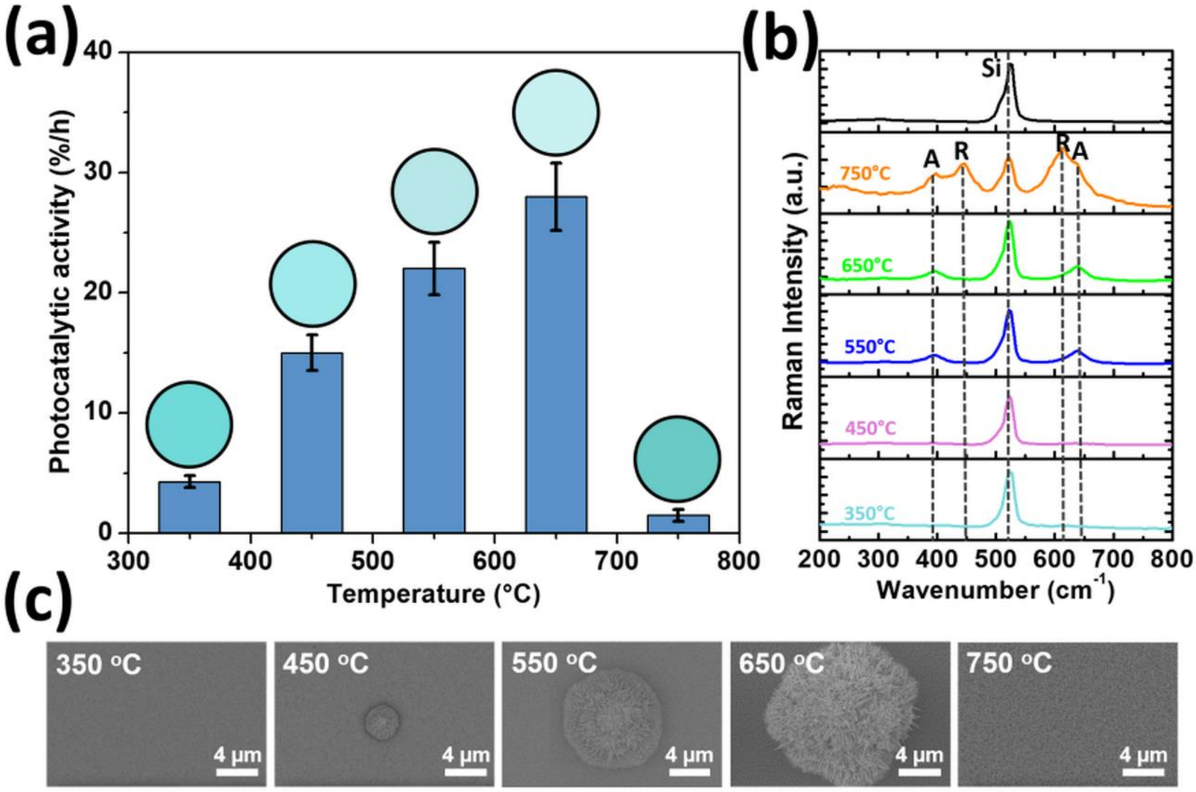

Figure 5.7. **(a)** Photocatalytic activity of TiO_2 thin films heat-treated at different temperatures (inset shows the change in the color of MB after 1h UV irradiation), **(b)** Raman spectra of TiO_2 thin films heat-treated at different temperatures and **(c)** SEM images of corresponding TiO_2 thin films after photocatalytic deposition of Au after 1h UV-irradiation (4.5 mW/cm^2)

5.3.4 Patterning TiO_2 Target by Selective Deposition of HAuNCs

The presented approach allows positioning and patterning HAuNCs on an active TiO_2 layer with the help of a simple polymer mask (shown in **Figure** 5.16a) as presented in the scheme given in **Figure** 5.8a. **Figure** 5.8b shows SEM images of HAuNCs deposited after 30 min UV irradiation through the polymer mask. Corresponding elemental imaging (**Figure** 5.16b) shows clearly that Au^{3+} ions were reduced selectively on the UV irradiated portions of TiO_2 layer. At a closer look one can see that HAuNCs are composed of extremely sharp needle-like structures (**Figure** 5.8c).

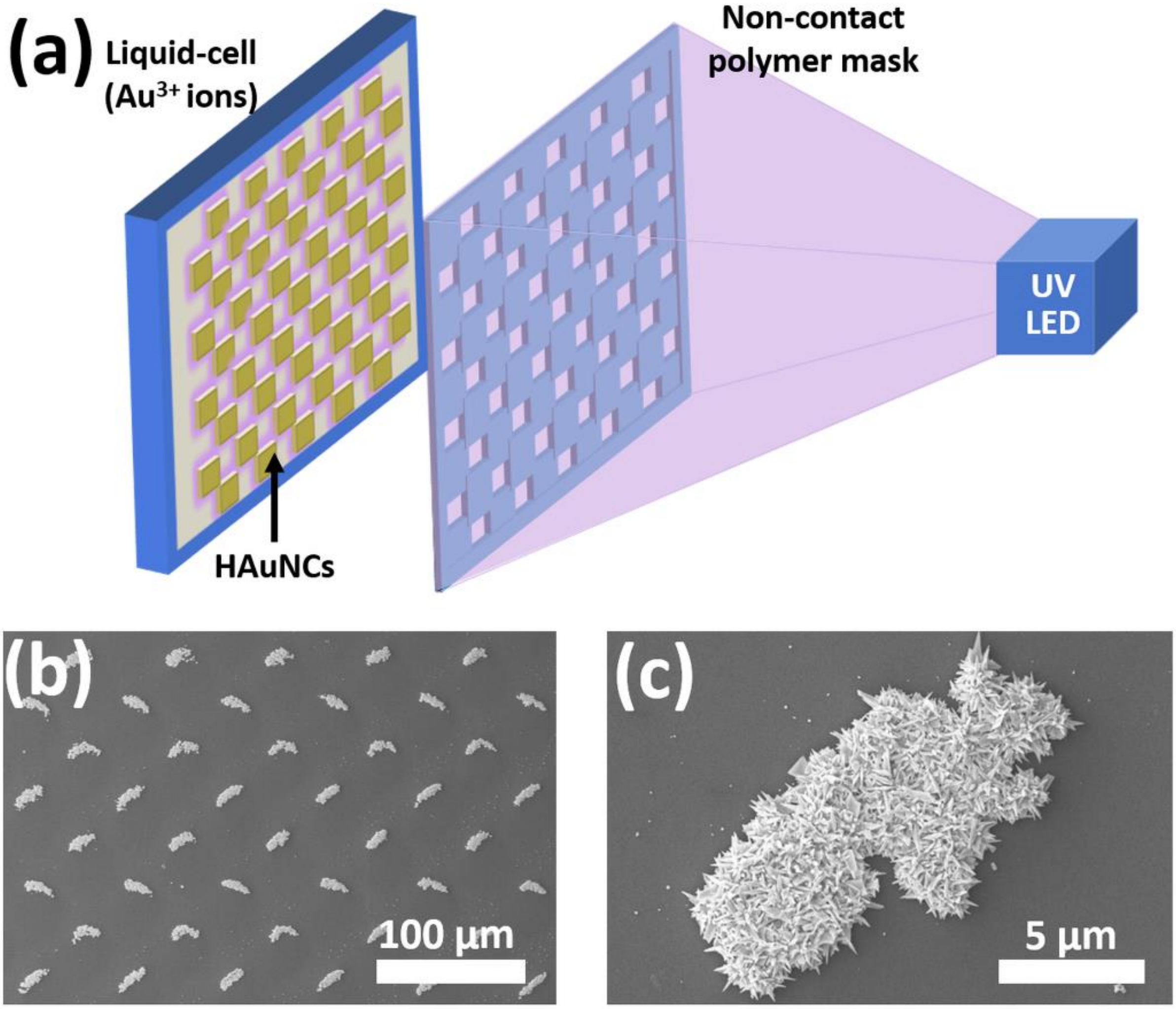

Figure 5.8. **(a)** Schematic representation of photocatalytic patterning of TiO_2 thin film with HAuNCs using a non-contact polymer mask. SEM images of **(b)** periodic HAuNCs arrays and **(c)** a single HAuNC.

5.4 Conclusion

In conclusion, we demonstrated a facile method to fabricate HAuNCs by photocatalytic reduction of Au^{3+} ions on TiO_2 film. This method allows positioning and patterning of HAuNCs without using any surfactant or stabilizer. This green synthesis approach enables controlling the size and the geometry of deposited HAuNCs by simply altering the photocatalytic activity of the TiO_2 target, UV light intensity and irradiation time. **Figure** 5.9 illustrates an understanding of the growth mechanism of HAuNCs and the influence of the process parameters (photocatalytic activity of TiO_2 target, UV light intensity and irradiation time) on the growth. Local irradiation of the active TiO_2 thin film through a simple non-contact mask led to local patterning with extremely sharp needle-like Au nanostructures, which may find application especially in catalysis, plasmonics and biomedical technologies (probing and manipulating biological processes)

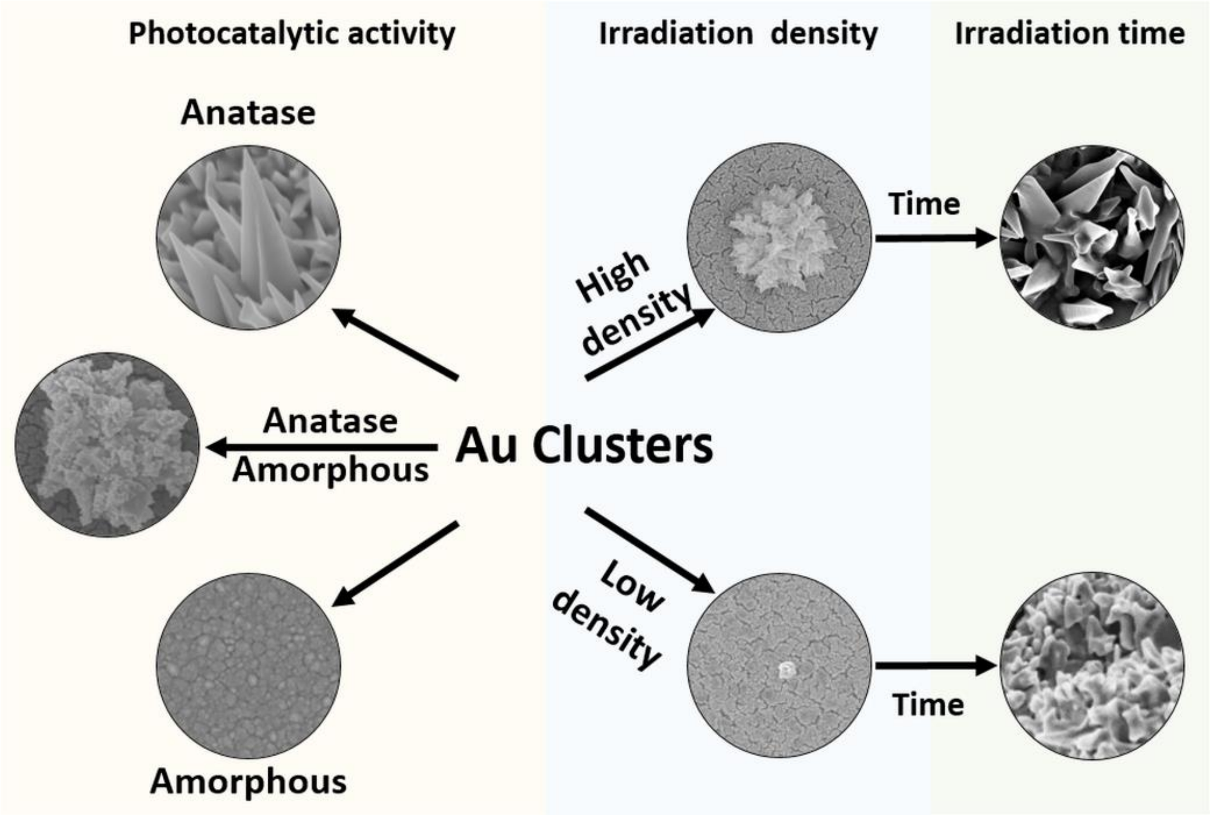

Figure 5.9. Proposed synthesis pathway for controlling the growth and morphology of HAuNCs.

Acknowledgements

Simulation for the work described in this paper was supported by the DeiC National HPC Centre, SDU. M. Z. Ghori acknowledge Graduate Center and Federal State Funding CAU Kiel for providing funding for his PhD study. Authors would like to thank Stefan Rehders for his continuous support for sputtering setup. Additionally, authors thank to Christin Szillus for assisting FIB sample preparation and Dr. Ulrich Schürmann for his invaluable contributions for TEM analysis.

Supporting Information

1	Photoreduction of Au^{3+} within the aqueous solution (Not observed at low irradiation density!)	$\xrightarrow{\lambda} Au^{3+}_{(aq)} + 3e^{-} \rightarrow Au^{0}_{(s)}$	High Energetic Light Source (e.g. UV Laser)
2	Indirect photoreduction of Au^{3+} at TiO_2 interface (Feasible at low irradiation density!)	$\xrightarrow{\lambda} TiO_2 \rightarrow e^{-} + h^{+}$ $Au^{3+}_{(aq)} + 3e^{-} \rightarrow Au^{0}_{(s)}$	Low Energetic Light Source (e.g. UV LED)

Over-all Reaction

$$TiO_2 + hv \rightarrow TiO_2 + e^- + h^+$$

$$Au^{3+} + 3e^- \rightarrow Au^0$$

$$3/2H_2O + 3h^+ \rightarrow 3/4O_2 + 3H^+$$

$$Au^{3+} + 4(OH)^- + 3/2H_2O + 3e^- + 3h^+ \rightarrow Au^0 + 3/4O_2 + 3H^+ + 4OH^-$$

Net reaction $Au^{3+} + 4(OH)^- + 3/2H_2O + 3e^- + 3h^+ \rightarrow Au^0 + 3/4O_2 + OH^- + 3H_2O$

Figure 5.10. Comparison of direct and indirect (by TiO_2 thin film) reduction of Au^{3+} ions (including the overall reaction mechanism).[129]

Representative structure model	**Definition**	**Aspect Ratio** (AR: h/w) h: height w: half width
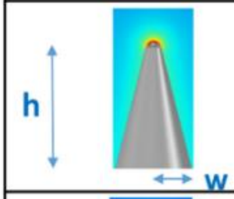	This model is created by considering the morphology of a single Au needle deposited after 1 min irradiation (high intensity) as shown in Figure 3a.	4
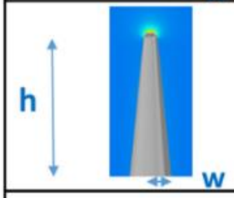	This model is created by considering the morphology of a single Au needle deposited after 60 min irradiation (high intensity) as shown in Figure 3a.	10
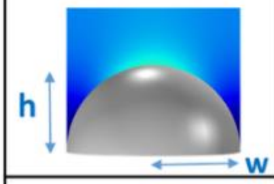	This model is created by considering the morphology of a single Au nanostructure deposited after 1 min irradiation (low intensity) as shown in Figure 3b.	-
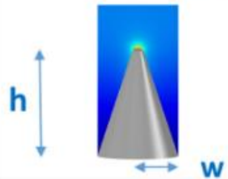	This model is created by considering the morphology of a single Au needle deposited after 60 min irradiation (low intensity) as shown in Figure 3b.	3

Figure 5.11. Description of the model structures for the electrochemical simulation.

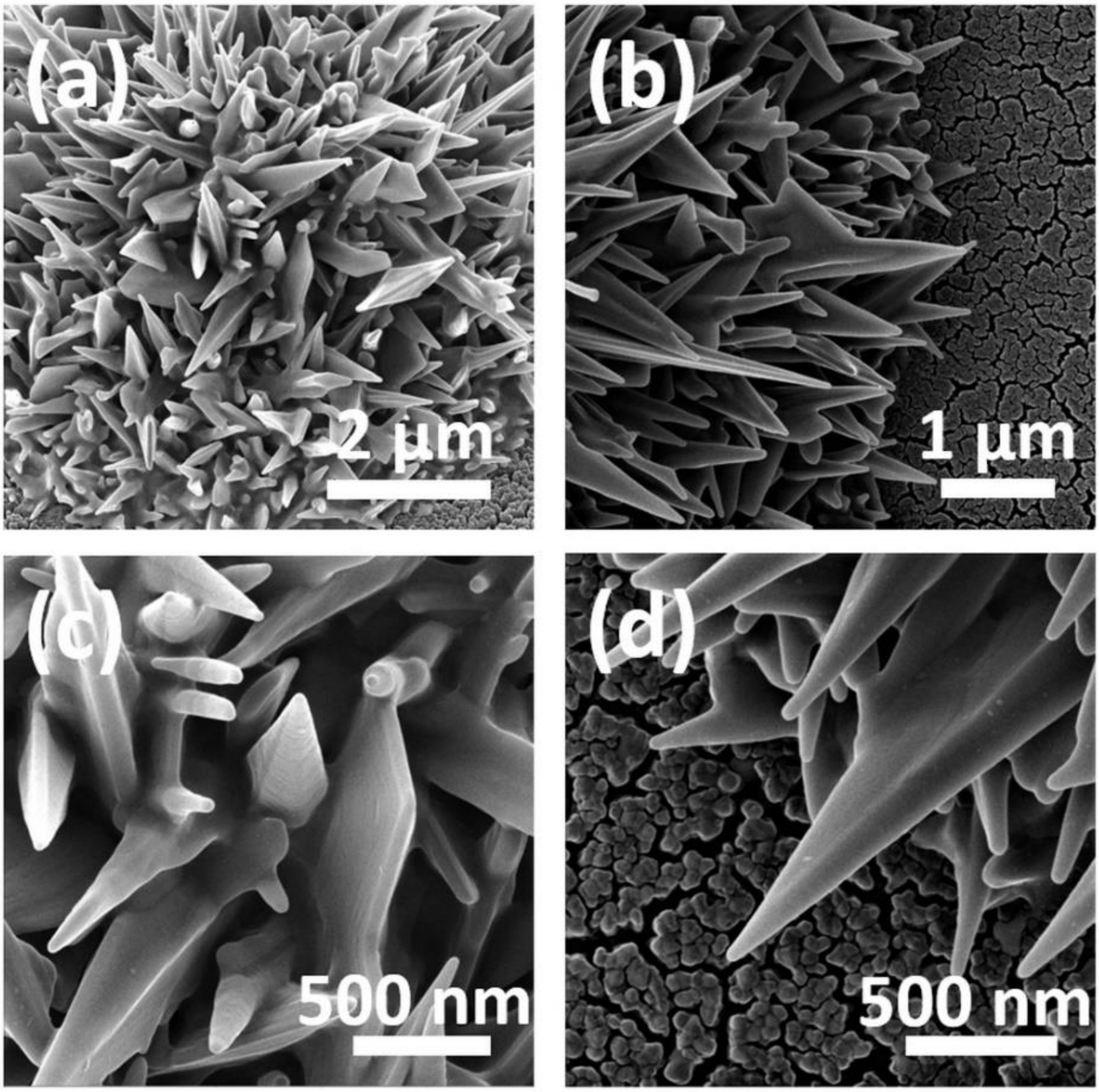

Figure 5.12. **(a-d)** Helium ion microscope images of HAuNCs at different magnifications.

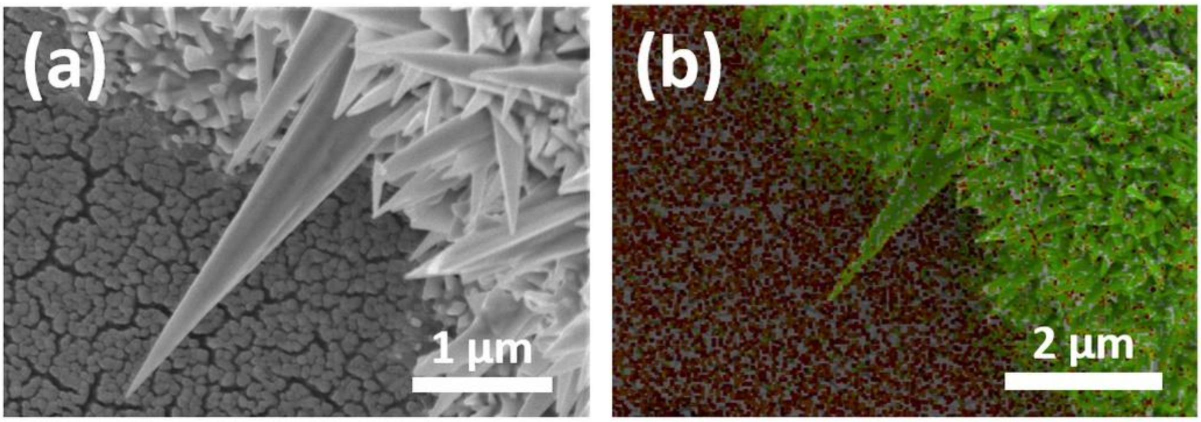

Figure 5.13. **(a)** SEM image of a HAuNC and **(b)** EDX compositional mapping of HAuNCs (green and red areas represent presence of Au and TiO_2, respectively).

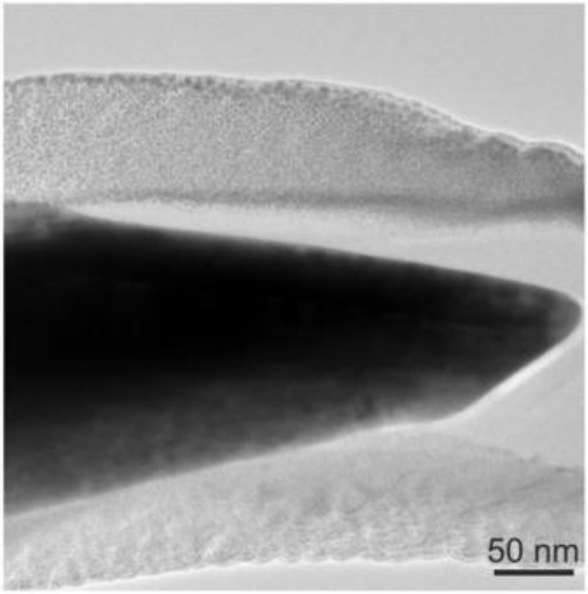

Figure 5.14. TEM image of a single Au needle after Focused Ion Beam (FIB) milling.

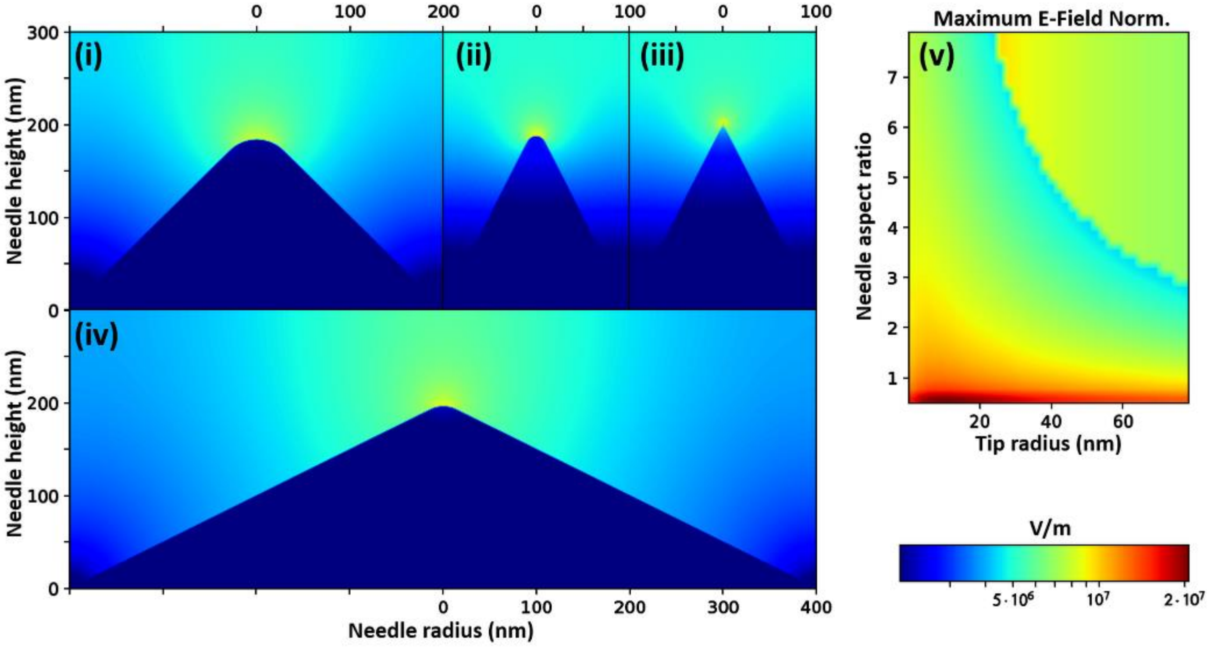

Figure 5.15. Electrical field (E-field) magnitude (cut plane), from numerical (FEM) investigations of Au nano-needles (of fixed 200 nm height) inside a water-filled capacitor arrangement (300 nm height, 1 V external voltage). The left display shows the E-field magnitude around (and inside) the needles for varying aspect ratio (AR, calculated by needle height (of the corresponding perfect needle (tip radius=0)) divided by needle half-width) and needle tip radii R: (**i)** R=40 nm and AR=1, **(ii)** R=10 nm and AR=2, **(iii)** R=0.5 nm AR=2, **(iv)** R=30 nm and AR=1/2. The right display **(v)** shows the maximum E-field norm (on the needle tip) for swept aspect ratios and tip radii. For comparability, all plots obey the same, logarithmic colour scale.

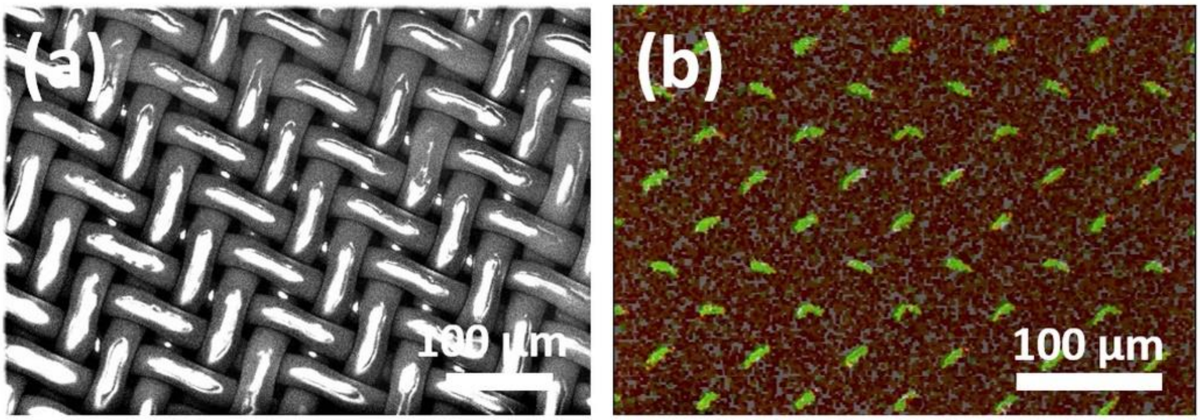

Figure 5.16. **(a)** SEM image of the polymer mask used for patterning of TiO_2 thin film with HAuNCs and **(b)** Elemental mapping analysis (by EDX) of TiO_2 thin patterned with HAuNCs arrays (green and red areas represent presence of Au and TiO_2, respectively).

FIB Sample Preparation Procedure

After cleaning step, the sample was coated with carbon by thermal evaporation with a high quality layer. This carbon layer provides an initial surface protection. Then a thin layer of Pt was deposited to protect the HAuNCs for cutting steps. Afterwards non-coated regions were selectively ablated with FIB, leaving a single HAuNC structure embedded between the substrate and protective Pt-layer. The sliced HAuNC (embedded in carbon matrix) structure was incorporated with the tip of Pt wire by sputtering and cut-out of the silicon substrate. In the next step, HAuNC was placed on FIB lift-out TEM grid fixed by sputtering with Pt-layer and cut from the wire tip. Finally, the fixed HAuNC was thinned by the FIB until its tip has reached a size about 50-75 nm.

6 Photodeposition of Au Nanoclusters for Enhanced Photocatalytic Dye Degradation over TiO_2 Thin Film

This chapter is based on an article published in ACS Applied Materials and Interfaces.[133]

Reprinted with permission from Salih Veziroglu, Anna-Lena Obermann, Marie Ullrich, Majid Hussain, Marius Kamp, Lorenz Kienle, Till Leißner, Horst-Günter Rubahn, Oleksandr Polonskyi, Thomas Strunskus, Jacek Fiutowski, Mohammed Es-Souni, Jost Adam, Franz Faupel, and Oral Cenk Aktas
ACS Applied Materials and Interfaces 12, (2020) 14983.
The article is available via the internet at https://doi.org/10.1021/acsami.9b18817

Abstract

Au nanoparticle (NP) decorated heterogeneous TiO_2 catalysts are known to be effective in the degradation of various organic pollutants. The photocatalytic performance of such Au–TiO_2 structures remarkably depends on the size, morphology, and surface coverage of the Au NPs decorating TiO_2. Here we propose an effective way of preparing a highly active Au nanocluster (NC) decorated TiO_2 thin film by a novel photodeposition method. By altering the solvent type as well as the illumination time, we achieved well-controlled surface coverage of TiO_2 by Au NCs, which directly influences the photocatalytic performance. Here the Au NCs coverage affects both the electron store capacity and the optical absorption of the hybrid Au–TiO_2 system. At low surface coverage, 19.2–29.5%, the Au NCs seem to enhance significantly the optical adsorption of TiO_2 at UV wavelengths which therefore leads to a higher photocatalytic performance.

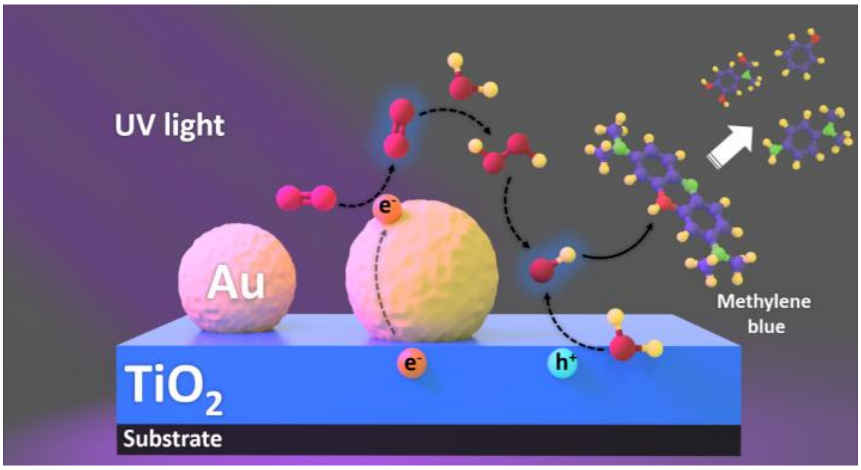

6.1 Introduction

Titanium oxide (TiO_2) is one of the most widely studied materials in the era of heterogeneous catalysis. As opposed to its various advantages such as low cost, earth abundance, and nontoxicity, its high electron–hole recombination rate is one of the main drawbacks.[86] In addition, the low electron mobility and small diffusion length (for holes) limit the practical use of TiO_2 in heterogeneous photocatalysis applications.[134] Doping or decorating TiO_2 with metallic elements is one of the common methods to improve its photocatalytic efficiency.

Among others, gold (Au) is the most attractive candidate for noble metal based photocatalysts due to its stability, nontoxicity, and high electronegativity.[135] Most commonly, the use of Au in combination with TiO_2 has been shown to enable the photocatalysis in visible wavelengths.[136] Basically, surface plasmons in Au nanostructures drive photochemical reactions including dissociation of O_2 and H_2, splitting of water, H_2 production from alcohols, and photocatalytic reduction of CO_2 under visible light illumination.[135] On the other hand, various studies have shown that the photocatalytic performance of Au–TiO_2 hybrid structures is far better under ultraviolet (UV) light in comparison to visible light.[43] Upon illumination of such Au–TiO_2 structures with UV light photogenerated electrons from TiO_2 are easily transferred to Au, thus improving charge separation. Because of its high electronegativity Au acts as reduction site, and the adsorbed oxygen (O_2) can easily trap the electrons from Au to form reactive species which can degrade organic molecules.[137–139] Such an enhancement of photocatalysis can be attributed to a nonplasmonic contribution of Au. On the other hand, it is an open question whether the Au nanostructures contribute to the optical absorption at UV wavelengths rather than a plasmonic enhancement at visible wavelengths. Various methods such as chemical reduction, controlled precipitation, impregnation, and electrodeposition have been established to prepare Au–TiO_2 hybrid structures.[139] Alternatively, photocatalytic deposition is an effective method; in comparison to other wet chemical approaches, a simple illumination is sufficient to synthesize Au nanostructures on TiO_2 without any need for an elevated temperature or a high electrical potential. It should be noted that the photocatalytic performance of Au decorated TiO_2 structures depends not only on the size and geometrical arrangement of the Au clusters on TiO_2 but also on the surface coverage of the Au clusters and the interfacial contact between with TiO_2.[140]

Herein, we performed a systematic study of the photocatalytic deposition of Au NCs on an active TiO_2 thin film under UV light illumination. In comparison to common approaches, where Au is usually deposited on colloidal TiO_2 micro- or nanoparticles (even using additional surfactant and similar encapsulating ligands), we used a TiO_2 thin film (as an immobilized layer) as the carrier to deposit Au NCs. By using a TiO_2 thin film, we aimed at getting a better quantitative analysis of the process parameters which govern the distribution density and surface coverage of the deposited Au NCs (schematically depicted in **Figure** 6.1**)**. We tried to reveal the effect of Au NCs on the optical absorption of TiO_2 at UV wavelength, which is mostly undermined for determining its influence on overall photocatalytic efficiency. The effect of the solvent and the illumination time on nucleation and growth of the Au NCs was studied systematically.

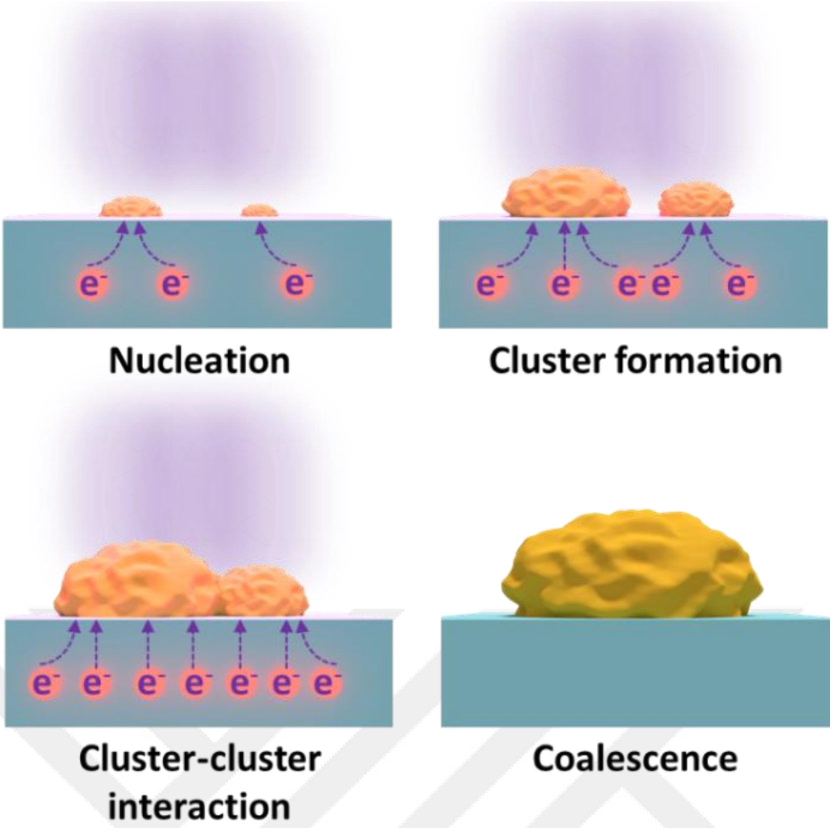

Figure 6.1. Scheme depicting the photocatalytic deposition of Au NCs on TiO_2 under UV light (nucleation and different steps of growth).

6.2 Results and Discussion

6.2.1 Effect of the Solvent Type on Au NCs Growth

We investigated the effect of different solvents on the photocatalytic depositions of Au NCs on TiO_2. We observed that when water was used as a solvent, only a few Au NCs were deposited on TiO_2 (**Figure** 6.2a). When a mixture of 1-hexanol–water (v/v: 20/80) was used, we achieved densely distributed Au NCs on TiO_2 (**Figure** 6.2d). As the TiO_2 thin film comes in contact with the solvent, a phase boundary forms at the solid–liquid interface. Grätzel et al. showed that the electrical potential distribution at the interface plays a major role on the thermodynamics as well as the kinetics of heterogeneous electron transfer from a catalyst surface to electron-acceptor species in the surrounding solution.[141]

As one can see differences in morphologies given in helium ion microscopy (HIM) images (**Figure** 6.2a-d) the solvent type affected basically the morphology but especially the distribution density of the deposited Au NCs. When only water was used as the solvent, we obtained a surface coverage (Au NCs) of 9.2% (**Figure** 6.2e). By switching to the 1-hexanol-water (v/v: 20/80), the surface coverage exceeded 51.6%.In general, the morphology and the distribution density of photodeposited metallic structures highly depend on the solvent viscosity, the size of reactant, and the electron transfer rate at the heterogeneous catalyst–solvent interface. [136,142] (**Figure** 6.11**, Figure** 6.12**, Figure** 6.13 **and Figure** 6.14).

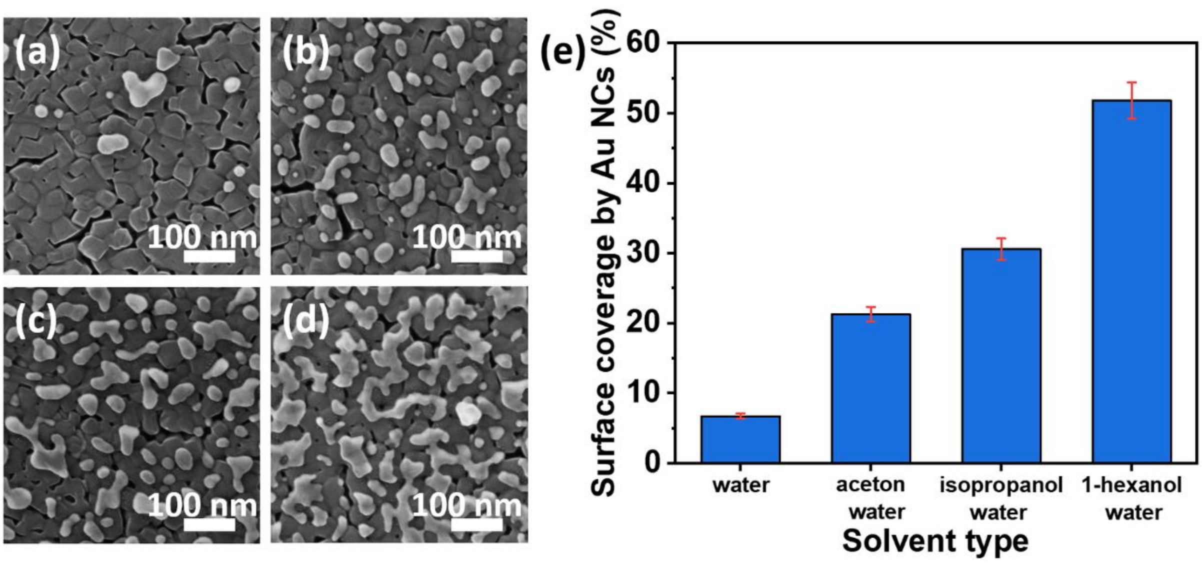

Figure 6.2. HIM images of Au NCs deposited onto TiO_2 in **(a)** water **(b)** acetone-water (v/v:20/80), **(c)** isopropanol-water (v/v:20/80), and **(d)** 1-hexanol-water (v/v:20/80) mixtures. **(e)** Surface coverage (%) by Au NCs deposited using different solvents.

Due to their high solubility in water and low viscosities all used solvents are able disperse Au^{3+} ions well. Therefore, we presume that the electron-transfer rate at the TiO_2–solvent interface governs the morphology and especially the distribution density of deposited Au NC. It is known that the electron-transfer rate in heterogeneous catalysis mainly depends on the electrical potential gradient at the catalyst–liquid interface.[143] The potential gradient at the TiO_2–solvent interface might be proportional to $\varepsilon^{1/2}$ of the solvent, where ε is the dielectric constant of the solvent.[143,144] As a result, the potential gradient and therefore the interfacial electron transfer rate should be inversely proportional to $\varepsilon^{1/2}$. This may explain that the interfacial electron transfer rate should be very low in the water due to its high ε (ε_{water}: 80.1), resulting in the deposition of fewer Au NCs on TiO_2. There are significant differences in calculated (normalized according to the highest ε value achieved in the case of 1-hexanol–water mixture) values of ε for preferred solvent mixtures as shown in **Figure** 6.3. This may explain the deposition of densely distributed Au NCs on TiO_2 when the 1-hexanol–water solvent mixture was used. Because the ε of 1-hexanol–water mixture ($\varepsilon_{1\text{-hexanol}}$: 12.5 and $\varepsilon_{1\text{-hexanol–water}}$: 66.69) is lower than that of pure water, the interfacial electron transfer rate should be much faster, leading to the deposition of more Au NCs on TiO_2. We tabulated the relative electrical potential gradient at the catalyst–liquid interface [143] in **Figure** 6.3b as calculated from **Figure** 6.3a.

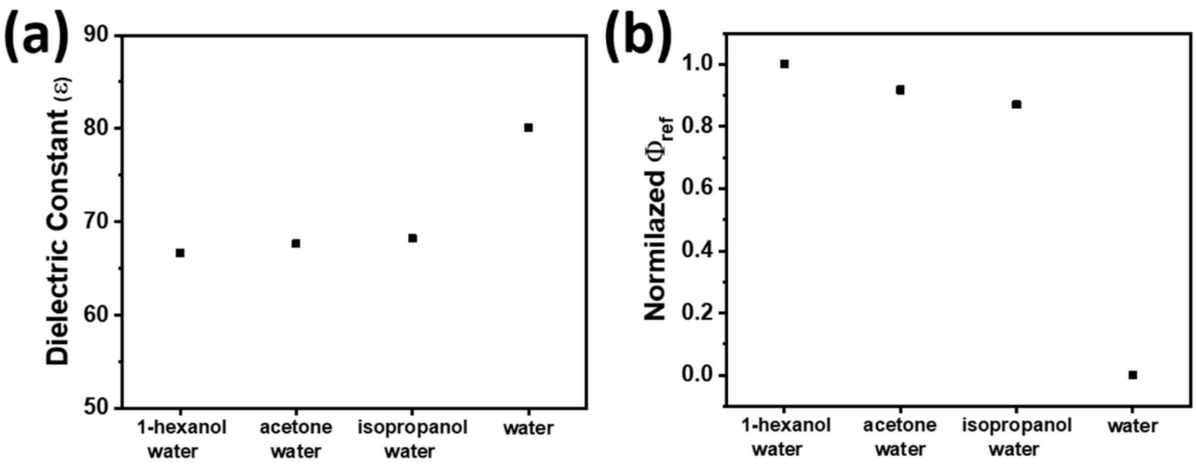

Figure 6.3. **(a)** Calculated dielectric constants of solvent mixtures and **(b)** Relative potential gradient on the TiO_2 surface.

We realized an interesting result when we compared the morphology and distribution density of Au NCs deposited in acetone–water and isopropanol–water mixtures. We chose acetone and isopropanol since both have quite similar ε values ($\varepsilon_{acetone}$: 20.7 and $\varepsilon_{isoproponal}$: 17.9) in comparison to the huge ε difference between 1-hexanol and water. One can see that in HIM images given in **Figure** 6.2b and **Figure** 6.2c there is a clear difference in the surface coverage (%) by Au NCs deposited in acetone–water and isopropanol–water mixtures. While the surface coverage by Au NCs was 21.2% in the case of the acetone–water mixture, it exceeded 30.6% when an isopropanol–water mixture was used as the solvent at identical UV illumination conditions (4.5 mW/cm^2 UV lamp at λ = 365 nm for 10 min). Both solvent mixtures have very close ε values ($\varepsilon_{acetone–water}$: 68.3 and $\varepsilon_{isopropanol–water}$: 71.7), therefore the significant difference in surface coverage (shown in **Figure** 6.2e seems to arise as a consequence of the significant difference in polarity indexes of acetone (5.1) and isopropanol (2.9). Besides the difference in their polarities, one should also keep in mind that acetone is an aprotic solvent whereas isopropanol is a protic solvent.[145] As the aprotic solvent acetone lacks acidic hydrogen, it cannot form significant hydrogen bonding. In contrast, isopropanol has a hydroxylic hydrogen which serves for the weak acidic properties. For instance, in our previous work we have shown acidic conditions that trigger the fast reduction of Au^{3+} ions and growth into stable Au clusters.[113] Therefore, the type of the solvent (aprotic/protic) should be also taken into account in addition to ε, which acts as the main determinant for Au structure formation on TiO_2.

6.2.2 Effect of the Illumination Time on Au NCs Growth

After adsorption of the first Au^{3+} ions onto TiO_2 and their reduction into Au nuclei, the subsequent growth of NCs can be considered as a diffusion-limited reaction. All used solvent mixtures have low viscosities, therefore the electron transfer rate should act as the rate-determining parameter for the growth of Au NCs on TiO_2. As we briefly discussed above, ε of the solvent may play an important role on the electron transfer rate.[141] On the other hand, the conversion efficiency of the TiO_2 catalyst also plays a critical role in the formation of metallic structures to be photodeposited. We recently showed that illumination intensity and time are important factors for controlling the density of photogenerated electrons on the TiO_2 surface.[113]

Figure 6.4 shows HIM images of Au NCs deposited on TiO_2 in an isopropanol–water mixture at different UV illumination times and without UV illumination (during 120 min) as a control experiment. We chose the isopropanol–water mixture as the solvent for studying the effect of the illumination time on the Au NCs formation since it provided a relatively better controllable deposition process in comparison to the extremely fast reduction observed in the case of the 1-hexanol–water mixture. As one can see in **Figure** 6.4, in the dark (without UV illumination), Au NCs could not be obtained on the TiO_2 surface even in 120 min, but within a very short time (5 min), we achieved a high surface coverage of 19.2%. When the illumination time was doubled, Au NCs started to coalesce, and the surface coverage by Au NCs reached 29.5%. By extending the illumination time to 240 min, we achieved a surface coverage of 94.2%. It is obvious that deposition rates got lower by extended illumination time. Here there are two critical points which should be taken into account: (i) Au NCs deposited on TiO_2 might act as electron trapping centers triggering the preferential reduction sites for further Au^{3+} ions and (ii) by the time increasing the coverage of the surface. By interpenetrating dense Au NCs might affect the overall absorption of UV by Au–TiO_2, which is essential for activation.

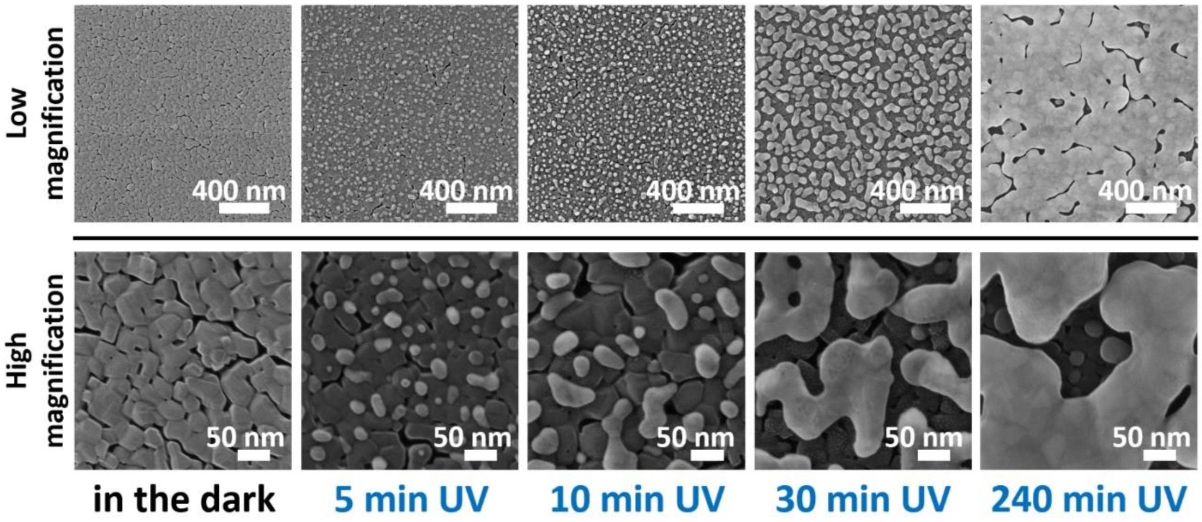

Figure 6.4. HIM images of Au NCs deposited on TiO_2 in isopropanol-water mixture without UV illumination (during 120 min in the dark) and at different UV illumination time.

In our previous study we observed that initial Au NCs deposited on TiO_2 might act as electron concentrating centers, and they act as preferential sites for further reduction of ions.[113] On the other hand, Au NCs can hinder the transmission of the UV light (at a wavelength of 365 nm, which we monitored the MB degradation) to an underlying TiO_2 layer as shown in **Figure** 6.15. One needs to separate absorption characteristics of TiO_2 from the (parasitic) absorption originating in Au NCs to get a better understanding of the optical contribution (whether plasmonic or nonplasmonic) of Au NCs to the photocatalysis. One can easily apply the optical transfer-matrix model (TMM) by incorporating corresponding optical data for TiO_2 to estimate the contribution of a Au layer deposited on TiO_2.[146] As shown in **Figure** 6.15, one can interpret that definitely a Au layer deposited on TiO_2 leads to totally different optical characteristics in comparison to bare TiO_2 (see details of TMM in the Experimental Section). While the TMM approach is applicable for estimating optical properties of a continuous layer regardless from the substrate, a more detailed analysis is needed for predicting the behavior of noncontinuous layers as we prepared (Au-TiO_2). Here, height, morphology, and coverage of Au NCs play a major role in optical characteristics.

To better understand the optical transmission through Au NCs, we performed finite-element method (FEM) simulations (see details in the Experimental Section) at an excitation wavelength of 365 nm (by using experimental data to incorporate the morphology and surface coverage of Au NCs as shown in **Figure** 6.5).

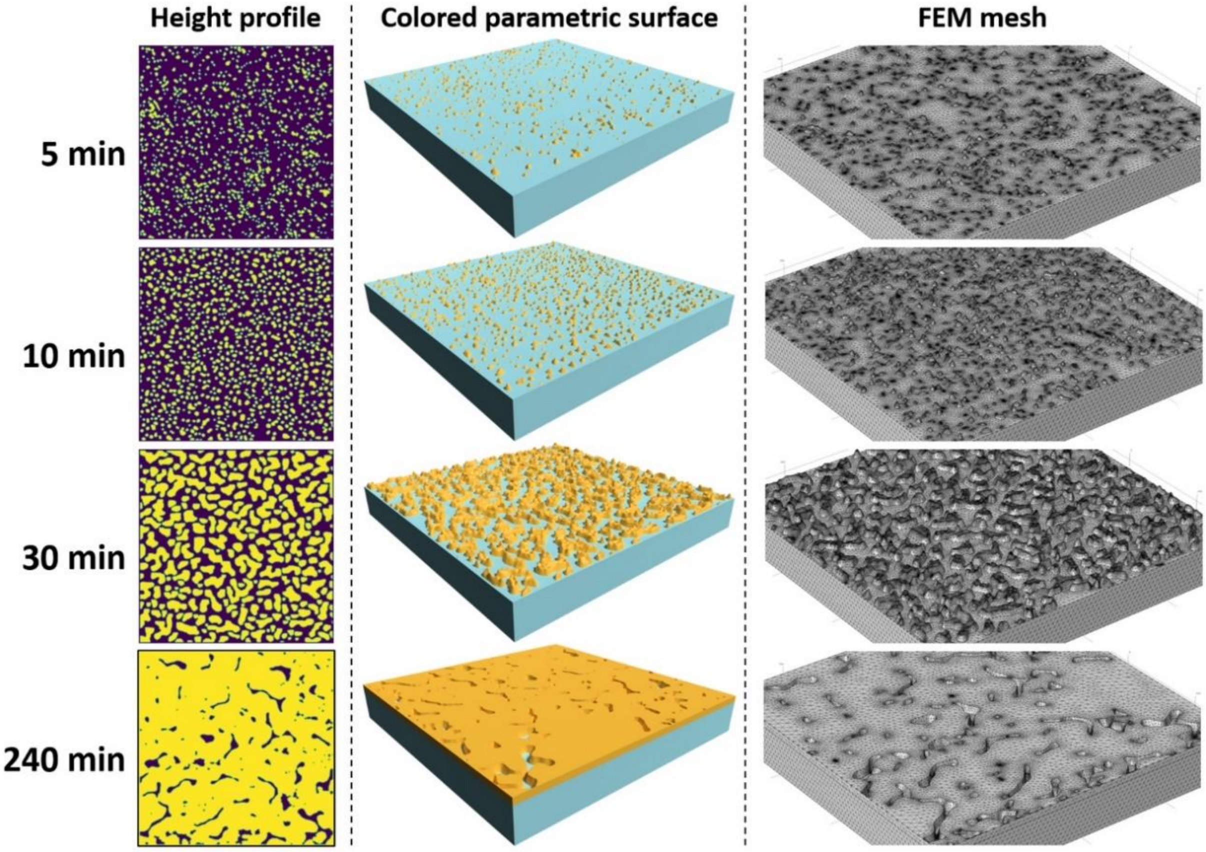

Figure 6.5. Construction of the optical models (height profile maps- parametric surface-FEM mesh integration) for FEM analysis. (Height profile maps are extracted from HIM images as given in **Figure** 6.4).

First, we transferred HIM images of Au–TiO_2 structures into height profile heat maps, employing standard image processing techniques. Afterward, we transferred the height profiles into parametric surfaces and integrated them as domain boundaries in an FEM simulation cell, created with COMSOL Multiphysics®. **Figure** 6.5 illustrates this integration procedure (the corresponding calculated surface coverage and Au–air interface surface areas are depicted in **Figure** 6.16).

After the integration of height profile maps into the optical model, we excited the Au–TiO_2 structures from the top (air region) with a 365 nm wavelength plane wave at normal incidence (schematically depicted in **Figure** 6.6a). The total reflection and transmission intensities were collected by surface transmission monitors located above and below the stack, respectively, and the corresponding total absorption is calculated as 100% transmission–reflection. Then, we performed two concurrent types of simulations; we compared the 365 nm excitation "bulk" values (both TiO_2 and Au comprise absorption) for reflection, transmission, and, consequently, absorption ("Abs_{Bulk}") to the same values when neglecting the absorption (k) coefficient of TiO_2 (only Au comprises absorption; "Abs_{Au}"). This way, the latter reveals only the (parasitic) absorption in Au NCs, while maintaining the diffractive behavior of the bulk (Au–TiO_2).

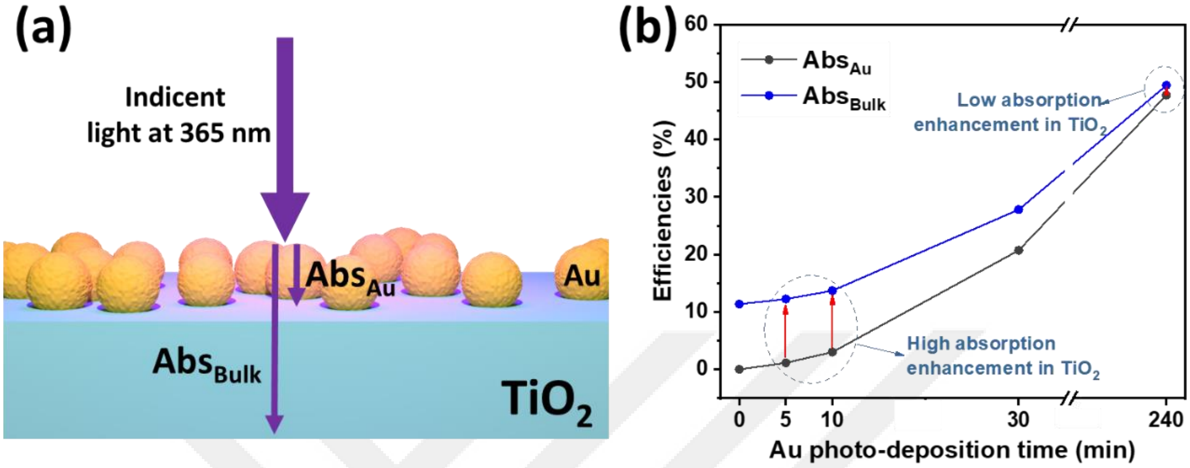

Figure 6.6. Simulated catalytic enhancement by Au-TiO_2 structures: **(a)** Schematic diagram depicting possible optical interactions on Au-TiO_2 structures and **(b)** Simulated (FEM) optical properties of Au-TiO_2 structures: red arrows indicate the catalytic enhancement for deposition times of 5 and 10 minutes.

The difference in absorption (as shown in **Figure** 6.6b, indicated by red arrows) indicated by red arrows) then corresponds to the catalytic activity enhancement of Au–TiO_2. The full reflection, transmission, and absorption spectra for the two cases, outlining our strategy, can be found in **Figure** 6.16. While there is a significant difference between Abs_{Au} and Abs_{Bulk} at low Au surface coverage (corresponding to photodeposition time of 5–10 min), both absorption values become almost identical at higher Au surface coverages (corresponding to photodeposition times >30 min).

Because we used a TiO_2 thin film instead of colloidal TiO_2 particles randomly moving within a solvent, the observation of the effect of light illumination on the morphology and distribution density led to a better quantitative comparison. In most of the studies the change of the optical absorption of the solvent, which contains active TiO_2 particles and $AuCl_3$, is monitored to reveal the Au deposition kinetics by the time. Unfortunately, the optical absorption is sensitive to different factors such as particle geometry and agglomeration rather than only the particle size. In addition, the change in the surrounding medium (Au^{3+}-rich solvent) may also interfere with optical absorption.[147] Because the solvent will act as an active component of the effective optical medium, one can expect broadening and shifting of the absorption peak.[148] Here our modeling results clearly support our experimental findings. The sweet spot in the photocatalytic enhancement occurs at moderate Au surface coverage (20–30% corresponding to 5 and 10 min deposition time), while for higher Au surface coverage the two major loss channels, namely enhanced reflection from Au and parasitic absorption at the air–Au interface, diminish the photocatalytic activity enhancement.

6.2.3 Structural and Compositional Characterization of Deposited Au NCs

To reveal structural details of the composite films, we analyzed selected area electron diffraction (SAED) patterns recorded from Au(10 min)–TiO_2. We compared SAED patterns of two different samples: (i) Au layer scratched from the top surface (delaminated from the underlying TiO_2 film) and (ii) Au–TiO_2 layer scratched from the underlying substrate, as shown in **Figure** 6.7a and **Figure** 6.7b, respectively. By the scratching of sample ii, many Au-NCs were mechanically removed; thus, sample ii is predominantly consisting of pure TiO_2. Both SAED patterns show well-resolved intensity on concentric rings, which is a clear indication of a highly crystalline structure. The extracted lattice parameters from the first sample (plain Au layer) can be assigned to Au fcc (**Figure** 6.7a) with a lattice constant of 4.09 Å (literature value: 4.0786 Å).[149] As expected, sample ii shows predominantly the intensities of the TiO_2 anatase phase with a lattice constant of a = 3.86 and c = 9.56 Å (literature values: a = 3.784 and c = 9.500 Å))[150] (**Figure** 6.7b).

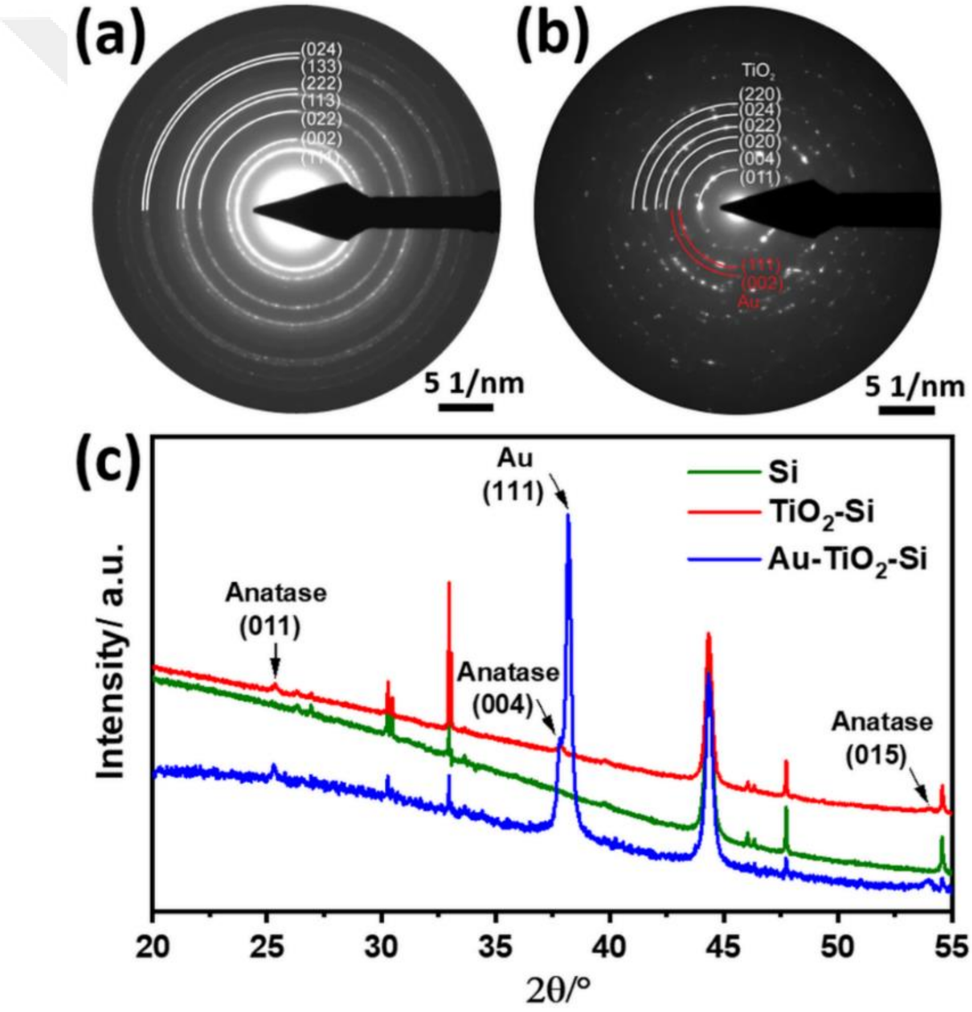

Figure 6.7. SAED patterns of **(a)** plain Au (corresponding TEM image is given in **Figure** 6.18) and **(b)** Au-TiO_2 (reflections of anatase TiO_2 phase and Au are indicated). **(c)** XRD patterns of silicon (Si) substrate, TiO_2-Si and Au-TiO_2-Si samples.

X-ray diffraction analysis (XRD) was performed to support the transmission electron microscopy (TEM) analysis. The XRD diffractogram shows reflections of the TiO_2 anatase and Au phases, marked in the diffractogram (**Figure** 6.7c). Additional reflections (not marked) arise from the Si substrate with a native SiO_2 layer, illustrated by the reference measurement of the bare Si substrate (green). The broadening of the reflections of Au and TiO_2 indicates a polycrystalline film with low crystallite size, observed in TEM analysis.

Energy dispersive X-ray (EDX) elemental maps are recorded from the marked area of a scanning transmission electron microscopy (STEM) *Z*-contrast image in low-magnification mode, (cf. **Figure** 6.8a). The EDX elemental maps (**Figure** 6.8b) suggest the presence of Ti, O, and Au throughout the Au(10 min)–TiO_2 layer. We did not observe any impurity elements as expected since no ligand capping or surfactants (mostly used for wet-chemical synthesis of metal decorated oxides) have been used.

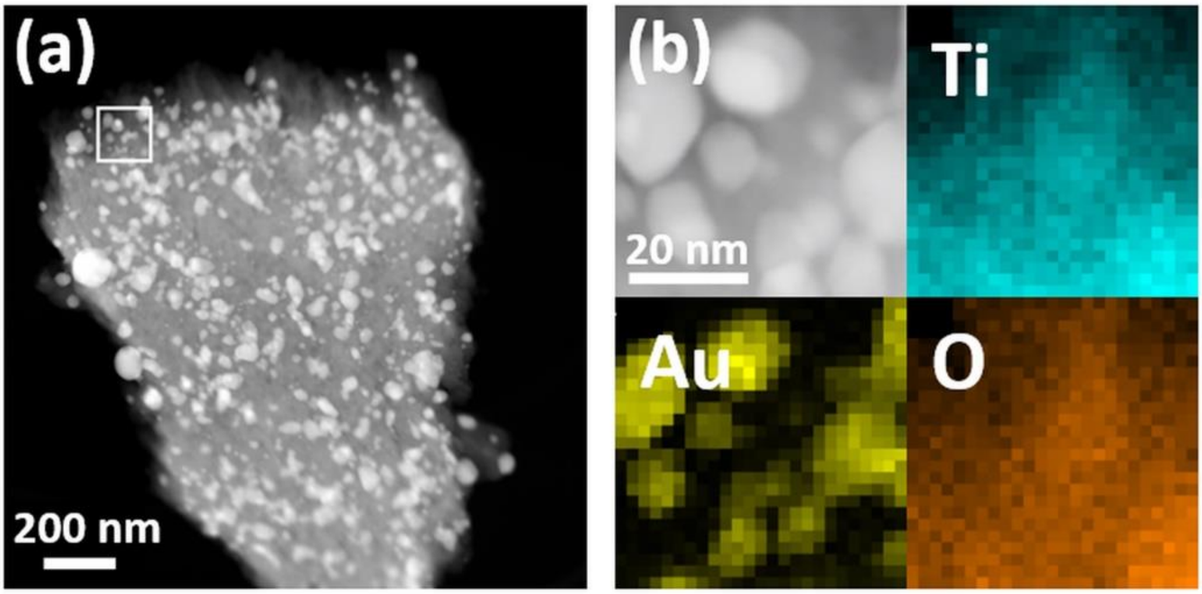

Figure 6.8. **(a)** Z-contrast image (STEM-HAADF) of Au-TiO_2 at low magnification and **(b)** Z-contrast image at higher magnification and EDX elemental maps of Au-TiO_2 from the marked area shown in **(a)**.

To confirm chemical states of deposited Au NCs on TiO_2, the Au(10 min)–TiO_2 sample was further characterized by XPS. The wide-scan XPS spectrum showed the presence of Ti, O, Au, and some adsorbed carbon C on the sample surface (**Figure** 6.9aThe XPS spectra of Ti-2p exhibited two dominant peaks, which correspond to Ti $2p_{1/2}$ at 464.9 eV and Ti $2p_{3/2}$ at 459.2 eV (for the annealed stoichiometric anatase TiO_2), as shown in **Figure** 6.9.[151,152] The binding energy between Ti $2p_{1/2}$ and Ti $2p_{3/2}$ (5.8 eV) indicated that Ti exists in the form of Ti^{4+} (TiO_2).[153] The O-1s XPS spectrum was fitted by two components, originating from lattice O_2(Ti–O–Ti) and adsorbed oxygen/hydroxyl (O_2/–OH) groups (**Figure** 6.9c).[154] The XPS spectrum of Au was split into two main peaks, with higher binding energy at 87.0 eV and lower binding energy at 83.2 eV, corresponding to Au $4f_{5/2}$ and Au $4f_{7/2}$, respectively (**Figure** 6.9d). Surprisingly, the Au $4f_{7/2}$ peak appears at 83.2 eV, which is lower than the typical binding energy (84.0 eV) for metallic Au (Au^0).[155] A decrease in the Au $4f_{7/2}$ binding energy (in a wide range from −0.2 to 1.2 eV) for Au–TiO_2 photocatalysts relative to that in bulk Au was observed in a number of studies.[156] Radnik et al. considered that the negative shift at the binding energy might be caused by the reduced coordination number of Au atoms.[157] Also, Arrii et al. showed that the particle (Au) and support (TiO_2) interactions play a crucial role in the negative shift. According to their results, the shift of the Au $4f_{7/2}$ peak toward the lower binding energy can be described by an initial state effect related to electron transfer from Ti^{3+} surface states to Au NCs.[158]

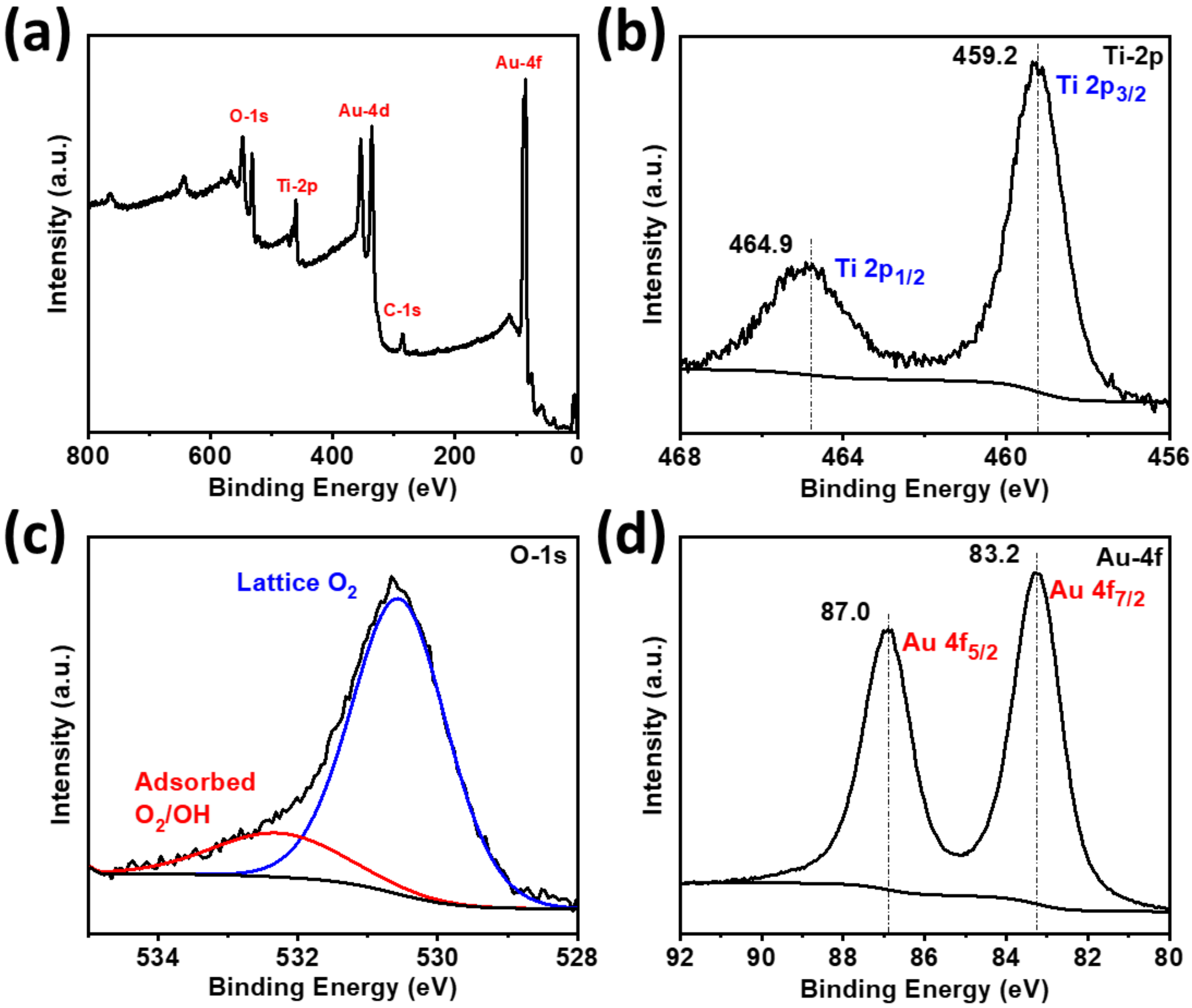

Figure 6.9. **(a)** Wide scan and high-resolution XPS spectra of **(b)** Ti-2p, **(c)** O-1s and **(d)** Au-4f.

6.2.4 The Photocatalytic Performance of Au NCs Decorated TiO_2

We evaluated the photocatalytic activity of prepared samples by decomposing methylene blue (MB) in water under UV illumination. First, we checked the stability of aqueous MB solution by irradiating it (at the absence of photocatalyst), and we did not observe any significant change in the absorption. We evaluated the decomposition of MB by observing the change in the absorption of the final concentration (C) divided by the initial MB concentration (C_0) as a function of the illumination time (t). The corresponding degradation curves are shown in **Figure** 6.10a and by fitting a first-order kinetic model we calculated the rate constants (Table 6-1). At a first look it can be clearly seen that while bare TiO_2 exhibited an extremely low photocatalytic effect, there is a noticeable enhancement after the deposition of Au NCs. We achieved the highest photocatalytic activity for Au NCs deposited at an illumination time of 10 min (with a degradation rate constant, $k[\mathrm{Au(10\ min)–TiO_2}] = -4.71 \times 10^{-3}$/s (see **Table** 6-1), which corresponds to a surface coverage of 29.5%. As opposed to various advantages of TiO_2 such as its nontoxicity, low cost, and high abundancy, its large band gap and massive recombination of photogenerated charge carriers diminish its photocatalytic efficiency. In accordance, bare TiO_2 exhibited an extremely low degradation rate, $k[\mathrm{TiO_2}] = -0.28 \times 10^{-3}$. Au NCs might store electrons and act as a sink for the interfacial charge transfer, enhancing the photocatalytic efficiency.[159,160]

It is known that Au NCs exhibit a surface plasmon band at visible wavelengths due to collective electron oscillations. In various studies covering Au–TiO_2 hybrid photocatalysts the plasmon resonance effect of Au NCs has been reported as the main reason for the enhanced photocatalytic activity.[161–163] In this mechanism, visible light photoexcites Au, and photogenerated electrons are injected into O_2 adsorbed on TiO_2. This is basically followed by the reduction of molecular O_2 to the superoxide radical O_2^- and the formation of the reactive hydroxyl radical, OH^-. Such O_2^- and OH^- radicals enhance the decomposition rate of MB.[164]

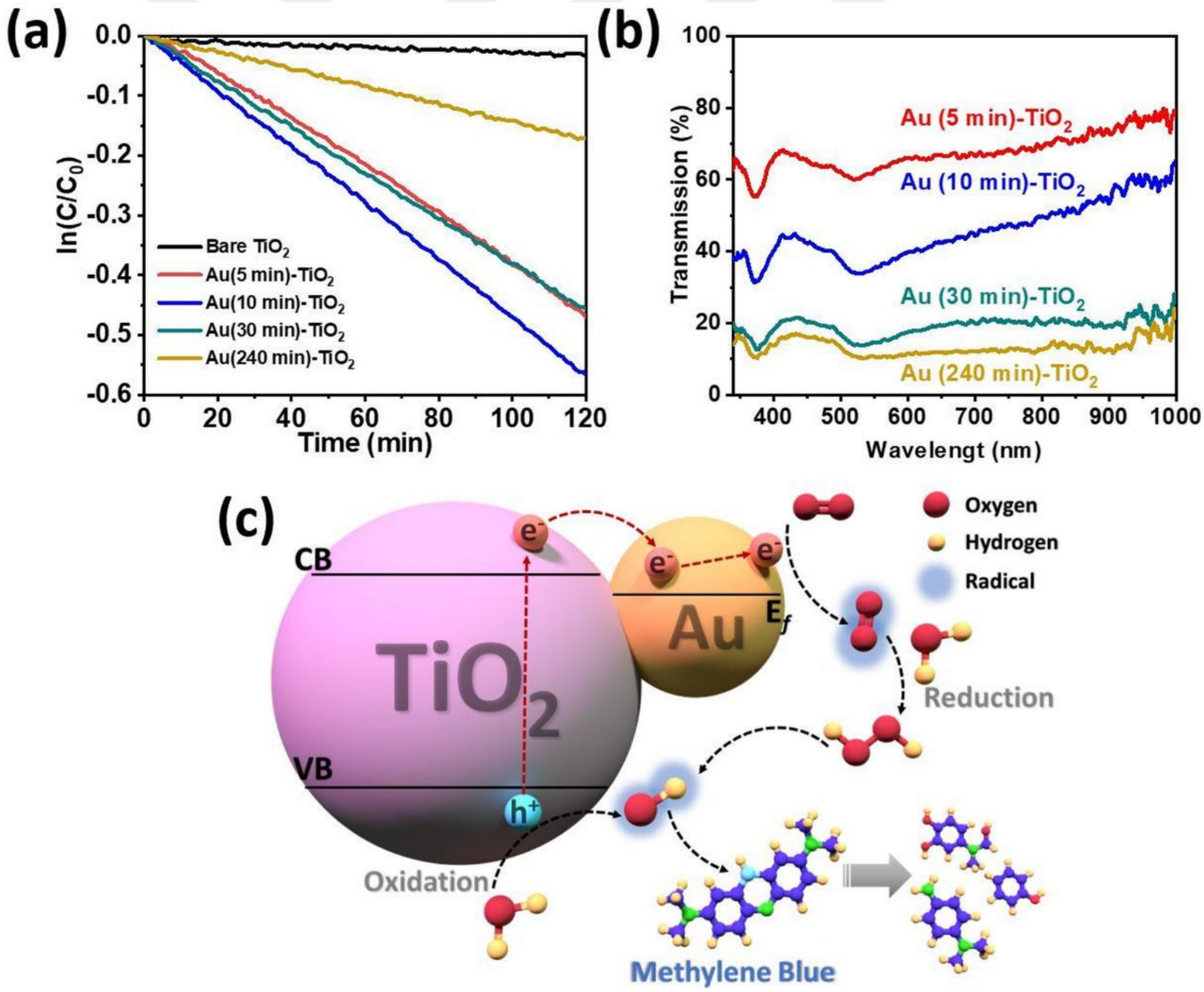

Figure 6.10. **(a)** Photocatalytic decomposition rate of MB under UV illumination, **(b)** Optical transmission spectra of Au NCs deposited (at different surface coverages) on TiO_2 substrate **(c)** Scheme depicting the mechanism of photocatalytic decomposition of MB by Au NCs decorated TiO_2.

On the other hand, we note two main differences when comparing our experimental study with these common approaches. Deposited Au NCs are larger in comparison to most plasmonic Au nanostructures presented so far, and our optical spectra (**Figure** 6.10b) do not exhibit a sharp plasmon peak at visible wavelengths (lack of a clear Au surface plasmon band); rather, we observed a broad absorption between 500 and 600 nm. Therefore, we conclude that in this scenario Au NCs foster a nonplasmonic (visible wavelength) enhancement of TiO_2 photocatalytic activity.

On the basis of our observations, we propose a scheme shown in **Figure** 6.10c for photocatalytic degradation of MB by Au NCs decorated TiO_2 surface. Under UV illumination TiO_2 becomes active, and Au NCs seem to act as cocatalysts. In a similar study Fang et al. showed that upon illumination of TiO_2 decorated with Au NCs with UV light electrons are promoted rapidly from the valence band to the conduction band of TiO_2 and then transferred to Au NCs due to the potential gradient established by the Schottky barrier between TiO_2 and Au NCs.[165] Afterward, the Au NCs act as reduction sites, and the adsorbed O_2 on the surface can easily trap the electrons from Au NCs to form reactive oxidative species, thus significantly improving the degradation of the MB as also shown Okuno et al. and Kumaravel et al.[44,166] The holes left in the valence band of TiO_2 may also react with H_2O to form reactive oxidative species.[167,168] These oxidative species or holes can attack and degrade MB molecules. Because the photocatalytic activity was analyzed under UV light in our experiments, a plasmonic contribution from Au NCs cannot be expected; therefore, the mechanism given in **Figure** 6.10c seems to be the most possible explanation, which is also in agreement with findings of Okuno et al. and Kumaravel et al.

6.3 Conclusion

We have shown that using a highly active TiO_2 substrate rather than colloidal TiO_2 nanoparticles allows controlled deposition of Au NCs (in terms of cluster distribution and surface coverage). The solvent type (acetone, isopropanol, and 1-hexanol) and the illumination time play an important role in the surface coverage of TiO_2 by Au NCs, which directly influences the photocatalytic performance. One should think about an optimization between two comprehensive effects of Au NCs: (i) the electron storage capacity and (ii) the optical absorption by controlling the surface coverage of TiO_2 by Au NCs. For instance, Au NCs (at low surface coverage) seem to enhance significantly the optical adsorption of TiO_2 at UV wavelengths and therefore lead to a higher photocatalytic performance. The presented facile approach opens a door to easy processing of Au–TiO_2-based catalytic and sensor devices.

6.4 Experimental Section

6.4.1 Materials

Silicon (Si) wafer pieces with native oxide (10 mm × 10 mm) were used as a substrate for deposition of the TiO_2 thin films. Gold(III) chloride ($AuCl_3$, 64.4% min, Alfa Aesar) and acetone, isopropanol, and 1-hexanol

(Sigma-Aldrich) were obtained for the decoration of the Au NCs on TiO_2. All reagents were used without any further purification.

6.4.2 Preparation of TiO_2 Thin Films

TiO_2 thin films were deposited by the pulsed DC reactive sputtering method from a metallic target (Ti-Goodfellow, 99.99%, 5 cm diameter) in the presence of argon (process gas) and oxygen (reactive gas).[23,169] Si substrates were cleaned in the ultrasonic bath with acetone, isopropanol, and deionized water and subsequently dried with nitrogen gas. Substrates were placed into the custom-made vacuum chamber, which was built out of commercially available components. The base pressure of the vacuum chamber was adjusted about 5×10^{-5} Pa by pumping system composed of a turbomolecular pump (Pfeiffer Vacuum, HiPace 400) and a rotary pump (Agilent Technologies, SH-110), while DC power (90 W) was pulsed at a frequency of 50 kHz with 55% duty cycle to reduce the excessive oxidation and the poisoning of the Ti target surface. An argon/oxygen gas mixture (250:10 sccm) was supplied by a precise mass flow control system (MKS, Multi-Gas controller 647C). Substrates were rotated at 30 rpm during the sputtering to prepare a homogeneous film. Following the sputtering (1 h), prepared TiO_2 thin films were heat-treated in an oven (Nabertherm, LE 4/11/R6) at 650 °C for 1 h and afterward directly quenched in the air.

6.4.3 Au NCs Deposition on TiO_2

Au NCs were deposited on the TiO_2 thin films by the photocatalytic reduction method with slight modification as previously reported.[113] The TiO_2 thin films deposited substrates were dipped into a quartz cuvette, filled with 5.2 mL of an aqueous $AuCl_3$ (0.8×10^{-3} M) and 1.3 mL of solvent (acetone, isopropanol, and 1-hexanol, separately) mixture (the total volume of the mixture is 6.5 mL). Samples were exposed by low-intensity UV illumination (4.5 mW/cm^2 UV lamp operating at $\lambda = 365$ nm) through the quartz cuvette. The illumination time was changed systematically from 5 to 240 min. After UV illumination, the samples were rinsed with water and dried with air to remove solution left on the substrate.

6.4.4 Structural and Chemical Characterization

The surface morphology of the samples was investigated by helium ion microscopy (HIM, Orion NanoFab-Carl Zeiss). No conductive coating was applied to the samples prior to HIM analyses to preserve the sample surface information. ImageJ software (1.51 version) was used to calculate the surface coverage of Au NCs on the TiO_2 thin film surface. Structural characterization was performed by transmission electron microscopy (TEM, Tecnai F30 STwin G^2 microscope, 300 kV) and a Si(Li) detector (EDAX system for elemental maps). Scanning TEM images were recorded by using a high angle annular dark field detector, resulting in Z-contrast images. X-ray diffraction (XRD) (SmartLab 9 kW, Rigaku, Japan) was used to identify the present phases and orientation in TiO_2 and Au. All measurements were done using Cu radiation with a Kβ filter. The phases were identified via the crystallographic information files (CIF) from inorganic crystal structure database (ICSD) with the following identification numbers: Au_icsd_64701 and TiO_2_icsd_93098. The chemical structure of the samples was analyzed by an X-ray photon electron spectrometer (XPS, Omicrometer Nano-Technology GmbH, Al anode, 240 W), and CasaXPS software was used to perform quantitative analyses and detailed peak investigations. The binding energy was calibrated with the reference to the C 1s peak centered at 284.8 eV.

6.4.5 Optical Characterization (Ellipsometry and Transfer-Matrix-Method)

To separate the absorption characteristics of TiO_2 from the (parasitic) absorption originating in the Au NCs, we first performed optical transmission measurements of a pristine 200 nm thick TiO_2 film on a glass substrate (by a spectroscopic ellipsometer (Ångstrom Sun Technologies Inc. SE200BM) covering the DUV to NIR spectrum range, 250–1100 nm), representing the (lower extreme) 0% Au coverage case. We compared these results to a transfer matrix method[170] (TMM) modeling approach using an in-house developed TMM code, incorporating TiO_2 data from ref.[146] **Figure** 6.15b demonstrates the agreement between the simulated and measured transmission spectra. The spectra numerically and experimentally derived for pristine TiO_2 furthermore agree with previously reported ones.[171] We extended the investigations to a stack also comprising a closed 40 nm thick (HIM analysis) Au film (material data adapted from ref [172] on top of the TiO_2 film and silica glass (with a constant refractive index $n = 1.45$), representing the (upper extreme) 100% Au coverage case. Here, we modeled two scenarios: first, we generated spectra incorporating the full, realistic TiO_2 refractive index and absorption coefficient (n, k) data. We compared these data to the same result, but with nulling the TiO_2 absorption (k) coefficient, while maintaining the dispersion characteristics (TiO_2-n) as in the first numerical experiment (**Figure** 6.15). By this approach, one can interpret the difference of both absorption spectra as the TiO_2-specific absorption in an Au-covered scenario, which we consider most relevant for an enhanced catalytic activity.

6.4.6 Optical Characterization (Finite-Element Modelling)

To better understand the photocatalytic activity enhancement of the prepared structures, we furthermore performed finite-element method (FEM) simulations, at an excitation wavelength of 365 nm, matching our experimental settings. To represent the experimental work as closely as possible, we started the FEM model generation with transferring the HIM images (entire field of view 1700 nm × 1700 nm) of Au–TiO_2 structures into height profile heatmaps, employing standard image processing techniques. To season the resulting profiles for a periodic discretization cell, we morphed the boundaries to a constant height (full height for the Au(240 min)–TiO_2 sample, zero height for all other samples). As a second step, we transferred the height profiles into parametric surfaces and integrated them as domain boundaries in an FEM simulation cell, created with COMSOL Multiphysics. This not only fosters realistic modeling, but it also admits for the precise calculation of the interface area, separating the top air region from the Au NCs, where we consider most of the parasitic absorption in Au NCs to happen. Note that the Au(240 min)–TiO_2 sample exhibits an even larger Au–air interface area as compared to the closed Au film (see **Figure** 6.16).

The complete simulation cell consists of a 200 nm TiO_2 thin film, carrying the 40 nm high Au (verified by cross-sectional HIM analysis), sandwiched between an air region on top and a glass substrate region at the bottom. Laterally, we considered it safe to choose periodic boundary conditions, since the 1700 nm period is way beyond the 365 nm excitation wavelength, such that lattice resonances should be of minimal effect. To mimic the necessary vertical radiation condition, the cell is furthermore vertically padded with perfectly matched layers, followed by scattering boundaries. We excite the structure from the top (air region) with a 365 nm wavelength plane wave at normal incidence. The total reflection and transmission intensities are collected by surface transmission monitors located above and below the stack, respectively. Again, we perform two concurrent types of simulations; we compare the 365 nm excitation bulk values for reflection, transmission, and consequently absorption to the same values when neglecting the absorption (*k*) coefficient of TiO_2. The latter produces only the (parasitic) absorption in Au NCs while maintaining the diffractive behavior of the Au–TiO_2 hybrid structure. The resulting calculated catalytic enhancement is depicted **Figure** 6.6b, while the detailed simulation results can be found in **Figure** 6.17.

6.4.7 Photocatalytic Activity Measurement

To assess the photocatalytic activity of the prepared samples, bleaching of the methylene blue (MB) was monitored by a UV–vis spectrophotometer (StellarNet EPP2000C-SR-50 with SL5-DH light source).[23,173] The solution (6.5 mL, 10 μmol/L) was magnetically stirred and irradiated under UV light (4.5 mW/cm^2 UV lamp at λ = 365 nm) for 2 h. The changing in the absorption at 664 nm was recorded by a UV–vis spectrophotometer.

Acknowledgments

S.V. acknowledges the Graduate Center and Federal State Funding, Kiel University, for providing funding for his Ph.D. study. The authors thank Stefan Rehders for his continuous support for the buildup and maintenance of deposition systems. The simulation work described in this paper was supported by the DeiC National HPC Centre, University of Southern Denmark.

Supporting Information

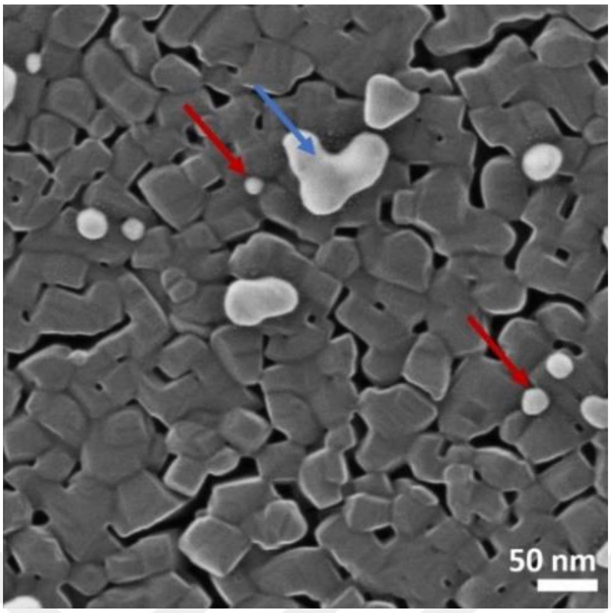

Figure 6.11. Helium ion microscope (HIM) image of Au NCs by photocatalytically deposited in water. (Red and blue arrows represent the cluster and coalescence formation of Au particles, respectively).

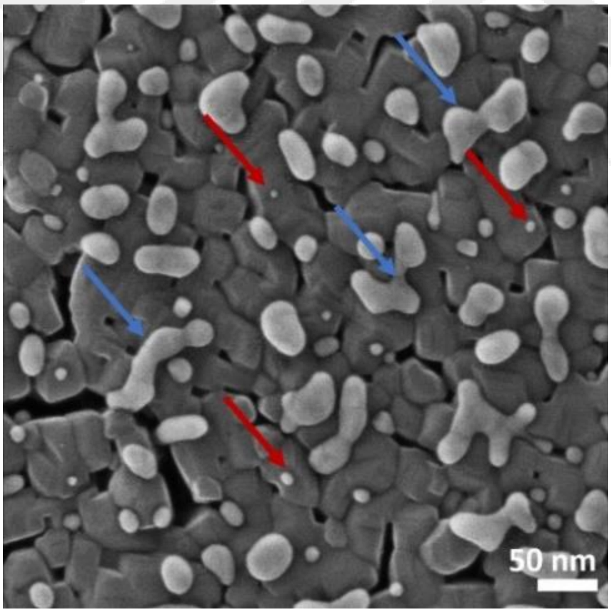

Figure 6.12. Helium ion microscope (HIM) image of Au NCs by photocatalytically deposited in acetone-water (v/v:20/80). (Red and blue arrows represent the cluster and coalescence formation of Au particles, respectively).

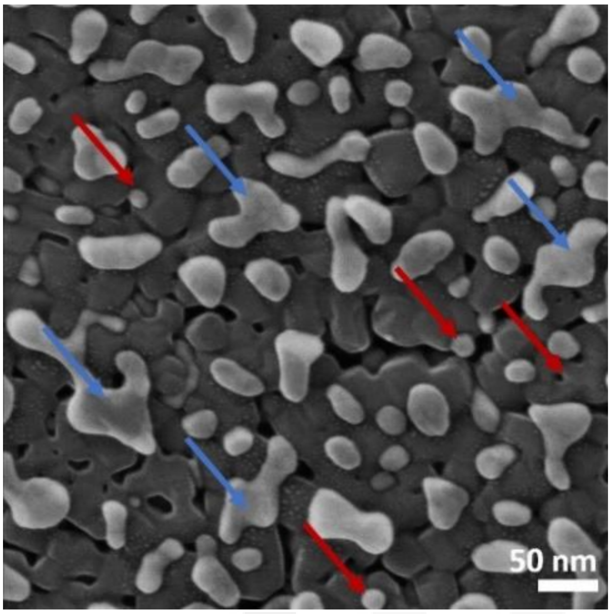

Figure 6.13. Helium ion microscope (HIM) image of Au NCs by photocatalytically deposited in isopropanol-water (v/v:20/80). (Red and blue arrows represent the cluster and coalescence formation of Au particles, respectively).

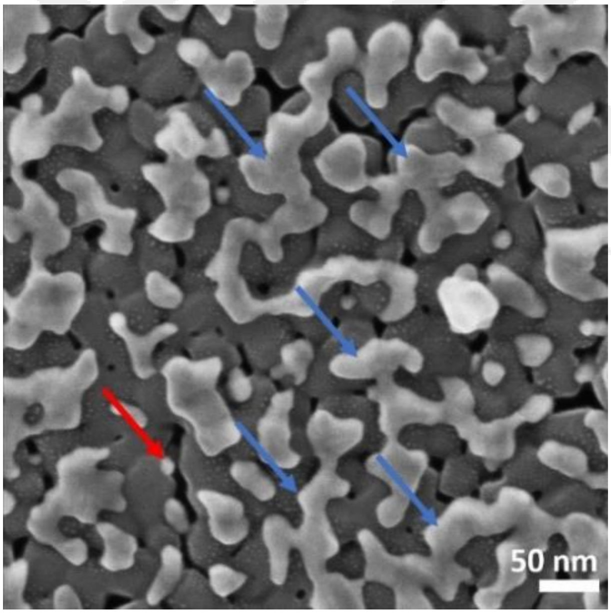

Figure 6.14. Helium ion microscope (HIM) image of Au NCs by photocatalytically deposited in 1-hexanol-water (v/v:20/80). (Red and blue arrows represent the cluster and coalescence formation of Au particles, respectively).

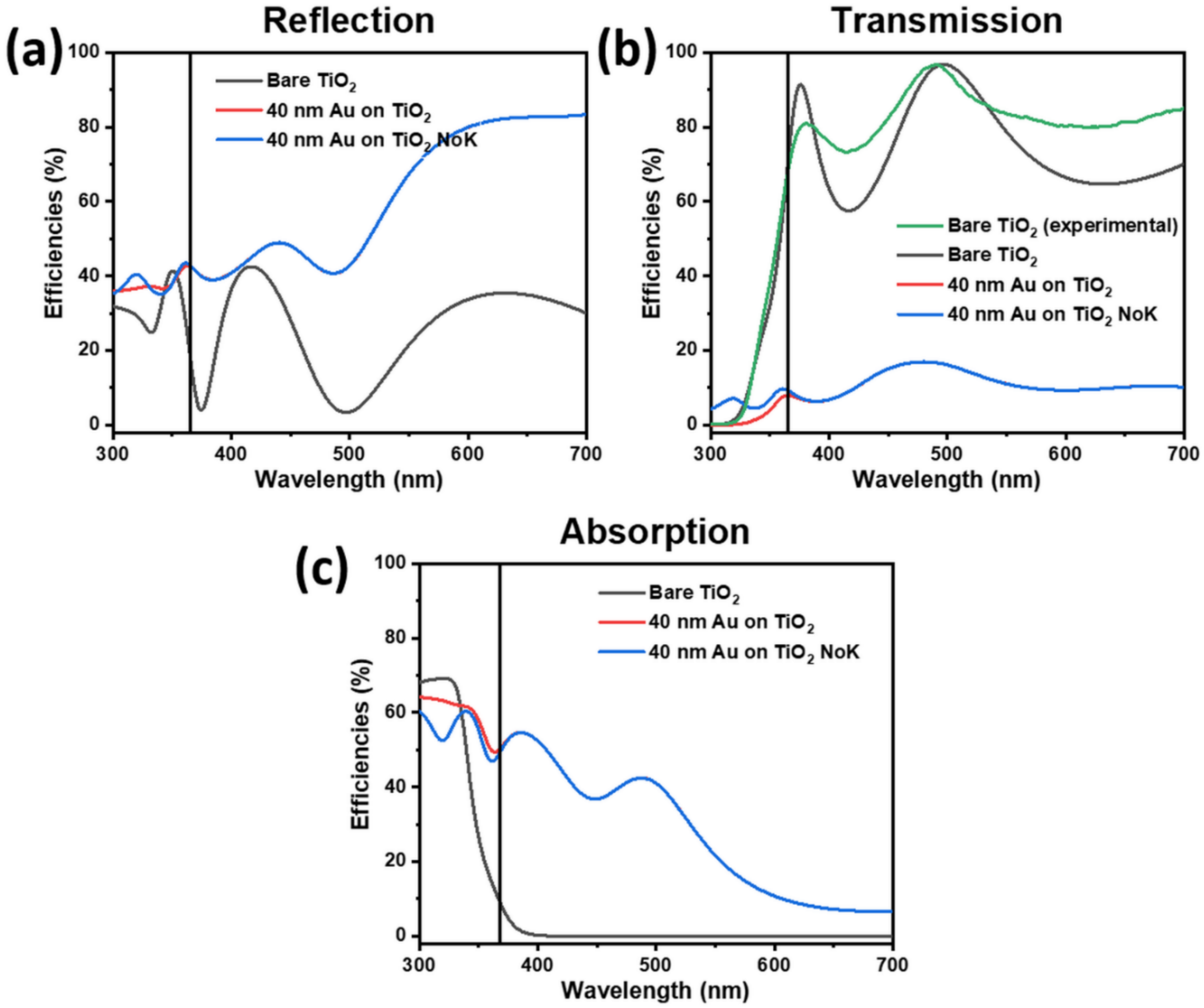

Figure 6.15. Modelled and measured **(a)** reflection, **(b)** transmission and **(c)** absorption spectra for bare TiO$_2$ (200nm TiO$_2$ film on glass) and Au(40nm)-TiO$_2$ (with at 40nm Au layer on top). NoK refers to a nulling the absorption coefficient (k) in TiO$_2$, revealing absorption only in Au, while maintaining the refractive behavior of the stack.

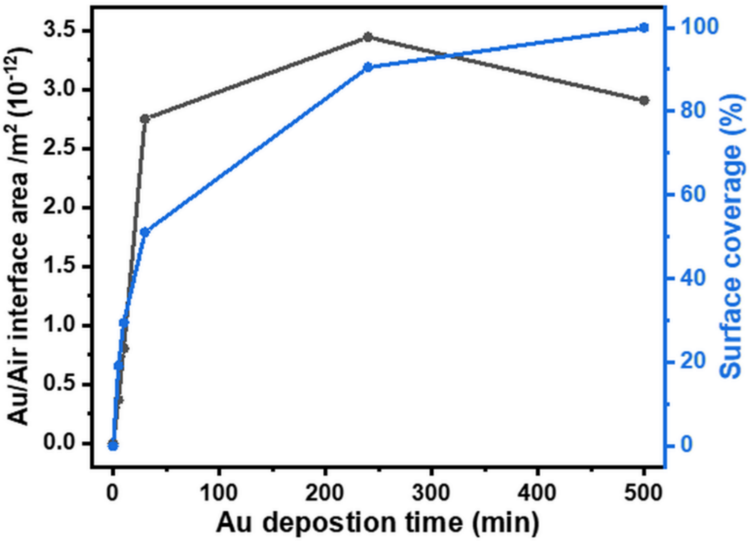

Figure 6.16. Simulated interface area between Au NCs and Air (relevant for parasitic absorption) and Au surface coverage (i.e. Au / TiO$_2$ interface fraction) according to Au deposition time.

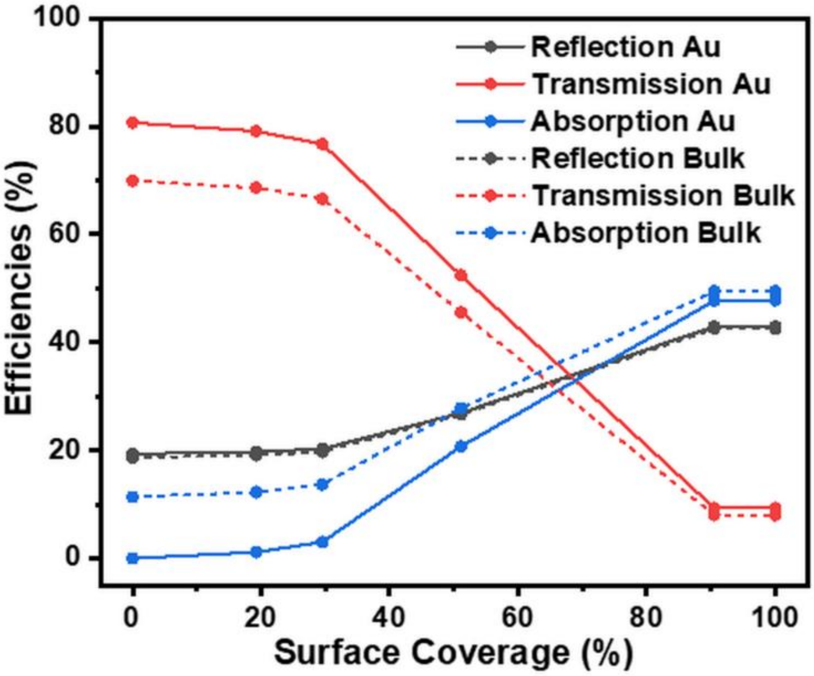

Figure 6.17. Finite element method (FEM) simulations for reflection, transmission and absorption in the Au-NCs-TiO_2 structure: As a function of surface coverage, we compare the 365 nm excitation "bulk" values (absorption takes place in both Au and TiO_2) to the simulated values when neglecting the absorption (k-) coefficient of TiO_2 ("Au").

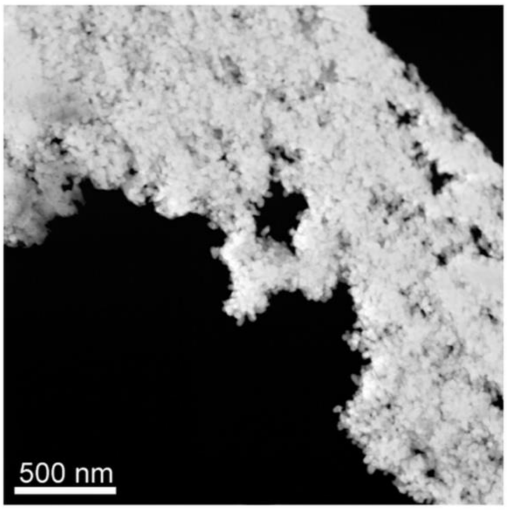

Figure 6.18. Transmission electron microscopy (TEM) image of Au NCs.

Table 6-1. Kinetics rate constants (k) for photocatalytic degradation of MB by prepared samples. **(Kinetics rate constants (k) were calculated according to *ln(C/C₀)=k.t*).**

Photocatalysts	Rate Constant (s^{-1})
Bare TiO_2	-0.28 x 10^{-3}
Au(5min)-TiO_2	-3.80 x 10^{-3}
Au(10min)-TiO_2	-4.71 x 10^{-3}
Au(30min)-TiO_2	-3.82 x 10^{-3}
Au(240min)-TiO_2	-1.43 x 10^{-3}

7 Plasmonic and Non-Plasmonic Contributions on Photocatalytic Activity of Au-TiO$_2$ Thin Film Under Mixed UV-visible Light

This chapter is based on an article published in Surface Coating and Technology [174]

Reprinted with permission from Salih Veziroglu, Marie Ullrich, Majid Hussain, Jonas Drewes, Josiah Shondo, Thomas Strunskus, Jost Adam, Franz Faupel, and Oral Cenk Aktas,
Surface Coating and Technology 389, (2020) 125613.
The article is available via the internet at https://doi.org/10.1016/j.surfcoat.2020.125613

Abstract

A highly photocatalytic Au-TiO$_2$ hybrid thin film was prepared by the photocatalytic deposition of Au nanoparticles (NPs) on reactive sputtered TiO$_2$ thin film. By altering the ratio of the visible (Vis) and ultra-violet (UV) light (Vis/UV), we investigated plasmonic and non-plasmonic contributions of Au NPs to the overall photocatalytic activity. While, a gradual increase of Vis/UV (≤0.24/1) led to a steady enhancement of the photocatalytic performance of Au-TiO$_2$ hybrid structures, further increase in Vis/UV (≥0.30/1) did not foster the enhancement further. At high Vis/UV, plasmon excited electrons seem to start promoting electron-hole recombination in TiO$_2$, which significantly reduces the photocatalytic performance.

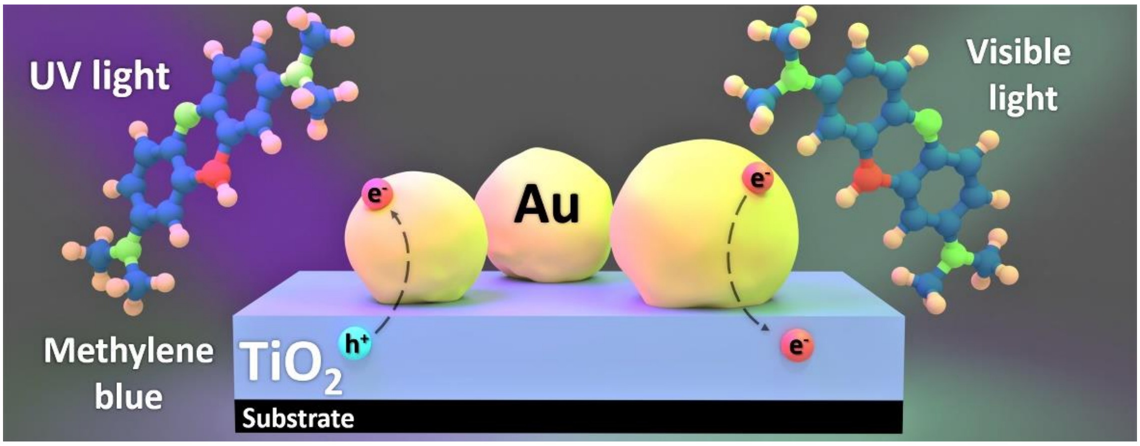

7.1 Introduction

In recent years, semiconductor photocatalysts have drawn an enormous attention due to their potential applications in water-cleaning [86,139], solar energy harvesting [175], CO_2 reduction [176] and hydrogen production.[177] Among various photocatalysts, titanium (IV) oxide (TiO_2) has attracted a great attention for industrial applications, due to its low cost, stability, and performance since its first discovery by Fujishima and Honda in 1972.[3,178] Besides its various advantages, TiO_2 has also some limitations regarding photocatalytic performance. Basically, TiO_2 is an n-type semiconductor with a wide bandgap (anatase, E_g=3.2 eV and rutile, E_g=3.0 eV), therefore its activation (the excitation of an electron from the valence band to the conduction band) is possible only at ultraviolet (UV) wavelengths.[179] This means only 4-5% of solar energy incoming from sunlight can be used for activating TiO_2.[180] Thus, great efforts have been attempted to expand the photo-response of TiO_2 to longer wavelengths.[159,181]

In order to extend the absorption of TiO_2 to the visible wavelengths and to prolong the lifetime of electron-hole pairs in TiO_2, various methods have been reported such as; decorating it with metallic nanoparticles (NPs) [15,17,136,169,175,182] and using it in combination with other semiconductor photocatalysts.[183,184] The decoration of TiO_2 with Au and Ag NPs extends its activation wavelength to the visible region thanks to the localized surface plasmon resonance (LSPR) of these noble metals.[185–187] Here, electrons in noble metals are excited by LSPR under visible light irradiation and subsequently, they are transferred to the conduction band of the TiO_2. Afterward, these electrons act as redox centres to trigger photocatalytic reactions.[37] Additionally, the noble metal NPs contact with TiO_2 surface to form Schottky barriers and this enhances the charge (electron-hole pairs) separation rate yielding a high photocatalytic activity.[188]

Most of studies reported that when an Au-TiO_2 hybrid structure is illuminated by visible light, electrons are transferred from Au NPs to TiO_2 due to the plasmonic absorption.[189] On the other hand, when such an Au-TiO_2 system is illuminated by ultra-violet (UV) light, Au NPs may trap the photoexcited electrons (on the conduction band of TiO_2) and they may act as electron sink centres (non-plasmonic contribution to the photocatalysis).[190] Both plasmonic and non-plasmonic contribution of Au NPs can influence the photocatalytic activity of Au-TiO_2 hybrid structures. For example, Yan et al. observed that under mixed, UV and visible (Vis), light irradiation, Au decorated TiO_2 NPs exhibited much higher photocatalytic performance in comparison to that achieved under only Vis or UV light.[45] But authors did not report whether the relative ratio of Vis and UV light intensities (Vis/UV) plays a role on the photocatalytic performance. Lin et al. reported Au NPs deposited on TiO_2 may induce positive and as well as negative effects on the photocatalytic activity of Au-TiO_2 depending on the irradiation wavelength.[43] They postulated that excited electrons (under Vis light) were transferred from Au NPs to TiO_2 by overcoming the Schottky barriers at Au-TiO_2 interface. This might increase the electron-hole recombination rate leading a decrease in the photocatalytic performance. Authors commented that Vis/UV might be critical for determining the photocatalytic activity. On the other hand, due to the use of high energy light sources (in several W range) in their study, the slight change in Vis/UV led to a huge change in the total energy input and this might hinder conducting a precise analysis. In addition, the change in Vis/UV seemed to be not systematically done; rather it reminds of randomly chosen ratios.[43] These make it difficult to understand the effect of Vis/UV on the photocatalytic performance of Au-TiO_2 hybrid structures.

In the literature, there are limited number of studies which report the effect of mixed UV-Vis light irradiation on the photocatalytic activity of Au-TiO_2 hybrid structures (in comparison to those which commonly highlight either only UV or Vis light irradiation). In most of these studies, Au structures are deposited on colloidal TiO_2 micro- or nanoparticles. Inhomogeneous size distribution and surface coverage of Au structures on such colloidal TiO_2 particles lead to diverse optical characteristics (differ from one particle to another). One should keep in mind that such Au decorated TiO_2 colloidal particles randomly move within the test solution (mostly MB solution) and they mostly form agglomerates thus yielding a change in the optical properties over time.[191] Therefore, it is challenging to monitor the effect of the illumination wavelength (λ_{UV}, λ_{Vis} or λ_{Vis-UV}) and as well as the light intensity (Vis/UV) on the photocatalytic performance of colloidal Au-TiO_2 hybrid structures. Therefore localizing Au structures on a robust (immobilized) TiO_2 thin film instead of colloidal TiO_2 NPs can overcome such problems.[23] Various methods have been reported to prepare stable noble metal NPs on TiO_2 thin films such as reactive sputtering [192], chemical reduction [43], electrodeposition [193] and photocatalytic deposition.[194] The photocatalytic deposition is considered an effective approach to synthesize metallic NPs directly on the TiO_2 thin film surface in terms of a strong adhesion between metallic NPs and the TiO_2 surface.[83] Photocatalytic deposition method provides a better control of the size and the distribution of metallic NPs on the TiO_2 thin film surface.[194]

In this study, we investigated the plasmonic and non-plasmonic contributions of Au NPs deposited on TiO_2 to the overall photocatalytic activity under extremely low UV and mixed UV–Vis light intensities. Here, we deposited Au NPs on a highly photocatalytic sputter deposited TiO_2 thin film by photocatalytic reduction under UV light. This Au-TiO_2 hybrid system (immobilized thin film rather than using a colloidal system) allows better understanding of the effect of the UV and Vis light intensities on the photocatalytic performance. Our results show that the ratio of UV and Vis light intensities plays a major role on the photocatalytic activity of Au NPs decorated TiO_2 thin films.

7.2 Materials and Methods

7.2.1 The Preparation of TiO_2 Thin Films

Prior to the deposition process, silicon (Si) and quartz substrates (10 mm × 10 mm) were cleaned with acetone, isopropanol and deionized water in the ultrasonic bath for 10 min, respectively and subsequently dried with nitrogen gas. DC reactive magnetron sputtering method (Titanium-Ti target, Goodfellow, 99.99%, 5 cm diameter) was used to deposit TiO_2 thin films (thickness: 300 nm) onto Si or quartz substrates using a mixture of argon (process gas) and oxygen (reactive gas) at a ratio of Ar/O_2: 250 sccm:10 sccm. We pulsed DC power at a frequency of 50 kHz with 55% duty cycle using a MOSFET based pulse generator (rectangular triggering signal with a peak-to-peak amplitude of 5 V) to reduce the oxidation of the Ti target surface. After the sputtering at room temperature for 1 h, prepared TiO_2 thin films were heat-treated in the oven at 650 °C for 1 h and afterwards directly quenched in the air. Details of the processes are given elsewhere [14,23].

7.2.2 The Synthesis of Au NPs on TiO_2 Thin Films

We applied photocatalytic deposition method to decorate TiO_2 thin films with Au NPs as schematically shown in **Figure** 7.1. The starting materials, gold (III) chloride ($AuCl_3$) was purchased from Alfa Aesar. An aqueous $AuCl_3$ solution (0.8×10^{-3} M) was filled into a quartz cuvette. The prepared TiO_2 thin films were dipped into the quartz cuvette and illuminated by low-intensity UV light (4.5 mW/cm^2, UV lamp operating at λ =365 nm) for 10 min. After UV illumination, the samples were rinsed with deionized water and dried with air to remove the solution left on the substrate surface. Details are given elsewhere.[113]

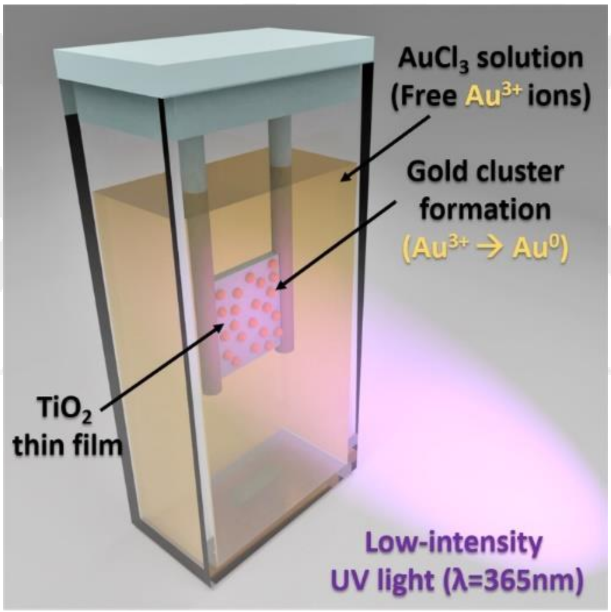

Figure 7.1. Schematic representation of the photocatalytic deposition of Au structures on TiO_2 thin film surface.

7.2.3 Materials Characterization

The surface morphology and structure of prepared Au-TiO_2 thin films were investigated by scanning electron microscopy (SEM, Supra55VP-Carl Zeiss). The chemical composition of the sample surface was characterized by X-ray photoelectron spectroscopy (XPS, Omicron Nano-Technology GmbH, Al anode, 240 W). All the binding energies (BE) were calibrated with reference to C1s peak at 285.0 eV of the absorbed carbon on the sample surface. The optical absorbance properties of bare TiO_2 and Au-TiO_2 were tested via UV–Vis spectrometer (Perkin Elmer Lambda 900 equipped with an integrating sphere) from 300 to 800 nm using a quartz substrate.

7.2.4 Photocatalytic Performance Analysis

The photocatalytic activity of bare TiO_2 and Au-TiO_2 thin films was evaluated by the photocatalytic bleaching of a dilute methylene blue (MB) solution, which is commonly used as a test dye. First prepared thin films were immersed into 6.5 mL MB aqueous solution (10 µmol/L), and while the solution was magnetically stirred and exposed to UV (λ=365 nm, which was also used for the photocatalytic deposition of Au on TiO_2 as given in section 2.2) and Vis (λ=520 nm) light illumination applying different intensity ratios for 4 h (for each). The change in the absorption of MB solution at 664 nm was recorded by UV–Vis spectrophotometer (StellarNet EPP2000C-SR-50 with SL5-DH light source) to monitor the photocatalytic degradation.

7.3 Results and Discussion

Figure 7.2 shows a top-view SEM image of bare and Au NPs decorated TiO_2 thin films at different magnifications. The TiO_2 thin film exhibited a typical sputter-deposited layer morphology and here the most striking observation is densely distributed nanocrack network (labelled with red arrows).

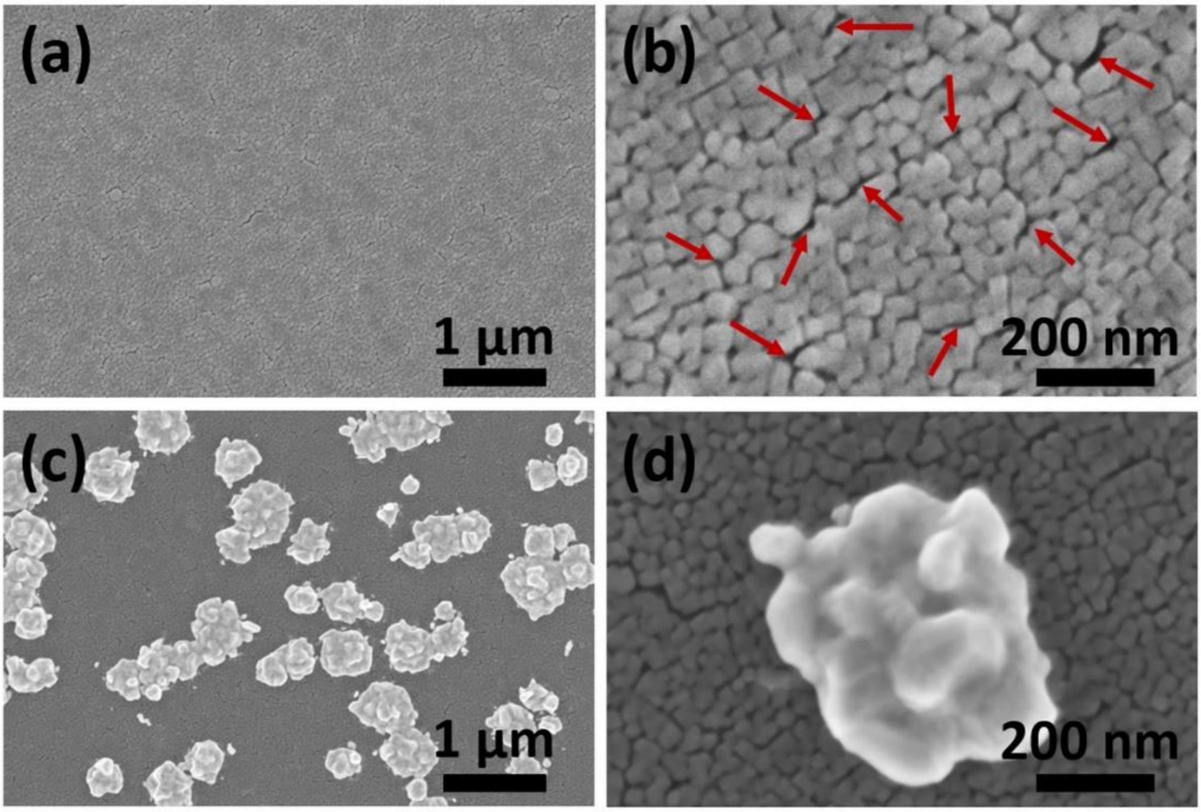

Figure 7.2. SEM images of TiO_2 thin film recorded at **(a)** low magnification and **(b)** high magnification (Red arrows represent nanoscale cracks on the TiO_2 thin film surface). SEM images of Au-TiO_2 hybrid thin film recorded at **(c)** low magnification and **(d)** high magnification.

We have shown that such cracks enhance the active surface area which promotes the photocatalytic performance.[14] After the photocatalytic reduction of $AuCl_3$ solution under UV light for 10 min, Au NPs with a wide size distribution of 50-250 nm were observed on TiO_2 thin films as shown in **Figure** 7.2c and **Figure** 7.2d (corresponding EDX mapping is given in **Figure** 7.7).

During the UV illumination, photo-excited charge carriers (electrons-holes) are generated on the photocatalytic TiO_2 surface (schematically depicted in **Figure** 7.3). The generated electrons to directly reduce the Au^{3+} ions into stable Au NPs on the TiO_2 surface (nucleation). Continuing UV illumination generated new electrons, which seem to reduce further Au^{3+} ions onto former Au NPs (particle formation) and these particles started to interact with each other (particle-particle interaction). Following this interaction, electron transfer between adjacent Au NPs may trigger agglomeration and growth (coalescence).

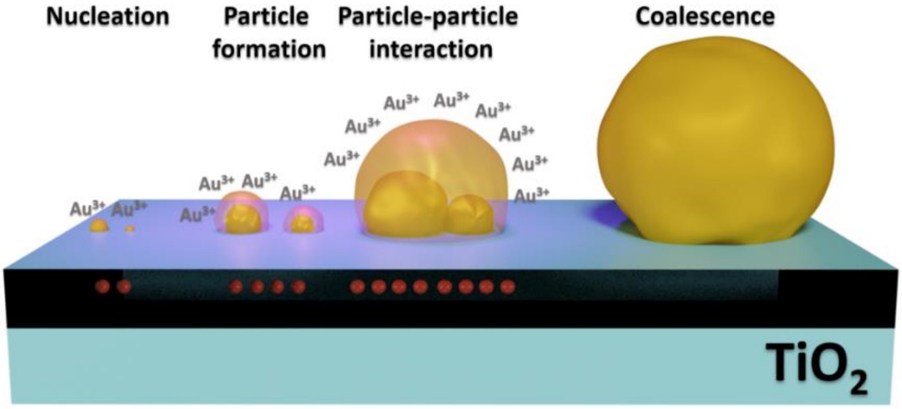

Figure 7.3. Scheme depicting the photocatalytic deposition of Au NPs on TiO_2 surface with different steps of growth UV illumination.

In order to investigate the chemical composition and states on Au NPs decorated TiO_2 surface, we compared XPS spectra recorded before and after deposition of Au NPs. **Figure** 7.4 shows that 4 different XPS spectra of TiO_2 after deposition of gold, one wide spectrum, and 3 high-resolution spectra. The wide spectrum shows Ti, O, Au and some adsorbed C on the sample surface (**Figure** 7.4a). The high-resolution scan of Ti-2p shows two main doublet peaks (Ti $2p_{1/2}$ at 464.2 eV and Ti $2p_{3/2}$ at 458.5 eV) with a good symmetry indicating that the oxidation state of Ti was +4 (TiO_2) in octahedral coordination with oxygen.[195–197] The O-1s peak was fitted by two components (**Figure** 7.4c). One component is located at a binding energy of 529.8 eV, which corresponds to the O bonded in the TiO_2 lattice (Ti-O-Ti).[154] The other component at 531.8 eV originates from adsorbed oxygen/hydroxyl (O_2/-OH).[198,199] Since the sample was measured prior and after the deposition of Au, in the support information also the O1s spectrum before a deposition can be found in **Figure** 7.8. The spectrum after deposition shows a higher amount of adsorbed oxygen/hydroxyl, which may originate from the deposition process.

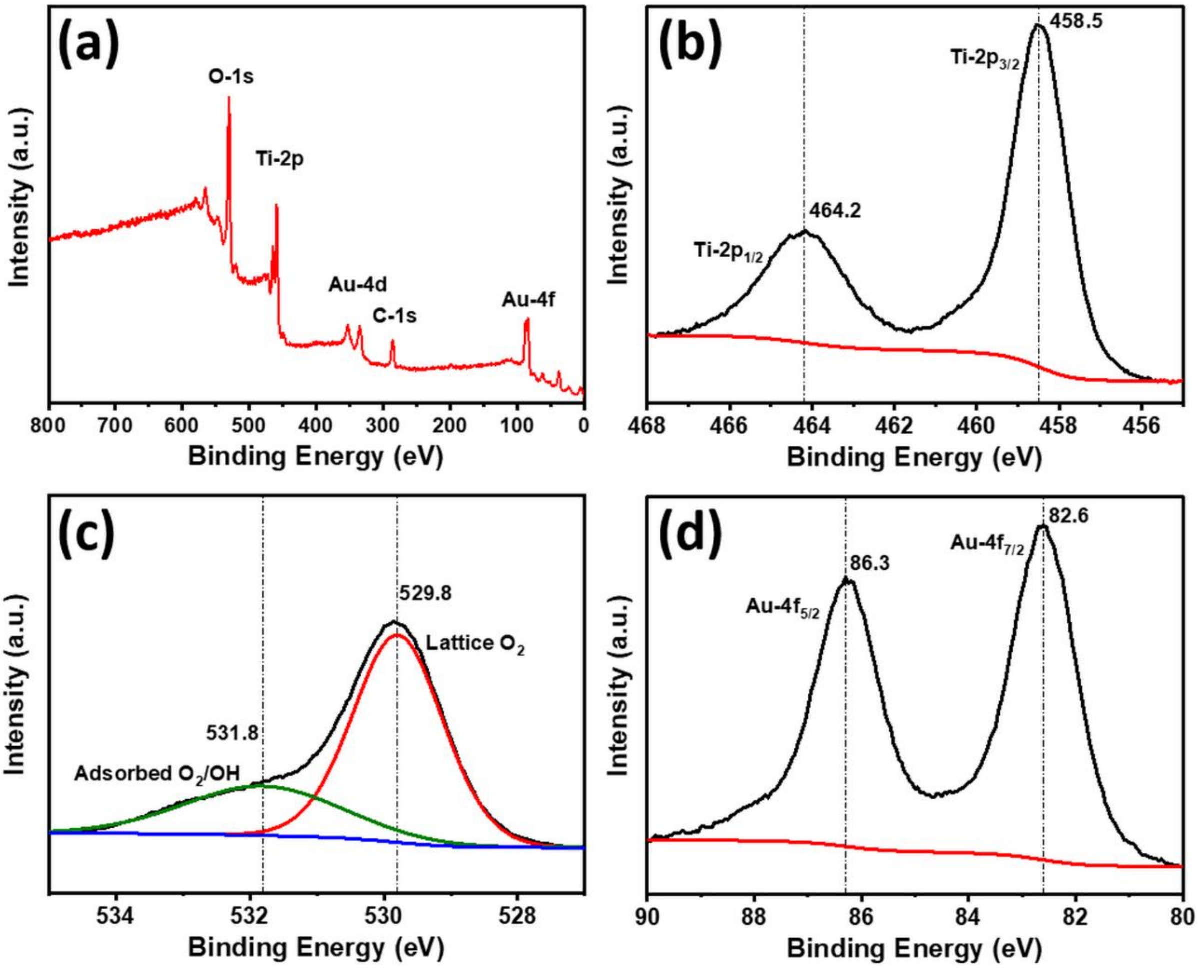

Figure 7.4. **(a)** Wide scan and high-resolution XPS spectra of **(b)** Ti-2p, **(c)** O-1s and **(d)** Au-4f.

The Au $4f_{5/2}$ and Au $4f_{7/2}$ peaks were found at 86.3 eV and 82.6 eV (**Figure** 7.4d). The binding energy of the Au $4f_{7/2}$ for pure Au is typically found at a higher binding energy of 84 eV.[200] The decrease of Au $4f_{7/2}$ binding energy is observed in several studies related to Au-TiO_2 photocatalysts.[156] One explanation of the decreased binding energy is according to Radnik et.al. the reduced coordination number of Au atoms.[157] Another explanation from Arrii et al. is that the particle (Au) and substrate (TiO_2) interaction play an important role in the negative shift. They relate the shift to an electron transfer from Ti^{3+} surface defect states to Au NPs.[158]

Figure 7.5a shows the UV-Vis spectra for bare TiO_2 and Au-TiO_2 photocatalysts. It has been well known that the absorbance edge of TiO_2 lies around 365 nm.[201] Bare TiO_2 film was highly transparent in the visible region with a transparency value exceeding 80%. The waved peaks between 450-800 nm can be attributed to the increased surface roughness of the films due to typical columnar structures and the presence of nanocrack networks.[171]. UV-Vis spectra of Au-TiO_2 photocatalyst exhibited an enhanced absorption in the visible region, which reminds of a typical the surface plasmon resonance.[43] The broad absorbance rather than a sharp peak seemed to arise due to the inhomogeneity in the particle size and as well as the distribution of Au NPs on TiO_2 thin film surface.[202,203]

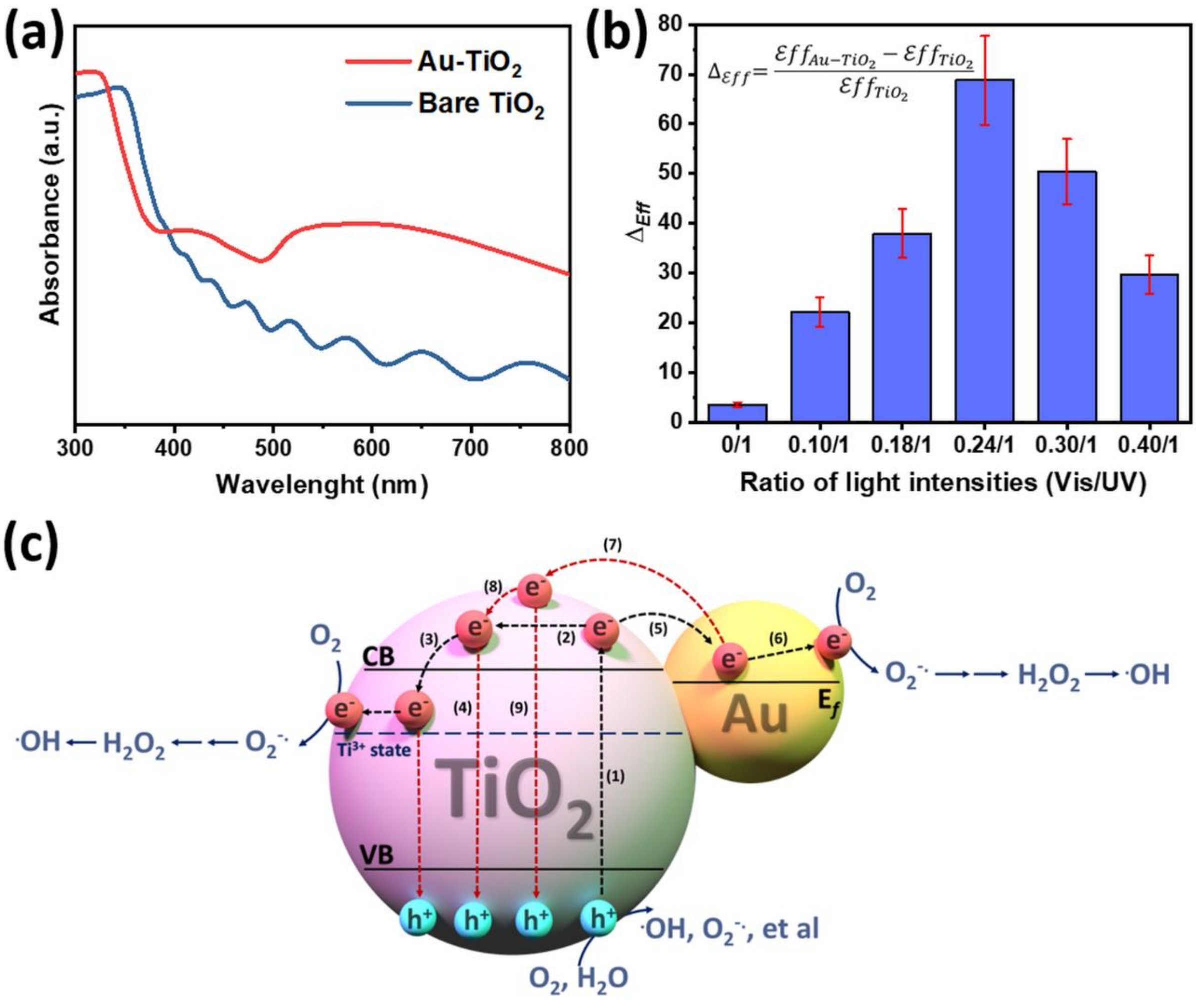

Figure 7.5. **(a)** UV-Vis absorbance spectra of bare TiO_2 and Au-TiO_2 photocatalysts, **(b)** The photocatalytic activity of TiO_2 and Au-TiO_2 under different ratios of Vis/UV intensities **(c)** The entire mechanism of plasmonic and non-plasmonic contributions on photocatalytic activity of Au-TiO_2 under mixed Vis-UV light irradiation.

After optical absorbance analysis, we revealed the contribution (Δ_{Eff}) of the Au NPs on photocatalytic activity of TiO_2 by applying different ratios of Vis and UV light intensities as represented in **Figure** 7.5b. Here, while the intensity of UV light (365 nm) was fixed to 37 mW/cm^2, we varied that of the Vis (green) light (520 nm). When we iridate the surface of Au-TiO_2 by only UV light we observed nearly no significant enhancement on the photocatalytic performance. When we used a mixed light (Vis/UV:0.1/1 and Vis/UV:0.18/1) we observed a clear enhancement in the photocatalytic performance (22.1% and 37.9%, respectively). We achieved the highest enhancement by 68.8% at Vis/UV:0.24/1.

Here, it is believed that Vis light excited electrons in Au NPs by LSPR were transferred to the conduction band of TiO_2 then they triggered the photocatalytic reaction as shown in **Figure** 7.5c (plasmonic contribution as shown in routes (7), (8) and (3), respectively) in addition to non-plasmonic photocatalytic mechanism shown in **Figure** 7.5c (routes (1), (5) and (6), respectively). While the non-plasmonic contribution by UV light plays the major role (from our previous reports [194]), the synergetic effect of both plasmonic and non-plasmonic promoted the photocatalytic activity of Au-TiO_2. Interestingly increasing Vis/UV further did not lead to higher photocatalytic enhancement.

Under UV irradiation, excited electrons migrate the conduction band of TiO_2 (1) and create holes in the valence band of TiO_2. If these exited electrons stay on the conduction band at enough time (2), they can find a chance to reduce Ti^{4+} cations to Ti^{3+} state (3) and these electron degrade the MB.[204] If these exited electrons do not stay on the conduction band at enough time, the photocatalytic reaction cannot be happened due to recombination of electrons and holes (4). Furthermore, the excited electrons can be trapped by Au NPs (5) and initiate the degradation of MB (6). Meanwhile, under green light irradiation, the electrons in the Au NPs are excited by LSPR and subsequently transferred the conduction band of TiO_2 (7).[45] These electrons can trigger the photocatalytic reaction (8) or recombination (9). But, if the intensity of green light increases further, more electrons are excited by LSPR and the transferring of these excited electrons from the Au NPs to TiO_2 (7) might surpass the electron transferring from the TiO_2 to AuNPs (5).[43]

In order to investigate the stability of Au-TiO_2 photocatalyst, its photocatalytic performance was re-tested in four consecutive cycles by monitoring its ability to bleach the MB solution. After each cycle, the Au-TiO_2 sample was rinsed with water and re-used again. **Figure** 7.6 shows that the photocatalytic bleaching efficiency of Au-TiO_2 thin film photocatalyst under mixed light (Vis/UV:0.24/1) remained almost constant (~90 %) after four consecutive cycles.

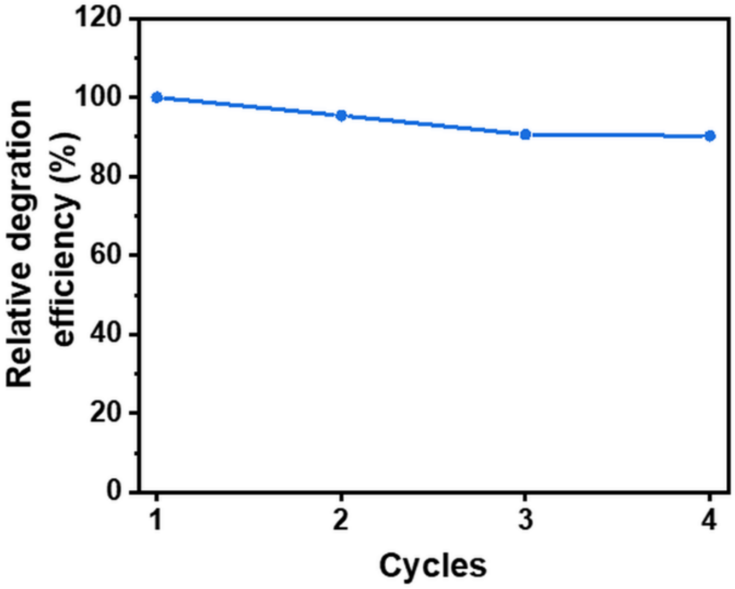

Figure 7.6. Reusability of Au-TiO_2 thin film photocatalyst under mixed light (Vis/UV:0.24/1). All values were normalized with respect to the bleaching of MB by Au-TiO_2 under mixed light for 4 hours.

7.4 Conclusion

In summary, we have prepared TiO_2 thin films decorated with Au NPs by photocatalytic deposition of Au^{3+} ions (under low-intensity UV irradiation) and studied structural and photocatalytic properties. Both plasmonic and non-plasmonic contributions of Au NPs to the photocatalytic activity of TiO_2 were investigated with altering Vis/UV systemically. The photocatalytic activity measurements showed that the increasing Vis/UV initially improves the photocatalytic activity of Au-TiO_2, but the further increase in Vis/UV ratio do not foster it. The optimum Vis/UV was found to be 0.24/1 and this led to the synergetic effect of plasmonic and non-plasmonic enhancement of the overall photocatalytic activity of Au-TiO_2 hybrid structures.

Acknowledgments

S. Veziroglu acknowledges the Graduate Center and Federal State Funding at Kiel University, for providing funding for his Ph.D. study. Authors would like to thank Stefan Rehders for his continuous support for building-up and the maintenance of deposition systems.

Supporting Information

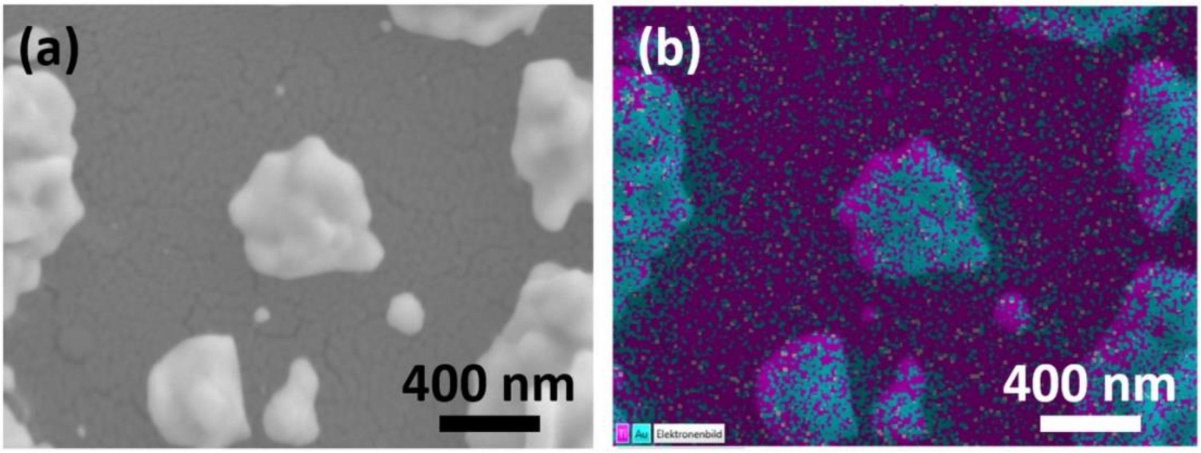

Figure 7.7. **(a)** Scanning electron microscopy (SEM) image of Au structures on TiO_2 thin film and **(b)** DX compositional mapping of Au structures (purple and cyan areas represent presence of Ti and Au, respectively).

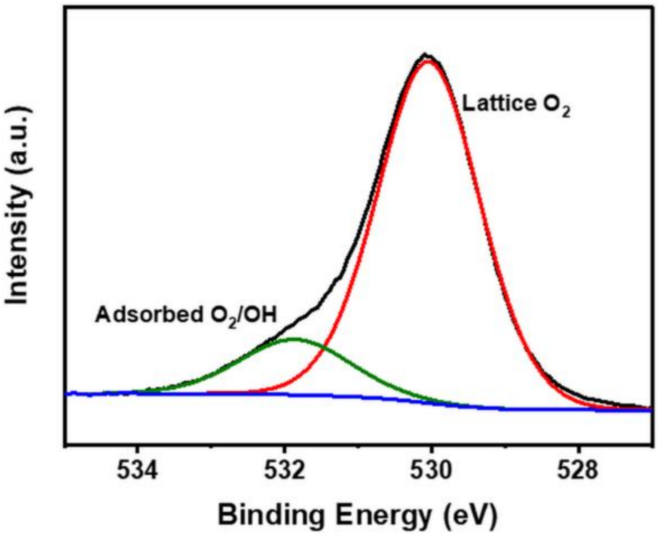

Figure 7.8. XPS spectra of O1-s before Au NPs deposition on TiO_2.

ISSN 1862-6300
Phys. Status Solidi A
216 · No. 14 July 24
(2019)

physica status solidi pss a

www.pss-a.com

applications and materials science

14
2019

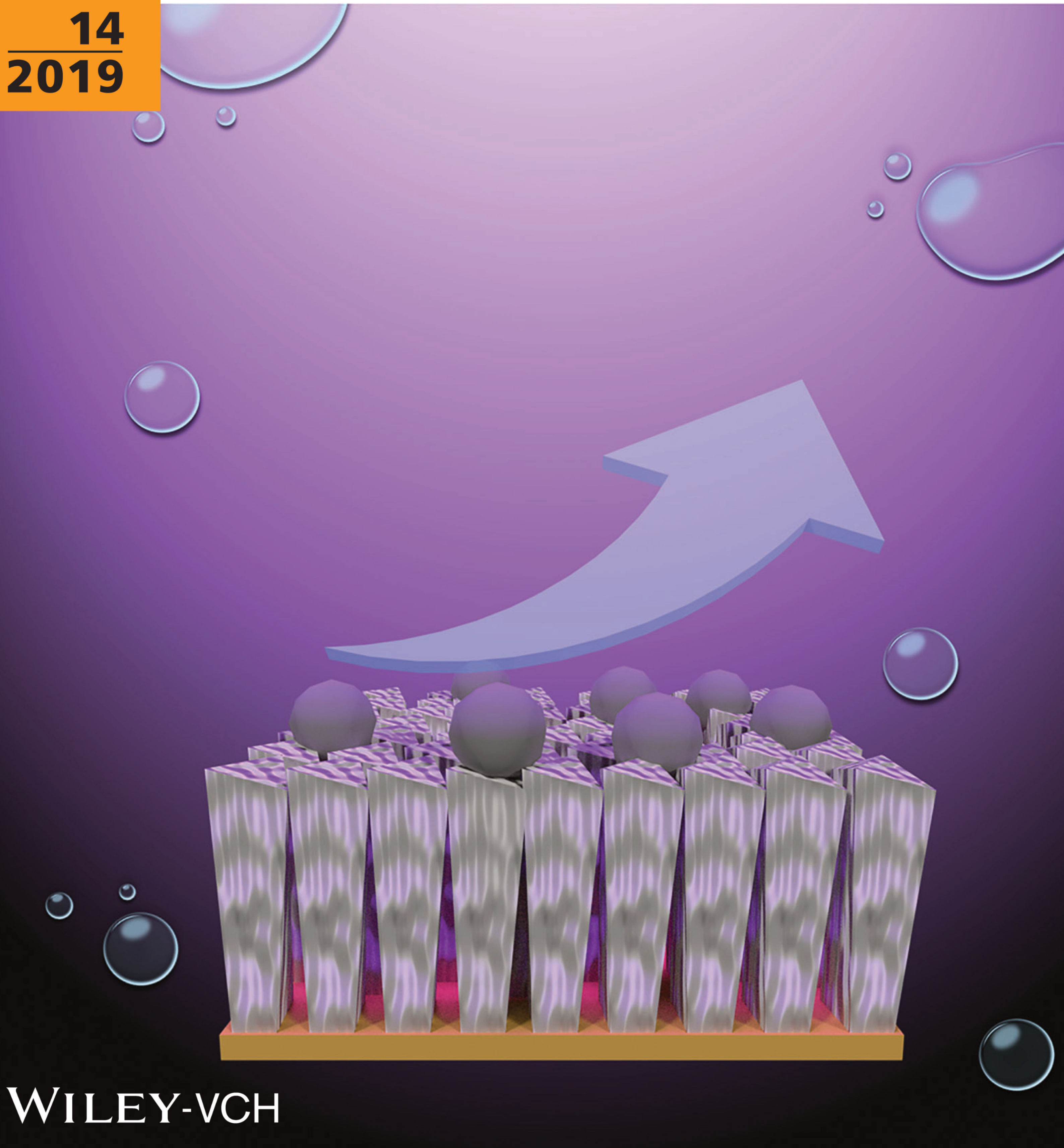

WILEY-VCH

8 Ag Nanoparticles Decorated TiO_2 Thin Films with Enhanced Photocatalytic Activity

This chapter is based on an article published in Physica Status Solidi (a) – applications and materials science.[194]

Reprinted with permission from Salih Veziroglu, Muhammad Zubair Ghori, Anna-Lena Obermann, Katharina Röder, Oleksandr Polonskyi, Thomas Strunskus, Franz Faupel, Oral Cenk Aktas
Phys. Status Solidi A, 216: 1800898.
The article is available via the internet at https://doi.org/10.1002/pssa.201800898

Abstract

A highly photocatalytic Ag/TiO_2 thin film was prepared by the photocatalytic deposition of Ag nanoparticles (NPs) on reactive sputtered columnar TiO_2 structures. By altering the ultra-violet (UV) exposure time, we controlled the morphology and surface coverage of deposited Ag NPs. While a surface coverage of 1-4 % (by Ag NPs) led to a significant increase in the photocatalytic activity, depositing more Ag NPs yielded a decrease in the photocatalytic performance (lower than that of bare TiO_2). This may arise due to the blocking of UV light incoming to the TiO_2 by the formation continuous network of Ag clusters on the surface. Such highly interconnected Ag clusters might also trigger the recombination of electron-hole pairs. After five consecutive photocatalysis tests, the Ag (1min)/TiO_2 thin film remained intact.

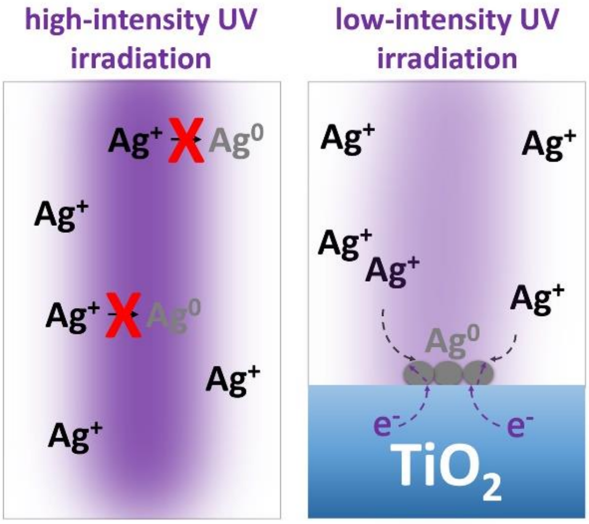

8.1 Introduction

In recent years, environmental pollution became a significant problem threatening the health and the quality of our life. The photocatalysis is one of the most promising routes for environmental remediation applications due to its low-cost and high efficiency in comparison to other methods.[205,206] Basically, the photocatalysis refers the conversion of the light energy into the chemical energy and various semiconductors have been explored for achieving high conversion efficiencies.[3] Titanium dioxide (TiO_2) is the most investigated semiconductor photocatalyst because of its high photocatalytic activity, non-toxicity, and good chemical stability.[207–209] However, the high recombination rate of the photogenerated electron-hole pairs (e^- and h^+) limits the photocatalytic activity of TiO_2.[86,210] Several studies have been reported to improve the lifetime of the photogenerated electron-hole pairs by decorating noble metal nanoparticles (NPs), which act as electron trapping sites, on the TiO_2 structure.[155,210–212] Among various NPs, silver (Ag) NPs are the most preferred ones due to their high catalytic efficiency, low-cost (compared to other noble metals), widespread optical properties, the potential use in biological and chemical sensing.[213–216] It is well known, Ag NPs can trap the excited electrons from TiO_2 and promote the interfacial charge transfer between Ag NPs and TiO_2 surface.[201] Therefore, the photocatalytic activity of TiO_2 can be enhanced by such an improved charge carrier separation.[217]

Various methods such as hydrothermal synthesis,[218] sol-gel,[219] spray-pyrolysis,[220] chemical reduction,[221] reactive sputtering,[222] electrochemical deposition[223] and photocatalytic deposition[196,224] have been reported to prepare Ag NPs on TiO_2. The photocatalytic deposition is considered an effective method to prepare Ag NPs directly on the TiO_2 surface, which provides a strong adhesion between particles and the surface.[225] Basically, when TiO_2 is irradiated by UV light, e^- and h^+ are generated and the photogenerated e^- reduce the surface-adsorbed Ag^+ ions into stable Ag NPs. Photocatalytic deposition of noble metals on TiO_2 has been extensively studied for a long period.[225] However, most of these studies cover the deposition of Ag on TiO_2 NPs.[83] TiO_2 NPs exhibit a high photocatalytic activity due to their high surface area and confined geometry. Nevertheless, the use of TiO_2 NPs counter with some limitations such as the difficulty of their filtration from the liquid medium to be cleaned up.[23,226] Additionally, in order to deposit Ag^+ ions on immobilized TiO_2 NPs, a high-intensity (400 W) UV irradiation is needed since within a liquid medium such NPs are continuously and randomly moving and this hinders effective exposure [155]. On the other hand, such a high-intensity UV irradiation may lead to the photoreduction of Ag^+ ions in the solution instead of the preferential photocatalytic reduction on the TiO_2 surface. Mostly the photoreduction at high light intensities yields the agglomeration of NPs (direct uncontrolled UV reduction rather than controlled photocatalytic reduction) at longer exposure time and this may decrease the overall photocatalytic activity.[212] Either by immobilizing TiO_2 NPs on a substrate or using TiO_2 thin films such problems can be overcome.[113]

In this current study, we reported a facile method to synthesize a highly photocatalytic Ag/TiO_2 thin film. Ag NPs were deposited on the TiO_2 thin film surface by the photocatalytic reduction of Ag^+ ions at low-intensity UV irradiation. We controlled the morphology of deposited Ag NPs and their surface coverage by applying different UV exposure time intervals. Our results show that the surface coverage by Ag NPs plays a major role on the photocatalytic efficiency.

8.2 Materials and Methods

8.2.1 Synthesis of Ag/TiO_2 Thin Film

First, highly photocatalytic TiO_2 thin films were prepared on a silicon substrates (10x10 mm) by pulsed DC reactive sputtering as we reported previously.[14,23] Second, prepared TiO_2 thin films were dipped in an aqueous solution of silver nitrate ($AgNO_3$, 6 x 10^{-3} M) and exposed to low-intensity UV irradiation (4.5 mW/cm^2 UV lamp operating at λ=365 nm) for different time intervals (1, 2, 3 and 5 min) as schematically shown in **Figure** 8.1. Samples were labeled as Ag(1min)/TiO_2, Ag(2min)/TiO_2, Ag(3min)/TiO_2, Ag(5min)/TiO_2 according to irradiation times. After photocatalytic deposition, samples were rinsed with pure water to remove excessive solution left on the surface and then they were dried in air at room temperature.

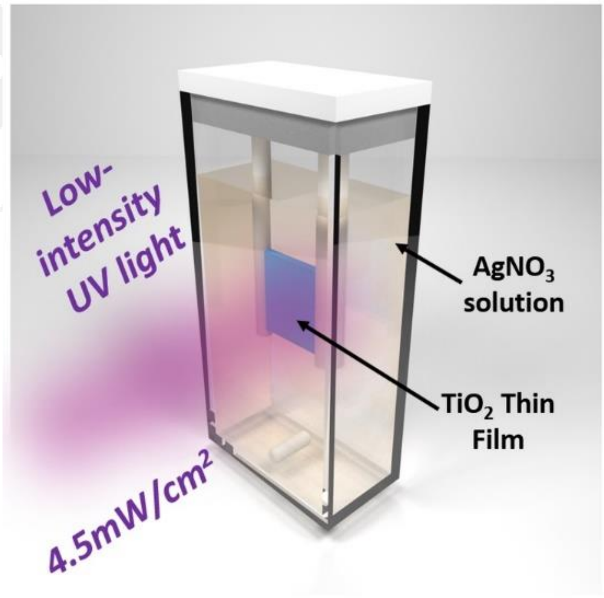

Figure 8.1. Schematic representation of the photocatalytic deposition under low-intensity UV irradiation.

8.2.2 Surface Characterization

The morphology and chemical composition of the prepared samples were revealed by scanning electron microscopy-SEM (Supra55VP-Carl Zeiss) and energy-dispersive X-ray spectroscopy- EDX (AZtecOne-Oxford Instruments), respectively. X-ray photoelectron spectroscopy-XPS (Omicron Nano-Technology GmbH, Al anode, 240 W) measurement was performed to determine chemical states on the surface. All the binding energies were referenced to the C 1s peak at 285.0 eV of the adventitious carbon on the sample surface. Raman spectra were recorded by the excitation of the sample surface using a laser source operating at a wavelength of 532 nm.

8.2.3 Photocatalytic Activity Test

The photocatalytic activity of samples was evaluated by the photocatalytic bleaching of methylene blue (MB). Ag NPs/TiO_2 thin films were immersed into 6.5 mL MB aqueous solution at a concentration of 10 μmol/L. The solution was magnetically stirred and irradiated under UV light (4.5 mW/cm^2 UV lamp at λ=365 nm) for 240 minutes. The changing in the absorption at 664 nm was recorded by UV-Vis spectrophotometer (StellarNet EPP2000C-SR-50 with SL5-DH light source).

8.3 Result and Discussion

Figure 8.2 shows the surface morphology of Ag/TiO_2 thin films prepared at different time intervals. The surface coverage of Ag NPs increased exponentially with the extension of the UV exposure time (**Figure** 8.2a). Additionally, by the extension of the UV exposure time, we observed a clear increase in the primary particle size and the agglomeration of Ag NPs (**Figure** 8.2b).

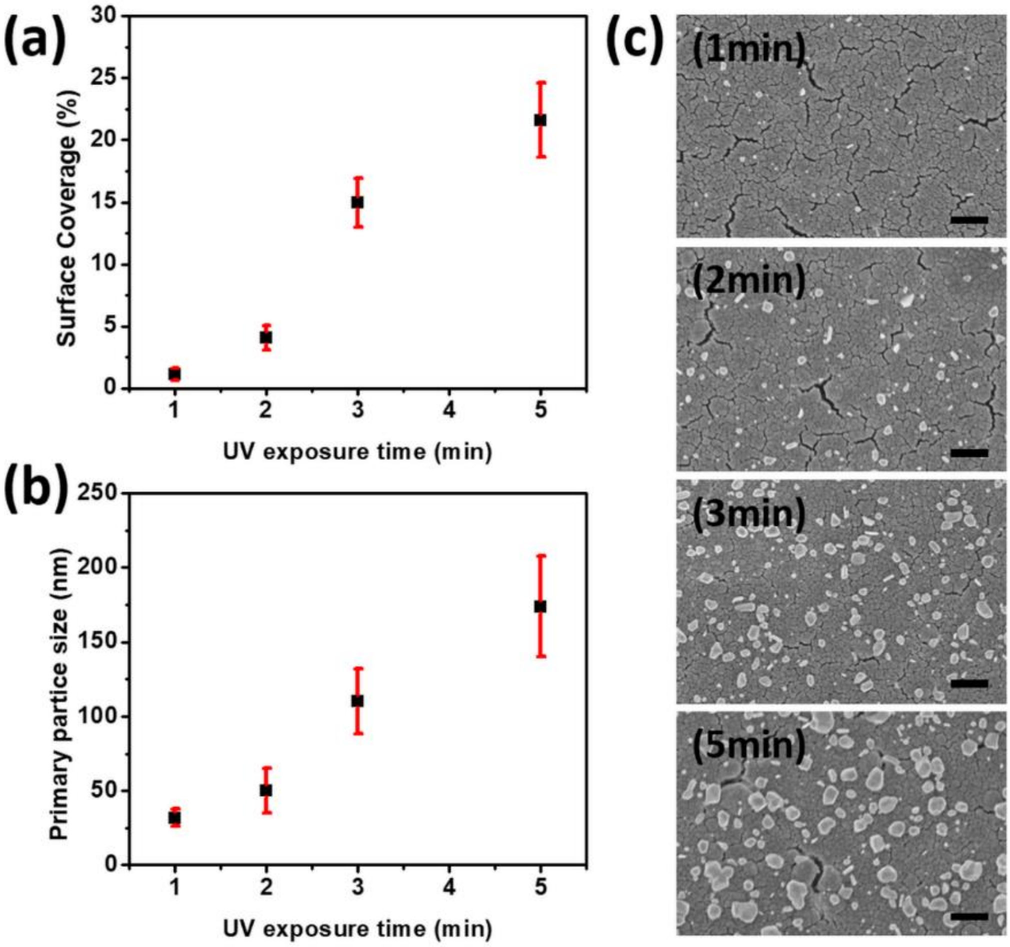

Figure 8.2. **(a)** Surface coverage of TiO_2 by deposited by Ag NPs (%), **(b)** Primary particle size (average) of Ag NPs at different UV exposure time intervals and **(c)** SEM images of Ag/TiO_2 thin film prepared at different UV exposure time intervals (Scale bar: 400 nm).

After 5 min UV exposure, 3 times larger particles than the primary size of Ag NPs were seen on the TiO_2 thin film surface. The primary particle size of the Ag NPs was revealed according to the schematic representation given in **Figure** 8.7. In **Figure** 8.2c, it can be seen that uniformly dispersed Ag NPs on the TiO_2 surface (with a network of deep nano-cracks) were obtained by photocatalytic deposition of Ag^+ ions. The EDX mapping images (**Figure** 8.8) shows the coexistence of titanium (Ti), oxygen (O) and silver (Ag) elements confirming the formation of Ag/TiO_2. The presence of Ag NPs did not alter the surface morphology of TiO_2 thin film. It is obvious, the distribution and the agglomeration of Ag NPs on TiO_2 surface were closely related to UV exposure time.

During the UV exposure, photo-excited charge carriers were generated on photocatalytic TiO_2 as shown in **Figure** 8.3. Ag^+ ions in aqueous solution were directly reduced into stable Ag NPs (covering TiO_2 thin film surface) by excited electrons (nucleation). Further UV exposure generated more excited electrons which were transferred to reduce more Ag^+ ions into Ag NPs (cluster formation/growth).[113] UV exposure time played a major role on the size and the morphology of Ag NPs.

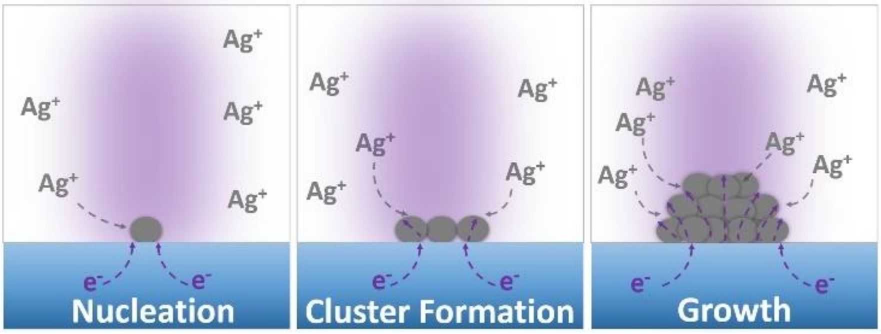

Figure 8.3. Scheme depicting the photocatalytic deposition (low-intensity UV irradiation) of Ag NPs on TiO_2 thin film.

In order to identify the chemical state, XPS spectra of the Ag(1min)/TiO_2 thin film was recorded. The wide-scan XPS spectrum showed the presence of Ti, O, Ag, and some adsorbed carbon on the sample surface (**Figure** 8.9).[227] Recorded Ti 2p spectrum indicated two main peaks at 459.2 and 464.8 eV which correspond to Ti $2p_{3/2}$ and Ti $2p_{1/2}$ orbitals, respectively.[228] The binding energy of 5.6 eV can be attributed to Ti^{4+} (indicating TiO_2) in **Figure** 8.4a. [196,229] The O 1s peak exhibited two chemical states (**Figure** 8.4b) which could be attributed to lattice oxygen surface oxygen and Ag oxide.[230] The peak located at 528.3 eV showed less amount Ag NPs oxidized.[231] The Ag 3d spectrum of Ag/TiO_2 (**Figure** 8.4c) comprised two peaks at 374.4 and 368.4 eV which may be attributed to Ag $3d_{5/2}$ and Ag $3d_{3/2}$ spin-orbit coupling respectively, indicating the formation of metallic silver (Ag^0). In addition, 6.0 eV difference between the binding energy of the Ag $3d_{5/2}$ and Ag $3d_{3/2}$ peaks also matches with the typical characteristic of Ag^0.[214,232] Briefly XPS analysis confirmed the formation of Ag/TiO_2 hybrid structures.

Figure 8.4d shows the Raman spectra of bare TiO_2 and of Ag/TiO_2 samples. Corresponding Raman spectra of bare TiO_2 showed bands at 140.0 cm^{-1} (E_g), 194.2 cm^{-1} (E_g), 393.6 cm^{-1} (B_{1g}), 637.4 cm^{-1} (E_g), which were consistent with the anatase phase TiO_2.[233] Deposited Ag NPs did not induce any new Raman active features, consistent with the formation of metallic Ag NPs.[208]

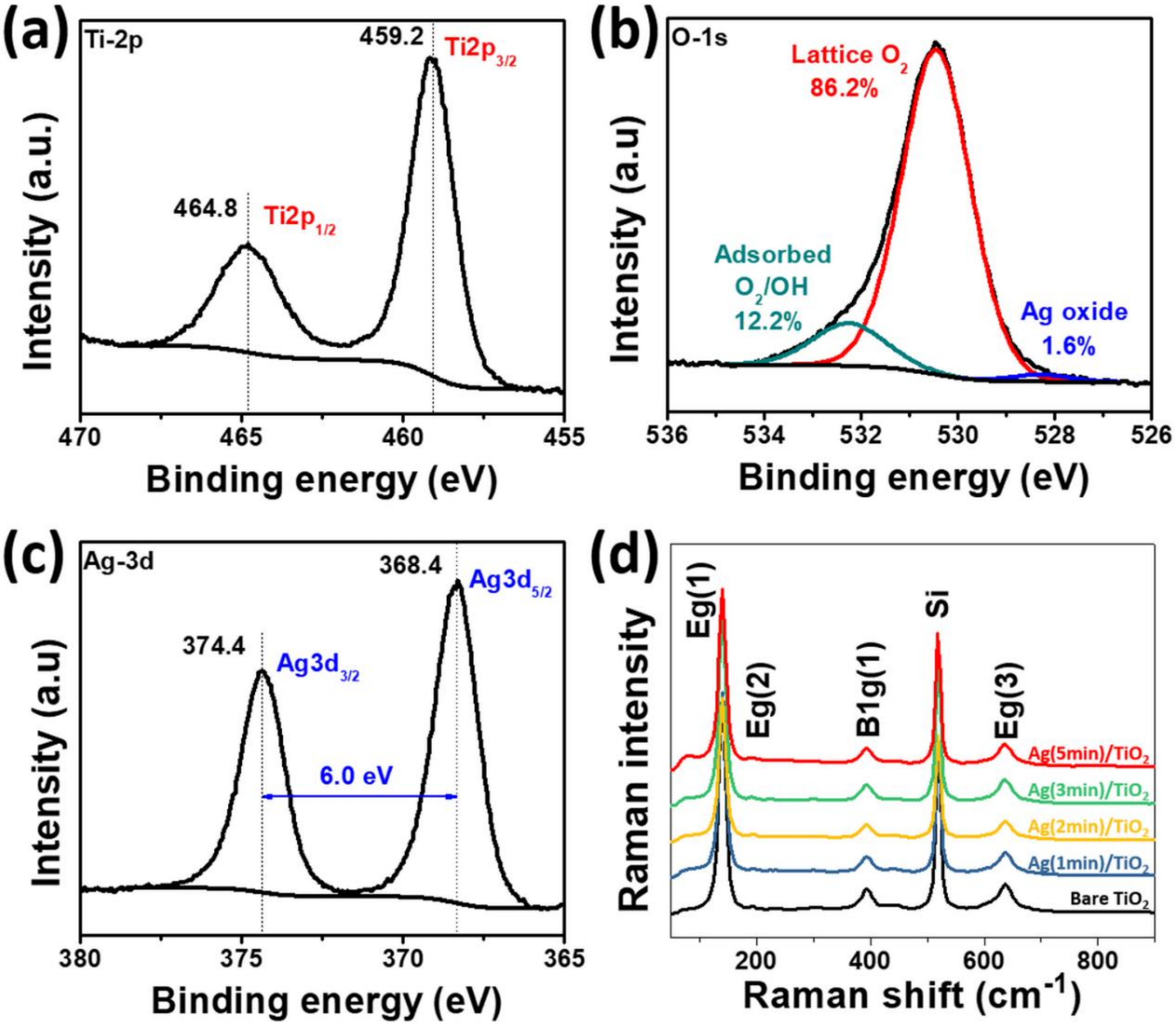

Figure 8.4. High resolution XPS spectra for **(a)** Ti-2p, **(b)** O-1s, **(c)** Ag-3d regions and **(d)** Raman spectra of prepared samples.

To reveal the photocatalytic activity, the bare TiO_2 and Ag/TiO_2 samples were tested for their ability to bleach aqueous MB solution under UV irradiation for 240 minutes (**Figure** 8.5a). The photocatalytic activity was evaluated by the change in C/C_0 ratio (where C_0 and C are the initial concentration of MB and the concentration of MB at the time, respectively). Ag(1min)/TiO_2 and Ag(2min)/TiO_2 exhibited higher photocatalytic activities in comparison to bare TiO_2. Additionally, we calculated kinetic rate constants (k) of corresponding thin film photocatalysts (**Table** 8-1). We observed that Ag(1min)/TiO_2 led to about 1.7 times higher reaction rate in comparison to bare TiO_2. This improvement in the photocatalytic activity was arisen due to the suppression of recombination of photoexcited charge carriers (e^- / h^+) due to the electron scavenging by Ag NPs.[234–236] However, the excessive Ag NPs amount on the TiO_2 surface might decrease the photocatalytic activity due to blocking of the incoming UV light to the TiO_2 surface. Because of this blocking, TiO_2 seemed to be not able to generate enough electrons for further reactions. Additionally, a large amount of Ag NPs aggregated together, might serve as recombination sites for e$^-$ and h$^+$, and this leads to lower performance.[237]

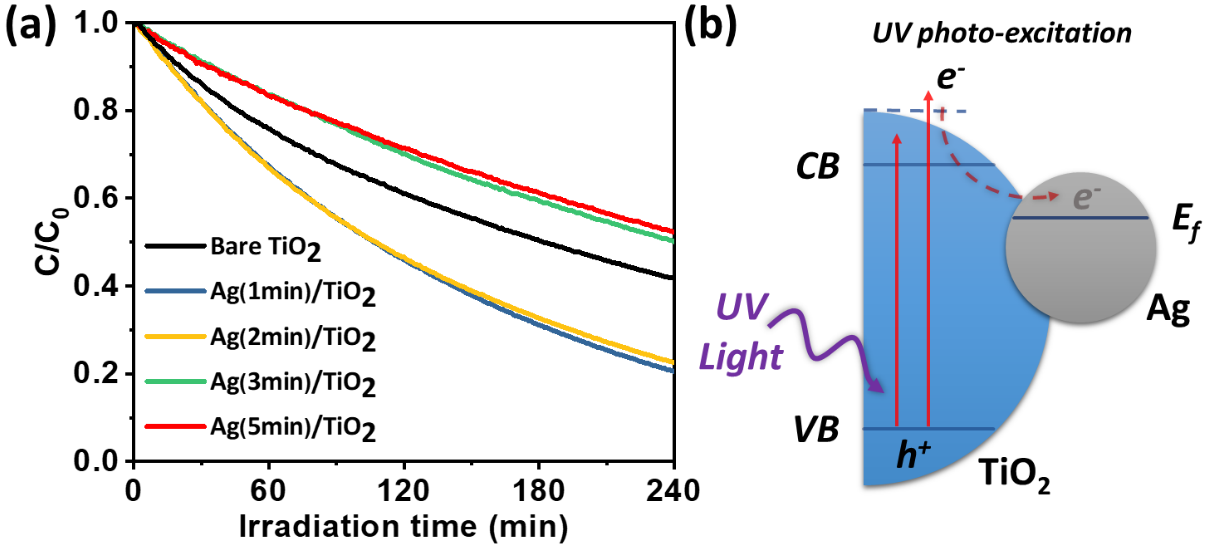

Figure 8.5. **(a)** Comparison of time-dependent photocatalytic bleaching of MB for bare TiO_2 and prepared Ag/TiO_2 samples and **(b)** the charge separation and transfer mechanism at UV irradiated Ag/TiO_2 thin film.

The improvement of the photocatalytic activity after Ag NPs deposition could be explained by the proposed mechanism shown in **Figure** 8.5b. Exposing Ag/TiO_2 thin film first led to the formation of e$^-$ and h$^+$. Electrons at conduction band of TiO_2 were injected into the Ag NPs owing to the fact that Fermi level of Ag NPs is lower than the conduction band of TiO_2.[208,238] Additionally, the effect of electric field localized between Ag NPs and TiO_2 might have accelerated electron transfer.[201] As a consequence, e$^-$ and h$^+$ seemed to find more chance to react with O_2 and H_2O molecules in the reaction medium. The transfer of electrons to the opposite direction (from Ag NPs to conduction band of TiO_2) might not be possible due to the Schottky barrier formed at Ag-TiO_2 interface.[201]

The stability and reusability of photocatalysts are also an important issue for practical applications. In order to show the stability of Ag(1min)/TiO_2 thin film, five consecutive photocatalysis tests (use, wash and re-use) were performed. After each photocatalytic activity test cycle, the sample was rinsed with water and re-used again. It can be clearly seen in **Figure** 8.6 that the photocatalytic bleaching efficiency of Ag(1min)/TiO_2 thin film photocatalyst remained almost constant. This confirmed the stability and reusability of Ag(1min)/TiO_2 thin film photocatalyst.

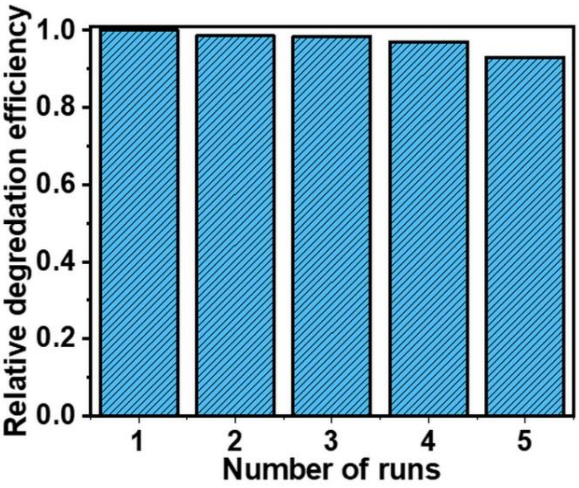

Figure 8.6. Reusability of Ag(1 min)/TiO_2 thin film photocatalyst for degradation of MB (All values are normalized with respect to the degradation of efficiency of Ag(1 min)/TiO_2 under UV irradiation for 240 min).

8.4 Conclusion

In summary, we have prepared Ag/TiO_2 photocatalytic hybrid structures (TiO_2 thin film decorated with Ag NPs) by photocatalytic deposition of Ag^+ ions (under low-intensity UV irradiation) and studied corresponding structural and photocatalytic properties. Decorating TiO_2 thin film with Ag NPs with a surface coverage of 1–4% significantly enhancement photocatalytic activity of TiO_2 thin film. It is believed that electron trapping Ag NPs suppressed the recombination of electron-hole pairs. Additionally, we have demonstrated that the deposition of excessive amount Ag NPs on TiO_2 thin film surface resulted a decrease in the photocatalytic activity (lower than the activity of bare TiO_2), which might arise due to the blocking UV light incoming to the TiO_2 thin film surface.

Acknowledgements

The authors thank Stefan Rehders for his continuous support of the sputtering setup.

Supporting Information

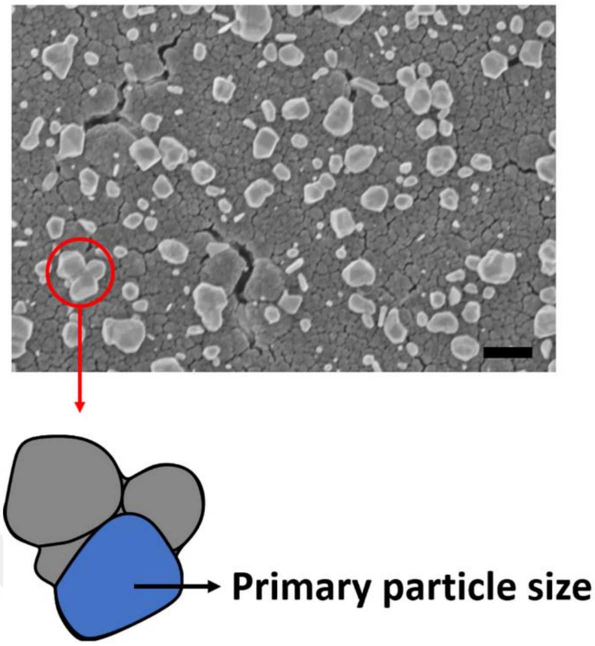

Figure 8.7. Schematic representation for the calculation of max. and min. size of the Ag NPs from SEM image (Scale bar: 400 nm).

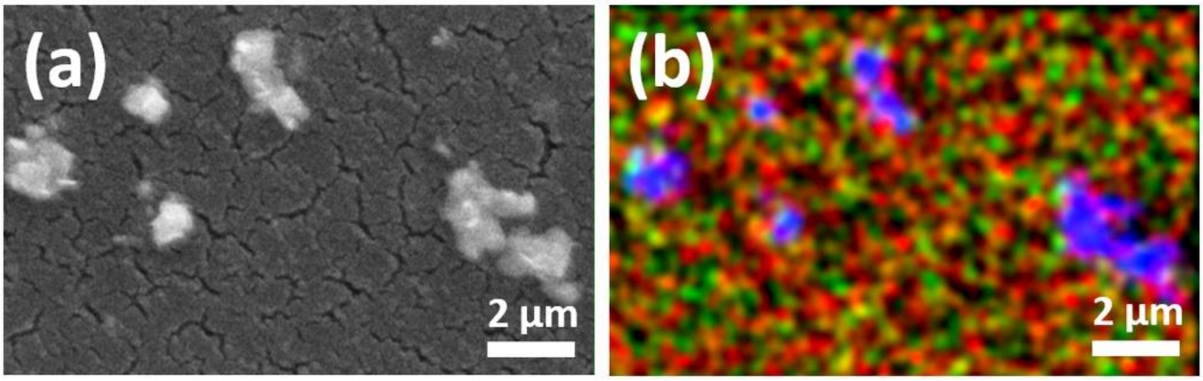

Figure 8.8. **(a)** SEM image of Ag NPs on TiO_2 thin film surface and **(b)** EDX compositional mapping (green, red and blue areas represent the presence of Ti, O, and Ag, respectively).

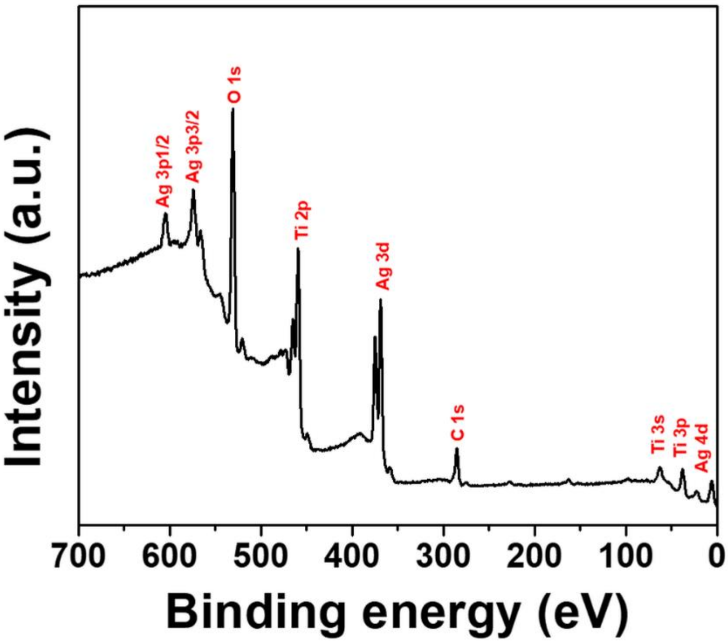

Figure 8.9. XPS wide scan energy spectrum of Ag(1min)/TiO_2 thin film.

Table 8-1. Kinetics rate constants of photocatalytic degradation of MB by prepared thin film photocatalysts

Photocatalysts	Rate Constant (s^{-1})
Bare TiO_2	3.8 x 10^{-3}
Ag(1min)/TiO_2	6.5 x 10^{-3}
Ag(2min)/TiO_2	6.3 x 10^{-3}
Ag(3min)/TiO_2	2.9 x 10^{-3}
Ag(5min)/TiO_2	2.7 x 10^{-3}

The kinetic rate constants (k), calculated from the rate equation $\ln(C/C_0)=kt$ where C_0 and C are the reaction and initial concentrations of MB at time (t) respectively. The linear regression plots fitted, from which the slopes of each plot were calculated and used to obtain the kinetic rate constants.[104]

ACS APPLIED NANO MATERIALS

August 2018
Volume 1
Number 8
pubs.acs.org/acsanm

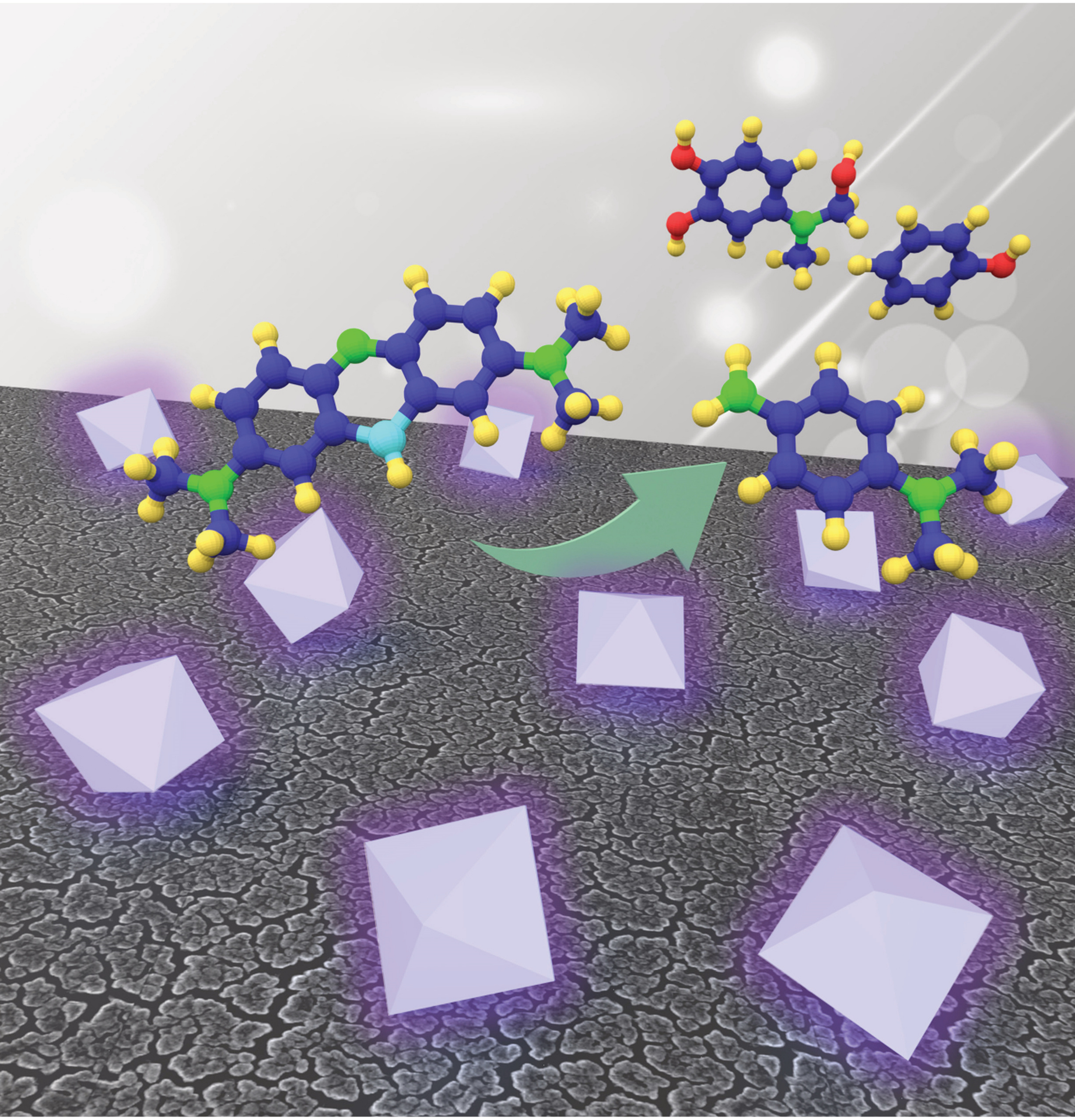

ACS Publications
Most Trusted. Most Cited. Most Read.

www.acs.org

9 Role of UV Plasmonics in the Photocatalytic Performance of TiO_2 Decorated with Aluminum Nanoparticles

This chapter is based on an article published in ACS Applied Nano Materials.[169]

Reprinted with permission from Muhammad Zubair Ghori, Salih Veziroglu, Alexander Hinz, Bill Brook Shurtleff, Oleksandr Polonskyi, Thomas Strunskus, Jost Adam, Franz Faupel, Oral Cenk Aktas
ACS Appl. Nano Mater. 1 (2018) 3760–3764.
The article is available via the internet at https://doi.org/10.1021/acsanm.8b00853

Abstract

We present a facile method, combining sputtering and gas aggregation techniques, to prepare a photocatalytic TiO_2 thin film decorated with stable aluminum plasmonic nanoparticles (Al NPs) to reveal the localized surface plasmon resonance (LSPR) effect on TiO_2 photocatalysis under UV irradiation. We demonstrate for the first time the negative and positive influences of LSPR on UV photocatalysis by irradiating Al NPs/TiO_2 hybrid structures at two different UV wavelengths: both at and above the plasmonic absorption of Al NPs. These findings open the door to design low-cost Al/TiO_2 photocatalytic hybrid surfaces that function in a broad spectral range from deep-ultraviolet to visible wavelengths.

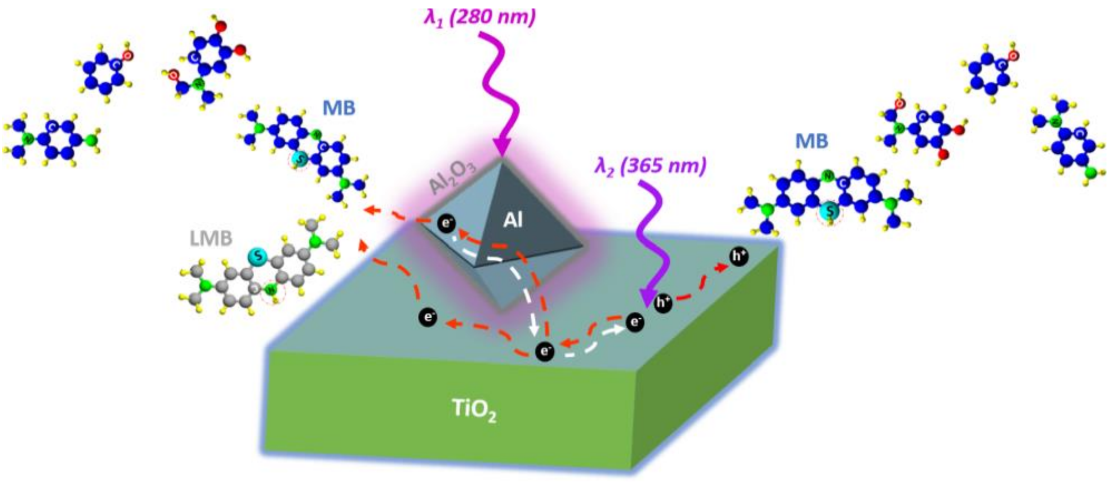

9.1 Introduction

Various methods have been proposed to enhance the photocatalytic performance of TiO_2, such as doping, preparing TiO_2 composite structures (incorporating metals or oxides), or decorating TiO_2 with plasmonic metal nanoparticles (NPs). Among others, plasmonic photocatalysis has been garnering enormous interest.[239–242] Basically, plasmonic photocatalysis utilizes localized surface plasmon resonance (LSPR) of metallic NPs, mainly gold (Au) and silver (Ag), to enhance the photocatalytic performance of TiO_2.[243] Recently, aluminum (Al) has attracted considerable attention in plasmonic photocatalysis research as an alternative plasmonic material with an extended response into the deep ultraviolet (UV).[244,245]

Besides various successful studies demonstrating enhancement of the photocatalytic performance of TiO_2 by LSPR, recent studies have shown the simultaneous existence of both pros and cons of LSPR in photocatalysis.[43] It has been shown that for TiO_2 decorated with Au NPs, hot electrons injected from Au to TiO_2 by LSPR may overcome the Schottky barrier (SB) and flow back into the TiO_2 under mixed UV and visible (Vis) irradiation. These electrons may compensate for those transferred from TiO_2 to Au NPs and promote the recombination of electron–hole pairs.[43] This can be considered as the negative effect of LSPR on photocatalysis. Because Au and Ag exhibit plasmonic properties in the Vis region of the spectrum, which is significantly far away from the absorption edge of TiO_2, a selective activation of such noble-metal NPs by Vis or TiO_2 by UV irradiation appears to be useful to reveal the pros and cons of LSPR in photocatalysis. On the other hand, such a systematic study is not trivial in the case of Al NPs because both, Al NPs and TiO_2 are active in the UV range. In addition, with respect to noble metallic NPs, it is challenging to get reproducible plasmonic properties in the case of Al NPs because of the difficulty in controlling the thickness of the surrounding oxide cover.[246]

9.2 Result and Discussion

Here, we present a facile method to prepare a photocatalytic TiO_2 thin film decorated with stable plasmonic Al NPs to reveal the LSPR effect on photocatalysis under UV irradiation. We demonstrate for the first time the negative and positive influences of LSPR on Al/TiO_2 photocatalysis by irradiating Al NPs/TiO_2 hybrid structures at two different UV wavelengths (both at and above the plasmonic absorption of Al NPs). The wavelength dependence of photocatalysis reveals two different mechanisms contributing to TiO_2 photocatalysis. An understanding of both of these mechanisms is crucial for designing cost-effective and broad-band (deep-UV to Vis) efficient photocatalytic surfaces.

Following sputter deposition of a TiO_2 thin film, a gas aggregation source (GAS, as shown schematically in **Figure** 9.1a) [247,248] was used to decorate the deposited film with Al NPs.

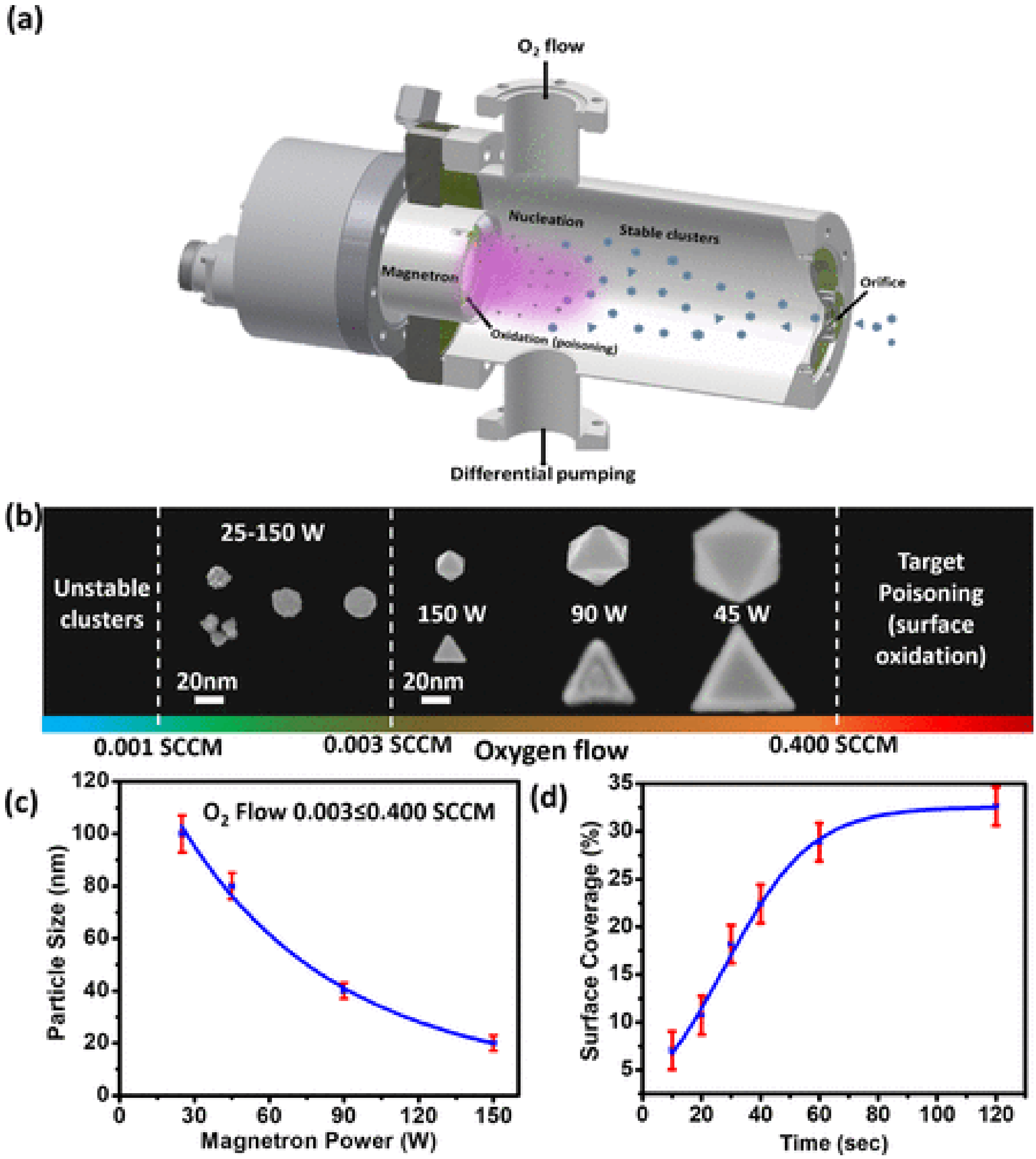

Figure 9.1. **(a)** Schematic representation of the GAS used to produce Al NPs. **(b)** Schematic representation of the influence of the O$_2$ flow rate on the shape and size of Al NPs (images of single NPs are implemented from SEM images given in **Figure** 9.6 and **Figure** 9.7). **(c)** Primary particle size of Al NPs as a function of the magnetron power. **(d)** Surface coverage of Al NPs as a function of the deposition time (details are provided in **Figure** 9.8).

In addition to argon (Ar), we introduced an extremely low amount of oxygen (O$_2$) during sputtering to promote Al cluster nucleation by binding O$_2$ to sputtered Al atoms.[248–250] It is known that Al–O binding is quite stable in comparison to the low dimer binding energy of Al–Al.[251] While at 0.001–0.400 SCCM O$_2$ flow range we were able to produce Al clusters (confirmed by both, in situ quartz crystal microbalance monitoring (**Figure** 9.5) and scanning electron microscopy (SEM) analysis (**Figure** 9.1b and **Figure** 9.6 and **Figure** 9.7)), at higher O$_2$ flow rates (>0.400 SCCM), we did not observe any cluster formation (**Figure**

9.1b), which might be attributed to target poisoning (oxidation). The proposed method allows the synthesis of stable Al NPs of well-controlled size (**Figure** 9.1c) and surface coverage (**Figure** 9.1d) over a wide range of O_2 flow rates.

Transmission electron microscopy (TEM) analysis showed that most of the deposited Al NPs (>95%) had a projected rhombus shape (**Figure** 9.2a) and a size of about 20 nm.

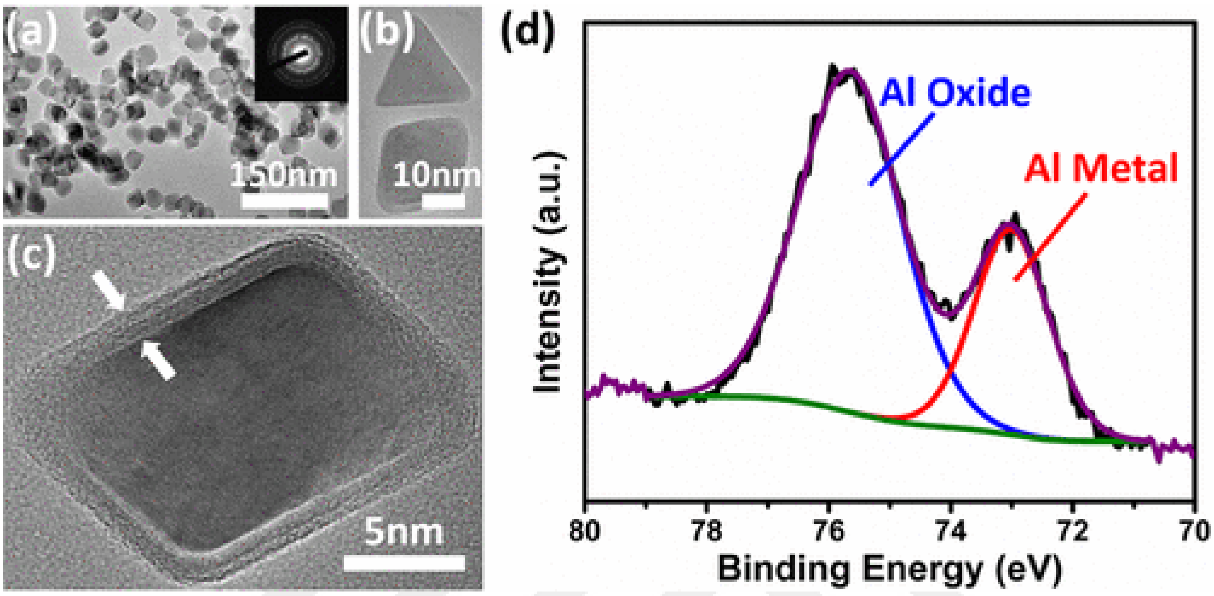

Figure 9.2. TEM images of **(a)** Al NPs deposited at a magnetron power of 150 W for 2 min (SAED analysis is given in the inset) and **(b)** octahedral and truncated triangular bipyramidal Al NPs. **(c)** HRTEM image of an octahedral Al NP (arrows indicate the oxide shell). **(d)** XPS spectrum of Al NPs.

The selected-area electron diffraction (SAED) rings could be indexed as face-centered-cubic Al. Further investigation by SEM showed that a majority of Al NPs have octahedral morphology (exhibiting a projected rhombus shape in TEM micrographs in **Figure** 9.2c), as shown in **Figure** 9.7 (the mechanism behind the coexistence of different particle morphologies is discussed in the Supporting Information) and the rest exhibit a truncated triangular pyramidal structure (exhibiting a projected triangular shape in TEM micrographs; **Figure** 9.2b). **Figure** 9.2c shows the high-resolution (HRTEM) image of a single Al NP with an octahedral structure exhibiting a metallic core (proven by the lattice fringes) and the surrounding shell of stable oxide about 2 nm thick. This oxide shell protects Al NPs from further oxidation and agglomeration. An X-ray photoelectron spectroscopy (XPS) spectrum (**Figure** 9.2d) verified the coexistence of an ultrathin oxide shell and the metallic Al core (more details are given in the Supporting Information).[251]

The spectral response of Al NPs deposited on quartz substrates (three different types of surfaces composed of 20 ± 3, 40 ± 3, and 80 ± 5 nm Al NPs) was calculated (as shown in detail in **Figure** 9.9) and measured as a function of increasing particle size. As is clearly seen in the calculated spectra, the presence of a 2 nm surface oxide redshifts the plasmon resonance significantly. While 20 nm Al NPs exhibited a sharp plasmon peak, the increase in the particle size led to redshifts and broader absorption spectra (**Figure** 9.3c,d).

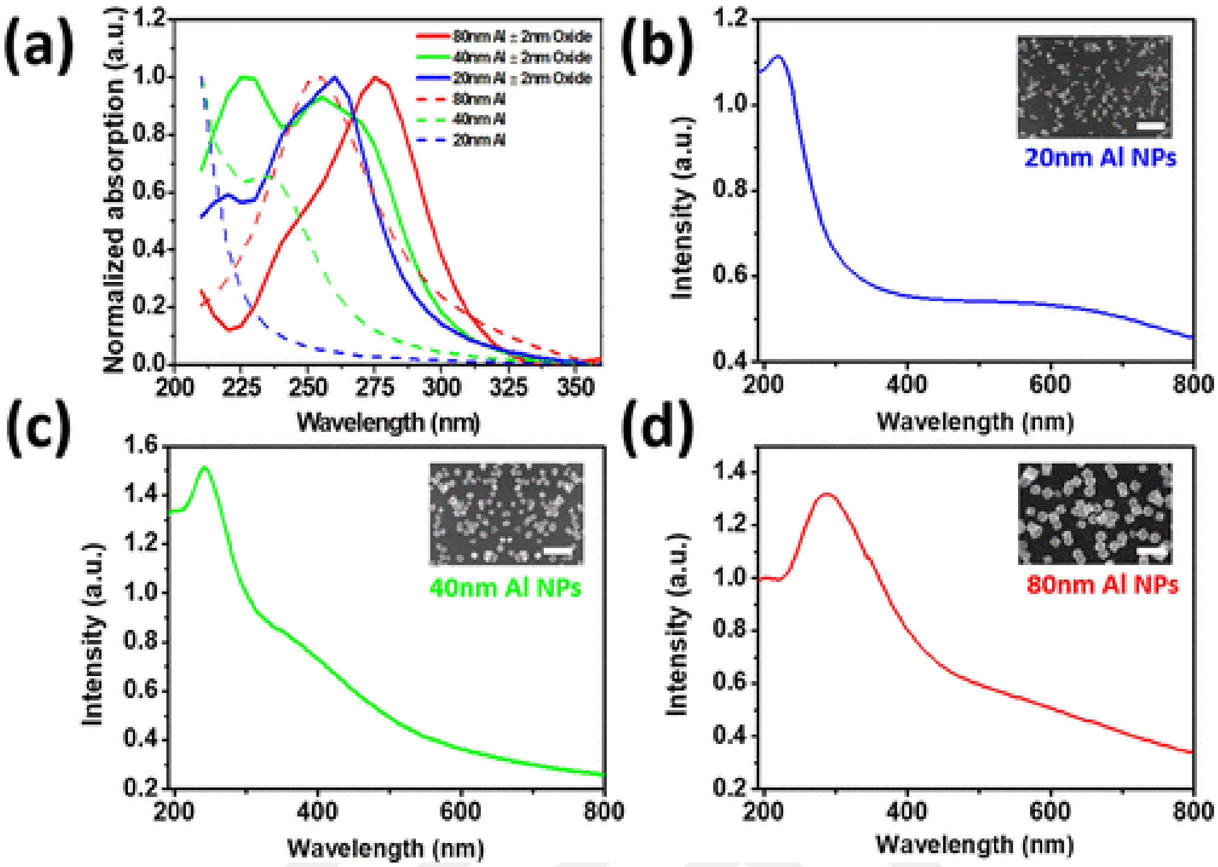

Figure 9.3. **(a)** Simulated (with and without 2 nm oxide cover) and **(b–d)** experimental absorption spectra of Al NPs with primary sizes of 20 ± 3, 40 ± 3, and 80 ± 5 nm, respectively (the insets show SEM images of the corresponding Al NPs with a scale bar of 200 nm).

The difference between the calculated and experimental spectra may arise because of particle–particle interactions. For instance, in SEM images (given as insets in **Figure** 9.3b–d), Al NPs are seen in the form of self-assembled aggregates rather than isolated NPs (details on the plasmonic properties of deposited Al NPs are further discussed in the Supporting Information).

We deposited Al NPs on sputter-deposited TiO_2 films to reveal the NP influence on photocatalysis (while keeping the surface coverage of Al NPs as comparable as possible at 30–35%, the particle size was systematically altered, as presented in **Figure** 9.10). A diluted aqueous solution of methylene blue (MB) was spin-coated on prepared surfaces, and the photocatalytic reaction was monitored by a change of the MB absorbance at 580 nm under UV irradiation (using UV-light-emitting diodes operating at wavelengths of 280 and 365 nm).[23] Parts a and b of **Figure** 9.4 show photocatalytic bleaching of MB on bare and Al NP-decorated TiO_2 layers at two different wavelengths, respectively.

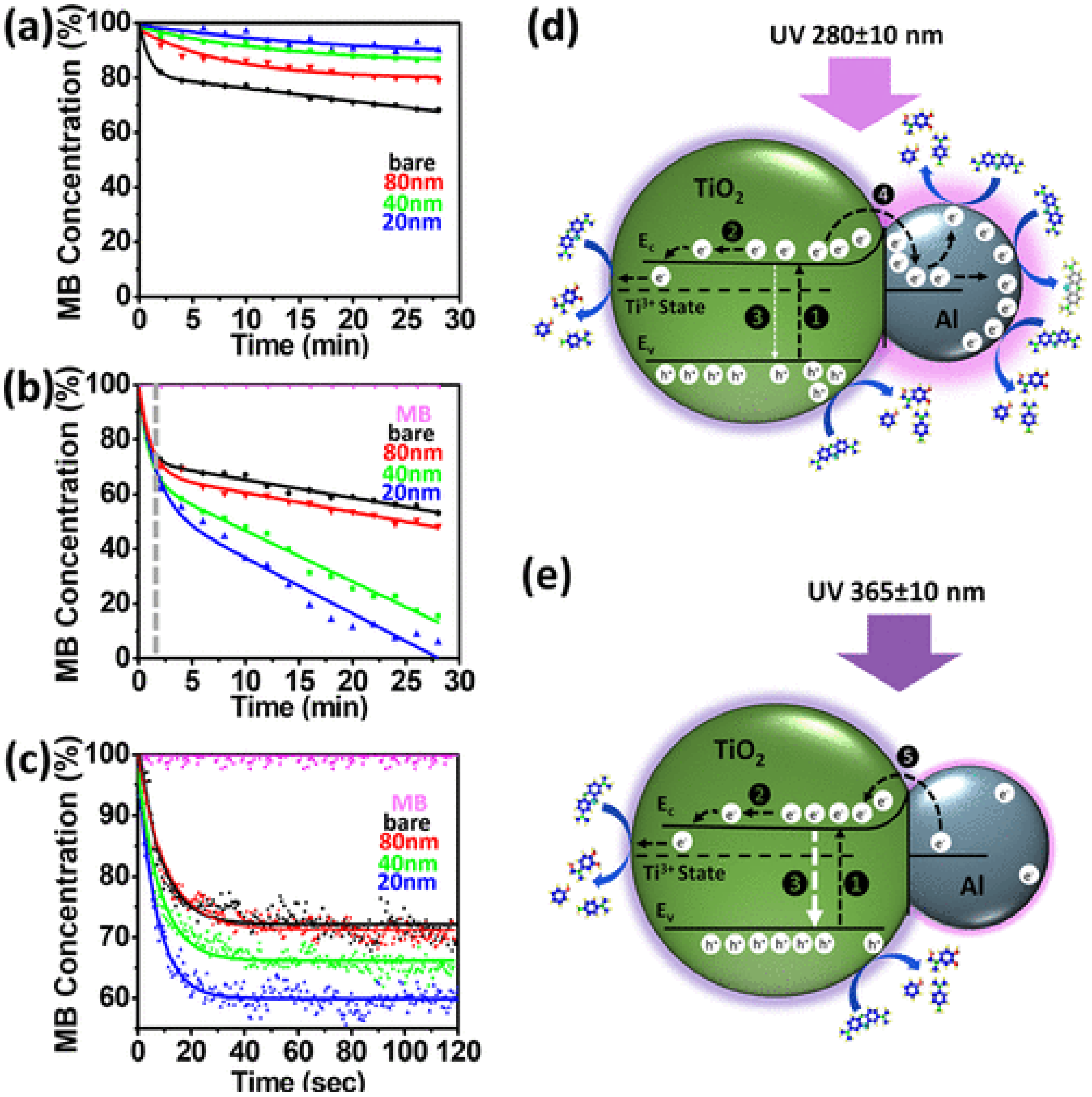

Figure 9.4. **(a)** Photocatalytic bleaching of MB at 365 ± 10 nm UV irradiation by Al/TiO_2 hybrid structures. Photocatalytic bleaching of MB at 280 ± 10 nm UV irradiation **(b)** at long term **(c)** at short term by Al/TiO_2 hybrid structures. Main mechanisms observed in photocatalytic bleaching of MB by Al/TiO_2 hybrid structures at **(d)** 280 ± 10 and **(e)** 365 ± 10 nm. (1) Electron–hole generation. (2) Reduction of Ti^{4+} cations to the Ti^{3+} state. (3) Recombination. (4) Trapping of electrons by Al NPs. (5) Injection of electrons by Al NPs. (4 and 5 coexist, but depending on the corresponding wavelength, one of them dominates. Schematics only show the dominating mechanism by considering an effective electron transfer through the thin oxide shell surrounding Al NPs, as discussed in the Supporting Information)

Plasmonic Al NPs/TiO_2 hybrid layers exhibited lower photocatalytic activity at 365 nm UV irradiation in comparison to the bare TiO_2 layer (**Figure** 9.4a). In contrast, the photocatalytic performance of plasmonic Al NPs/TiO_2 hybrid layers significantly increased at 280 nm UV irradiation (**Figure** 9.4b). A TiO_2 layer decorated with 20 nm Al NPs exhibited the highest photocatalytic activity. Honda et al. similarly demonstrated a significant enhancement of TiO_2 photocatalysis by incorporating Al NPs.[252] On the other hand, they reported a recovery in the MB absorbance after switching off the UV irradiation. We also observed a similar recovery (**Figure** 9.4b, indicated with the dashed line), and this may be attributed to the conversion of MB to its colorless form leuco-MB (LMB).

Recently, we showed a detailed analysis of such a phenomenon, [244] where decomposition of a 60–80-nm-thick MB layer even took several minutes rather than seconds as Honda et al. claimed.[253] Therefore, the sudden change in the MB absorbance (within seconds) cannot be described as photocatalytic bleaching. As shown in **Figure** 9.4c, the absorption went down drastically within 20 s on the TiO_2 layer decorated with 20 nm Al NPs (in situ UV–vis analysis), which is even much faster than the time interval reported by Honda et al.[253] Thus, to monitor irreversible photocatalytic mineralization of MB, longer irradiation and observation time periods are mandatory.

The difference between the photocatalytic performance at 365 and 280 nm UV irradiation can be explained by two different mechanisms, as depicted schematically in **Figure** 9.4d. At both wavelengths, electron–hole pairs are generated (mechanism 1, **Figure** 9.4d,e) because in both cases bare TiO_2 exhibits photocatalytic activity (**Figure** 9.4a,b). The low photocatalytic activity of the deposited TiO_2 layer can be explained by the limited thickness and the lack of a high surface area (due to the lack of dense crack networks in such thin layers, as we presented recently.[14]

Photogenerated electrons can reduce Ti^{4+} cations to the Ti^{3+} state, and this may be followed by the degradation of MB (by directly attacking acceptors, as shown by mechanism 2, **Figure** 9.4d,e).[254] On the one hand, some photogenerated electrons from TiO_2 may overcome the SB and be trapped and localized in adjacent Al NPs (mechanism 4, **Figure** 9.4d).[43] These electrons may have the chance to gather on the surface of Al NPs (LSPR-induced movement to the surface) and enhance the degradation of MB by promoting interaction with surrounding acceptors (**Figure** 9.4d). On the other hand, some of trapped electrons can be injected back to TiO_2 (mechanism 5, **Figure** 9.4e), which significantly triggers electron–hole recombination, [43] thus negatively influencing the photocatalytic effect. At 280 nm UV irradiation, mechanism 4 seems to dominate because the irradiation wavelength matches well with the plasmon absorption of Al NPs. However, at 365 nm UV irradiation, the effect of LSPR is not strong enough to trigger the movement of trapped electrons to the surface of Al NPs. Rather, mechanism 5 (injection of electrons back to TiO_2) possibly dominates and reduces the overall photocatalytic activity. It should be kept in mind that in both cases (280 and 365 nm irradiation) mechanisms 4 and 5 coexist, but depending on the corresponding wavelength, one of them dominates.

One can think about the shading effect of Al NPs on the TiO_2 surface, thus reducing the UV-light-irradiated area during 365 nm UV irradiation. However, then 80 nm Al NPs should have exhibited the lowest photocatalytic effect; conversely, at 365 nm UV irradiation, 80 nm Al NPs exhibited slightly higher photocatalytic performance in comparison to 20 and 40 nm Al NPs. This may be explained by the injection of some electrons into Al NPs (mechanism 4, **Figure** 9.4d) because the red-shifted plasmon peak of 80 nm Al NPs provides relatively higher absorption (in comparison to 20 and 40 nm Al NPs) at 365 nm, but in all cases, the second mechanism seems to dominate under UV irradiation at a wavelength slightly further from the plasmonic absorption peak of Al NPs. These findings are in accordance with those of Lin et al., who similarly presented two mechanisms by selectively activating Au NPs and TiO_2 using two different wavelengths of 525 and 365 nm, respectively.[43]

9.3 Conclusion

The research on plasmonic photocatalysis has progressed steadily, but still the underlying mechanism has not yet been fully understood. Here, we could demonstrate for the first time the coexistence of effects both negative (injection of electron from Al NPs) and positive (trapping of electrons by Al NPs) of UV plasmonics on the photocatalytic activity of TiO_2. We are aware that LSPR can influence the photocatalysis by various mechanisms, including sensitization (shifting absorption of TiO_2), tuning band-gap energy (e.g., SB barrier formation), and radiative and nonradiative decays, and most of the time these mechanisms can coexist. Therefore, the current study assists in understanding the mechanism of UV plasmonic photocatalysis under UV irradiation, which may help in designing cheaper and highly efficient photocatalysts functioning at a broad spectral range.

Acknowledgements

The simulation for the work described in this paper was supported by the DeiC National HPC Centre, Southern Denmark University. M.Z. Ghori acknowledges the Graduate Center and Federal State Funding, Christian-Albrechts-University of Kiel, for providing funding for his Ph.D. study. The authors thank Stefan Rehders for his continuous support of the sputtering setup.

Supporting Information

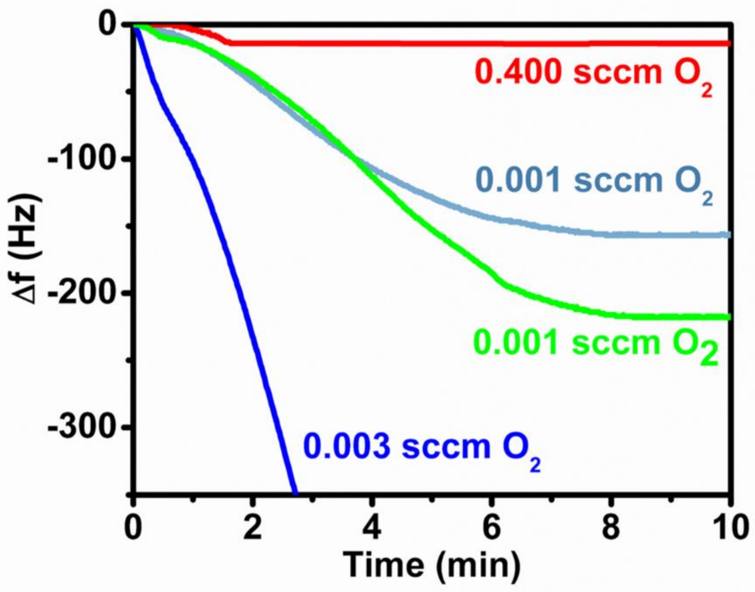

Figure 9.5. In-situ deposition rate analysis by monitoring the change in the resonance frequency of quartz crystal microbalance (QCM) at different oxygen flow rates.

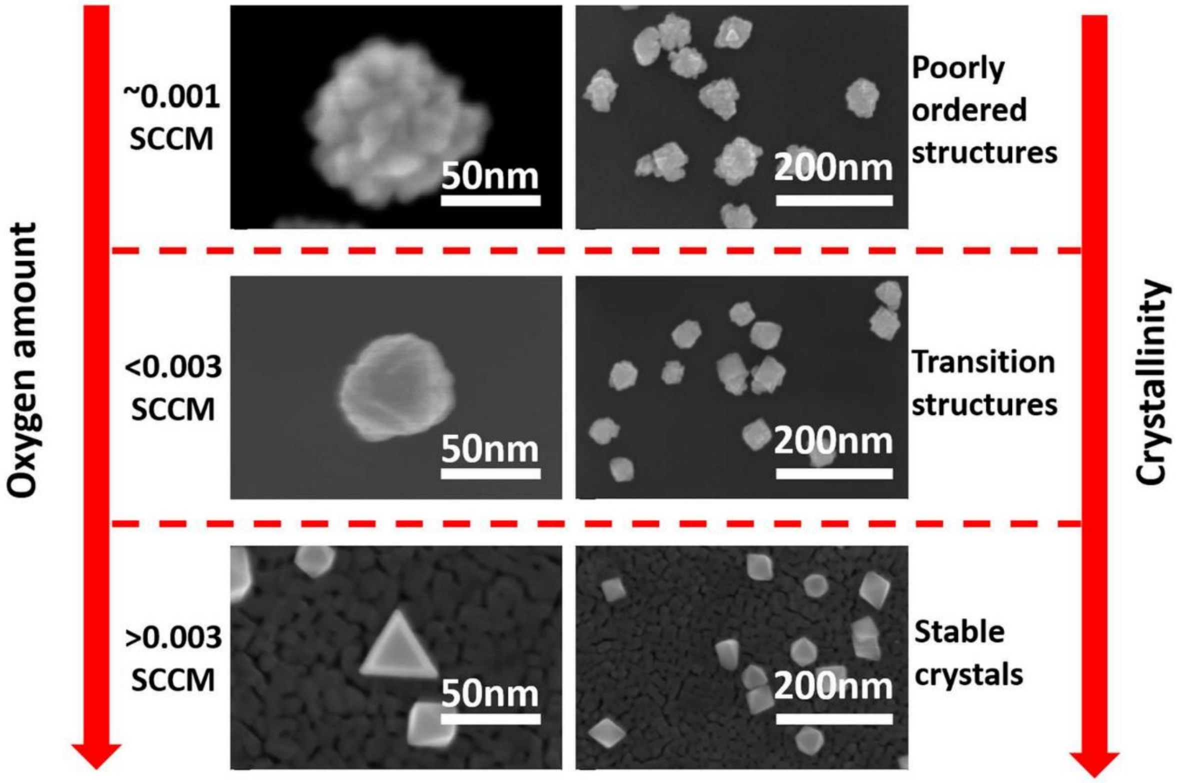

Figure 9.6. SEM images of Al NPs at different oxygen flow rates (oxygen flow vs. crystallinity correlation).

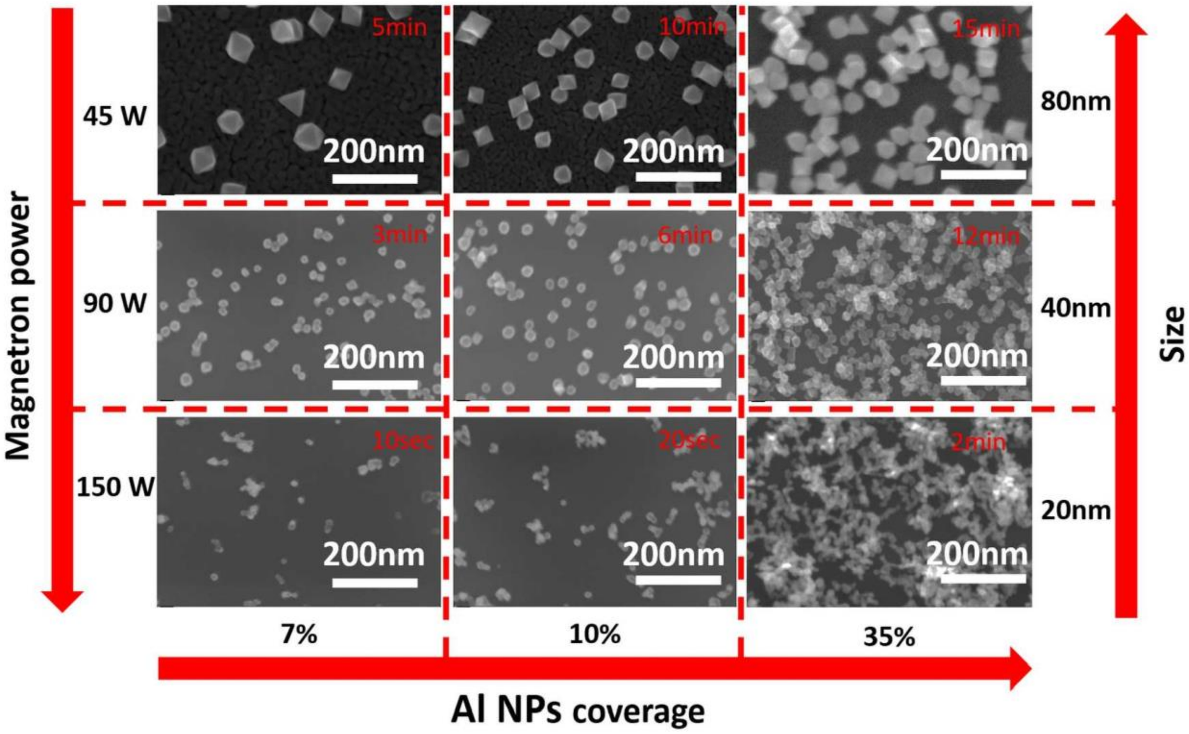

Figure 9.7. SEM images of Al NPs prepared at different magnetron power and deposition times (particle size and coverage)

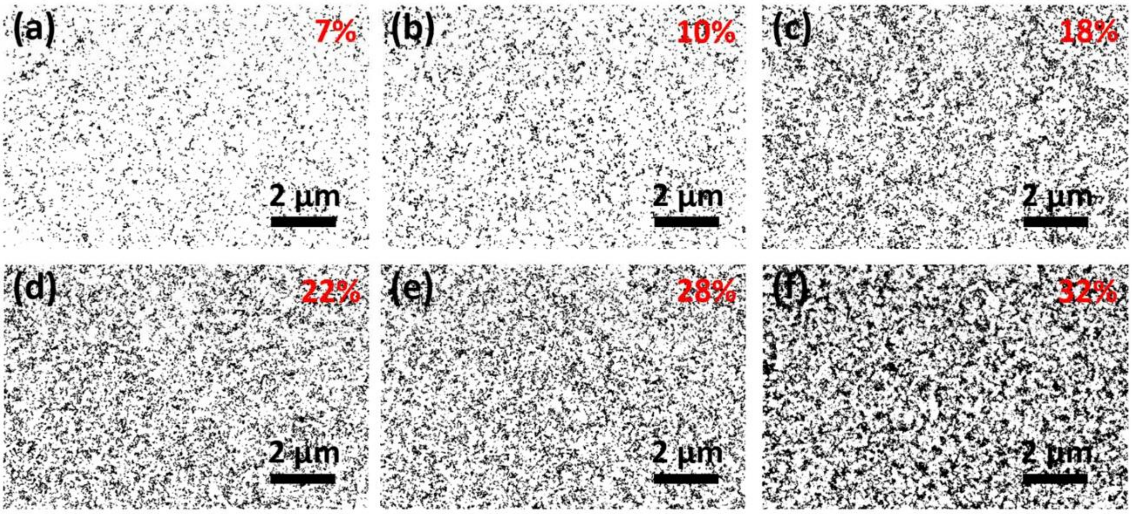

Figure 9.8. **(a-f).** Binary (B/W) SEM images showing the gradual increase in the Al NPs surface coverage at time 10 s, 20 s, 30 s, 40 s, 60 s and 120 s, respectively.

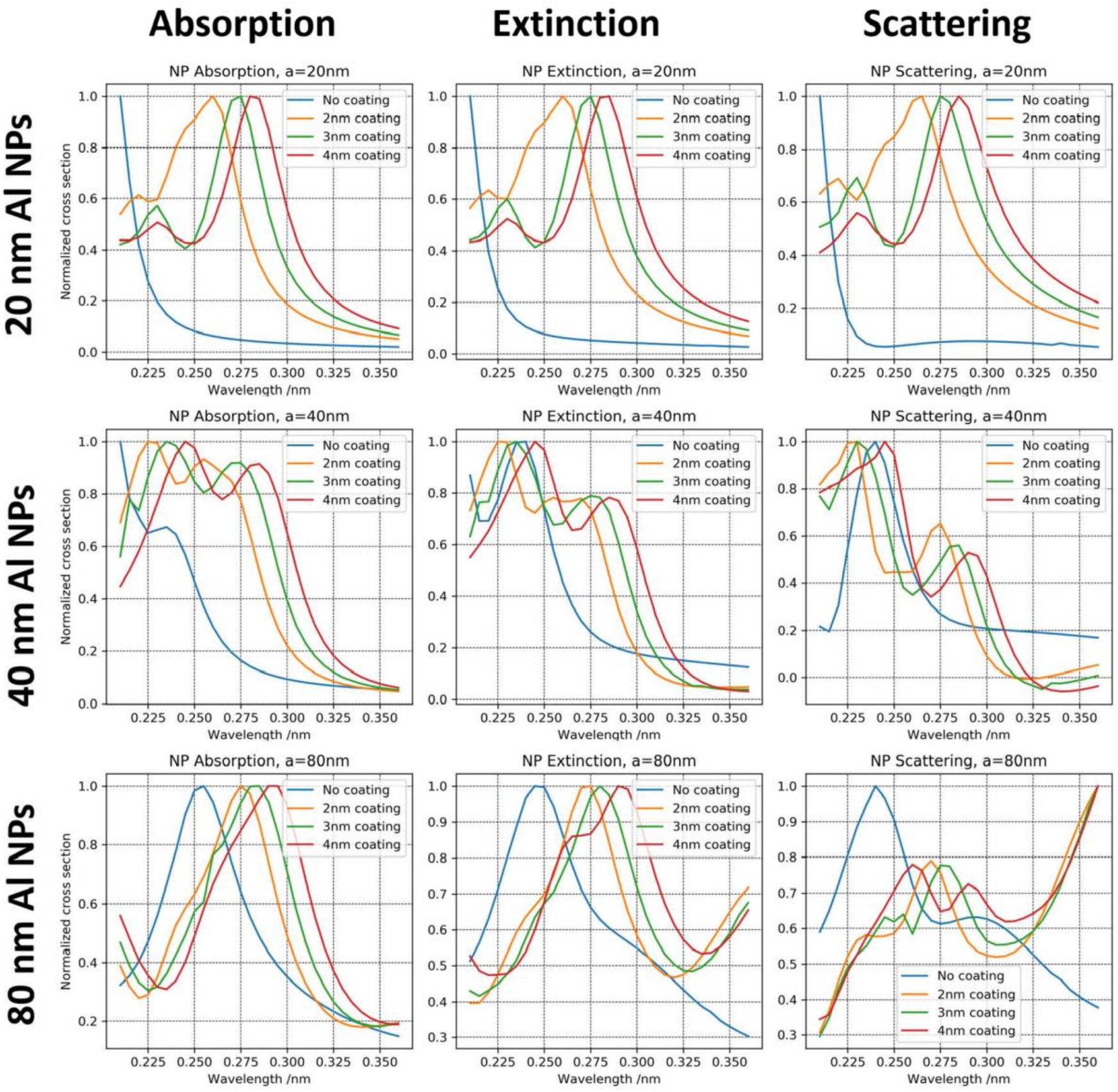

Figure 9.9. Simulated absorption, extinction and scattering cross sections of octahedral Al NPs on a SiO_2 surface, with Al_2O_3 coatings of varying thickness (see Numerical Methods for details).

Numerical Methods: Since particle scattering and particle plasmonics phenomena are largely governed by the particle scattering, absorption and hence extinction cross section, we modelled these quantities in order to support our experimental findings. To this end, we performed finite-element modelling (FEM) simulations with the commercially available software COMSOL Multiphysics. The NPs on the surface are surrounded by perfectly matched layers (PML) to mimic scattering boundary conditions in all cartesian directions, and a two-port arrangement excites the structure from the top by normally incident, linearly polarized light of various frequencies. By a two-step simulation procedure, we extract the scattered electromagnetic field, that is, the electromagnetic field perturbation induced by the Al NP, from the excited total electromagnetic field. With the resulting scattering Poynting vector $\boldsymbol{S}_{sc}$ we calculate the scattering cross section $\boldsymbol{\sigma}_{\mathrm{sc}}$ by integrating $\boldsymbol{S}_{sc}$ over the closed particle surface, while the absorption cross section $\boldsymbol{\sigma}_{\mathrm{abs}}$ is given by the (particle-)volume integral over the power loss density. Finally, the extinction cross section $\boldsymbol{\sigma}_{\mathrm{ext}}$ comprises the sum of the preceding ones: $\boldsymbol{\sigma}_{\mathrm{sc}} + \boldsymbol{\sigma}_{\mathrm{abs}} = \boldsymbol{\sigma}_{\mathrm{ext}}$. All quantities are usually normalized by the incident light energy.

Note: It might be possible to produce Al NPs without any oxide layer under vacuum conditions but unfortunately such reactive metal prompt to form a protective oxide layer when exposed to the atmosphere (highly reactive with oxygen). The spectra shown in **Figure** 9.3b-d contains protective oxide layer with thickness around 2 nm (proven by TEM analysis). We have used simulation method to predict the absorption spectrum of Al NPs without any oxide cover but it was not possible to show ex-situ absorption spectrum of Al NPS without any oxide cover after taking out of vacuum into the atmosphere.

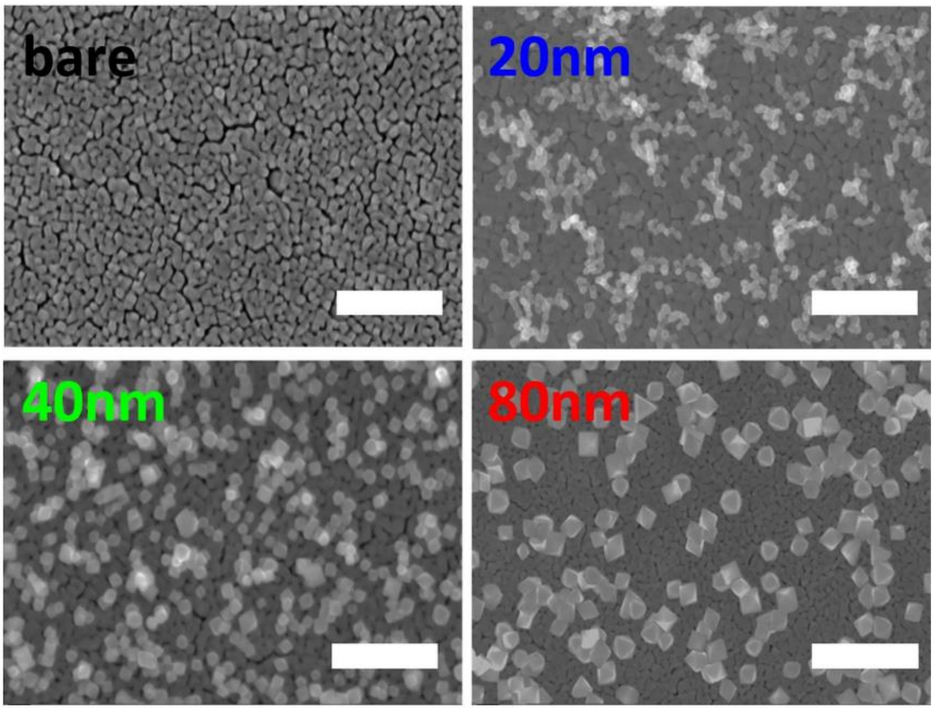

Figure 9.10. SEM images of bare and Al NPs (with primary size of 20±3 nm, 40±3 nm and 80±5 nm) decorated TiO_2 films (scale bar 300 nm).

10 PdO Nanoparticles Decorated TiO_2 Film with Enhanced Photocatalytic and Self-Cleaning Properties

This chapter is based on an article published in Materials Today Chemistry.[255]

Reprinted with permission from Salih Veziroglu, Jaeho Hwang, Jonas Drewes, Igor Barg, Josiah Shondo, Thomas Strunskus, Oleksandr Polonskyi, Franz Faupel, and Oral Cenk Aktas,
Materials Today Chemistry, 16 (2020) 100251
The article is available via the internet at https://doi.org/10.1016/j.mtchem.2020.100251

Abstract

Magnetron sputtering and gas aggregation source (GAS) approaches were combined for the preparation of columnar TiO_2 structures decorated with PdO nanoparticles (NPs). Totally solvent-free synthesis approach provides a good control of surface coverage, size, morphology, and stoichiometry of PdO NPs in comparison to wet-chemical synthesis methods. X-ray photoelectron spectroscopy (XPS) analysis showed that the heat treatment led to formation of a mixed oxide state PdO/PdO_2 on TiO_2 layer. A steady equilibrium between PdO (oxidation by free and adsorbed •OH) and PdO_2 (reduced by trapped photogenerated electrons) phases under UV irradiation seems to provide an efficient electron-hole pair separation. Such robust PdO-TiO_2 thin films have a strong potential for use as photocatalytic and self-cleaning windows or similar out-door technical surfaces.

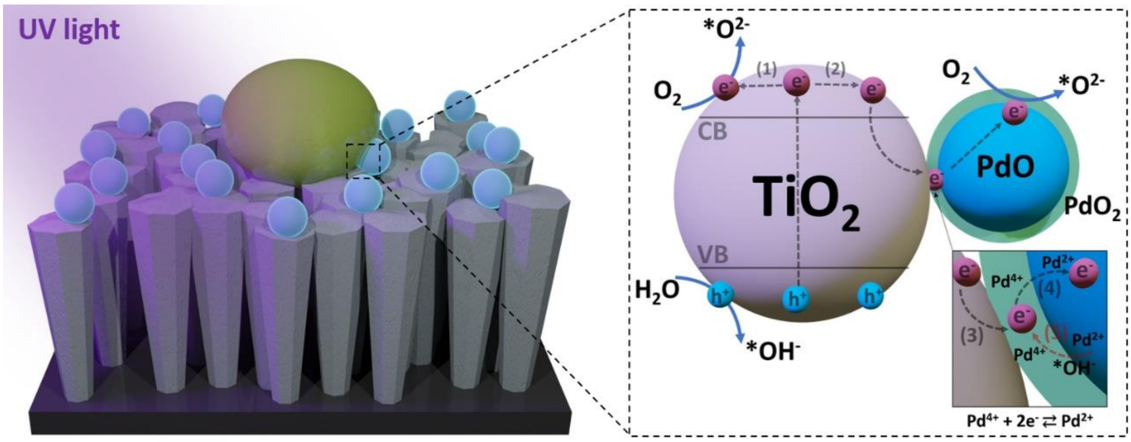

10.1 Introduction

Titanium (IV) oxide (TiO_2) has been used in diverse products, including paints, coatings, glazes, paper, inks, fibers, foods, pharmaceuticals, and cosmetics.[3,256–258] It is also the most extensively used material for photocatalytic and photovoltaic applications owing to its high conversion efficiency, stability, chemical inertness, and low cost.[86,259] Today TiO_2 based photodegradation is accepted as one of the most effective technologies for environmental remediation.[260] Especially the use of colloidal TiO_2 particles for the treatment of various kinds of wastes have been shown by various studies, as well as technology applications.[1,258] On the other hand, in some specific applications, such as water treatment, air, and odor cleaning, the use of TiO_2 in the thin-film form (rather than colloid form) is preferable because of its continuous nature and advantage in the catalyst regeneration process.

Besides various advantages of TiO_2, its fast recombination rate (of photogenerated electron–hole pair) and large bandgap limits its use as an effective photocatalyst.[7,135,261,262] For instance, in the case of using TiO_2 in the thin-film form, the limited surface area (outperformed by their colloidal counterparts) becomes an additional restriction.[263] Recently we proposed a simple approach to enhance the surface area of TiO_2 thin films by inducing nanocrack networks in sputter-deposited films.[14] On the other hand, charge separation in such TiO_2 thin films should also be improved to foster their use in photocatalytic applications.

Various approaches, for instance, doping, metal loading, and/or introducing a heterojunction, have been proposed to efficiently separate the photogenerated electron–hole pairs in TiO_2.[15,113,144] Among all proposed methods, creating a heterojunction (the interface between two different semiconductors with unequal band structure can result in band alignment) by incorporating a second oxide photocatalyst with TiO_2 has been proved to be one of the most promising ways for achieving a high photocatalytic performance because of its feasibility and effectiveness for the spatial separation of electron–hole pair.[264–266] For instance, recently we demonstrated that TiO_2–CeO_2 hybrid nanostructures exhibited excellent photocatalytic activity in comparison to bare TiO_2 and CeO_2 structures used separately.[183] A number of studies have been carried out on the incorporation of metal oxides, such as CeO_2, WO_3, Fe_2O_3, ZnO, and PdO with TiO_2 to enhance the photocatalytic activity.[83,267,268]

In recent years, Pd and PdO catalysts have been extensively studied, and they are considered as effective catalysts, particularly for CO oxidation and CH_4 combustion.[269] They exhibit not only low volatility at high temperatures but also high catalytic activity at low temperatures. Incorporating PdO with other metal oxides, especially with TiO_2, also leads to superior photocatalytic properties, which attract the attention of environmental redemption applications.[22,53,270,271] Khojasteh et al. demonstrated that incorporating Pd and PdO can reduce the bandgap of TiO_2.[22] Zhou et al. showed that PdO–TiO_2 nanobelts heterostructures exhibited extremely high photoactivity toward the degradation of methylene blue (MB) and rhodamine B (RhB) under UV–Visible light irradiation, which was ascribed to the energy-level matching effect for PdO–TiO_2.[53] On the other hand, the reported synthesis route was composed of multiple steps, including coprecipitation and reduction processes, which limits its practical use and upscaling. Similarly, Ismail et al. reported that mesoporous PdO–TiO_2 nanocomposite showed excellent photocatalytic performance for methanol oxidation in comparison to the so-called "golden standard TiO_2–P25".[270] Although authors claimed a one-step and easy route (sol–gel) to synthesize such hybrid structures, the use of nonionic surfactant was emerging for avoiding the agglomeration of such highly active structures. Huang et al. reported that such an agglomeration problem became more critical by increasing the PdO content in PdO–TiO_2 hybrid structures.[271] For the synthesis of such PdO–TiO_2 hybrid structures, wet chemical methods have been extensively used due to their relative simplicity and low cost. On the other hand, such wet chemical methods have some limitations in controlling stoichiometry, size, and shape of such hybrid structures. In most of these synthetic approaches capping agents and surfactants are needed to control the particle size and to achieve a good dispersion, but additional steps, such as etching, and washing-filtering are needed to get rid of these organic residuals at the end. In addition, these approaches are more relevant preparation of colloidal photocatalyst particles. On the other hand, the difficulty in handling suspended photocatalyst particles (especially which are at nanoscale), and the interest in expanding the use of photocatalyst in air-cleaning applications, self-cleaning windows and similar out-door applications (walls, exterior parts of building, etc.) make it obvious that there is a need for robust and immobilized photocatalytic layers applicable to technical surfaces.

Herein, we propose a solvent-free gas-phase synthesis method for the preparation of PdO nanoparticles (NPs) decorated TiO_2 thin films. Basically, we combined pulsed magnetron sputtering and gas aggregation source (GAS) approaches for the preparation of columnar TiO_2 structures decorated with PdO NPs with controlled coverage, size, morphology, and composition. Prepared heterostructure exhibited superior photocatalytic performance and self-cleaning capability (in non-aqueous medium).

10.2 Materials and Methods

10.2.1 Preparation of PdO NPs Decorated TiO_2 Thin Films

First, TiO_2 thin films were deposited on silicon substrates using a custom-built DC magnetron sputtering system.[23] A titanium target (Ti-Goodfellow, 99.99%) with a 50 mm diameter and 6 mm thickness, attached to a balanced magnetron was sputtered at a discharge power of 90 W pulsed at a frequency of 50 kHz with 55% duty cycle. Argon (Ar) and oxygen (O_2) were used as sputtering and reactive gases, respectively. Flow rates of respective gases were monitored individually by sensitive mass flow controllers (MFCs) to keep a constant ratio of 250 sccm Ar and 10 sccm O_2. A base pressure of 5×10^{-5} Pa was achieved by a turbopump (Pfeiffer Vacuum, HiPace 400) backed by a dry mechanical pump (Agilent Technologies, SH-110) and monitored by an active Pirani gauge. Substrates were rotated at a speed of 10 rpm to achieve a uniform thickness. The deposition time was kept around 1 h to achieve a thickness of 300 nm, as described previously.[23]

Sputtering gas-aggregation source (GAS) was used to prepare PdO NPs inside a custom-built ultra-high vacuum chamber. The source and deposition chambers were pumped down to a base pressure of 4×10^{-6} mbar using a turbo molecular pump (Pfeiffer Vacuum, TMU 261) in combination with the scroll pump (Varian SH-110). As process gas Argon was introduced to the system, and the flow was regulated using a precise mass-flow controlling system (MKS, 1179B). The used magnetron was custom-made and equipped with a Pd target (99.95% Testbourne). The NPs were then produced in the GAS at a high flow rate (40 sccm Ar) and high pressure of 4×10^{-6}mbar to enable three-body collision of the sputtered Pd atoms and the gas molecules, which finally leads to cluster formation.[77] Three different samples were prepared by altering the deposition time (30s, 60s, and 90s) at a constant sputtering discharge power (100 W). The variation in deposition time affects mainly the surface of coverage of PdO NPs on the TiO_2. After the deposition of PdO NPs, all samples were subjected to heat treatment at 650°C. The heat treatment aimed: (1) crystallization of TiO_2 into anatase phase, (2) increasing the adhesion between deposited PdO NPs and TiO_2 thin film, and (3) full oxidation of PdO NPs (vanishing metallic Pd).

10.2.2 Characterization

The morphology of PdO NPs and TiO_2 thin films was investigated by Scanning Electron Microscopy (SEM, Zeiss Ultra Plus) operating at an accelerating voltage of 5 kV and a working distance of 4 mm. Particle size and size distribution analyses of PdO NPs were performed using ImageJ (Version 1.52q 13). X-ray Photoelectron Spectroscopy (XPS) was used to reveal the surface chemistry of the prepared samples. XPS analysis was performed in an ultrahigh vacuum (UHV) system (Omicron Nano-Technology GmbH) using an Al Kα X-ray source (1486.6 eV) and a VSW 125 hemispherical electron analyzer. All spectra were taken at constant pass energy (100 eV for the survey, and 30 eV for high-resolution spectra of the different elements present). Structural characterization was performed by Transmission Electron Microscopy (TEM, JEOL JEM-2100) operating at 200 kV.

10.2.3 Photocatalytic Activity Measurement

Photocatalytic activity of prepared samples was investigated by the bleaching of aqueous methylene blue (MB) test solution under UV illumination using a custom measurement setup, as previously reported.[9,23] A dilute solution of MB (Sigma-Aldrich) at a concentration of 10 µmol/L was prepared and poured into a quartz cuvette. Then the photocatalytic active surface of prepared samples was brought into contact with the MB solution, and the test cuvette was sealed with a Teflon cap to keep the volume of water constant (6.5 mL). While the test solution was magnetically stirred, a UV LED (OTLH-0480-UV, Laser Components GmbH) operating at an intensity of 4.5 mW/cm² and a wavelength of λ=365 nm, was used to iridate the cuvette. De-coloration of the MB solution was monitored by measuring the change in the absorbance at λ_{max} = 664 nm, where MB exhibits a high absorption.

10.3 Results and Discussion

We followed a two-step synthesis (as schematically depicted in **Figure** 10.1a) method to prepare PdO NPs decorated TiO_2 thin films using pulsed DC magnetron sputtering and GAS (**Figure** 10.1b) subsequently. Following the cleaning and conditioning of the silicon substrate, first, we deposited the TiO_2 layer with a thickness of 300 nm on the silicon substrate (Step 1). Following the sputter deposition process, we deposited PdO NPs on the as-deposited TiO_2 layer using the GAS approach (Step 2). Finally, we heat treated the sample for three reasons: (i) to achieve a highly crystalline (fully anatase phase) TiO_2 layer, (ii) to improve the adhesion between PdO NPs and underlying TiO_2 layer and (iii) to oxidize PdO NPs completely.

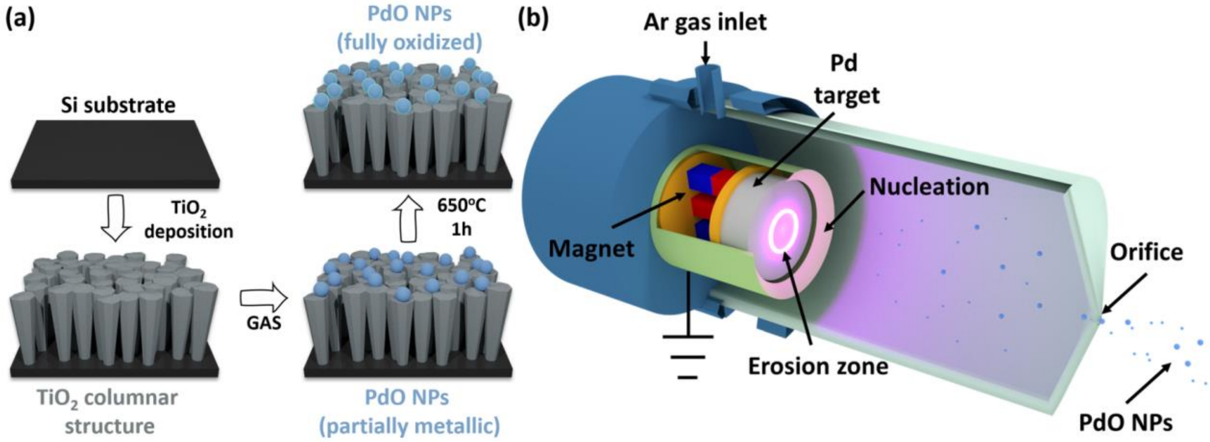

Figure 10.1. Schematic representation of **(a)** the preparation steps of PdO-TiO_2 photocatalysts and **(b)** PdO NPs deposition by gas aggregation source (GAS).

Prepared samples were investigated by SEM to reveal morphological and structural properties. As shown in **Figure** 10.2, TiO_2 thin film exhibits a columnar grain structure, which is typical for sputter-deposited layers; at a closer look, one can see dense nanocrack networks (**Figure** 10.7). As reported previously, such nanocracks are performed during the sputtering at high oxygen partial pressure (oxygen oversaturation prevents the formation of a dense contact between adjacent TiO_2 columnar structures (**Figure** 10.7)).[14,15] After the heat treatment, the change in the volume (crystallization-densification) and heating/cooling cycle triggers the formation of nanocrack networks. In SEM, PdO NPs exhibit a lighter appearance (leading to a strong color contrast to the TiO_2 base layer) due to the difference in the atomic mass numbers between Pd and Ti. They appear to be always in spherical form regardless of the deposition time. The relative coverage (%) of PdO NPs (after each deposition time) on the TiO_2 thin films was determined using the Image J software. Through binary SEM images, which consisted of small dark-colored dots (deposited PdO NPs) and white background (TiO_2 thin film), the ratio of the areas between the background and the black dots was calculated (**Figure** 10.8). We obtained the following surface coverages for PdO NPs: 1.1%, 2.7%, and 3.6% at 30s, 60s, and 90s deposition time, respectively.

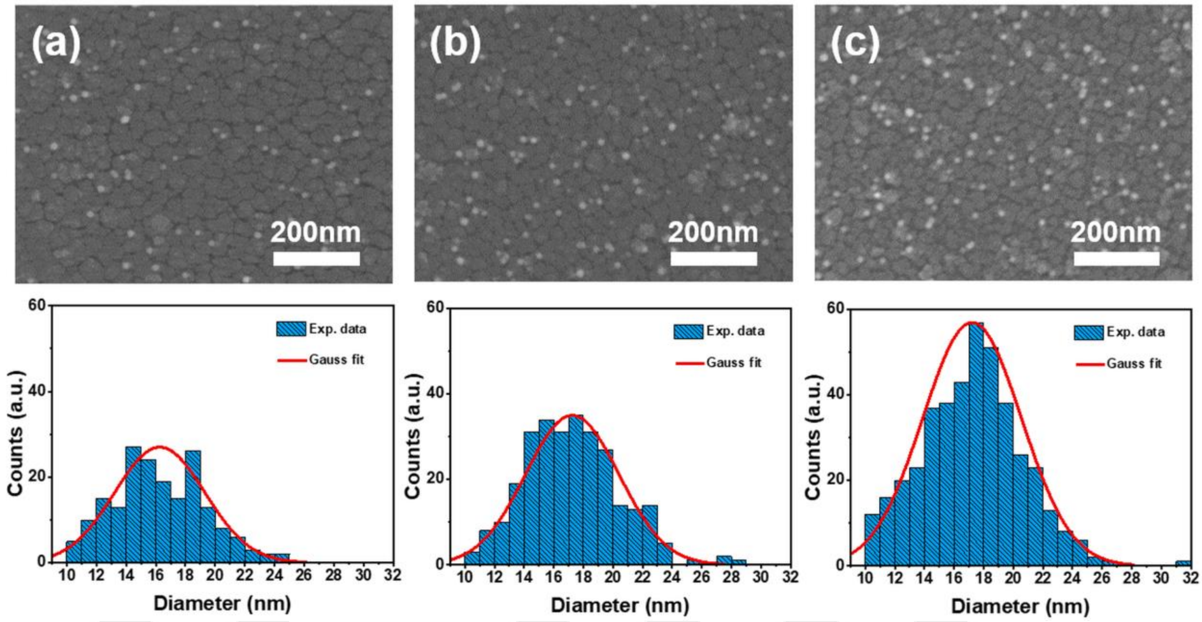

Figure 10.2. SEM images and corresponding size distribution histograms of PdO NPs deposited for **(a)** 30s, **(b)** 60s and **(c)** 90s. (PdO NPs appear as white dots on the darker TiO_2 layer).

We determined PdO NP size distribution for each deposition time, as shown in **Figure** 10.2 below corresponding SEM images) by using a dedicated module of Image J (Version 1.52q 13). Our measurements indicate that deposited PdO NPs show a Gaussian type size distribution, and all have a similar average particle size of 16.7 ± 0.5 nm regardless of the deposition time. As we reported previously, the discharge potential and gas flow rate play a major role in the final size of the deposited NPs.[169] In addition, one can control the particle size by adjusting aggregation length (the distance between the target and the exit aperture) and the orifice dimensions. Here our aim was to reveal the sole effect of the surface coverage (by PdO NPs) on the photocatalytic performance regardless of the individual particle size. In this connection, the GAS approach allows very good and independent control of the size and surface coverage of the NPs, which is usually not possible in the case of wet chemical synthesis methods.[18] On the other hand, we observe a poor adhesion between PdO NPs and underlying TiO_2 layer. NPs from a GAS are deposited in a soft-landing regime and have very low adhesion to the substrate surface.[272] To improve surface adhesion, one can use the electrostatic acceleration of charged NPs or embed them into the matrix.[273] In order to improve the adhesion of PdO NPs to the TiO_2 layer, we heat treated the samples at 650°C for 1h in the air. The heat treatment under mentioned conditions is compulsory to achieve a highly crystalline TiO_2 layer (anatase phase) with a high photocatalytic performance.[23,274] But here the heat treatment is also used to improve the adhesion of Pd NPs to the TiO_2 layer. At this stage, it was necessary to check if this heat treatment leads to any structural or/and a compositional change of the PdO NPs.

XPS analysis was conducted to determine the chemical composition of the PdO NPs, and as well as the TiO_2 layers, before and after the heat treatment (**Figure** 10.3). To avoid excessive exposure to the atmosphere and to prevent subsequent oxidation, as prepared Pd(60s)-TiO_2 samples were directly transferred to the analysis chamber after the deposition. Charge referencing was carried out using an adventitious carbon peak on the surface (C-1s) located at 285.0 eV. The wide-scan XPS showed the presence of titanium (Ti), oxygen (O), palladium (Pd), and some adsorbed carbon on the sample surface (**Figure** 10.9).

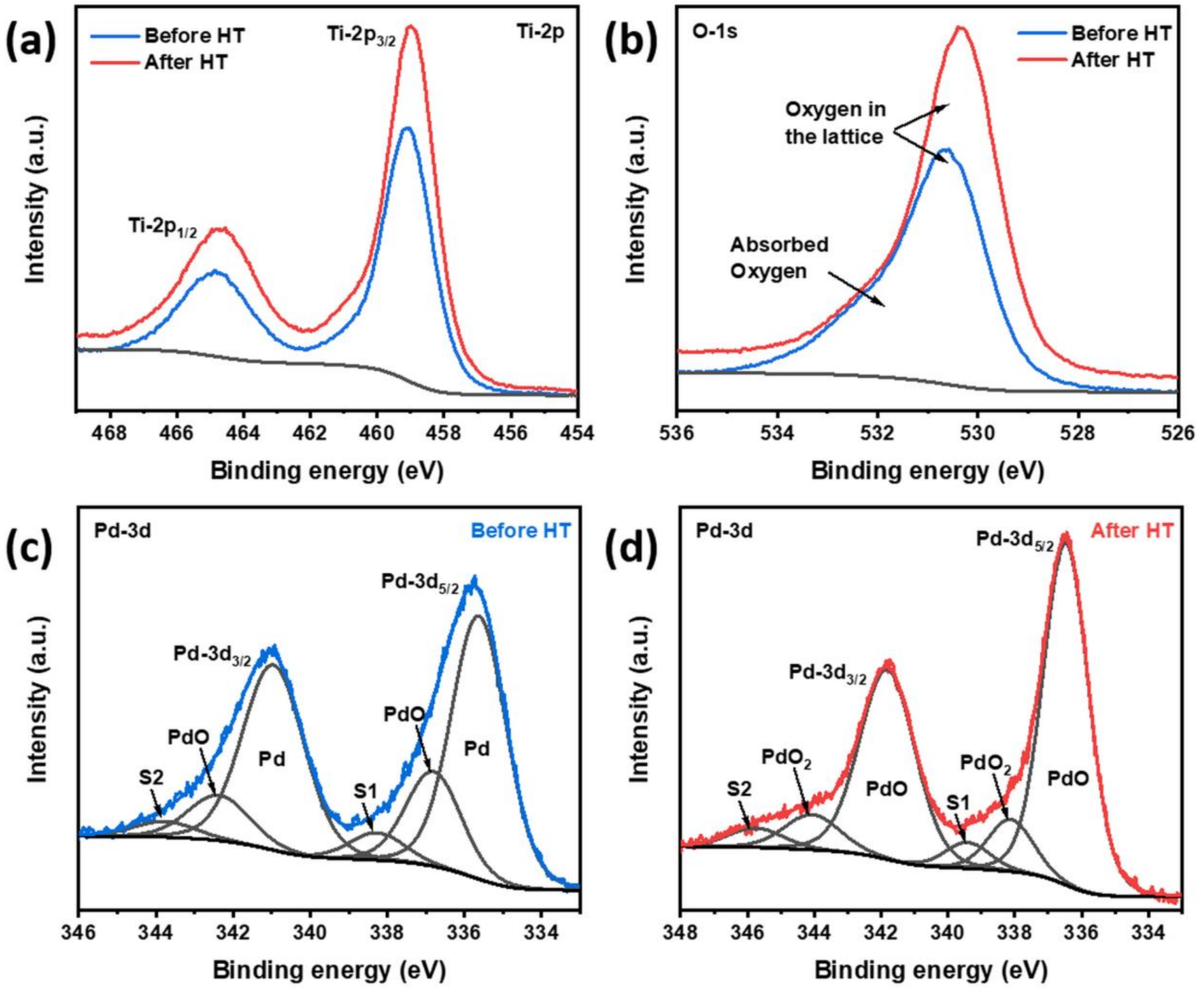

Figure 10.3. The XPS spectra of **(a)** Ti-2p, **(b)** O-1s and Pd-3d **(c)** before and **(d)** after heat treatment (HT).

Figure 10.3a shows the high-resolution Ti-2p spectrum, which is indicated two main peak corresponding Ti-2p$_{3/2}$ and Ti-2p$_{5/2}$. The position of Ti-2p$_{3/2}$ (~459.0 eV) and almost ~5.6 eV confirm that Ti is in Ti^{4+} state in the TiO$_2$ thin film.[196,228] The peaks for the O-1s were poisoned at around 530.6 eV, which is due to the oxygen in the lattice, and the peak position for the other ones were at around 532.5 eV, caused by adsorbed oxygen on the surface (**Figure** 10.3b).[275] After heat treatment, however, the binding energies for Ti-2p and O-1s were not changed while that Pd-3d had been showed significant change, as shown in **Figure** 10.10. The Pd-3d was observed within the region of 334–346 eV with two well-defined doublet of Pd-3d$_{5/2}$ and Pd-3d$_{3/2}$ (with spin-orbit separation of 5.4eV).[276]

Before heat treatment, the Pd-3d$_{5/2}$ peak showed two components located at 335.6 and 336.8 eV (**Figure** 10.3c). The peak at 335.6 eV indicates the metallic Pd (Pd^0, 75.3%), while the peak at 336.8 eV assigned to Pd^{2+} (PdO, 24.7%).[277,278] Moreover, the satellite peak (S1) corresponding to the PdO compound was observed at 338.2 eV, which was binding energy shifted from the main PdO peak by 1.4 eV. However, it is difficult to clearly identify that peak due to energy matching with Pd^{4+} (PdO_2). Basically, one can say that before the heat treatment, deposited NPs exhibit metallic character rather than a full oxide phase. After heat treatment, the Pd-$3d_{5/2}$ peak shifted to higher binding energy values (**Figure** 10.3d) and this peak was deconvoluted into two components located at 336.4 and 338.1 eV assigned to Pd^{2+} and Pd^{4+}, respectively.[275,279] Additionally, the peak at 339.1 eV, which is obtained 2.7 eV difference, can be assigned satellite peak (S1) corresponding PdO after heat treatment. It is clearly seen that after heat treatment, metallic Pd character vanished totally and two different oxide states, namely PdO (83.4%) and PdO_2 (16.6%) became dominant, which can be named as PdO_x (the use of this notification in the manuscript is avoided in order to eliminate any confusion).

Additionally, we performed TEM analysis in order to reveal the structural characteristics of deposited layers. In accordance with SEM results, the deposited PdO NPs have relatively uniform size distribution and shape, as seen in the TEM micrograph (**Figure** 10.4a). In **Figure** 10.4b, a high-resolution TEM (HRTEM) micrograph of a PdO NP before the heat treatment can be seen.

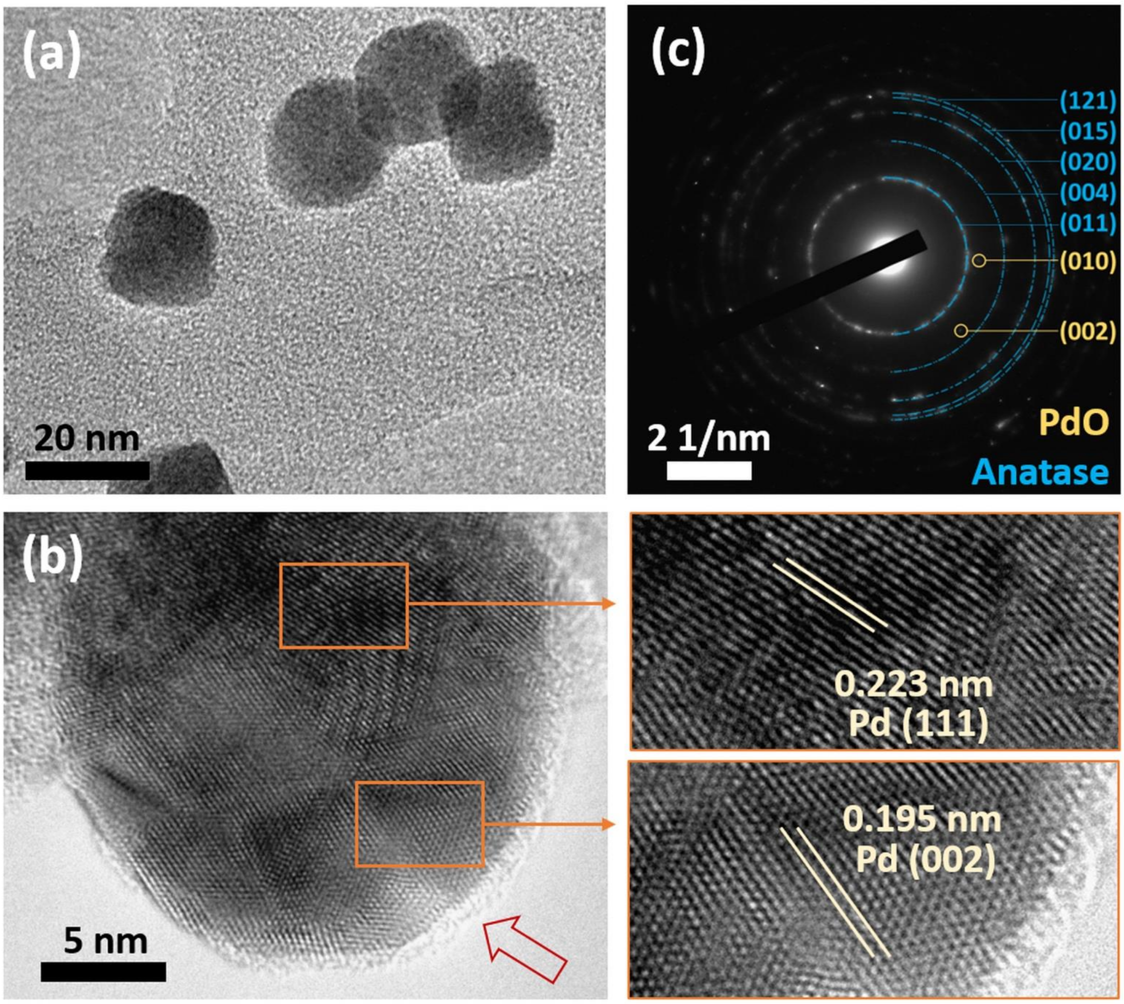

Figure 10.4. **(a)** TEM and **(b)** HR-TEM micrograph of PdO NPs (red arrow represents a thin shell of oxidized Pd) before heat treatment. **(c)** SAED pattern of PdO NPs and TiO_2 anatase phase after heat treatment.

The measured lattice fringes with a d-spacing of 0.223 nm and 0.195 nm correspond to metallic Pd lattice planes (111) and (002), respectively. Toward the edge of the particle a narrow region with a distinctive change, in contrast, is visible, which could correspond to a thin shell oxidized Pd (in the form of PdO), as similarly described by Zhang et al.[280] However, after heat treatment, metallic Pd was totally oxidized, which can be seen from selected-area electron diffraction (SAED) given in **Figure** 10.4c. Here the concentric rings correspond to differently sized crystallites of the TiO_2 (anatase phase).

Furthermore, multiple single Bragg reflexes (for instance (002) reflex with a d-value of 0.268 nm) can be attributed to the tetragonal phase of PdO.[280] However, no unique reflex can be attributed to PdO_2, which can be explained by the low total fraction of NPs and the low ratio of PdO_2 to PdO as discussed previously (for a detailed discussion see **Figure** 10.11, **Table** 10-1, **Table** 10-2 and **Table** 10-3). Overall this result confirms that the metallic Pd character totally vanished after the heat treatment, which is in agreement with the previous XPS analysis.

We compared the photocatalytic performance of the bare TiO_2 and PdO–TiO_2 samples (prepared with different deposition times: 30, 60, and 90s) by monitoring their capability to photodegrade MB under UV irradiation. First, we recorded the change in the absorbance of MB solution with time using optical absorption spectroscopy. Then the change in the absorption was correlated with the degradation of MB (the change in C/C_0 ratio, where C_0 and C are the initial concentration of MB and the concentration of MB at a certain time, respectively). We calculated the rate constants (k) as given in **Table** 4-1(k_1: Bare TiO_2, k_2: Pd(30s)-TiO_2, k_3: Pd(60s)-TiO_2 and k_4: Pd(90s)-TiO_2) by fitting a first-order kinetic model. **Figure** 10.5a shows that all PdO–TiO_2 samples exhibited higher photocatalytic activity in comparison to the bare TiO_2. The PdO(60s)-TiO_2 showed the highest photocatalytic activity with a reaction rate of k_3: $1.8 \times 10^{-3}\ s^{-1}$, whereas bare TiO_2 has a much lower reaction rate (k_1: $0.3 \times 10^{-3}\ s^{-1}$). Increasing the surface coverage of Pd NPs may hinder the activation of TiO_2 (Pd(90s)-TiO_2 exhibits a reaction rate of k_4: $1.5 \times 10^{-3}\ s^{-1}$) by blocking the incoming UV light as we also observed a similar mechanism in case of Ag–TiO_2 hybrid structures.[194] In some cases, porous structures with the high surface area may act as strong adsorption sites for contaminants (here MB molecules), and this adsorptive removal can contribute to the decolorization of the test solution. In order to verify that decolorization of the MB solution was governed by photocatalytic degradation, we performed the same measurement under dark environment (without UV illumination) for 2 h. **Figure** 10.12 shows that without UV illumination, Pd(60s)-TiO_2 was not able to degrade the MB test solution. This shows the absorption of the MB molecules on Pd–TiO_2 thin film surface is limited and negligible for the overall photocatalytic reactions. To further study the stability of photocatalytic bleaching MB by Pd(60s)-TiO_2 photocatalyst, the cyclic stability experiments were performed under the same conditions. After four cycles, the Pd(60s)-TiO_2 photocatalyst showed a good photocatalytic effect, as shown in **Figure** 10.5b.

In addition to monitoring the de-colorization of the MB solution, we verified the capability of photocatalytic decomposition of the oleic acid layer (as a model for organic contaminants) by the prepared samples to reveal their photocatalytic performance (for potential applications, such as self-cleaning out-door coatings). First, we measured the water contact angle (WCA) of the prepared sample Pd(60s)-TiO_2, which exhibited the highest photocatalytic activity (highest MB degradation rate). Pd(60s)-TiO_2 showed totally hydrophilic behavior with a WCA of ~18°, as shown in **Figure** 10.5c. Afterward, we contaminated the surface of the sample by immersing it into a dilute solution of oleic acid (50 µL, 10 mmol/L in acetone). After drying the surface with dry air, we measured the WCA once more. As can be seen, WCA increased to 57° by adsorption of oleic acid. Then we exposed the sample to UV light for different time intervals and correspondingly we checked the change in WCA. As it is seen in **Figure** 10.5c, after 210 min, the original WCA is recovered, which is a clear indicator of total oleic acid decomposition on the sample surface.

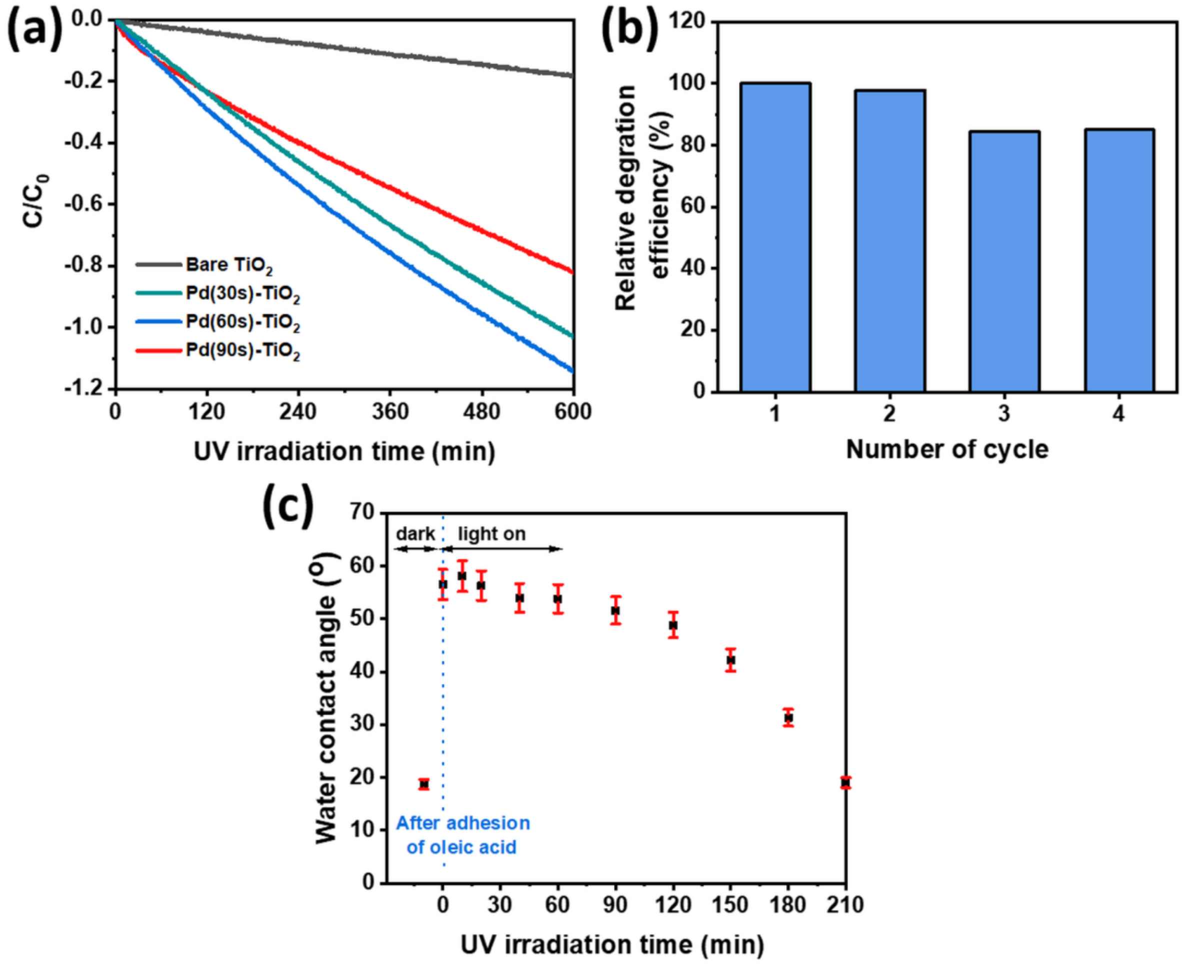

Figure 10.5. **(a)** Comparison of time-dependent photocatalytic bleaching of MB for bare TiO_2 and PdO-TiO_2 samples with different deposition times, **(b)** Stability of Pd(60s)-TiO_2 photocatalyst for bleaching of MB (all values were normalized with respect the bleaching of MB by photocatalyst under UV illumination for 4h) and **(c)** Changes in the water contact angle (WCA) of oleic acid-treated Pd(60s)-TiO_2 surface under UV light irradiation.

It is well-known that •OH radicals (e.g. generated by photocatalytic dissociation of H_2O by TiO_2) are very strong oxidants. Such highly reactive •OH radicals, both adsorbed on PdO NPs and freely found within the aqueous medium, can further oxidize PdO NPs deposited on TiO_2 ($PdO \rightarrow PdO_2$). PdO_2 is known to have a higher electron affinity than PdO, and therefore, PdO_2 can be readily reduced by capturing the photogenerated electrons.[281] Basically, under UV irradiation PdO NPs on TiO_2 can be oxidized, and PdO_2

species may be localized at the block boundaries of these particles (similar to a core-shell structure and the whole cluster can be termed as PdO_x), as shown in **Figure** 10.6a.

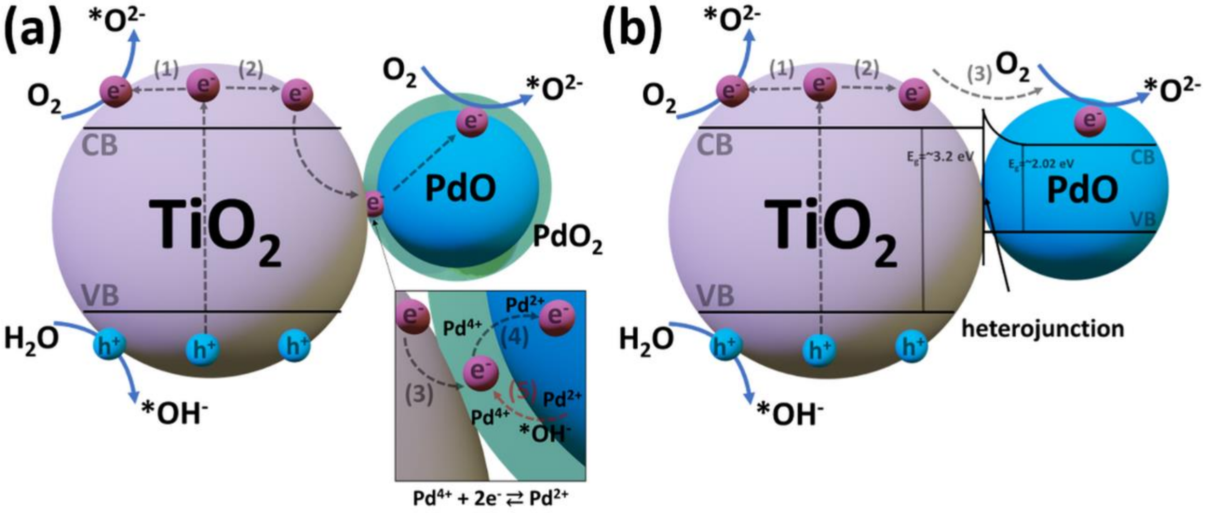

Figure 10.6. **(a)** Dynamic switching mechanism and **(b)** direct electron transfer mechanism of PdO-TiO_2 photocatalysts under UV illumination.[53,271]

When the photogenerated electrons are trapped by higher electrophilic PdO_2, the electron–hole pairs are efficiently separated, producing more •OH on the TiO_2 surface. Thus, the photocatalytic activity on Pd–TiO_2 is significantly enhanced.[282] One should keep in mind that there is a steady equilibrium between the formation of PdO_2 (oxidation by free and adsorbed •OH) and PdO (reduced by trapped photogenerated electrons) under UV irradiation (as once can see both species in XPS spectrum given in **Figure** 10.3d), resulting in higher separation efficiency of photogenerated charges (as shown in **Figure** 10.6a).[282] In addition to the contribution of highly reactive •OH radicals to the photocatalytic performance, O_2 adsorbed on both TiO_2 and PdO_x could be activated into $*O_2^-$ radicals, which also play a major role on the decomposition of organic contaminants including MB.[283]

The mechanism of dynamic switching of PdO ⇄ PdO_2 and its effect on the photocatalysis was also suggested by Fu et al.[282] But it is difficult to prove such a mechanism fully through even an in-situ high-resolution transmission electron microscopy (HR-TEM) analysis. One of the main difficulties in such an analysis arises because of the high electron affinity of PdO_2. Exposing PdO–PdO_2 mixed oxide system to an intense electron beam can easily induce the reduction of PdO_2 into PdO, which reminds of similar difficulty in distinguishing polymorphs of Al_2O_3 in TEM analysis (usually operating at accelerating voltage of several tens of kV [284]). Nevertheless, one can easily postulate that mixed oxide system PdO–TiO_2 definitely brings advantages in terms of redox potentials to achieve a high photodegradation rate. The bandgap of PdO (~2.02 eV) is smaller than the bandgap of TiO_2 (~3.2 eV) [271] and the large bandgap difference between them may trigger the formation of a heterojunction at the interface. Such a heterojunction barrier may enhance the electron-hole pair separation as schematically shown in **Figure** 10.6b, which definitely leads to higher photocatalytic performance.[53,278]

10.4 Conclusion

In this work, we investigated the photocatalytic performance of TiO_2 film decorated with PdO NPs and the corresponding mechanism of the decomposition of organic contaminants (methylene blue and oleic acid). We followed a two-step synthesis method to prepare PdO NPs decorated TiO_2 thin films using pulsed DC magnetron sputtering and GAS subsequently. This solvent-free synthesis approach provides good control of the size and surface coverage of PdO NPs in comparison to wet chemical synthesis methods (precipitation, photodeposition, sol-gel, etc.). Subsequent heat treatment significantly improved the adhesion between PdO NPs and TiO_2. During heat treatment PdO NPs (which mainly exhibited metallic character) were fully oxidized as observed in the XPS spectra, indicating the coexistence of both PdO and PdO_2. Possibly the steady equilibrium between the formation of PdO and PdO_2 under UV irradiation seemed to foster the charge separation efficiency, and this enhanced the photocatalytic performance. The dynamic $PdO \rightleftarrows PdO_2$ transformation needs to be studied in situ to reveal its effect on the photocatalysis.

Acknowledgements

S. Veziroglu acknowledges the Graduate Center and Federal State Funding at Kiel University for providing funding for his Ph.D. study. The authors would like to thank Stefan Rehders for his continuous support for building-up and the maintenance of deposition systems.

Supporting Information

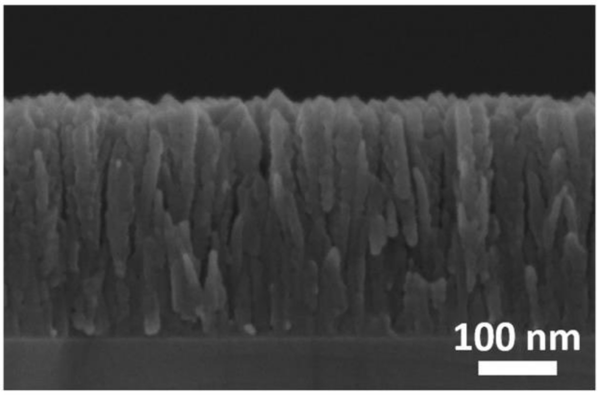

Figure 10.7. Cross-sectional scanning electron microscopy (SEM) image of TiO_2 thin film.

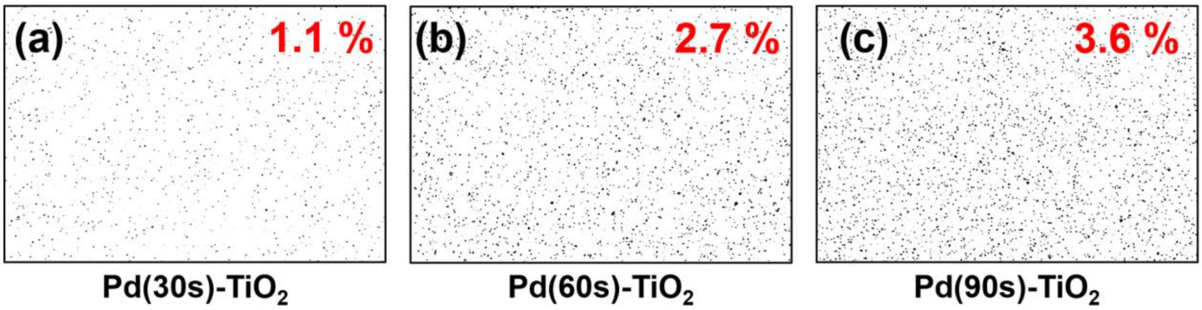

Figure 10.8. Binary scanning electron microscopy (SEM) image of Pd clusters and estimated surface coverage (%).

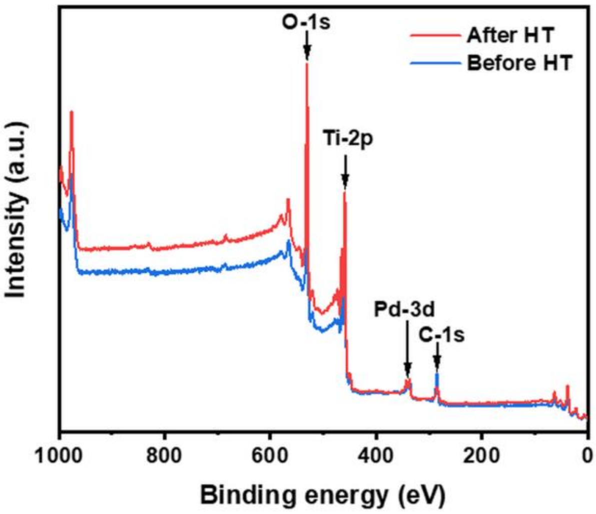

Figure 10.9. Comparative XPS wide scan energy spectrum of Pd(60s)-TiO_2 before and after heat treatment (HT).

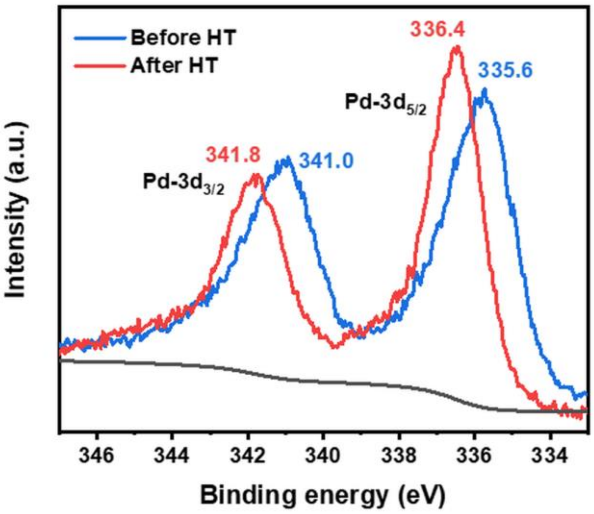

Figure 10.10. Comparative high-resolution XPS of Pd-3d for before heat treatment and after heat treatment (HT).

Figure 10.11 shows the result of azimuthal integration for the SAED pattern. Peak positions were determined using a top-hat filter. In case of single reflexes line integrals were used for clarification, e.g. for the reflex 2. **Table** 10-1 shows peak positions, *d*-spacing values and corresponding structures. All crystallographic information for common Pd and PdO modifications can be found in [281]. Anatase TiO_2

crystallographic was taken from the Inorganic Crystal Structure Database (ICSB) (identification number 93098).

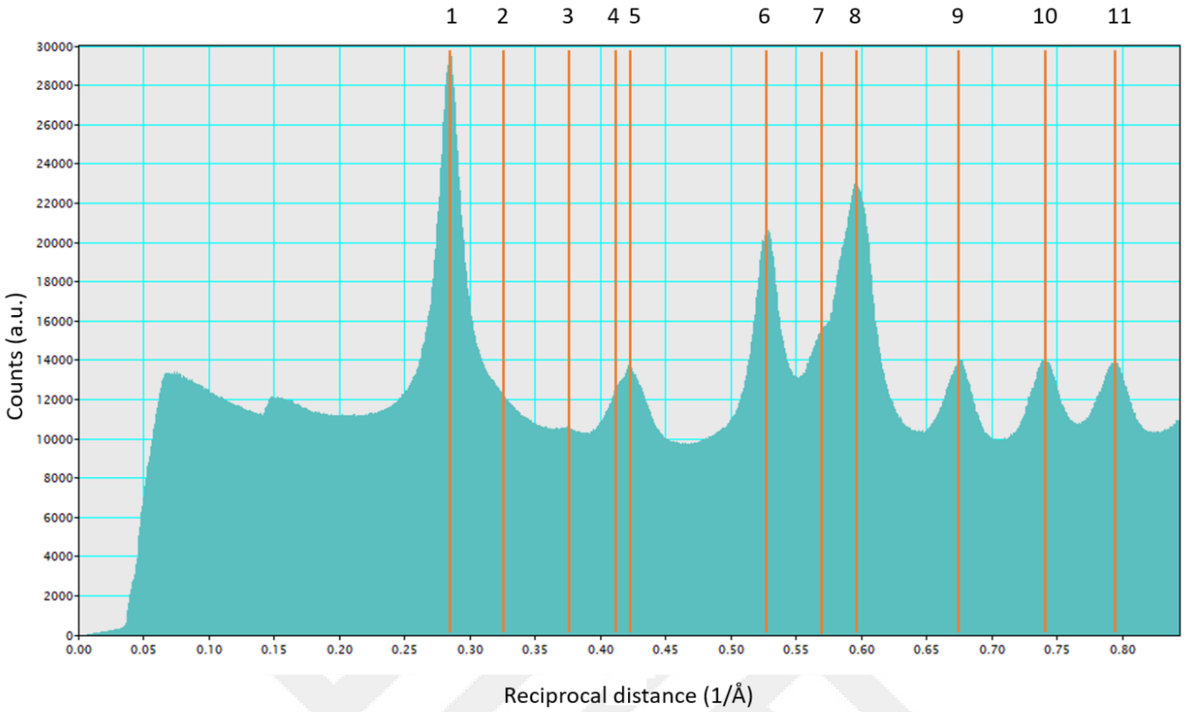

Figure 10.11. The azimuthal integration for the SAED pattern.

Table 10-1. The peak positions, *d*-spacing values and corresponding structures.

No.	Peak location (1/ Å)	*d*-spacing (Å)	Identification
1	0.284	3.52	TiO_2 (011)
2	0.328	3.05	PdO (010)
3	0.373	2.68	PdO (002)
4	0.423	2.36	TiO_2 (004)
5	0.434	2.30	TiO_2 (112)
6	0.527	1.90	TiO_2 (020)
7	0.599	1.67	TiO_2 (121) / PdO (112)
8	0.677	1.48	TiO_2 (024)
9	0.741	1.35	TiO_2 (220)

Table 10-2 and **Table** 10-3 show the *d*-spacing and lattice planes for the anatase phase of TiO_2 and $P4_2/mmc$ PdO crystal structures respectively.

Table 10-2. The *d*-spacing and lattice planes for the anatase phase of TiO_2 crystal structure.

No.	***d*-spacing (Å)**	**Intensity (a.u.)**	**hkl**
1	3.515	519177	011
2	2.429	25237	013
3	2.375	116916	004
4	2.331	23809	112
5	1.892	167670	020
6	1.698	106841	015
7	1.666	102417	121
8	1.493	16777	123
9	1.480	84176	024

Table 10-3. the *d*-spacing and lattice planes for the $P4_2/mmc$ PdO crystal structure.

No.	***d*-spacing (Å)**	**Intensity (a.u.)**	**hkl**
1	3.030	11161.72	010
2	2.665	82163	002
3	2.634	464021	011
4	2.143	90598	110
5	2.001	4495	012
6	1.670	144430	112
7	1.533	83688	013
8	1.515	50850	020
9	1.355	734	120

Table 10-4. Kinetics rate constants (k) for photocatalytic bleaching of MB by prepared thin film photocatalysts. **(Kinetics rate constants (k) were calculated according to slopes of graph in Figure** 10.5a**).**

Photocatalysts	**Rate Constant (s^{-1})**
Bare TiO_2	k_1: -0.3 x 10^{-3}
Pd(30s)-TiO_2	k_2: -1.5 x 10^{-3}
Pd(60s)-TiO_2	k_3: -1.8 x 10^{-3}
Pd(90s)-TiO_2	k_4: -1.3 x 10^{-3}

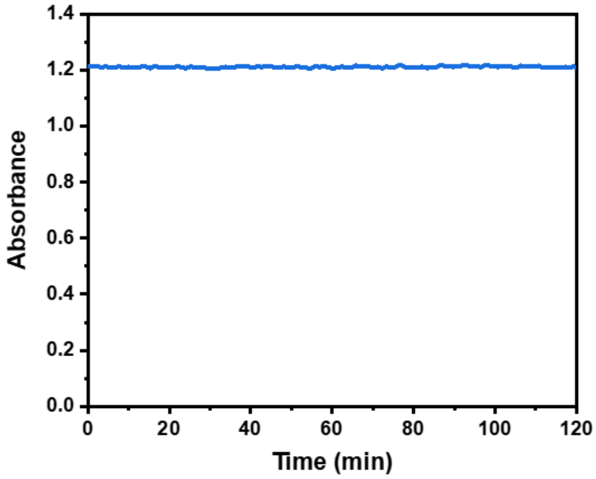

Figure 10.12. The time-dependent absorbance changing of MB by Pd(60s)-TiO_2 photocatalyst under dark environment (without UV illumination).

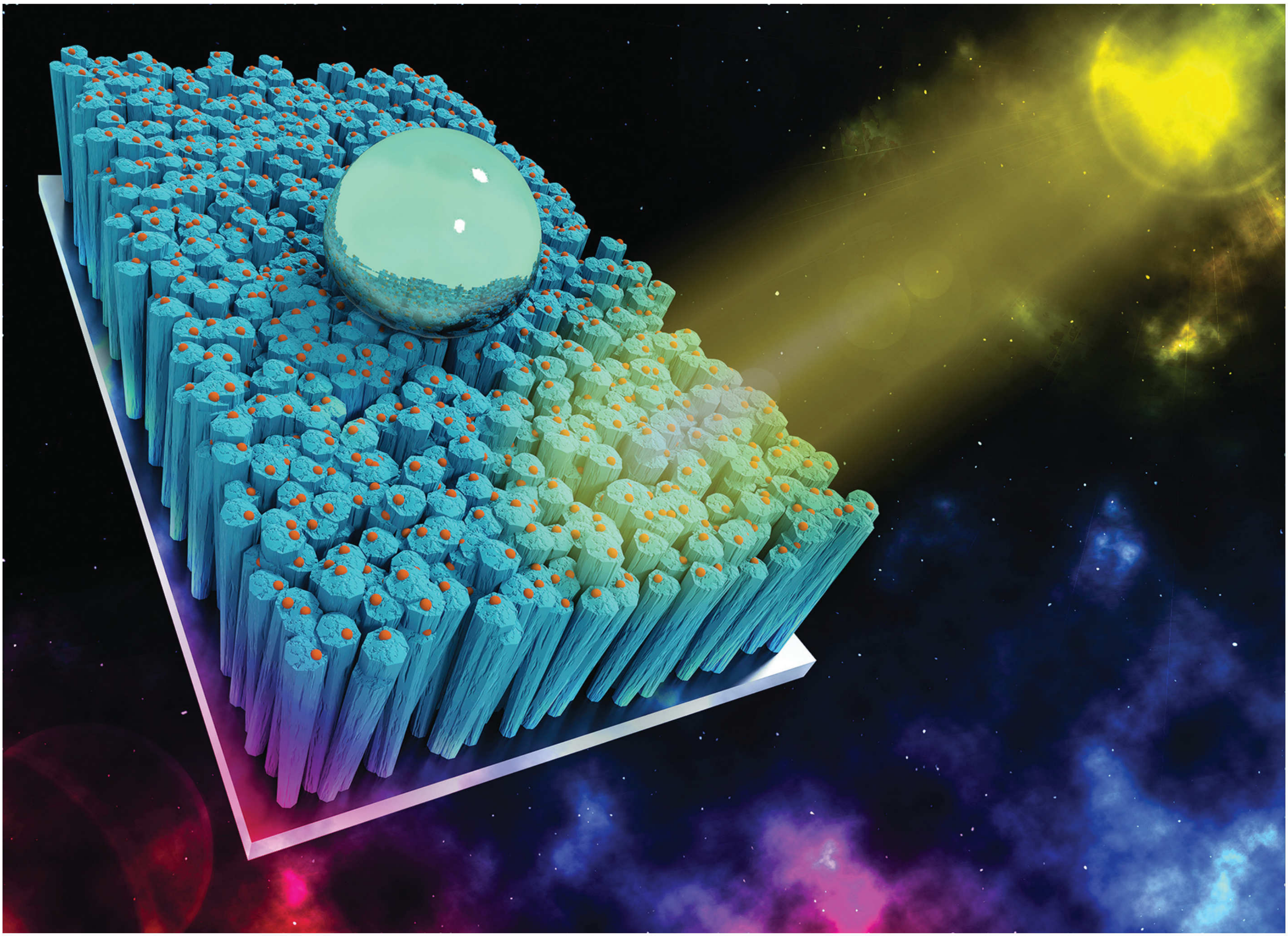

Showcasing research from the Institute for Materials Science, Faculty of Engineering, Christian-Albrechts-University of Kiel, Germany and Mads Clausen Institute, NanoSYD, University of Southern Denmark, Denmark.

Cauliflower-like CeO_2–TiO_2 hybrid nanostructures with extreme photocatalytic and self-cleaning properties

Heterogeneous photocatalytic systems have attracted enormous interest due to increasing concerns about environmental pollution problems. The cauliflower-like CeO_2–TiO_2 heterostructures exhibit excellent photocatalytic activity, which can be attributed to the improvement of the separation of photogenerated electron–hole pairs and dynamic shifting between Ce^{3+} and Ce^{4+} oxidation states. Such CeO_2–TiO_2 hybrid structures are promising for photocatalytic and self-cleaning outdoor and as well as indoor applications.

As featured in:

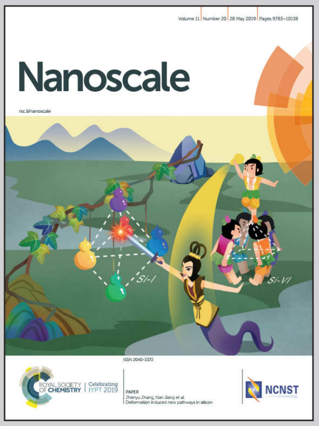

See Franz Faupel, Oral Cenk Aktas *et al.*, *Nanoscale*, 2019, **11**, 9840.

11 Cauliflower-like CeO_2–TiO_2 Hybrid Nanostructures with Extreme Photocatalytic and Self-cleaning Properties

This chapter is based on an article published in Nanoscale.[183]

Reprinted with permission from Salih Veziroglu, Katharina Röder, Ole Gronenberg, Alexander Vahl, Oleksandr Polonskyi, Thomas Strunskus, Horst-Günter Rubahn, Lorenz Kienle, Jost Adam, Jacek Fiutowski, Franz Faupel, and Oral Cenk Aktas
Nanoscale, 2019,11, 9840-9844.
The article is available via the internet at https://doi.org/10.1039/C9NR01208G

Abstract

In recent years, heterogeneous photocatalysis has gained enormous interest due to increasing concerns about environmental pollution. Here we propose a facile approach to synthesize cauliflower-like CeO_2–TiO_2 hybrid structures by magnetron reactive sputtering, exhibiting an extremely high photocatalytic activity. While heating and air-quenching of the sputter deposited TiO_2 thin film (first layer) triggered the formation of a nanocrack network, the second heat-treatment led to transformation of the CeO_2 film (second layer) into CeO_2 nanoclusters (NCs). We attribute the resulting high photocatalytic activity to the confined structure of the CeO_2 NCs and the CeO_2–TiO_2 interface, which allows Ce^{3+}/Ce^{4+} dynamic shifting. In addition to high photocatalytic activity in an aqueous medium, the prepared CeO_2–TiO_2 hybrid structures exhibited significant self-cleaning properties in air (non-aqueous).

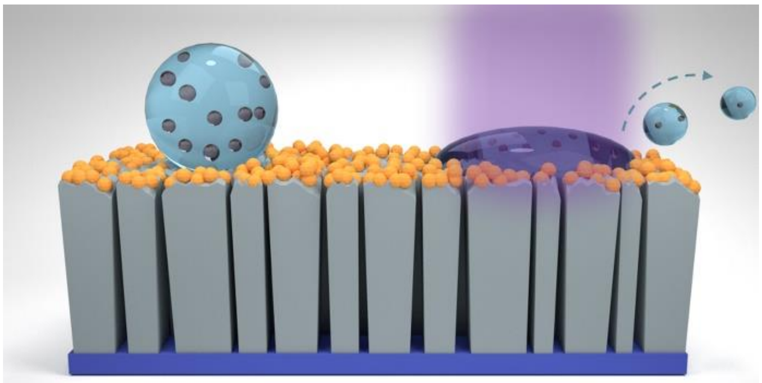

11.1 Introduction

TiO_2 is an attractive material for a large number of applications including high-refractive-indexed optical films, high-density dynamic-memory devices, solar cells, supercapacitors, and photocatalytic processes.[285,286] As the environmental pollution has become the focus of attention all over the world, the interest in heterogeneous photocatalysis involving TiO_2 has increased immensely at both fundamental science as well as application levels.[3,135,287] Beside its various advantages such as low cost, earth abundance, and non-toxicity, high electron-hole recombination rate is one of the main drawbacks of TiO_2.[288] In addition, low electron mobility and small diffusion length (for holes) limit the practical use of TiO_2 in heterogeneous photocatalytic applications.[289]

Doping or decorating TiO_2 with metallic elements is one of the common methods to improve its photocatalytic efficiency [5]. Especially noble metals such as silver (Ag) and gold (Au) have been intensively used to extend the absorption to visible wavelengths and to enhance electron-hole separation.[290,291] Alternatively, combining TiO_2 with rare-earth elements and their oxides has been shown to be an effective way to improve the conversion efficiency of TiO_2. Especially mixed oxides are of great interest due to superior catalytic properties owing to synergetic effects. Among various mixed oxides, CeO_2-TiO_2 combination attracts the attention of catalytic applications due to its novel physicochemical and electronic properties, which are totally different than their individual components.[292]

The redox couple Ce^{3+}/Ce^{4+} with the ability of shifting between CeO_2 and Ce_2O_3 under oxidizing and reducing conditions make Ce based oxides exceptional in heterogeneous catalysis.[18,293] In addition, the CeO_2 structure facilizes the formation of labile oxygen vacancies with relatively high mobility of bulk oxygen species. At CeO_2-TiO_2 hybrid structures, TiO_2 acts as chemical, thermal and mechanical stabilizer for achieving stable nanoscale CeO_2.[294] Beside the role of TiO_2 as a simple support, similar to other oxides, the CeO_2-TiO_2 interface has been reported to exhibit unique chemical properties.[292]

Various wet chemical routes have been developed to synthesize hybrid CeO_2-TiO_2 structures with different morphology, size, and stoichiometry.[295] Thanks to their high surface area CeO_2-TiO_2 hybrid nanoparticles have been shown to decompose various organic contaminants effectively in water; however, their practical use as slurry type suspensions is limited because of the difficulty of the separation of such small particles after the photocatalytic process. For outdoor (e.g. self-cleaning windows) as well as indoor applications (e.g. odor cleaning devices) immobilized, robust and highly adhering photocatalytic particles or films are needed. In general, suspended photocatalytic nanoparticles exhibit much higher activity (thanks to their high active surface area) in comparison to immobilized nanoparticles or thin films of the same material.[296]

11.2 Results and Discussion

Here, we prepared columnar TiO_2 structures decorated with CeO_2 nanoclusters (NCs) by a novel reactive sputtering process followed by the subsequent heat-treatment. In general, sputter deposited thin films offer high adherence and mechanical stability, but typically they are outperformed (due to lack of large surface area) in terms of photocatalytic properties by colloidal nanoparticles. Firstly, a 300 nm TiO_2 thin film was deposited on quartz and silicon substrates by magnetron reactive sputtering at a gas pressure (O_2:Ar, 10 sccm:250 sccm) of 2.9 Pa. We have previously shown that such a high working pressure led to the growth of isolated (poor interaction between adjacent structures) columnar structures (as schematically depicted in **Figure** 11.1a).[14,113]

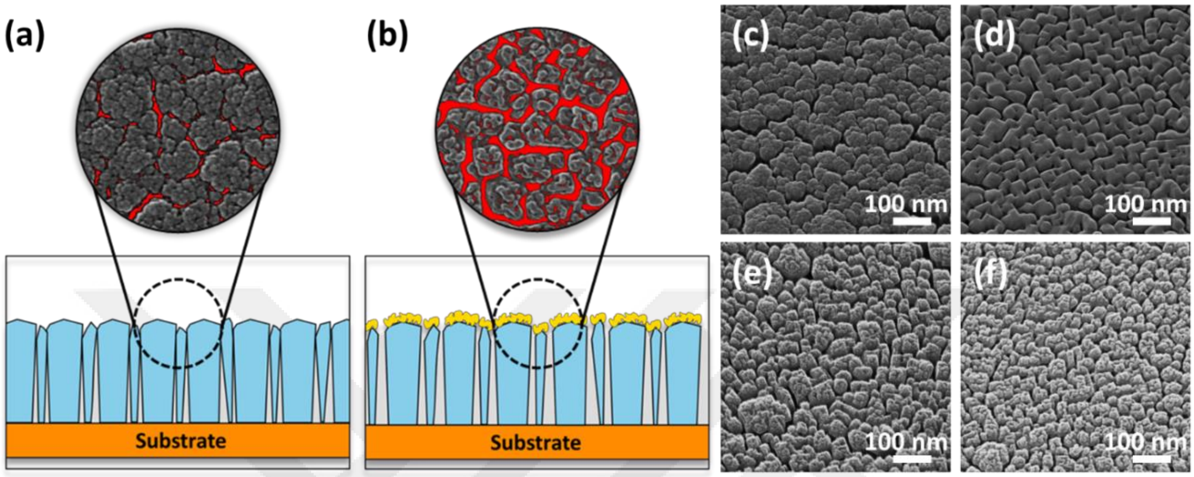

Figure 11.1. Schematic presentation of the morphology of **(a)** as-deposited TiO_2 thin film and **(b)** CeO_2 NC decorated TiO_2 thin film. Circularly shaped insets show top-view of as-deposited and CeO_2 NC decorated TiO_2 for comparison (red color indicates the presence of nanoscale cracks between adjacent structures). HIM images of **(c)** as-deposited TiO_2, **(d)** heat-treated TiO_2, **(e)** as-deposited CeO_2–TiO_2 and **(f)** heat-treated CeO_2–TiO_2.

Afterwards by heating the sample at 650°C and air-quenching we induced nanocrack networks to enhance the active surface area (as schematically explained in **Figure** 11.1a and **Figure** 11.1b). Following the heat-treatment, a 6-8 nm thick CeO_2 layer was deposited on columnar TiO_2 structures and we subjected the CeO_2-TiO_2 bilayer to a second heat-treatment step at 650°C for 1 h to crystallize both oxides fully and to transform the ultra-thin non-continuous CeO_2 layer into CeO_2 NCs. Finally, we achieved cauliflower-like TiO_2 structures decorated with fine CeO_2 NCs (as schematically depicted in **Figure** 11.1b).

Helium Ion Microscope (HIM) images of bare and CeO_2 NCs decorated TiO_2 films are shown in **Figure** 11.1c-f (before and after heat-treatment). The columnar morphology of TiO_2 is typical for a sputter deposited film.[14,23] Heat-treating and air-quenching induced thermal cracking which led to higher surface area (**Figure** 11.1d). After second heat-treatment and air-quenching (following CeO_2 deposition) we observed the formation of CeO_2 NCs on top of former TiO_2 columnar structures (**Figure** 11.1e and **Figure** 11.8). The lattice mismatch between CeO_2 (cubic fluorite structure) and TiO_2 (anatase) seemed to generate a high stress, which might have caused the island-like re-organization of CeO_2 structures during heat-treatment.[293] In the wet-chemical synthesis of TiO_2 supported CeO_2, structures tend to grow in the out-of-plane direction to minimize total added strain energy thereby limiting in-plane growth and triggering the island growth. We observed a similar morphology even after the deposition of the CeO_2 layer and such a morphology became more dominant after the heat-treatment (**Figure** 11.1e and **Figure** 11.1f). For details see **Figure** 11.8 (Supplementary Information).

As expected, prior to heat-treatment the deposited TiO_2 film was amorphous (as demonstrated by selected-area electron diffraction (SAED) shown in **Figure** 11.9). After heat-treatment and air-quenching, TiO_2 crystallizes to a polycrystalline mixture of mainly anatase and a small portion of brookite (**Figure** 11.2a). In addition, we observed the contraction of the c-axis in the tetragonal unit cell of anatase from 9.51 Å to 9.14 Å. Such a contraction was detected in some crystallites by fast Fourier transformation (FFT) of corresponding HRTEM images (**Figure** 11.10) as shown in **Figure** 11.11. This contraction cannot be explained by the crystal-size below 20 nm as nanocrystalline samples typically show expansions of the unit cell.[297]

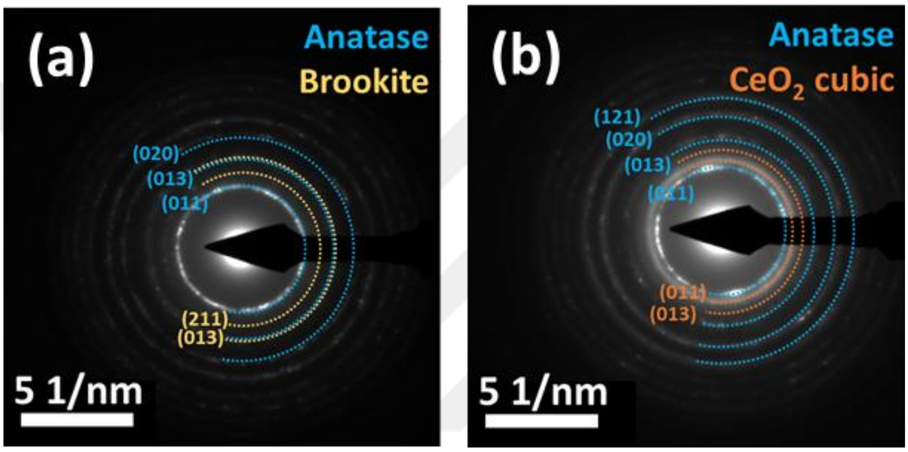

Figure 11.2. Selected area diffraction (SAED) of **(a)** TiO_2 and **(b)** CeO_2-TiO_2 hybrid structure after heat-treatment.

A more probable reason may be the oxygen deficiency induced by the heat-treatment. After heat-treatment and air-quenching we observed that hybrid structure consists of anatase and cubic CeO_2 phases (**Figure** 11.2b). Here, the anatase structure was not distorted; the CeO_2 top layer seemed to prevent excessive oxygen-desorption from the anatase structure during heat-treatment. Cross-sectional (prepared by focused ion beam as described in **Figure** 11.12) TEM-examination of deposited layer suggested that there is no interfacial correlation between anatase and cubic CeO_2 phases, rather CeO_2 crystals seem to be randomly oriented (**Figure** 11.13 and **Figure** 11.14).

In order to reveal the chemical state of prepared CeO_2-TiO_2 hybrid catalyst, the surface was investigated by XPS. The high-resolution spectra of C-1s, O-1s, Ti-2p, and Ce-3d were acquired for pure and hybrid catalysts. Charge referencing was done using adventitious carbon peak (C-1s) located at 285.0 eV.[298] XPS spectra of Ce-3d for CeO_2 and CeO_2-TiO_2 are presented in **Figure** 11.3a. In order to maximize visibility of the changes in Ce-3d, recorded spectra were normalized and plotted in an overlapped way. Peaks labeled as u and v are attributed to $3d_{3/2}$ and $3d_{5/2}$ spin-orbit states, respectively.[299] The u/v, u2/v2, and u3/v3 doublets are attributed to $3d^{10}4f^{0}$ initial electronic state corresponding to Ce^{4+}. On the other hand, in the XPS spectrum of CeO_2-TiO_2 hybrid structures, we observed some slight changes. Although it is difficult to detect their presence due to persisting predominant Ce^{4+} peaks, we believe that small peaks labeled with u1 and v1 indicate $3d^{10}4f^{1}$ electronic state which corresponds to Ce^{3+}. Co-existence of both $Ce^{4+}/^{3+}$ states is crucial for achieving high conversion efficiency. Moreover, the presence of Ce^{3+} may inhibit the reduction of Ti^{4+} because of the favorable electron compensation.[300]

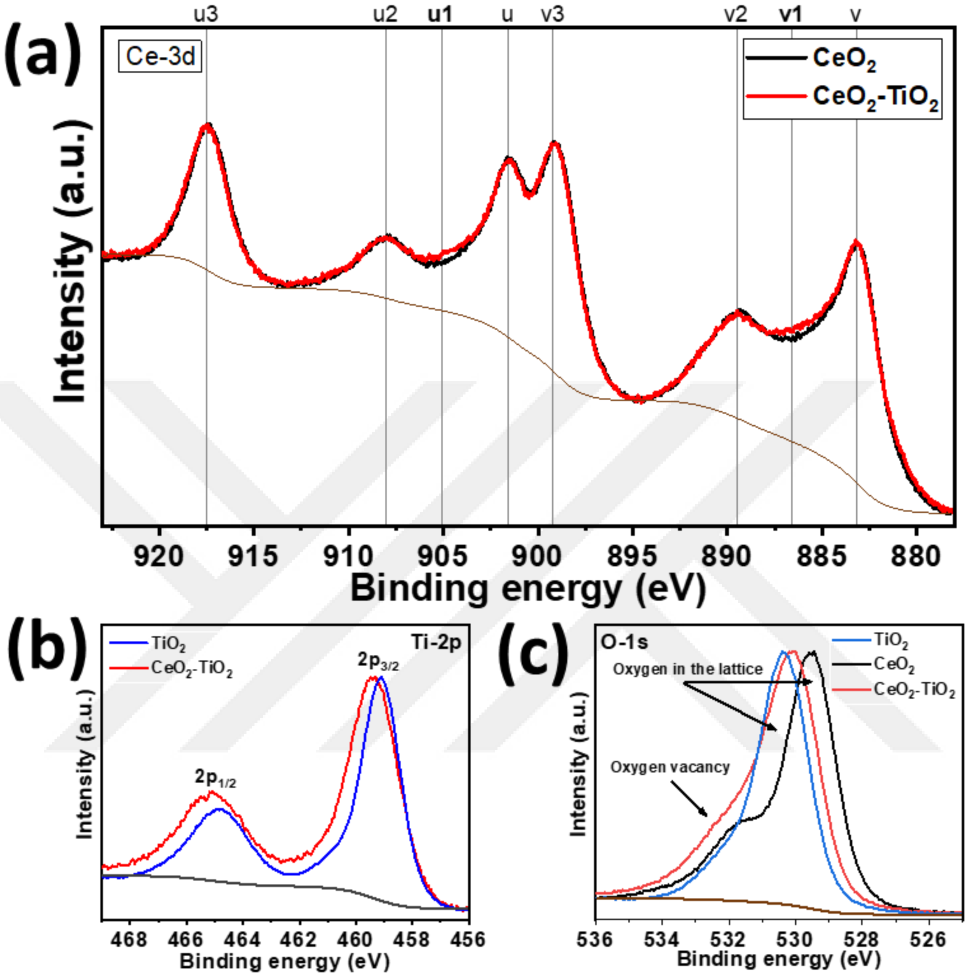

Figure 11.3. XPS spectra of **(a)** Ce 3d for CeO_2 and CeO_2-TiO_2. XPS spectra of Ti 2p for TiO_2 and **(b)** CeO_2-TiO_2. **(c)** XPS spectra of O1s TiO_2, CeO_2, and CeO_2-TiO_2.

As shown in **Figure** 11.3b, we observed differences in binding energies of Ti-2p core level (Ti-$2p_{3/2}$ and Ti-$2p_{1/2}$ spin-orbit splitting) acquired for TiO_2 and CeO_2-TiO_2 hybrid structures. The position of Ti-$2p_{3/2}$ (~459.0 eV) confirms that Ti is in Ti^{4+} state in the original TiO_2 thin film. On the other hand, there is a slight shift of binding energy towards higher value as well as the larger full width of half maximum of Ti-$2p_{3/2}$ peak for the CeO_2-TiO_2 hybrid structures. This can be interpreted by the formation of a very intimate composite between the two oxides that influences the structural environment of Ti^{4+}. Moreover, the formation of heterointerfaces between ceria and titania with different band bending, which can be a result of shown enhanced photocatalytic performance.[292,301] Similarly we observed differences in oxygen binding energies of TiO_2 and CeO_2-TiO_2 as shown in **Figure** 11.3c. In general, low binding energies given by O-1s peak confirm the presence of oxygen (O_1) in the lattice. In contrast, high oxygen binding energies (shifted by ~2.5 eV) are related to the presence of a higher amount of oxygen vacancies (O_2). Moreover, the peak located at around 533.3 eV (O_3) for the hybrid film could be an indication for adsorbed oxygen. The relative high area ratio O_2/O_1, (0.38) in the CeO_2-TiO_2 O-1s spectrum in comparison to that of TiO_2 (0.16) could point to an increase of oxygen vacancies.[300] Detailed deconvolution of O-1s core levels is shown in the supplementary information (**Figure** 11.15).

The photocatalytic activity of the prepared CeO_2-TiO_2 hybrid catalyst was first evaluated by degrading Methylene Blue (MB) under ultra-violet (UV) light irradiation (in comparison to bare TiO_2) as shown in **Figure** 11.4. The degradation of MB was evaluated by observing the change in the absorption of the initial concentration (C_0) divided by the final concentration (C) of the dye as a function of irradiation time (t); the corresponding results are shown in **Figure** 11.4. By fitting a first-order kinetic model we calculated rate constants (Table S1). As-deposited TiO_2 film exhibited a very low photocatalytic efficiency (k_1=1.4x10^{-4}/s) and after the heat-treatment, there was only a slight improvement (k_2=1.5x10^{-4}/s). On the other hand, after depositing a 6-8 nm CeO_2 layer a significant increase (k_3=6.9x10^{-4}/s) has been observed.

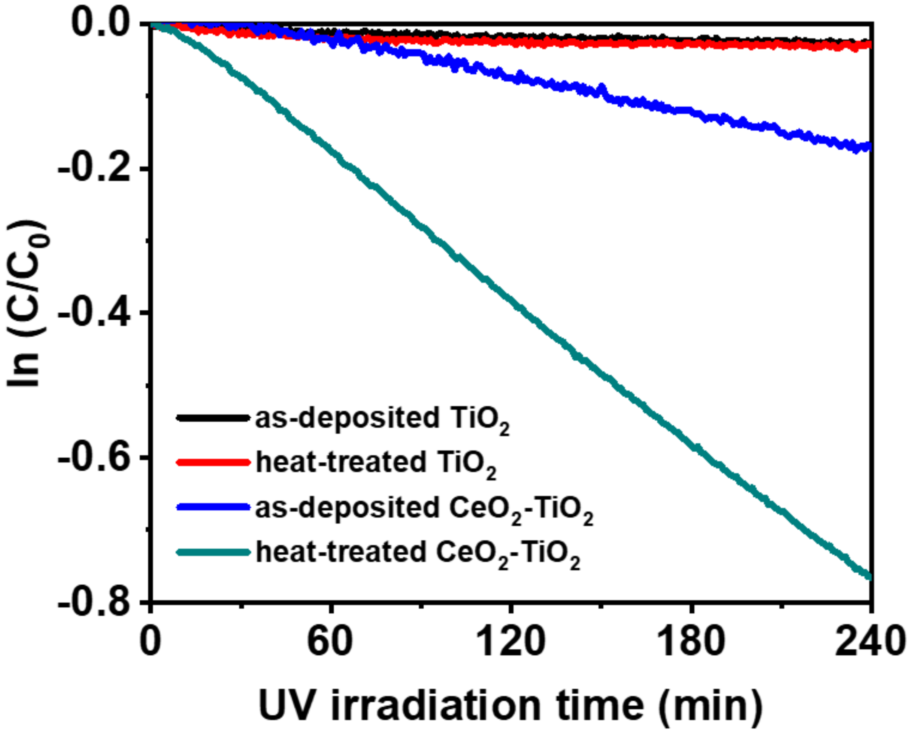

Figure 11.4. Plot of $\ln(C/C_0)$ versus reaction time for photocatalytic degradation of MB.

Following the heat-treatment, CeO_2-TiO_2 hybrid structures exhibit an extremely high photocatalytic efficiency with a rate constant of k_4=3.4x10^{-3}/s. This extremely high difference in rate constants indicates that it is not simply the effect of mixed oxide induced dynamic charge flow and separation due to band leveling effects between the corresponding conduction bands of CeO_2 and TiO_2.

It is believed that the confined structure of CeO_2 (on TiO_2 structures) and the CeO_2-TiO_2 interface are key factors for achieving such a high activity. For instance, when we increased the thickness of the CeO_2 deposit we achieved activities similar to bare TiO_2 (**Figure** 11.16). Therefore, we believe that the coexistence of both Ce^{3+}/Ce^{4+} states is important for the observed high activity. In other words, the fluorite structure probably plays a role in the behavior of reduced Ce and/or oxygen vacancy sites. This in accordance with studies which reported that oxygen vacancies alter their electron-capturing properties as a function of their isolated or associated nature, and basically such nature is a function of the CeO_2 primary particle size and other morphological variables.[302] The CeO_2-TiO_2 interface seems to stabilize electron-capturing oxygen-vacancy-related centers.[303]

In addition to analysis of the photocatalytic performance of CeO_2-TiO_2 by monitoring MB bleaching in aqueous solution, we verified the capability of photocatalytic bleaching in a non-aqueous environment. First, a thin MB layer was spin-coated onto a CeO_2-TiO_2 deposited quartz substrate. Prior to the spin-coating, we prepared a diluted MB solution using de-ionized (DI) water. Following the ultrasonication, the MB solution was mixed by a magnetic stirrer operating for 3h. Before the spin coating, the solution was filtered to eliminate any undissolved or agglomerated solid particles. **Figure** 11.5 shows the optical images of MB coated CeO_2-TiO_2 deposited quartz glass before and after 5 min irradiation. It is clearly seen that the MB layer was quickly decomposed by highly active CeO_2-TiO_2 structures. This indicates that such hybrid structures may be applicable for outdoor applications such as photocatalytic windows.

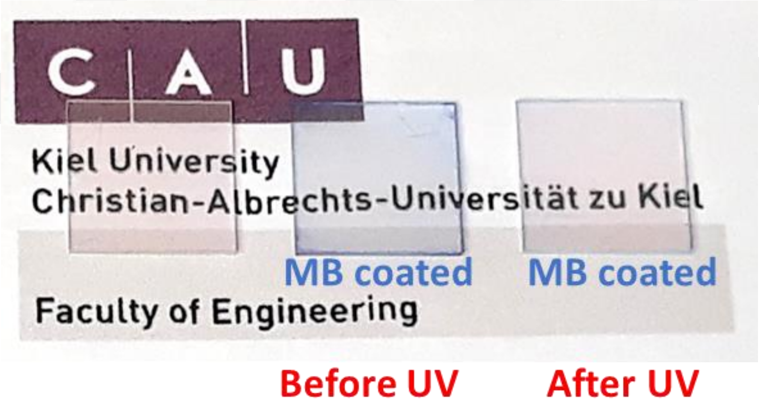

Figure 11.5. The optical image of MB coated CeO_2 -TiO_2 deposited quartz glass before and after 5 min UV irradiation.

To reveal the self-cleaning property of prepared CeO_2-TiO_2 hybrid structures, we treated the sample surface with oleic acid (as a model for organic contaminants) and afterward we monitored its photocatalytic decomposition by measuring the decrease in water contact angle (WCA) during UV irradiation. A diluted oleic acid solution in acetone (50 µL, 10 mmol/L) was prepared and drop-casted onto test samples. While a WCA of 30° was observed on CeO_2-TiO_2 hybrid structures; after oleic acid deposition, the WCA changed to 75° (**Figure** 11.6). This clearly indicated the contamination of the surface.

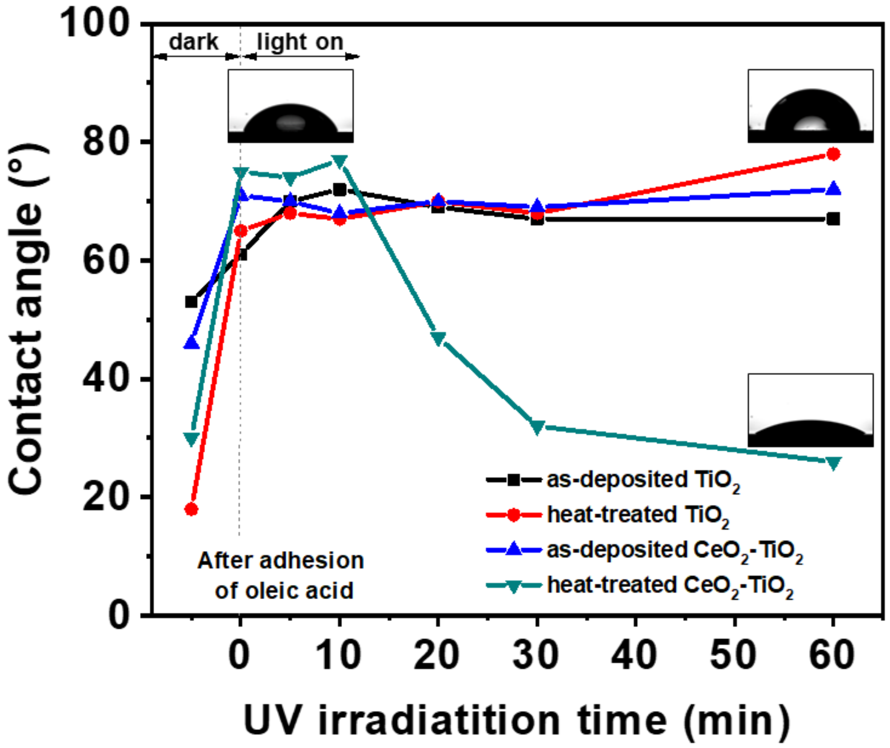

Figure 11.6. Changes in the water contact angle (WCA) of oleic acid-treated surfaces under UV light irradiation.

The oleic acid treated CeO_2-TiO_2 hybrid structures were exposed to UV light and, as a result, the WCA decreased gradually from 75° to 26° during 60 min irradiation time. The decrease in WCA after UV irradiation confirms the photocatalytic degradation of oleic acid by CeO_2-TiO_2 hybrid structures. On the other hand, WCAs of oleic acid on as-deposited and heat treated TiO_2, and as-deposited CeO_2-TiO_2 did not decrease during the same irradiation time. The self-cleaning ability of prepared samples was visualized by observing the change in the optical appearance of oleic acid residues after UV irradiation. As one can see in **Figure** 11.7 while the residue left after oleic acid treatment on CeO_2-TiO_2 hybrid structures vanished totally within 60 min of UV irradiation, residues on other samples persisted.

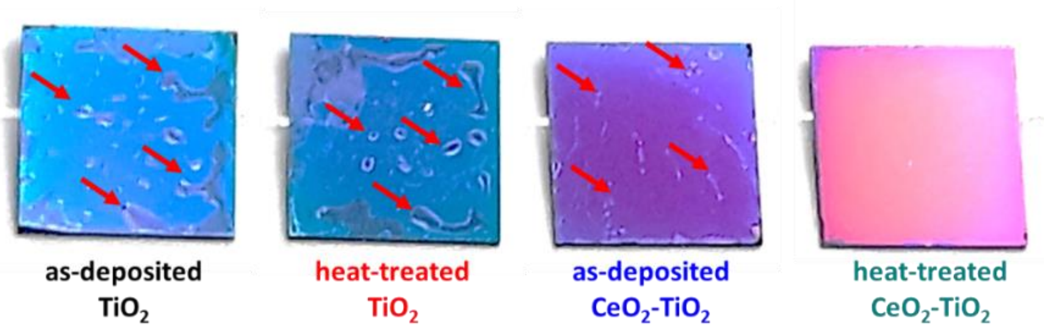

Figure 11.7. Optical images of oleic acid treated samples after 60 min UV irradiation (Red arrows represent oleic acid residues on the surface after 60 min UV irradiation.).

11.3 Conclusion

We fabricated cauliflower-like CeO_2-TiO_2 hybrid structures by a simple reactive sputtering method followed by heating and air-quenching. The heat-treatment induced the formation of nanocrack networks between well-separated columnar TiO_2 structures, enhancing the active surface area. Due to the lattice mismatch between CeO_2 (cubic fluorite structure) and TiO_2 (anatase), island-like re-organization of the CeO_2 layer during heat-treatment led to the formation of fine CeO_2 NCs. The formation of such fine clusters and the CeO_2-TiO_2 interface seems to stabilize electron-capturing oxygen-vacancy-related centers. Therefore, the prepared surfaces exhibit an extreme photocatalytic performance. Besides the high photocatalytic performance in an aqueous test medium, we showed that the same CeO_2-TiO_2 hybrid structures are able to effectively decompose non-aqueous organic contaminants (MB and oleic acid) within a few minutes. CeO_2-TiO_2 hybrid structures are promising for photocatalytic and self-cleaning outdoor and indoor applications.

Acknowledgments

S. Veziroglu acknowledges the Graduate Center and Federal State Funding, Christian-Albrechts-University of Kiel, for providing funding for his Ph.D. study. Authors would like to thank Stefan Rehders for his continuous support for building-up and the maintenance of deposition systems.

Supporting Information

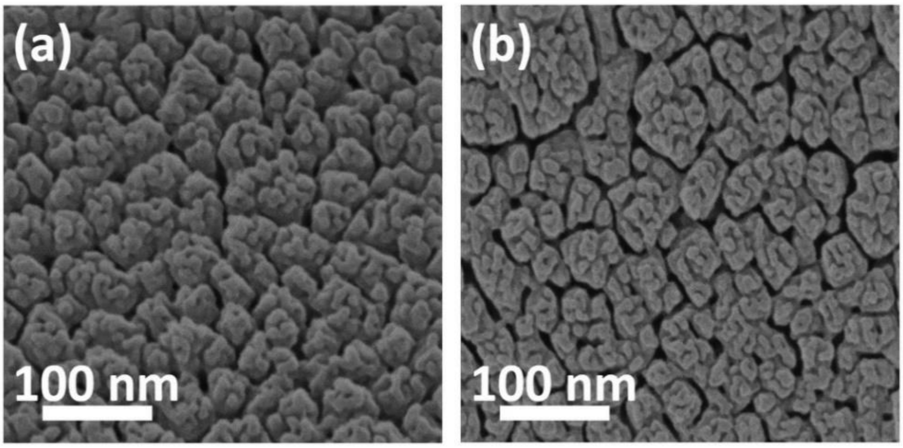

Figure 11.8. HIM images of heat-treated CeO_2-TiO_2 at different angles **(a)** 30^0 and **(b)** 0^0.

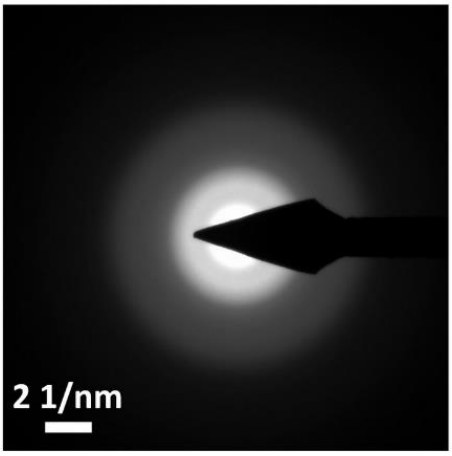

Figure 11.9. Selected-area electron diffraction (SAED) of as-deposited TiO_2.

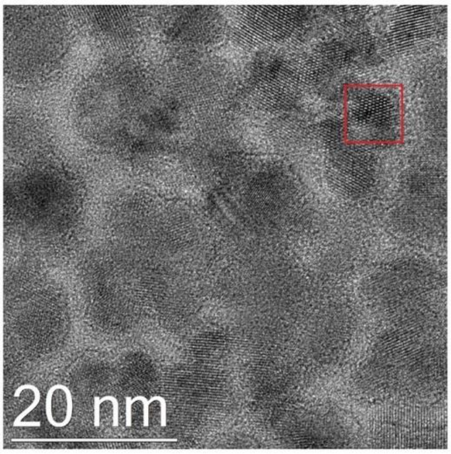

Figure 11.10. The high-resolution transmission electron microscopy (HRTEM) image of heat-treated CeO_2-TiO_2.

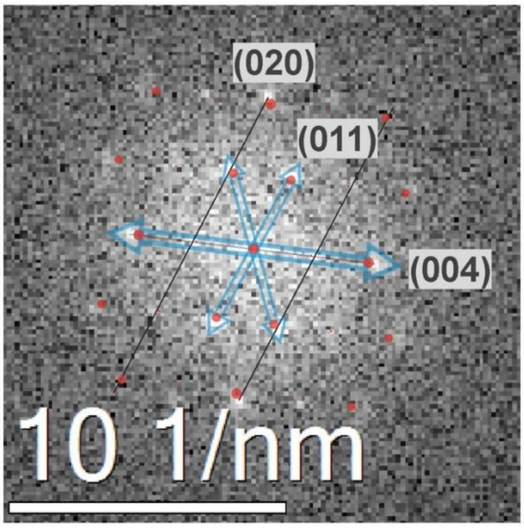

Figure 11.11. Fast Fourier transform (FTT) analysis of heat-treated TiO_2 structure.

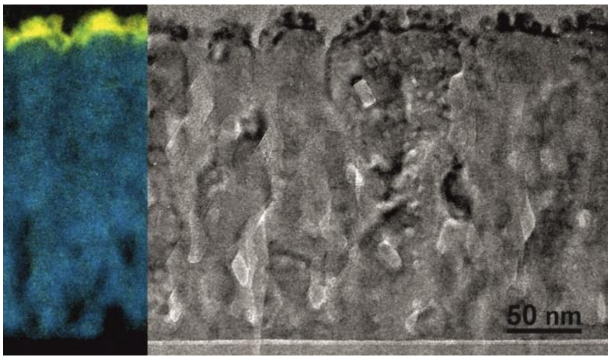

Figure 11.12. High-resolution transmission electron microscopy (HRTEM) image of the bi-layer (cross-section) prepared by focused ion beam (FIB). (The colored image on the left side is an energy filtered TEM-micrograph where yellow and turquoise represent cerium (Ce) and titanium (Ti) elements, respectively).

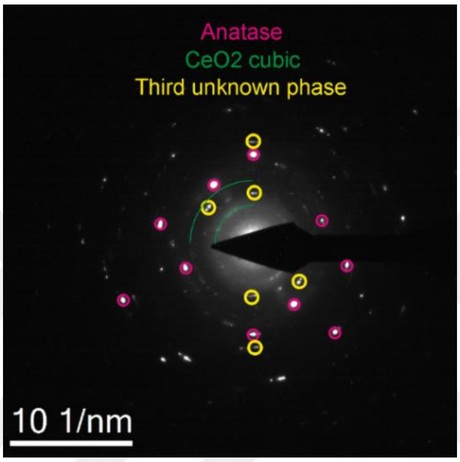

Figure 11.13. Selected-area electron diffraction (SAED) of the cross-section of heat-treated CeO_2-TiO_2.

The reflections clearly demonstrated the presence of both anatase and cubic CeO_2 phases. The anatase seems to be not epitaxially grown on Si-substrate. Additionally, we observed a third phase with d-spacings of 2.05 Å and 2.40 Å which might be attributed to either cubic TiO or a mixed oxide composed of one-third CeO_2 and two-third TiO_2.

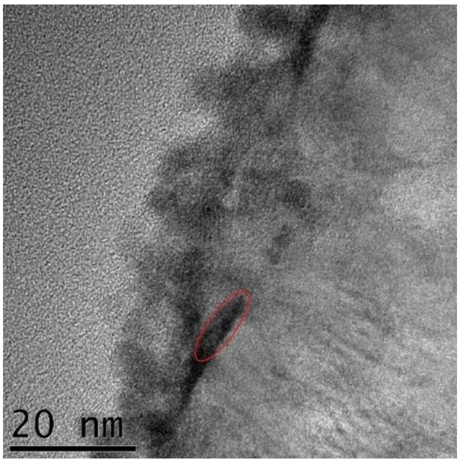

Figure 11.14. The high-resolution transmission electron microscopy (HRTEM) image of the cross-section of heat-treated CeO_2-TiO_2.

In HRTEM analysis we observed a different phase, which was neither a CeO_2 nor a TiO_2 phase, at CeO_2-TiO_2 interface, too. Only in few cases we could observe a clear interface between CeO_2 and this third phase (area marked by red color shown in **Figure** 11.14). Here 5-nm-thick CeO_2 crystals were essentially randomly arranged as it can be seen in **Figure** 11.12 and **Figure** 11.14.

On the other hand, this third phase was neither observed in top-view HRTEM nor SAED. This might be due to a special texture of this third phase; or mostly probably FIB-preparation might have induced a structural artifact.

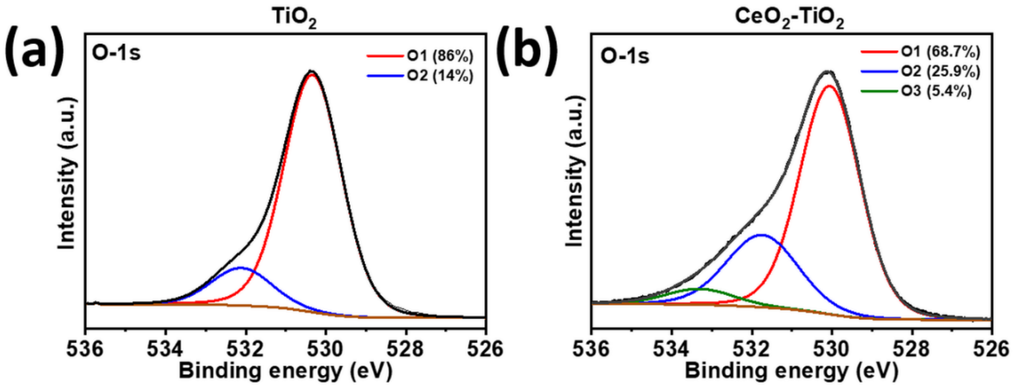

Figure 11.15. Detailed deconvolution of a high-resolution XPS O-1s for: **(a)** TiO_2 and **(b)** CeO_2-TiO_2 hybrid structure.

Table 11-1. Kinetics rate constants (k) for photocatalytic degradation of MB by prepared thin film photocatalysts. **(Kinetics rate constants (k) were calculated according to $\ln(C/C_0)=k.t$).**

Photocatalysts	Rate Constant (s^{-1})
as-deposited TiO_2	-0.14×10^{-3}
heat-treated TiO_2	-0.15×10^{-3}
as-deposited CeO_2 - TiO_2	-0.69×10^{-3}
heat-treated CeO_2 - TiO_2	-3.40×10^{-3}

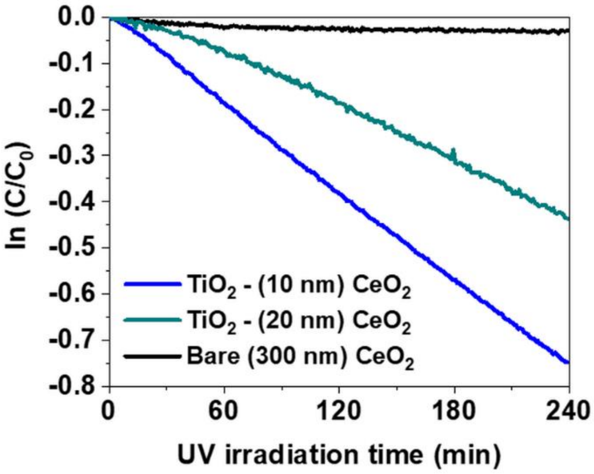

Figure 11.16. The plot of $\ln(C/C_0)$ versus reaction time for photocatalytic degradation of methylene blue (MB) at different CeO_2 thicknesses.

6 • No. 4 • February 22 • 2019

w.advmatinterfaces.de

ADVANCED MATERIALS INTERFACES

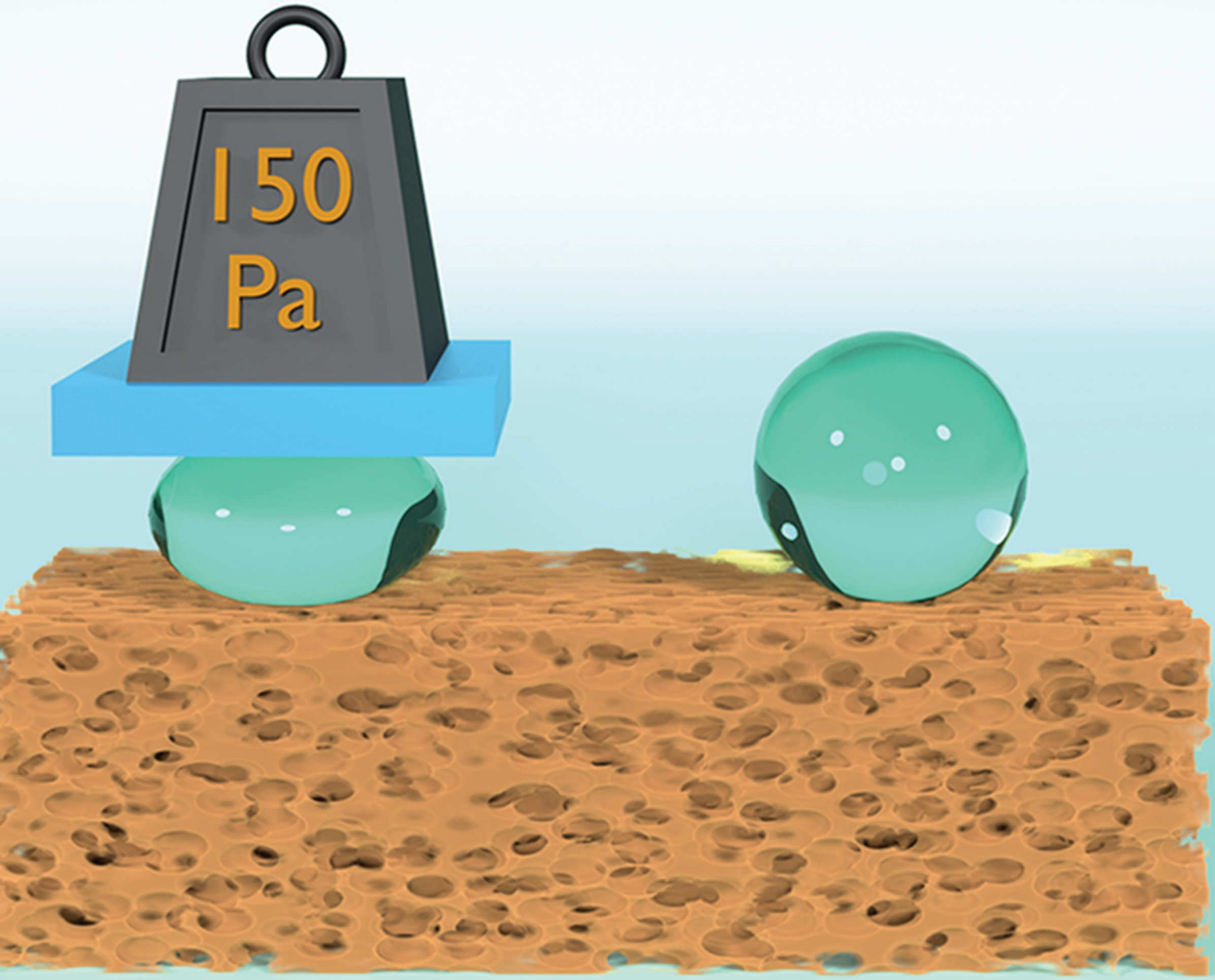

ILEY-VCH

12 Superhydrophobic 3D Porous PTFE/TiO₂ Hybrid Structures

This chapter is based on an article published in Advanced Materials Interfaces.[304]

Reprinted with permission from Oral Cenk Aktas, Stefan Schröder, Salih Veziroglu, Muhammed Zubair Ghori, Ayman Haidar, Oleksandr Polonskyi, Thomas Strunskus, Karen Gleason, Franz Faupel
Adv. Mater. Interfaces 2019, 6, 1801967.
The article is available via the internet at https://doi.org/10.1002/admi.201801967

Abstract

Combining hard-templating and infiltration processes, micro- and nanoscale topography induced by 2D assembling of TiO_2 nanoparticles is extended to 3D TiO_2. By applying an ultrathin and highly conformal polytetrafluoroethylene (PTFE) layer on prepared 3D TiO_2 via initiated chemical vapor deposition (iCVD), a robust superhydrophobic bulk material (3D PTFE/TiO_2) is achieved. A comparative study is conducted to reveal the stability of Cassie state for 3D PTFE/TiO_2 against the external pressure by squeezing a water droplet between 2D and 3D PTFE/TiO_2 structures. The use of such a stable 3D superhydrophobic PTFE/TiO_2 structure for the controlled release medium is shown by a case study.

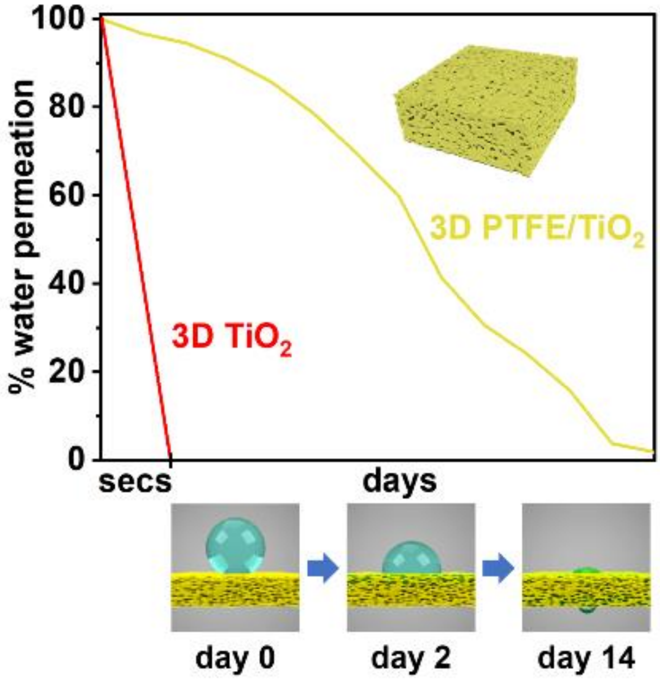

12.1 Introduction

For preparing a superhydrophobic surface, both low surface energy and micro/nano-level surface roughness should be considered.[305] Such a synergy between the topography and surface chemistry can be achieved either by inducing roughness on low surface energy materials or by applying them as a coating on rough surfaces.[306] Coating a low surface energy material on a micro- and nanostructured surface is the mostly preferred approach to achieve a superhydrophobic surface.[307] Micro- and nanostructures lead to an extremely high surface area which provides a giant energy barrier to create a liquid-solid interface.[308] Here the entrapped air plays a major role, as Cassie model states such air trapped within surface features forms a composite (solid/air) hydrophobic surface, resulting in a larger contact angle (CA).[309]

Superhydrophobic coatings get easily damaged and are not durable since their non-wetting behaviour exists only on the surface of the materials.[310] Once the active surface is damaged or partially removed, superhydrophobicity properties vanish easily. Such 2D surfaces provide a metastable superhydrophobic state since the limited entrapped air in such surfaces disappears quickly in contacting with water and the surface gets completely wetted within a short time. In contrast, 3D structures maintain trapped air at the surface and as well as through whole bulk.[311] These kinds of structures may provide a stable and long-running superhydrophobicity since penetrating water will meet continuously with a fresh trapped-air barrier. It is essential to extend the surface topographies responsible for superhydrophobicity into the bulk by creating both roughness and low surface energy to achieve superhydrophobic 3D materials.

12.2 Experimental Section

12.2.1 Fabrication of 2D and 3D TiO_2

2D TiO_2 was prepared through tape casting method, and the slurry consists of TiO_2 nanoparticles (Sigma Aldrich) with an average size of 20-25 nm, binder (87-89% hydrolyzed polyvinyl alcohol with Mw 85,000-124,000), dispersant (BYK110) and solvent (water: ethanol: isopropanol = 75:15:10 v/v %). The slurry was ball-milled for 5 h, and it is subsequently degassed in a vacuum oven for 45 minutes. The green layer (thickness = 200μm–225μm) was obtained by a double doctor blade coating on a quartz substrate, and then it was dried for 24 h at room temperature. The dried green sheet was sintered at 800–850°C. We used solution-immersion process where polyurethane (PU) foam (with PPI of 60-80) was used as the sacrificing template. After cutting the PU foam in the desired shape, it was immersed into the TiO_2 slurry (explained above) for 2 h under ultrasonication. Afterwards the excessive amount of slurry was cleaned away from the surface of PU foam and the foam was dried at room temperature for 24 h. Then a gradual heat treatment was applied to sacrifice PU (RT to 500 °C at heating rate of 5°C/min) and two steps (600-650 °C, 2 h and 800-850 °C, 3 h) sintering was applied to get 3D TiO_2 skeleton (see schematic presentation in given **Figure** 12.5 and **Figure** 12.6, Supporting Information).

12.2.2 PTFE Coating with iCVD

Polytetrafluoroethylene (PTFE) thin films were deposited on 2D and 3D TiO_2 inside a custom-built reactor operating at a base pressure of 0.375 mTorr. Perfluorobutanesulfonylfluoride (PFBSF) was used as the initiator while hexafluoropropylene oxide (HFPO) was used as the monomer. Nichrome filaments were resistively heated at temperature less than 400 ℃ and the substrate surface was cooled down to 20 ℃. Monomer and initiator were introduced into the reaction chamber using a needle valve for PFBSF vapor and mass flow controller for HFPO. The deposition time was 5 minutes to yield a thickness around 10 nm.

12.2.3 Surface Characterization

Morphology of 2D and 3D TiO_2 structures were observed before and after PTFE coating by using an SEM (Zeiss Ultraplus operating at 3 kV and 15 mA). XPS data were acquired using a spectrophotometer (X-ray photoelectron spectroscopy-XPS, Omicron Nano- Technology GmbH). The setup was operating with an Al Kα X-ray source at a power of 240 W. CasaXPS software was used to perform a quantitative analyses and detailed peak deconvolution. The spectra were charge-referenced by using aliphatic carbon C1s at 285.0 eV. Raman spectral measurements were performed on a confocal Raman spectroscopy (WITec, alpha300AR) with laser excitation line 532 nm, a power of 5 mW in the range of 200-1600 cm^{-1} with spectral resolution 5 cm^{-1}. Integration time was kept for 20 s and spectra were recorded as the average of five measurements.

12.2.4 Wettability Analysis

Contact-angle measurements were performed using a contact-angle meter (OCA 30, Dataphysics). For static contact-angle measurements, 2 µL of water droplets were used and advancing/receding contact angles were videotaped and measured by the addition and subtraction of water to/ from droplets sitting on the surfaces. A custom-built contact-compress-release set-up was used to analyze the stability of Casie state of prepared TiO_2 structures. First, a sessile water droplet was immobilized on the 2D PTFE/TiO_2, which acted as the upper plate and then with the help of micro-screw bottom plate (test plate) was gradually raised up. During squeezing the droplet between two plates, the change in the contact angle was videotaped and analysed. Water permeation through 3D PTFE/TiO_2 was analysed by a custom built test set modified from Tuvshindorj et al.[312]

12.3 Results and Discussion

Herein, a commercially available polyurethane (PU) foam was utilized as the sacrificial hard template to infiltrate TiO_2 nanoparticles in its interstitial pores. By simply burning out PU template and sintering at 850-900°C, a 3D TiO_2 skeleton (forming inner and outer macropores) was achieved by 2D assembling of TiO_2 nanoparticles through the whole bulk. By combining macrolevel pores and the micro-/nanostructured topography, a 3D high surface roughness was achieved (**Figure** 12.1a and **Figure** 12.5, Supporting Information).

The prepared TiO_2 slurry was also applied to planar quartz substrates by double-doctor blade coating technique to achieve micro-/nanostructured 2D TiO_2 (**Figure** 12.1a and **Figure** 12.6, Supporting Information). Afterwards, initiated chemical vapor deposition (iCVD) was carried out to coat 2D and 3D TiO_2 homogenously with a thin layer of polytetrafluoroethylene (PTFE) while conserving the inner micro- and nanotopography (as shown schematically in **Figure** 12.1b). iCVD allows coating various types of substrates varying from simple 2D to complex 3D structures with a high conformity (without altering topographic details of the pristine structure).[313] After coating a thin layer of PTFE, 3D TiO_2 showed an extraordinary superhydrophobicity.

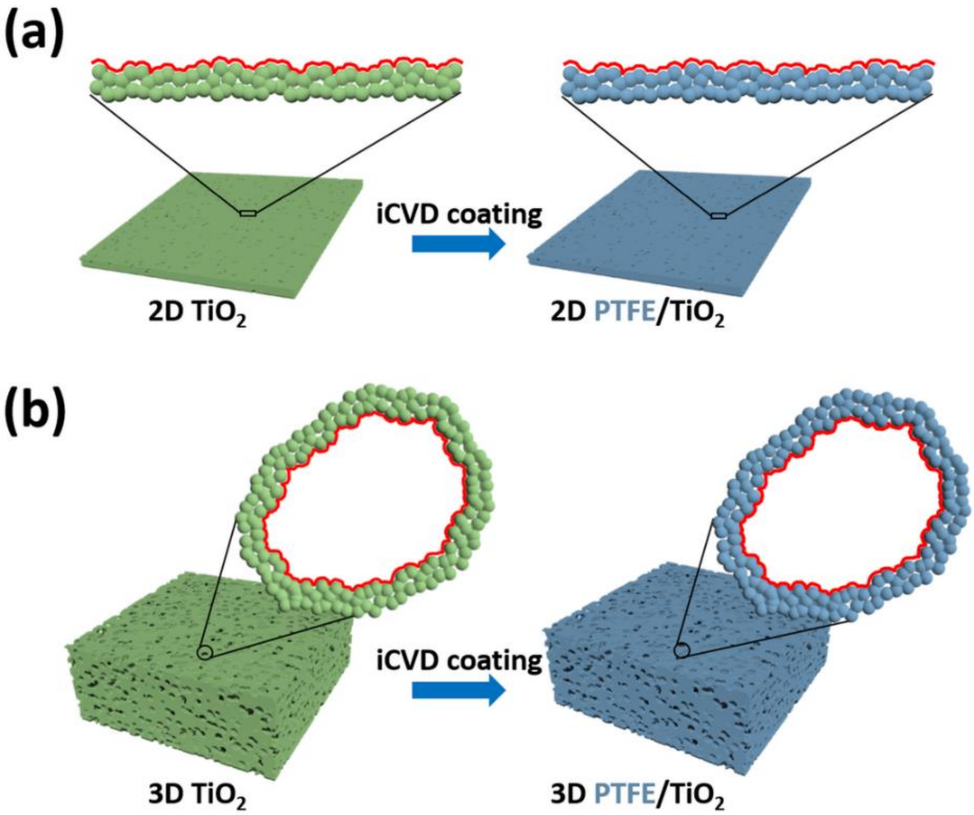

Figure 12.1. Schematic representation of surface modification by iCVD (PTFE coating) without altering the surface topography **(a)** from 2D TiO_2 to 2D PTFE/TiO_2 and **(b)** from 3D TiO_2 to 3D PTFE/TiO_2. Red curvy lines represent line profile of the surface topography (identical line profiles, before and after iCVD, indicate the conservation of the surface topography)

3D TiO_2 has a porous structure with the pore size of ≈100-150 μm (**Figure** 12.2a) and exhibits approximately the same micro- and nanoscale structures with 2D TiO_2 surface prepared for the comparison by the well-established doctor blade technique.[314]

While 2D surface was composed of micro/nano hierarchical porous texture, 3D surface consists additionally macro-pores (**Figure** 12.2a). Clearly micro- and nanoscale roughness was provided through the whole bulk in 3D TiO_2. Following the iCVD step, we did not observe any significant change in the morphology of both 2D and 3D TiO_2. This indicates that the deposited PTFE layer was extremely thin and highly conformal. **Figure** 12.2b shows the XPS survey spectra of the uncoated and coated 3D TiO_2. Simply coated sample (PTFE/TiO_2) contains fluorine peaks (F-KLL and F1s) confirming the presence of a PTFE layer.[315–317] The deposited PTFE layer seemed to be extremely thin (≤10 nm) since Ti 2s and Ti 2p peaks were still detectable (as seen in also uncoated 3D TiO_2). Since XPS sampling depth is limited to a few nm (around ~10 nm), additionally we conduced Raman spectroscopy to compare chemical composition of PTFE through 3D PTFE/TiO_2 with that of a reference bulk PTFE. As shown in **Figure** 12.2b both spectra look quite similar and this indicates a good conformal coating through the whole bulk.[318]

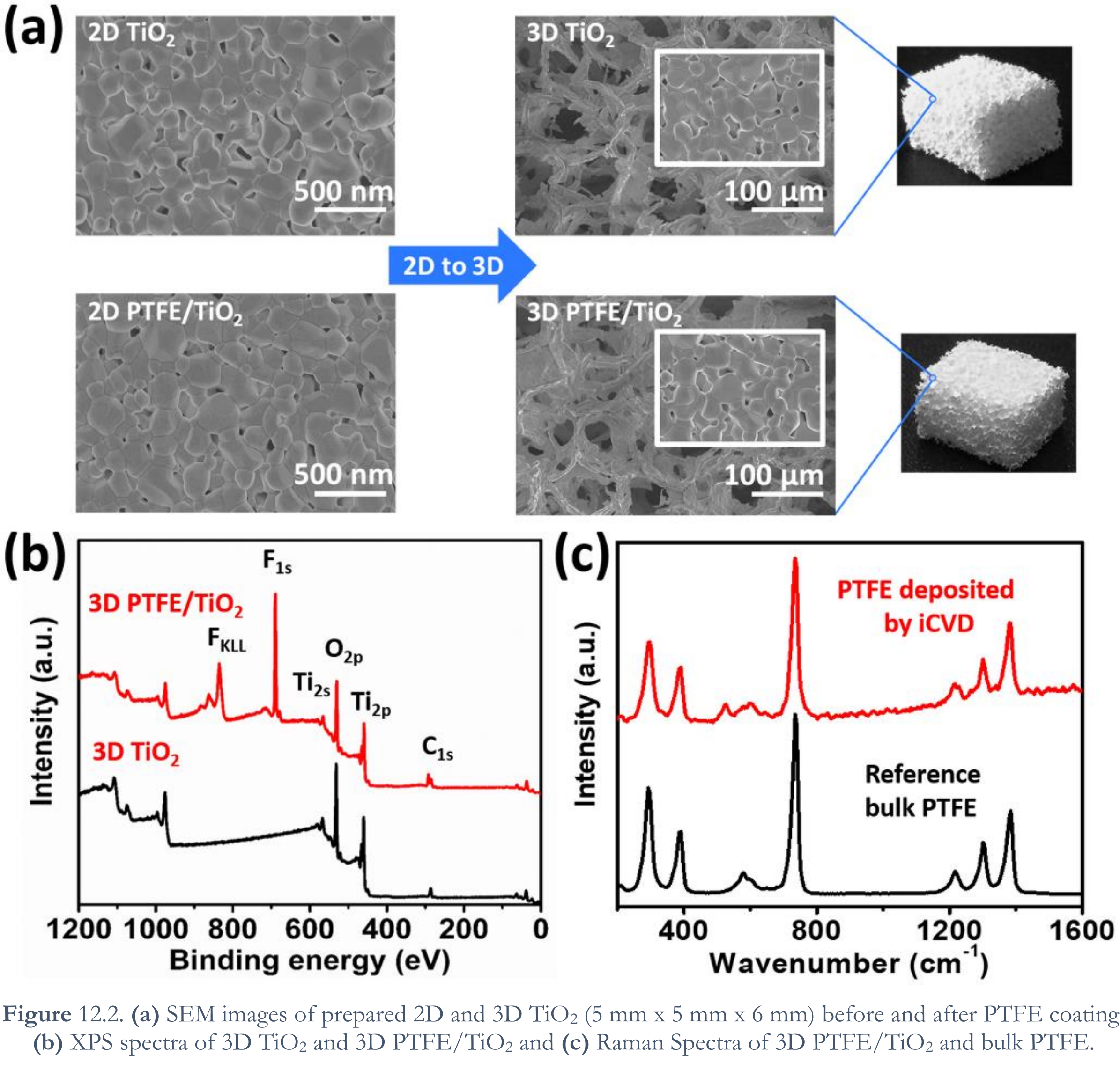

Figure 12.2. **(a)** SEM images of prepared 2D and 3D TiO_2 (5 mm x 5 mm x 6 mm) before and after PTFE coating, **(b)** XPS spectra of 3D TiO_2 and 3D PTFE/TiO_2 and **(c)** Raman Spectra of 3D PTFE/TiO_2 and bulk PTFE.

Since water droplets do not come to rest on especially 3D PTFE/TiO_2, we tried to deduce the wetting behavior by videotaping many advancing and receding angles. A 2 µl volume water drop was initially brought in contact with the sample surface and subsequently, the volume of the drop was increased and then decreased to advance and retract the liquid front. This was repeated several times to check the reproducibility of the results.

Figure 12.3a shows the advancing and receding conditions created by dispensing and retracting water at a rate of ~0.20 µl/s. By pushing the droplet on the surface advancing contact angle (θ_A) was measured around 167 ± 2°. We measured a slightly lower receding angle (θ_R) of 164 ± 2° just before the droplet detaches from the surface.

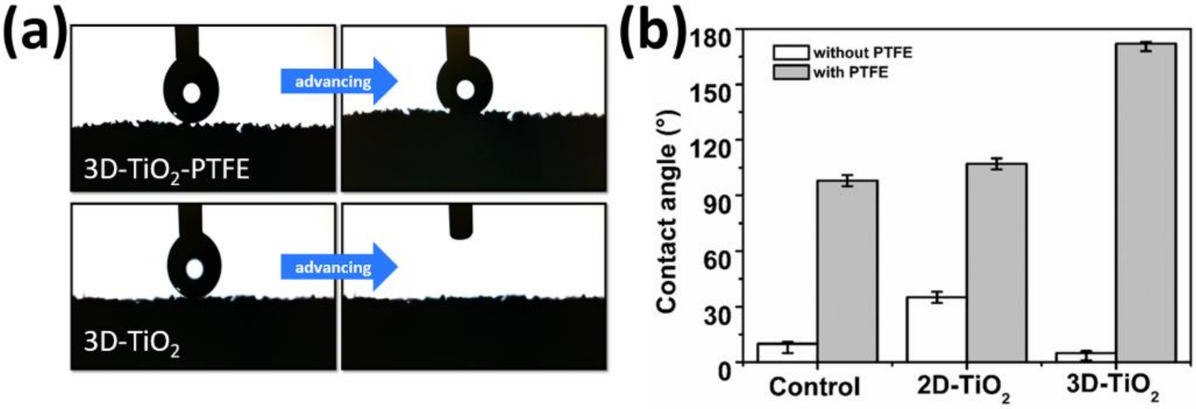

Figure 12.3. **(a)** Advancing/Receding states on 3D TiO_2 and 3D PTFE/TiO_2 **(b)** Static contact angles measured on a smooth (prepared by sputtering), 2D and 3D TiO_2 before and after PTFE coating by iCVD.

When we tried to bring a water droplet in contact with 3D TiO_2 surface, we observed that water droplet was sucked into the porous structure (**Figure** 12.3a) which might be due to high capillary interaction [319]. It is known that high oxygen adsorption capacity and defect sites on TiO_2 imparts superhydrophilicity.[320] According to Wenzel state, increasing roughness of such hydrophilic component will lead to super wetting condition.[321] We purposely chose TiO_2 to show the tuning of wetting angle over a wide range approaching to 170°. In comparison to 3D TiO_2, we could tune CA only from 35° to 123° on 2D TiO_2 after PTFE coating (**Figure** 12.3b). We observed that CA (112°) on 2D PTFE/TiO_2 exceeded that achieved on the reference (smooth) PTFE coating, and this indicates the contribution of the micro-and nanoscaled topography to the non-wetting behavior. On the other hand, clearly this 2D topography was not as effective as the 3D TiO_2 for attaining a water repelling state; instead the water droplet was pinned on the texture.

Determining contact angles exceeding 160°-170° (especially when water droplets do not come to rest on a horizontal surface) by using conventional static analysis is not trivial. Recently we presented an alternative approach by recording a videotape during compressing a water droplet attached to a relatively hydrophobic surface with a counter superhydrophobic (to be tested) surface.[322] This method is known as the contact-compress-release technique.[323] Here, the sessile droplet was supported on 2D PTFE/TiO_2 surface and then the superhydrophobic 3D PTFE/TiO_2 was raised up towards this sessile drop. This allowed us to reveal a contact angle, θ_A of 167 ± 2° which is very close to the one as we measured by analyzing video recorded advancing and receding angles (**Figure** 12.4a, Stages 1-2).

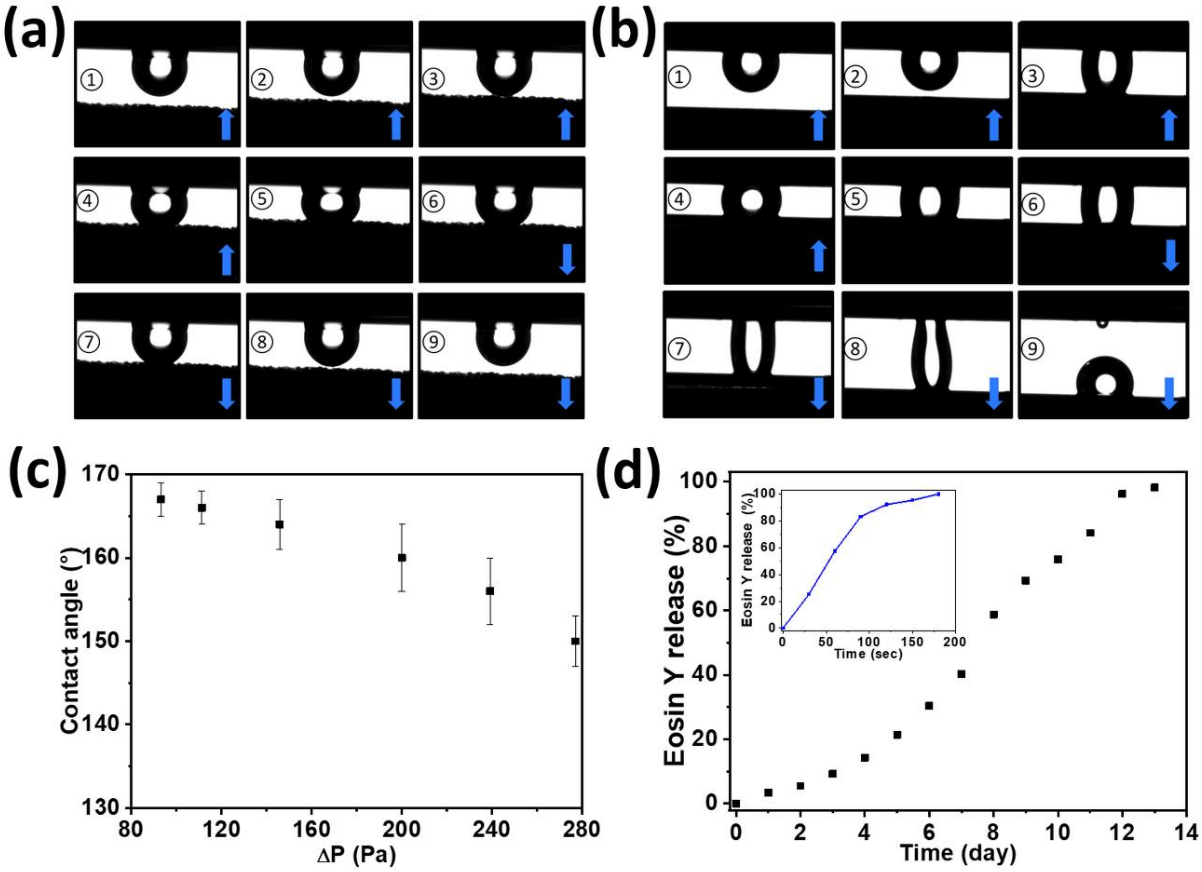

Figure 12.4. Testing stability of Casie state (by Contact-Compress-Release method) of **(a)** 3D PTFE/TiO_2 and **(b)** 2D PTFE/TiO_2 (blue arrows show the movement direction). Graphical presentation of **(c)** The change of contact angle on 3D PTFE/TiO_2 by the applied external pressure and **(d)** The comparison of the water penetration profile of 3D TiO_2 and PTFE/TiO_2.

We extended the use of contact-compress-release approach to estimate the tendency of the transition from the Cassie state to the Wenzel state. Basically, we compressed the attached water droplet between 2D and 3D PTFE/TiO_2 plates with the help of a micrometric screw system. By measuring the gap, d between two plates we deduced the applied pressure (ΔP) using the Laplace equation:[312]

$$\Delta P=\gamma\,|\cos\theta_{\mathrm{Bottom}} + \cos\theta_{\mathrm{Top}}|/d, \text{ for } d << R$$

where γ is the surface tension of the water, R is the radius of the droplet, d is the gap between bottom (3D PTFE/TiO_2) and top (2D PTFE/TiO_2) plates, $\cos\theta_{\mathrm{Bottom}}$ and $\cos\theta_{\mathrm{Top}}$ are the water contact angles of bottom and top plates, respectively.

In **Figure** 12.4b, Stages 1-9 show sequences of gradually squeezed water droplet attached to 2D PTFE/TiO_2 by moving the superhydrophobic 3D PTFE/TiO_2 upwards. For each pressure ΔP, we took micrographs of the edge of the drop in order to deduce the contact angle θ and to plot it as a function of ΔP (**Figure** 12.4b). We did not observe any significant change in the CA even at high pressures reaching to 145 Pa, indicating the stability of trapped air in 3D PTFE/TiO_2. At pressures above 200 Pa, the CA started to decline which can be interpreted as the penetration of the water drop partially inside 3D

PTFE/TiO_2 texture, transition to Wenzel state. We observed the clear decrease of the contact angle to 150 ± 5°, but after releasing the pressure the drop recovered its previous geometry (**Figure** 4b, Stages 7-9). We do believe that the inorganic core of our 3D structure provides a high stability. Kim et al. prepared a superhydrophobic sponge (totally organic based material) using iCVD, where both 3D porous core structure and coated layer are both organic.[324] Our 3D hybrid structure (PTFE: organic layer and TiO_2: inorganic skeleton) seem to resist chemical and physical environment better.

In case of squeezing a water droplet of the same volume between identical hydrophobic 2D PTFE/TiO_2, the situation was totally different (**Figure** 12.4c). Just after squeezing the water drop with raising up of the counter 2D PTFE/TiO_2 surface we saw a strong interaction with the surface texture (bottom plate). This showed clearly that the trapped air was not sufficient enough (in comparison to that of 3D TiO_2) to prevent water pinning; after relaxing the applied pressure we observed splitting of the droplet into two pieces. The formation of the larger droplet at the bottom plate indicated a strong interaction with the surface texture; here also the gravity effect might have played a role, too.

We used a simple experimental setup (**Figure** 12.7, Supporting Information), in which 3D PTFE/TiO_2 was used as a membrane to monitor the water penetration characterizes. This membrane was sealed to a glass tube and all were placed at the top of a beaker. The upper tube was filled with a diluted Eosin Y solution and its penetration through the 3D PTFE/TiO_2 membrane to the beaker filled with water was monitored. Basically, the penetration of the colored solution was monitored by recording the increase in absorption (by UV-Vis spectroscopy). **Figure** 12.4d shows the penetration profiles correlated with the recorded absorption spectra. This approach may lead to various controlled release mechanism including drug release since both PTFE and TiO_2 are known as biocompatible materials. In recent years the use of porous superhydrophobic structures have been proposed for drug delivery applications; but most of these materials are producible in only mat form which have a limited thickness.[311] In comparison, our approach allows the fabrication of mm-to-cm superhydrophobic 3D structures.

12.4 Conclusion

In summary, we turned highly porous and extremely hydrophilic 3D TiO_2 into a superhydrophobic material with the aid of the iCVD process. Due to the porous nature of the 3D TiO_2 and the inherent hydrophobicity of the fluorine-based PTFE we achieved a bulk superhydrophobicity. We verified the stability of 3D PTFE/TiO_2 hydrophobicity using the contact-compress-release technique. As an example, a controlled release mechanism was also demonstrated. Such a release mechanism can find applications in drug delivery systems.

Acknowledgments

Authors would like to thank Stefan Rehders for the design and fabrication of the custom iCVD and the German Research Foundation (DFG) for financial support within the frame of Research Training Group GRK 2154.

Supporting Information

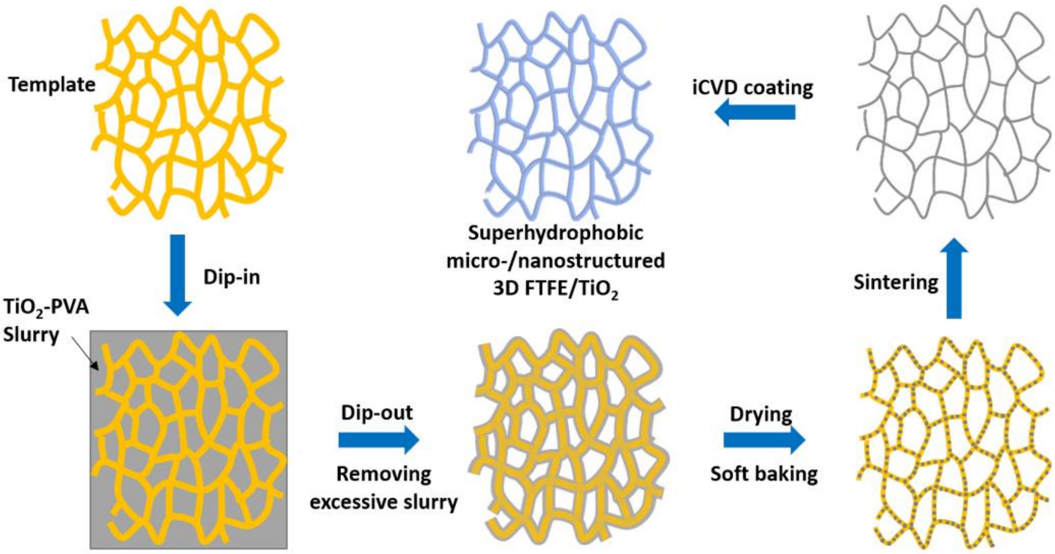

Figure 12.5. Preparation of 3D PTFE/TiO_2

A porous PU sponge (60-80 ppi, New England Foam, Inc.) was used as the hard template. The slurry for 3D TiO_2 fabrication was prepared by dissolving polyvinyl alcohol (PVA, Sigma Aldrich-Mw 85,000-124,000, 87-89% hydrolyzed) in deionized water and alcohol mixture (water: ethanol: isopropanol = 75:15:10 v/v %) at a ratio of 0.02 mol/L at 75 C for 1 hour. After adding three droplets of surfactant (BYK 110) and 20-25 nm TiO_2 nanoparticles (Sigma Aldrich) with concentrations of up to 55 wt-%, the slurry was ball-milled for 5 h, and it was subsequently degassed in a vacuum oven for 45 minutes. Afterwards PU was first cut into small cubes of 5 mm x 5 mm x 6 mm and these cubes were immersed into prepared slurry for 2 h under ultrasonication. The modified PU sponges were then taken out. The excess of coating solution on the surface was swiped with a tissue paper and then cubes were dried at room temperature for 24 h. Then a gradual heat treatment was applied to sacrifice PU (RT to 500 °C at a heating rate of 5 °C/min) and two steps (600-650 °C, 2 h and 800-850 °C, 3 h) sintering was applied to get 3D TiO_2 skeleton.

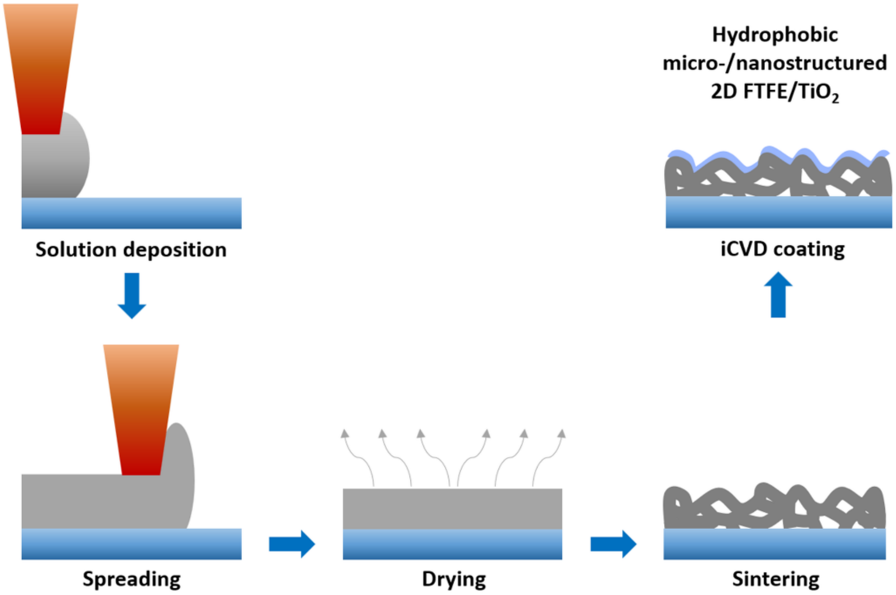

Figure 12.6. Preparation of 2D PTFE/TiO$_2$.

For 2D TiO$_2$, different than templating doctor blade technique was used. The green layer (thickness = 200 μm–225 μm) was obtained by a double doctor blade coating (doctor blade head with a width of 50 mm was set at a height of 500-600 μm and casting rate was set to 5 mm/sec) of the TiO$_2$ slurry given above (**Figure** 12.5) on a quartz substrate, and then it was dried for 24 h at room temperature. The dried green sheet was sintered at 800–850 °C.

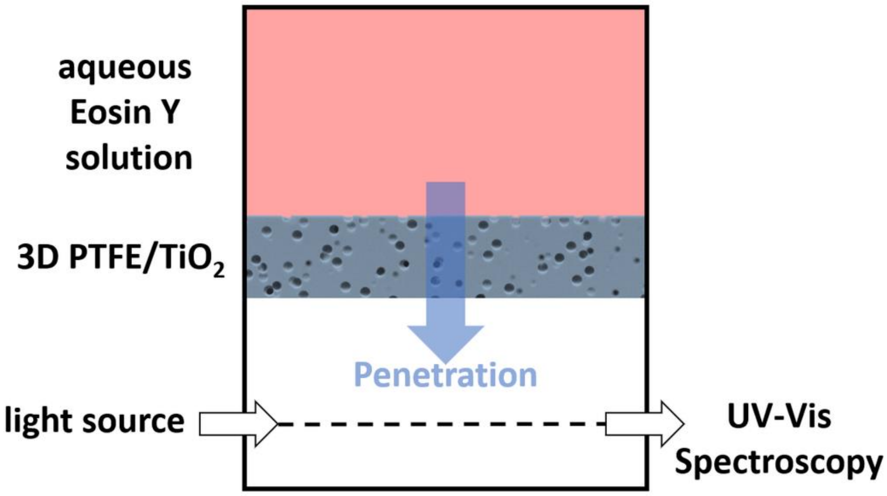

Figure 12.7. Schematic presentation of the permeability set-up.

13 Summary & Conclusion

Within this dissertation, functional metal oxides surfaces were studied and examined for photocatalytic, self-cleaning, and micro-/nanostructuring applications, which were outlined by nine research papers as followings:

1. Ultra-fast degradation of methylene blue by Au/ZnO-CeO_2 nano-hybrid catalyst, ***Mater. Lett.*** 209 (2017) 486–491.

2. Photocatalytic Growth of Hierarchical Au Needle Clusters on Highly Active TiO_2 Thin Film, ***Adv. Mater. Interfaces.*** 5 (2018) 1800465.

3. Photo-deposition of Au Nanoclusters for Enhanced Photocatalytic Dye Degradation over TiO_2 Thin Film, ***ACS Applied Materials and Interfaces.*** 12, (2020) 14983.

4. Plasmonic and non-plasmonic contributions on photocatalytic activity of Au-TiO_2 thin film under mixed UV-Visible light, ***Surface & Coatings Tech.*** 389, (2020) 125613.

5. Ag Nanoparticles Decorated TiO_2 Thin Films with Enhanced Photocatalytic Activity, ***Phys. Status Solidi Appl. Mater. Sci.*** (2019) 1800898.

6. Role of UV Plasmonics in the Photocatalytic Performance of TiO_2 Decorated with Aluminum Nanoparticles, ***ACS Appl. Nano Mater.*** 1 (2018) 3760–3764.

7. PdO Nanoparticles Decorated TiO_2 Film with Enhanced Photocatalytic and Self-Cleaning Properties, ***Materials Today Chemistry.*** 16 (2020) 100251.

8. Cauliflower-like CeO_2 –TiO_2 hybrid nanostructures with extreme photocatalytic and self-cleaning properties, ***Nanoscale.*** 11 (2019) 9840–9844.

9. Superhydrophobic 3D Porous PTFE/TiO_2 Hybrid Structures, ***Adv. Mater. Interfaces.*** 6 (2019) 1801967.

The prepared Au/ZnO-CeO_2 hybrid structure exhibits extremely high catalytic activity in the presence of $NaBH_4$, via electron relay process. It is shown that the incorporation of CeO_2 and ZnO triggers the dynamic switching between Ce^{3+} and Ce^{4+}, which has a huge effect on the catalytic properties of the hybrid structure. Also, the optimum ratio between CeO_2 and ZnO is crucial to provide a stable support for Au nanoparticles and promote the dynamic $Ce^{3+} \rightleftarrows Ce^{4+}$ conversion. However, active nanoparticles are prone to severe agglomeration (due to their high surface and reactivity), which drastically reduces their performance at long term. Moreover, it is difficult to remove/isolate these active nanoparticles from an aqueous medium by conventional methods after their use. This can create secondary pollution, which might lead to more serious problems for humans and nature. Au/ZnO-CeO_2 hybrid nanostructures acted as a clear model to reveal the mechanism of dynamic $Ce^{3+} \rightleftarrows Ce^{4+}$ conversion and its significant effects on the catalytic and photocatalytic properties. This study showed clearly that robust and immobilized systems, especially catalytic or photocatalytic thin films, are highly desired for water and air cleaning applications.

The catalytic and photocatalytic activity of thin films are extremely limited in comparison to colloidal materials (composed of micro- and/or nanoparticles) due to their limited surface area. However, the surface area and similar properties of thin films can be tuned by controlling the preparation or deposition parameters. Recently, the photocatalytically active (comparable with the performance of a colloidal system) sputter deposited TiO_2 thin film was demonstrated by the Chair for Multicomponents at Faculty of Engineering, Kiel University. Basically, the photocatalytic activity of this thin film can be controlled by a thermally induced nanocrack networks on the surface. Such nanocrack networks improve the photocatalytic activity of TiO_2 thin films significantly.

Decorating TiO_2 with metallic nanoparticles is another common approach used to enhance the overall photocatalytic performance via plasmonic, non-plasmonic, and heterojunction formation. Here the critical issue is to maintain a strong adhesion between metallic nanoparticles and TiO_2 thin film surface. In order to achieve a good adhesion between TiO_2 thin film surface and deposited micro- and nanostructures, a new photodeposition method is proposed. A photocatalytically active TiO_2 thin film rather than a usual TiO_2 colloid system was used to synthesize plasmonic and non-plasmonic metal structure by UV illumination. The proposed photocatalytic deposition (surfactant-free) method allowed good control of the size and shape of metallic micro- and nanostructures on the TiO_2 surface. Moreover, the proposed photodeposition method could be also used for local patterning of extremely sharp needle-like Au nanostructures on TiO_2 only by using a simple mask (published as Frontispiece from Advanced Materials Interfaces-Wiley). This approach can be a potential alternative to costly and time-consuming lithography techniques, especially in catalysis, sensor, and biomedical applications. Proposed photodeposition approach was used to control the surface coverage of TiO_2 by Au nanoclusters to achieve a photocatalytic activity. Basically, by altering the solvent type (acetone, isopropanol, and 1-hexanol) and the illumination time one can precisely control the formation of Au structures on TiO_2. This allows a well-controlled deposition (in terms of size and surface coverage) for also other metallic structures including Ag nanostructures (published as Front Cover from Physica Status Solidi (a) – applications and materials -Wiley).

The photodeposition method allows good control of the particle size and distribution on the TiO_2 surface. It also enhances the electron transferring between metal (e.g. Au) and semiconductor (e.g. TiO_2) due to the strong chemical adhesion between both structures. Prepared Au-TiO_2 hybrid structures showed higher photocatalytic activity in comparison to bare TiO_2 thin film (inducing non-plasmonic contribution) under UV illumination. We observed that also an optimum ratio between visible light (Vis) and ultra-violet (UV) light (Vis/UV) intensities is needed to achieve a high photocatalytic activity on TiO_2 thin film decorated with Au structures (inducing both plasmonic and non-plasmonic contributions).

Gas aggregation source (GAS) approach is also an effective way to produce metallic and metal oxide nanoparticles on TiO_2 thin film surface. Al nanoparticles were prepared with controlled shape, size, and crystallinity by controlling to deposition parameters. Surprisingly not only the positive but also the negative effect of local surface plasmon resonance (LSPR) on UV photocatalysis was revealed by irradiating Al/TiO_2 hybrid structure at two different UV wavelengths (280 and 365 nm) (accepted as Front Cover from ACS Applied Nano Materials). Afterward, magnetron sputtering and GAS approaches were combined for the preparation of columnar TiO_2 structures decorated with PdO nanoparticles. The steady equilibrium between the formation of PdO and PdO_2 under UV irradiation was demonstrated to foster the charge separation efficiency, and this enhanced the photocatalytic performance. Similarly, consecutive magnetron sputtering of TiO_2 and CeO_2 was used to synthesize cauliflower-like CeO_2–TiO_2 hybrid structure exhibiting an extremely high photocatalytic activity. Here, the dynamic shifting between $Ce^{3+}$and Ce^{4+} states was demonstrated as an effective tool for photocatalytic and self-cleaning applications in CeO_2–TiO_2 hybrid thin film structures (published as Inside Back Cover from Nanoscale-RSC).

Beside its use for active surface cleaning (photocatalytic degradation of organic pollutants), TiO_2 can be applied as passive surface to retard the pollution by its superhydrophilic nature. By inducing a special surface topography and high roughness also hydrophobic TiO_2 structures can be achieved for easy-to-clean applications. Here, porous 3D TiO_2 structure was prepared by combining hard-templating and infiltration processes from the 2D assembling of TiO_2 nanoparticles. Then this structure was converted to superhydrophobic 3D TiO_2 structure (composed of micro-and nanoscale topography) by using initiated chemical vapor deposition (iCVD) technique. iCVD is a one-step gas-phase surface polymerization technique and can functionalize surfaces of complex and porous 3D structures without altering the underlying topographies. Prepared superhydrophobic 3D TiO_2 structure showed high water-repelling behavior and this effect is stable under extreme pressure levels. Proposed 3D TiO_2 structure may act as smart drug depots in biomedical applications (published as Inside Front Cover from Advanced Materials Interfaces-Wiley).

14 Outlook

In this PhD thesis, some specific strategies have been developed for photocatalytic, self-cleaning, and micro-/nanostructuring applications. Based on these strategies new concepts have been proposed and but these need to be realized by further studies (bachelor, master, and PhD studies). Some of these are already planned:

The properly designed semiconductor photocatalysts are promising materials for solving the current serious energy and environmental problems. Recently, the direct Z-scheme photocatalysts, mimicking the natural photosynthesis system, have many merits, including enhanced light-harvesting, and strong redox ability, which promotes the photocatalytic performance. For this purpose, DC reactive sputtering and photodeposition methods can be combined for designing and preparation of new type Z-scheme photocatalysts (e.g. CeO_2-Au-TiO_2 as shown in **Figure** 14.1).

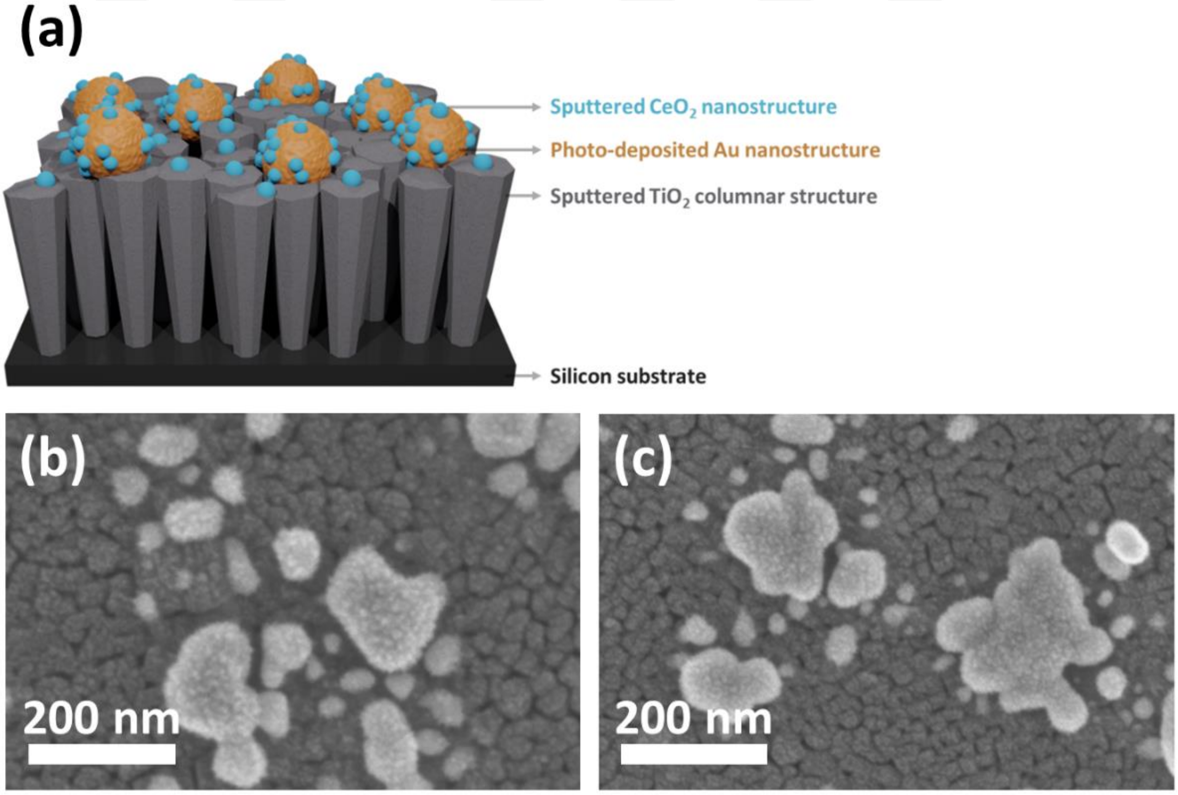

Figure 14.1. (a) The schematic representation of the new generation Z-scheme photocatalyst. (b) and (c) SEM images of the TiO_2-Au-CeO_2 photocatalyst from a different position on the same sample.

Metallic nanoparticles (Pt, Au, and Ag) have attached a considerable attention in numerous fields due to their unique physical and chemical properties. These properties can be easily tuned by controlling their size, shape, and composition. Especially, Pt nanoparticles are extensively studied in catalysts, photonics, and medical applications due to their superior properties. However, their high cost limits their use for practical applications. Recently, bimetallic nanoparticles have gained significant attention due to their unique properties achieved by synergetic effect of two metals. They can be also possible solution for high-cost issue of Pt by reducing Pt content in the main structure. The photodeposition approach, which is proposed in this PhD dissertation, can be modified to prepare Au-Pt and Ag-Pt bimetallic structures as shown in **Figure** 14.2

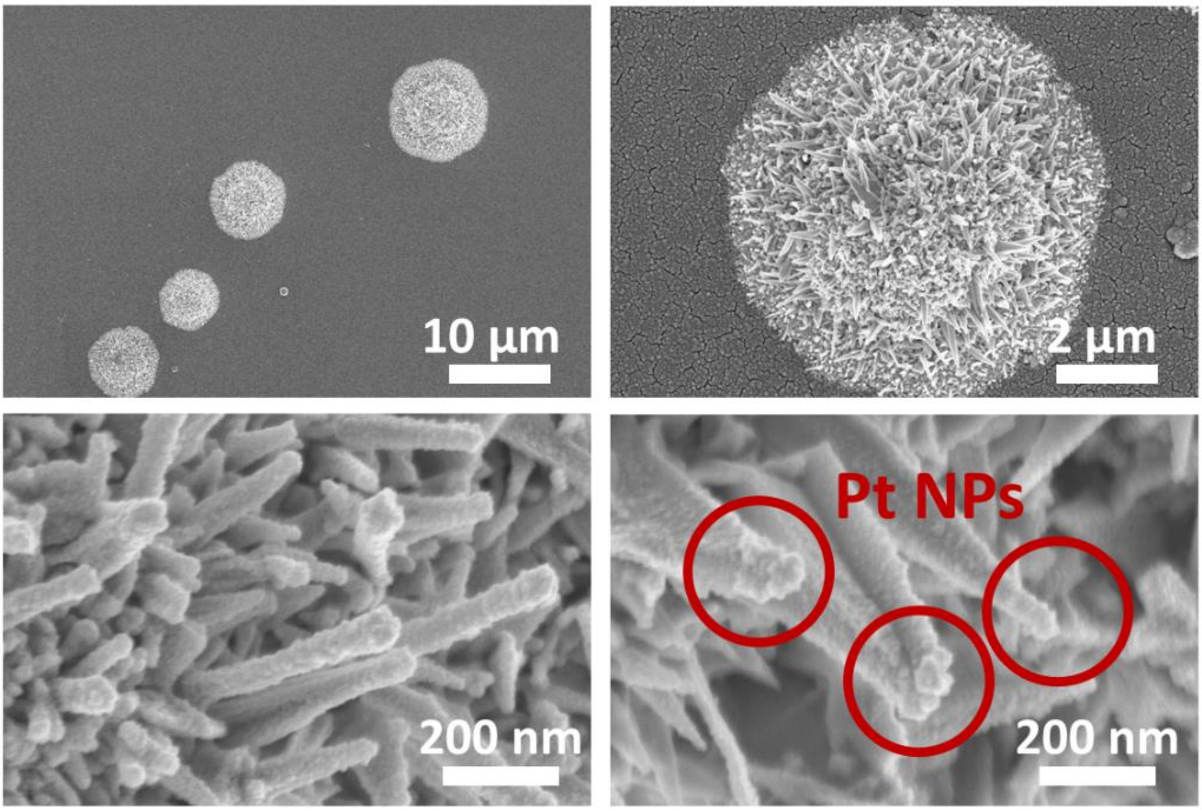

Figure 14.2. **(a-d)** SEM images of the Pt nanoparticles deposited on hierarchical Au needle clusters at different magnification. Investigation of the effect of the mask type (non-contact mask and laser interference) and pore size on micro-/nanostructuring.

Pt-Au bimetallic nanoparticles are commonly used as electrode materials in the sensing field to detect some organic molecules. The bimetallic nanoparticles can be prepared by consecutive photodeposition of Au and Pt. However, this structure can be also formed by simultaneous photodeposition of Au and Pt together as shown in **Figure** 14.3. Then, they might be functionalized by self-assembly monolayers (SAMs) for diverse applications including sensors and biomedicine.

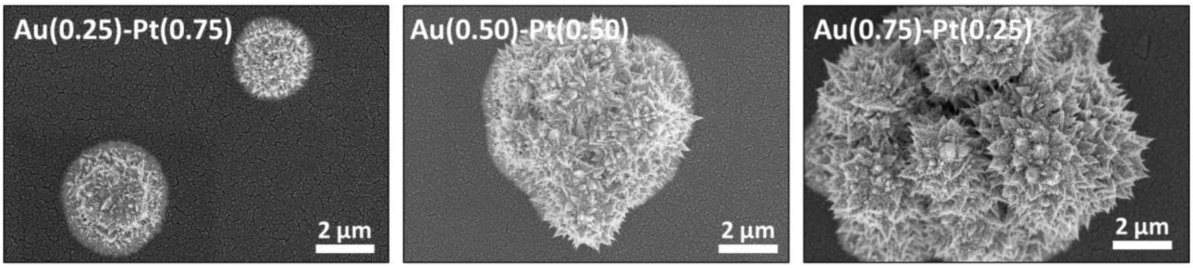

Figure 14.3. SEM images of simultaneously deposition Pt-Au bimetallic structure by photodeposition method at different molar ratio.

The synthesis of photocatalysts by wet chemical methods (colloidal chemistry in liquid environments) have been extensively used due to their relative simplicity and low cost. However, wet chemical methods have some limitations in controlling stoichiometry, size, and shape of such photocatalysts. A multi-target single magnetron GAS approach can be used to prepare hybrid bi-phasic TiO_x-CeO_x structures (in different forms as schematically shown in **Figure** 14.4). The effect of process parameters including pressure, power, and gas flow rate on the size, the composition, and the morphology of hetero-oxide structures can be studied systematically for photocatalytic applications.

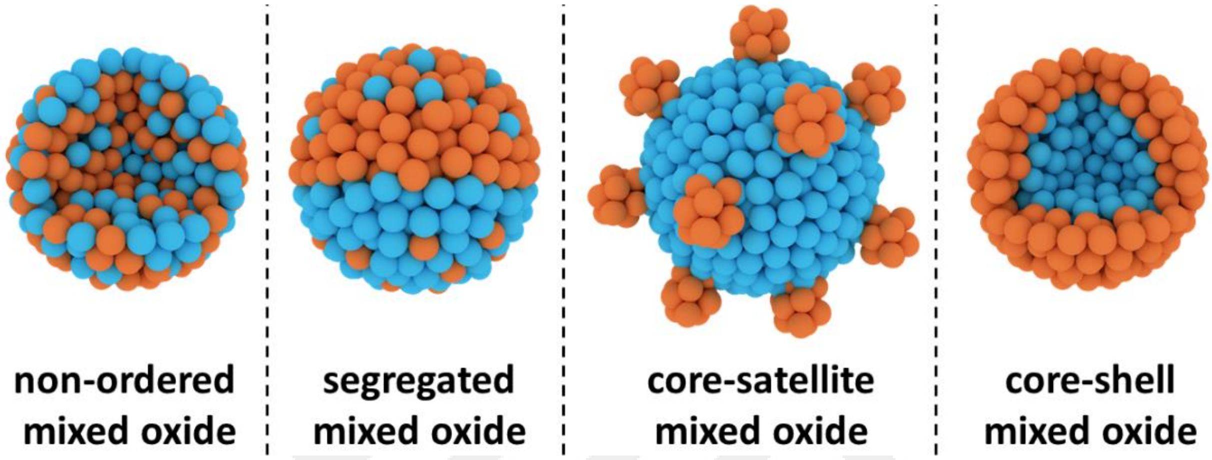

Figure 14.4. Schematic representation of possible hetero-oxide particle morphologies: non-ordered, segregated, core-satellite and core-shell mixed oxides (Blue and orange colors represent Ti and Ce atoms, respectively).

15 Bibliography

[1] Y. Deng, R. Zhao, *J. Ind. Eng. Chem.* **2015**, *1*, 167.

[2] M. R. Hoffmann, S. T. Martin, W. Choi, D. W. Bahnemann, *Chem. Rev.* **1995**, *95*, 69.

[3] A. Fujishima, K. Honda, *Nature* **1972**, *238*, 37.

[4] R. Daghrir, P. Drogui, D. Robert, *Ind. Eng. Chem. Res.* **2013**, *52*, 3581.

[5] R. Asahi, T. Morikawa, T. Ohwaki, K. Aoki, Y. Taga, N. Series, *Science (80-.).* **2001**, *293*, 269.

[6] M. Zayat, P. Garcia-Parejo, D. Levy, *Chem. Soc. Rev.* **2007**, *36*, 1270.

[7] M. Ni, M. K. H. Leung, D. Y. C. Leung, K. Sumathy, *Renew. Sustain. Energy Rev.* **2007**, *11*, 401.

[8] K. Kočí, L. Obalová, L. Matějová, D. Plachá, Z. Lacný, J. Jirkovský, O. Šolcová, *Appl. Catal. B Environ.* **2009**, *89*, 494.

[9] B. Henkel, T. Neubert, S. Zabel, C. Lamprecht, C. Selhuber-Unkel, K. Rätzke, T. Strunskus, M. Vergöhl, F. Faupel, *Appl. Catal. B Environ.* **2016**, *180*, 362.

[10] U. G. Akpan, B. H. Hameed, *Appl. Catal. A Gen.* **2010**, *375*, 1.

[11] M. Aghaee, J. Verheyen, A. A. E. Stevens, W. M. M. Kessels, M. Creatore, *Plasma Process. Polym.* **2019**, *16*, 1900127.

[12] J. B. Chemin, S. Bulou, K. Baba, C. Fontaine, T. Sindzingre, N. D. Boscher, P. Choquet, *Sci. Rep.* **2018**, *8*, 1.

[13] N. Inoue, H. Yuasa, M. Okoshi, in *Appl. Surf. Sci.*, **2002**.

[14] B. Henkel, A. Vahl, O. C. Aktas, T. Strunskus, F. Faupel, *Nanotechnology* **2018**, *29*, 035703.

[15] A. Vahl, S. Veziroglu, B. Henkel, T. Strunskus, O. Polonskyi, O. C. Aktas, F. Faupel, *Materials (Basel).* **2019**, *12*, 2840.

[16] L. G. Devi, R. Kavitha, *Appl. Surf. Sci.* **2016**, *360*, 601.

[17] T. H. Tan, J. Scott, Y. H. Ng, R. A. Taylor, K.-F. F. Aguey-Zinsou, R. Amal, *ACS Catal.* **2016**, *6*, 1870.

[18] S. Veziroglu, M. Kuru, M. Z. Ghori, F. K. Dokan, A. M. Hinz, T. Strunskus, F. Faupel, O. C. Aktas, *Mater. Lett.* **2017**, *209*, 486.

[19] T. Montini, M. Melchionna, M. Monai, P. Fornasiero, *Chem. Rev.* **2016**, *116*, 5987.

[20] B. M. Reddy, A. Khan, Y. Yamada, T. Kobayashi, S. Loridant, J.-C. Vilta, *J. Phys. Chem. B* **2003**, 5162.

[21] F. Chen, P. Ho, R. Ran, W. Chen, Z. Si, X. Wu, D. Weng, Z. Huang, C. Lee, *J. Alloys Compd.* **2017**, *714*, 560.

[22] H. Khojasteh, M. Salavati-Niasari, A. Abbasi, F. Azizi, M. Enhessari, *J. Mater. Sci. Mater. Electron.* **2016**, *27*, 1261.

[23] M. Z. Ghori, S. Veziroglu, B. Henkel, A. Vahl, O. Polonskyi, T. Strunskus, F. Faupel, O. C. Aktas, *Sol. Energy Mater. Sol. Cells* **2018**, *178*, 170.

[24] C. Rao, *Annu. Rev. Phys. Chem.* **1989**, *40*, 291.

[25] T. Guo, M. S. Yao, Y. H. Lin, C. W. Nan, *CrystEngComm* **2015**, *17*, 3551.

[26] M. S. Chavali, M. P. Nikolova, *SN Appl. Sci.* **2019**, *1*, 607.

[27] Y. Nosaka, A. Nosaka, *Introduction to Photocatalysis*, The Royal Society Of Chemistry, **2016**.

[28] C. Kittel, *Wiley Sons, New York, NY* **2004**.

[29] G. Sun, in *Adv. Lasers Electro Opt.*, **2010**.

[30] D. Sumanth Kumar, B. Jai Kumar, H. M. Mahesh, in *Synth. Inorg. Nanomater.*, **2018**, pp. 59–88.

[31] S. N. Habisreutinger, L. Schmidt-Mende, J. K. Stolarczyk, *Angew. Chemie - Int. Ed.* **2013**, *52*, 7372.

[32] K. R. Kim, S. Choi, C. T. Yavuz, Y. S. Nam, *ACS Sustain. Chem. Eng.* **2020**, *8*, 7359.

[33] Y. Lu, X. L. Liu, L. He, Y. X. Zhang, Z. Y. Hu, G. Tian, X. Cheng, S. M. Wu, Y. Z. Li, X. H. Yang, L. Y. Wang, J. W. Liu, C. Janiak, G. G. Chang, W. H. Li, G. Van Tendeloo, X. Y. Yang, B. L. Su, *Nano Lett.* **2020**, *20*, 3122.

[34] J. Zhang, P. Zhou, J. Liu, J. Yu, *Phys. Chem. Chem. Phys.* **2014**, *16*, 20382.

[35] T. Luttrell, S. Halpegamage, J. Tao, A. Kramer, E. Sutter, M. Batzill, *Sci. Rep.* **2015**, *4*, 4043.

[36] Z. Gong, J. Ji, J. Wang, *Catalysts* **2019**, *9*, 193.

[37] K. Awazu, M. Fujimaki, C. Rockstuhl, J. Tominaga, H. Murakami, Y. Ohki, N. Yoshida, T. Watanabe, *J. Am. Chem. Soc.* **2008**, *130*, 1676.

[38] P. Wang, B. Huang, Y. Dai, M. H. Whangbo, *Phys. Chem. Chem. Phys.* **2012**, *14*, 9813.

[39] G. Kawamura, A. Matsuda, *Catalysts* **2019**, *9*, 982.

[40] N. Wu, *Nanoscale* **2018**, *10*, 2679.

[41] M. Lemos de Souza, D. Pereira Dos Santos, P. Corio, *RSC Adv.* **2018**, *8*, 28753.

[42] J.-G. Kang, Y. Sohn, *J. Mater. Sci.* **2012**, *47*, 824.

[43] Z. Lin, X. Wang, J. Liu, Z. Tian, L. Dai, B. He, C. Han, Y. Wu, Z. Zeng, Z. Hu, *Nanoscale* **2015**, *7*, 4114.

[44] V. Kumaravel, S. Mathew, J. Bartlett, S. C. Pillai, *Appl. Catal. B Environ.* **2019**, *244*, 1021.

[45] J. Yan, G. Wu, N. Guan, L. Li, *Chem. Commun.* **2013**, *49*, 11767.

[46] A. Sanchez, S. Abbet, U. Heiz, W. D. Schneider, H. Häkkinen, R. N. Barnett, U. Landman, *J. Phys. Chem. A* **1999**, *103*, 9573.

[47] J. Zhao, S. C. Nguyen, R. Ye, B. Ye, H. Weller, G. A. Somorjai, A. P. Alivisatos, F. Dean Toste, *ACS Cent. Sci.* **2017**, *3*, 482.

[48] Z. Fan, F. Meng, J. Gong, H. Li, Y. Hu, D. Liu, *Mater. Lett.* **2016**, *175*, 36.

[49] H. Liu, M. Wang, Y. Wang, Y. Liang, W. Cao, Y. Su, *J. Photochem. Photobiol. A Chem.* **2011**, *223*, 157.

[50] X. Lu, X. Li, J. Qian, N. Miao, C. Yao, Z. Chen, *J. Alloys Compd.* **2016**, *661*, 363.

[51] J. Tian, Y. Sang, Z. Zhao, W. Zhou, D. Wang, X. Kang, H. Liu, J. Wang, S. Chen, H. Cai, H. Huang, *Small* **2013**, *9*, 3864.

[52] D. Tomova, V. Iliev, A. Eliyas, S. Rakovsky, *Sep. Purif. Technol.* **2015**, *156*, 715.

[53] W. Zhou, Y. Guan, D. Wang, X. Zhang, D. Liu, H. Jiang, J. Wang, X. Liu, H. Liu, S. Chen, *Chem. - An Asian J.* **2014**, *9*, 1648.

[54] W. Zhu, S. Xiao, D. Zhang, P. Liu, H. Zhou, W. Dai, F. Liu, H. Li, *Langmuir* **2015**, *31*, 10822.

[55] M. Ghanashyam Krishna, M. Vinjanampati, D. Dhar Purkayastha, *Eur. Phys. J. Appl. Phys.* **2013**, *62*, 30001.

[56] S. Banerjee, D. D. Dionysiou, S. C. Pillai, *Appl. Catal. B Environ.* **2015**, *176–177*, 396.

[57] W. Barthlott, C. Neinhuis, *Planta* **1997**, *202*, 1.

[58] S. Nishimoto, B. Bhushan, *RSC Adv.* **2013**, *3*, 671.

[59] D. Sun, K. Böhringer, *Micromachines* **2019**, *10*, 101.

[60] T. Zubkov, D. Stahl, T. L. Thompson, D. Panayotov, O. Diwald, J. T. Yates, *J. Phys. Chem. B* **2005**, *109*, 15454.

[61] A. Fujishima, X. Zhang, D. A. Tryk, *Surf. Sci. Rep.* **2008**, *63*, 515.

[62] Q. Ye, P. Y. Liu, Z. F. Tang, L. Zhai, *Vacuum* **2007**, *81*, 627.

[63] S. Sepeur, *Nanotechnology: Technical Basics and Applications*, Vincentz Network GmbH & Co KG, **2008**.

[64] N. Li, P. Zhao, D. Astruc, *Angew. Chemie - Int. Ed.* **2014**, *53*, 1756.

[65] K. Zhang, J. Wei, H. Zhu, F. Ma, S. Wang, *Mater. Res. Bull.* **2013**, *48*, 1338.

[66] A. Yu, Z. Liang, J. Cho, F. Caruso, *Nano Lett.* **2003**, *3*, 1203.

[67] Z. Zheng, B. Huang, X. Qin, X. Zhang, Y. Dai, M.-H. H. Whangbo, *J. Mater. Chem.* **2011**, *21*, 9079.

[68] D. Depla, S. Mahieu, J. E. Greene, in *Handb. Depos. Technol. Film. Coatings*, **2010**, pp. 253–296.

[69] Y. Medkour, A. Roumili, D. Maouche, L. Louail, in *Adv. Sci. Technol. M*, **2012**, pp. 159–176.

[70] J. W. Haus, *Fundamentals and Applications of Nanophotonics*, **2016**.

[71] D. M. Mattox, *Handbook of Physical Vapor Deposition (PVD) Processing*, **2007**.

[72] J. E. Greene, *J. Vac. Sci. Technol. A Vacuum, Surfaces, Film.* **2017**, *35*, 05C204.

[73] Y. Huttel, Ed. , *Gas-Phase Synthesis of Nanoparticles*, Wiley-VCH Verlag GmbH & Co. KGaA, Weinheim, Germany, **2017**.

[74] I. Kolev, A. Bogaerts, *Contrib. to Plasma Phys.* **2004**, *44*, 582.

[75] F. Shi, in *Magnetron Sputtering [Working Title]*, IntechOpen, **2018**.

[76] K. Sattler, J. Mühlbach, E. Recknagel, *Phys. Rev. Lett.* **1980**, *45*, 821.

[77] H. Haberland, M. Karrais, M. Mall, Y. Thurner, *J. Vac. Sci. Technol. A Vacuum, Surfaces, Film.* **1992**, *10*, 3266.

[78] J. Kratochvíl, A. Kuzminova, O. Kylián, H. Biederman, *Surf. Coatings Technol.* **2015**, *275*, 296.

[79] M. Khojasteh, V. V. Kresin, *Appl. Nanosci.* **2017**, *7*, 875.

[80] J. Polte, *CrystEngComm* **2015**, DOI 10.1039/c5ce01014d.

[81] W. C. Clark, A. G. Vondjidis, *J. Catal.* **1965**, *4*, 691.

[82] B. Kraeutler, A. J. Bard, *J. Am. Chem. Soc.* **1978**, *100*, 4317.

[83] K. Wenderich, G. Mul, *Chem. Rev.* **2016**, *116*, 14587.

[84] N. P. Dasgupta, C. Liu, S. Andrews, F. B. Prinz, P. Yang, *J. Am. Chem. Soc.* **2013**, *135*, 12932.

[85] L. L. Ma, Z. D. Cui, Z. Y. Li, S. L. Zhu, Y. Q. Liang, Q. W. Yin, X. J. Yang, *Mater. Sci. Eng. B Solid-State Mater. Adv. Technol.* **2013**, *178*, 77.

[86] J. Schneider, M. Matsuoka, M. Takeuchi, J. Zhang, Y. Horiuchi, M. Anpo, D. W. Bahnemann, *Chem. Rev.* **2014**, *114*, 9919.

[87] A. Tanaka, K. Fuku, T. Nishi, K. Hashimoto, H. Kominami, *J. Phys. Chem. C* **2013**, *117*, 16983.

[88] J. M. Herrmann, J. Disdier, P. Pichat, A. Fernández, A. González-Elipe, G. Munuera, C. Leclercq, *J. Catal.* **1991**, *132*, 490.

[89] A. Ul-Hamid, *A Beginners' Guide to Scanning Electron Microscopy*, Springer International Publishing, Cham, **2018**.

[90] L. Reimer, *Meas. Sci. Technol.* **2000**, *11*, 1826.

[91] W. Zhou, R. Apkarian, Z. L. Wang, D. Joy, in *Scanning Microsc. Nanotechnol. Tech. Appl.*, **2007**, pp. 1–40.

[92] J. I. Goldstein, D. E. Newbury, P. Echlin, D. C. Joy, A. D. Romig, C. E. Lyman, C. Fiori, E. Lifshin, *Scanning Electron Microscopy and X-Ray Microanalysis*, Springer US, Boston, MA, **1992**.

[93] M. T. Postek, A. E. Vladar, J. Kramar, L. A. Stern, J. Notte, S. McVey, in *AIP Conf. Proc.*, **2007**, pp. 161–167.

[94] M. S. Joens, C. Huynh, J. M. Kasuboski, D. Ferranti, Y. J. Sigal, F. Zeitvogel, M. Obst, C. J. Burkhardt, K. P. Curran, S. H. Chalasani, L. A. Stern, B. Goetze, J. A. J. Fitzpatrick, *Sci. Rep.* **2013**, *3*, 3514.

[95] B. Fultz, J. M. Howe, *Transmission Electron Microscopy and Diffractometry of Materials*, **2008**.

[96] D. B. Williams, C. B. Carter, *Transmission Electron Microscopy*, Springer US, Boston, MA, **2009**.

[97] J. F. Moulder, W. F. Stickle, P. E. Sobol, K. D. Bomben, *Handbook of X-Ray Photoelectron Spectroscopy: A Reference Book of Standard Spectra for Identification and Interpretation of XPS Data*, **1992**.

[98] P. van der Heide, *X-Ray Photoelectron Spectroscopy*, John Wiley & Sons, Inc., Hoboken, NJ, USA, **2011**.

[99] E. Smith, G. Dent, *Modern Raman Spectroscopy - A Practical Approach*, John Wiley & Sons, Ltd, Chichester, UK, **2004**.

[100] A. Horsthemke, J. J. Schröder, *Chem. Eng. Process. Process Intensif.* **1985**, *19*, 277.

[101] V. K. Gupta, A. Nayak, *Chem. Eng. J.* **2012**, *180*, 81.

[102] B. Ding, Y. Zhou, M. He, T. Huang, S. Li, S. Huang, W. Pan, *RSC Adv.* **2016**, *6*, 100427.

[103] K. Mallick, M. J. Witcomb, M. S. Scurrell, *Appl. Phys. A Mater. Sci. Process.* **2005**, *80*, 797.

[104] M. M. Khan, J. Lee, M. H. Cho, *J. Ind. Eng. Chem.* **2014**, *20*, 1584.

[105] Y. Wang, H. Arandiyan, J. Scott, A. Bagheri, H. Dai, R. Amal, *J. Mater. Chem. A* **2017**, *5*, 8825.

[106] Y. Liu, B. Liu, Q. Wang, Y. Liu, C. Li, W. Hu, P. Jing, W. Zhao, J. Zhang, *RSC Adv.* **2014**, *4*, 5975.

[107] R. Saravanan, E. Sacari, F. Gracia, M. M. Khan, E. Mosquera, V. K. Gupta, *J. Mol. Liq.* **2016**, *221*, 1029.

[108] S. Rajendran, M. M. Khan, F. Gracia, J. Qin, V. K. Gupta, S. Arumainathan, *Sci. Rep.* **2016**, *6*, 31641.

[109] K. Yoshikawa, H. Sato, M. Kaneeda, J. N. Kondo, *J. CO2 Util.* **2014**, *8*, 34.

[110] C.-Y. Kung, S.-L. Young, H.-Z. Chen, M.-C. Kao, L. Horng, Y.-T. Shih, C.-C. Lin, T.-T. Lin, C.-J. Ou, *Nanoscale Res. Lett.* **2012**, *7*, 372.

[111] B. M. Reddy, A. Khan, P. Lakshmanan, M. Aouine, S. Loridant, J. C. Volta, *J. Phys. Chem. B* **2005**, *109*, 3355.

[112] T.-Y. Ma, Z.-Y. Yuan, J.-L. Cao, *Eur. J. Inorg. Chem.* **2010**, *2010*, 716.

[113] S. Veziroglu, M. Z. Ghori, M. Kamp, L. Kienle, H. G. Rubahn, T. Strunskus, J. Fiutowski, J. Adam, F. Faupel, O. C. Aktas, *Adv. Mater. Interfaces* **2018**, *5*, 1800465.

[114] K. A. Stoerzinger, W. Hasan, J. Y. Lin, A. Robles, T. W. Odom, *J. Phys. Chem. Lett.* **2010**, *1*, 1046.

[115] B. Tangeysh, K. Moore Tibbetts, J. H. Odhner, B. B. Wayland, R. J. Levis, *Nano Lett.* **2015**, *15*, 3377.

[116] C. G. Khoury, T. Vo-Dinh, *J. Phys. Chem. C* **2008**, *112*, 18849.

[117] M. Liu, Y. Pang, B. Zhang, P. De Luna, O. Voznyy, J. Xu, X. Zheng, C. T. Dinh, F. Fan, C. Cao, F. P. G. de Arquer, T. S. Safaei, A. Mepham, A. Klinkova, E. Kumacheva, T. Filleter, D. Sinton, S. O. Kelley, E. H. Sargent, *Nature* **2016**, *537*, 382.

[118] Y. Qin, Y. Song, N. Sun, N. Zhao, M. Li, L. Qi, *Chem. Mater.* **2008**, *20*, 3965.

[119] J. Xie, Q. Zhang, J. Y. Lee, D. I. C. Wang, *ACS Nano* **2008**, *2*, 2473.

[120] M. Bechelany, P. Brodard, J. Elias, A. Brioude, J. Michler, L. Philippe, *Langmuir* **2010**, *26*, 14364.

[121] W.-E. Lu, M.-L. Zheng, W.-Q. Chen, Z.-S. Zhao, X.-M. Duan, *Phys. Chem. Chem. Phys.* **2012**, *14*, 11930.

[122] M. Lechuga, M. Fernández-Serrano, E. Jurado, J. Núñez-Olea, F. Ríos, *Ecotoxicol. Environ. Saf.* **2016**, *125*, 1.

[123] J. Fang, S. Du, S. Lebedkin, Z. Li, R. Kruk, M. Kappes, H. Hahn, *Nano Lett.* **2010**, *10*, 5006.

[124] O. M. Bakr, B. H. Wunsch, F. Stellacci, *Chem. Mater.* **2006**, *18*, 3297.

[125] J.-H. Kim, T. Kang, S. M. Yoo, S. Y. Lee, B. Kim, Y.-K. Choi, *Nanotechnology* **2009**, *20*, 235302.

[126] T. Saberi Safaei, A. Mepham, X. Zheng, Y. Pang, C.-T. Dinh, M. Liu, D. Sinton, S. O. Kelley, E. H. Sargent, *Nano Lett.* **2016**, *16*, 7224.

[127] M. Pradhan, J. Chowdhury, S. Sarkar, A. K. Sinha, T. Pal, *J. Phys. Chem. C* **2012**, *116*, 24301.

[128] F. Kim, J. H. Song, P. Yang, *J. Am. Chem. Soc.* **2002**, *124*, 14316.

[129] R. Kydd, J. Scott, W. Y. Teoh, K. Chiang, R. Amal, *Langmuir* **2010**, *26*, 2099.

[130] S. F. Chen, J. P. Li, K. Qian, W. P. Xu, Y. Lu, W. X. Huang, S. H. Yu, *Nano Res.* **2010**, *3*, 244.

[131] X. Huang, X. Qi, Y. Huang, S. Li, C. Xue, C. L. Gan, F. Boey, H. Zhang, *ACS Nano* **2010**, *4*, 6196.

[132] V. Zaporojtchenko, J. Zekonyte, A. Biswas, F. Faupel, *Surf. Sci.* **2003**, *532–535*, 300.

[133] S. Veziroglu, A.-L. Obermann, M. Ullrich, M. Hussain, M. Kamp, L. Kienle, T. Leißner, H.-G. Rubahn, O. Polonskyi, T. Strunskus, J. Fiutowski, M. Es-Souni, J. Adam, F. Faupel, O. C. Aktas, *ACS Appl. Mater. Interfaces* **2020**, *12*, 14983.

[134] N. Liu, V. Häublein, X. Zhou, U. Venkatesan, M. Hartmann, M. MačKović, T. Nakajima, E. Spiecker, A. Osvet, L. Frey, P. Schmuki, *Nano Lett.* **2015**, *15*, 6815.

[135] D. A. Panayotov, A. I. Frenkel, J. R. Morris, *ACS Energy Lett.* **2017**, *2*, 1223.

[136] T.-W. Liao, S. Verbruggen, N. Claes, A. Yadav, D. Grandjean, S. Bals, P. Lievens, *Nanomaterials* **2018**, *8*, 30.

[137] S. Sarina, E. R. Waclawik, H. Zhu, *Green Chem.* **2013**, *15*, 1814.

[138] J. C. Durán-Álvarez, E. Avella, R. M. Ramírez-Zamora, R. Zanella, *Catal. Today* **2016**, *266*, 175.

[139] A. Ayati, A. Ahmadpour, F. F. Bamoharram, B. Tanhaei, M. Mänttäri, M. Sillanpää, *Chemosphere* **2014**, *107*, 163.

[140] A. Gołąbiewska, A. Malankowska, M. Jarek, W. Lisowski, G. Nowaczyk, S. Jurga, A. Zaleska-Medynska, *Appl. Catal. B Environ.* **2016**, *196*, 27.

[141] M. Grätzel, *Heterogenous Photochemical Electron Transfer*, CRC Press, **2018**.

[142] Y. C. Pu, G. Wang, K. Der Chang, Y. Ling, Y. K. Lin, B. C. Fitzmorris, C. M. Liu, X. Lu, Y. Tong, J. Z. Zhang, Y. J. Hsu, Y. Li, *Nano Lett.* **2013**, *13*, 3817.

[143] A. Chanaewa, J. Schmitt, M. Meyns, M. Volkmann, C. Klinke, E. von Hauff, *J. Phys. Chem. C* **2015**, *119*, 21704.

[144] M. Jakob, H. Levanon, P. V. Kamat, *Nano Lett.* **2003**, *3*, 353.

[145] T. L. Greaves, C. J. Drummond, *Chem. Rev.* **2015**, *115*, 11379.

[146] T. Siefke, S. Kroker, K. Pfeiffer, O. Puffky, K. Dietrich, D. Franta, I. Ohlídal, A. Szeghalmi, E.-B. Kley, A. Tünnermann, *Adv. Opt. Mater.* **2016**, *4*, 1780.

[147] P. Wagener, J. Jakobi, C. Rehbock, V. S. K. Chakravadhanula, C. Thede, U. Wiedwald, M. Bartsch, L. Kienle, S. Barcikowski, *Sci. Rep.* **2016**, *6*, 23352.

[148] S. K. Ghosh, S. Nath, S. Kundu, K. Esumi, T. Pal, *J. Phys. Chem. B* **2004**, *108*, 13963.

[149] H. E. Swanson, E. Tatge, *Standard X-Ray Diffraction Patterns*, **1951**.

[150] P. Ballirano, R. Caminiti, *J. Appl. Crystallogr.* **2001**, *34*, 757.

[151] R. L. Kurtz, V. E. Henrich, *Surf. Sci. Spectra* **1998**, *5*, 179.

[152] M. J. Jackman, A. G. Thomas, C. Muryn, *J. Phys. Chem. C* **2015**, *119*, 13682.

[153] R. Sanjinés, H. Tang, H. Berger, F. Gozzo, G. Margaritondo, F. Lévy, *J. Appl. Phys.* **1994**, *75*, 2945.

[154] J. Sun, W. Wen, J.-M. Wu, *J. Am. Ceram. Soc.* **2013**, *96*, 2109.

[155] A. A. Melvin, K. Illath, T. Das, T. Raja, S. Bhattacharyya, C. S. Gopinath, *Nanoscale* **2015**, *7*, 13477.

[156] N. Kruse, S. Chenakin, *Appl. Catal. A Gen.* **2011**, *391*, 367.

[157] J. Radnik, C. Mohr, P. Claus, *Phys. Chem. Chem. Phys.* **2003**, *5*, 172.

[158] S. Arrii, F. Morfin, A. J. Renouprez, J. L. Rousset, *J. Am. Chem. Soc.* **2004**, *126*, 1199.

[159] A. Bumajdad, M. Madkour, *Phys. Chem. Chem. Phys.* **2014**, *16*, 7146.

[160] J. Li, Suyoulema, W. Wang, Sarina, *Solid State Sci.* **2009**, *11*, 2037.

[161] H. Chen, G. Liu, L. Wang, *Sci. Rep.* **2015**, *5*, 10852.

[162] S. Shuang, R. Lv, Z. Xie, Z. Zhang, *Sci. Rep.* **2016**, *6*, 26670.

[163] S. S. Rayalu, D. Jose, M. V. Joshi, P. A. Mangrulkar, K. Shrestha, K. Klabunde, *Appl. Catal. B Environ.* **2013**, *142–143*, 684.

[164] A. Houas, *Appl. Catal. B Environ.* **2001**, *31*, 145.

[165] Y. Fang, Y. Jiao, K. Xiong, R. Ogier, Z.-J. Yang, S. Gao, A. B. Dahlin, M. Käll, *Nano Lett.* **2015**, *15*, 4059.

[166] T. Okuno, G. Kawamura, H. Muto, A. Matsuda, *J. Solid State Chem.* **2016**, *235*, 132.

[167] V. Sharma, S. Kumar, V. Krishnan, *ChemistrySelect* **2016**, *1*, 2963.

[168] S. Lakshmi, R. Renganathan, S. Fujita, *J. Photochem. Photobiol. A Chem.* **1995**, *88*, 163.

[169] M. Z. Ghori, S. Veziroglu, A. Hinz, B. B. Shurtleff, O. Polonskyi, T. Strunskus, J. Adam, F. Faupel, O. C. Aktas, *ACS Appl. Nano Mater.* **2018**, *1*, 3760.

[170] L. G. Parratt, *Phys. Rev.* **1954**, *95*, 359.

[171] P. B. Nair, V. B. Justinvictor, G. P. Daniel, K. Joy, K. C. James Raju, D. Devraj Kumar, P. V. Thomas, *Prog. Nat. Sci. Mater. Int.* **2014**, *24*, 218.

[172] L. Gao, F. Lemarchand, M. Lequime, *Thin Solid Films* **2011**, *520*, 501.

[173] A. Haidar, A. A. Ali, S. Veziroglu, J. Fiutowski, H. Eichler, I. Müller, K. Kiefer, F. Faupel, M. Bischoff, M. Veith, O. C. Aktas, H. Abdul-Khaliq, *Nanoscale Adv.* **2019**, *1*, 4659.

[174] S. Veziroglu, M. Ullrich, M. Hussain, J. Drewes, J. Shondo, T. Strunskus, J. Adam, F. Faupel, O. C. Aktas, *Surf. Coatings Technol.* **2020**, *389*, 125613.

[175] L. Qin, G. Wang, Y. Tan, *Sci. Rep.* **2018**, *8*, 16198.

[176] Y. Li, W. N. Wang, Z. Zhan, M. H. Woo, C. Y. Wu, P. Biswas, *Appl. Catal. B Environ.* **2010**, *100*, 386.

[177] P. Yilmaz, A. M. Lacerda, I. Larrosa, S. Dunn, *Electrochim. Acta* **2017**, *231*, 641.

[178] A. Mills, S. Le Hunte, *J. Photochem. Photobiol. A Chem.* **1997**, *108*, 1.

[179] S. Linic, P. Christopher, D. B. Ingram, *Nat. Mater.* **2011**, *10*, 911.

[180] N. S. Lewis, *Nature* **2001**, *414*, 589.

[181] C. G. Silva, R. Juá rez, T. Marino, R. Molinari, H. García, *J. Am. Chem. Soc.* **2011**, *133*, 595.

[182] L. Guo, K. Liang, K. Marcus, Z. Li, L. Zhou, P. D. Mani, H. Chen, C. Shen, Y. Dong, L. Zhai, K. R. Coffey, N. Orlovskaya, Y. H. Sohn, Y. Yang, *ACS Appl. Mater. Interfaces* **2016**, *8*, 34970.

[183] S. Veziroglu, K. Röder, O. Gronenberg, A. Vahl, O. Polonskyi, T. Strunskus, H.-G. Rubahn, L. Kienle, J. Adam, J. Fiutowski, F. Faupel, O. C. Aktas, *Nanoscale* **2019**, *11*, 9840.

[184] K. Song, X. Wang, Q. Xiang, J. Xu, *Phys. Chem. Chem. Phys.* **2016**, *18*, 29131.

[185] S. W. Verbruggen, M. Keulemans, B. Goris, N. Blommaerts, S. Bals, J. A. Martens, S. Lenaerts, *Appl. Catal. B Environ.* **2016**, *188*, 147.

[186] Y. Yu, W. Wen, X.-Y. Qian, J.-B. Liu, J.-M. Wu, *Sci. Rep.* **2017**, *7*, 41253.

[187] M. Karbalaei Akbari, Z. Hai, Z. Wei, J. Hu, S. Zhuiykov, *Mater. Res. Bull.* **2017**, *95*, 380.

[188] D. Tsukamoto, Y. Shiraishi, Y. Sugano, S. Ichikawa, S. Tanaka, T. Hirai, *J. Am. Chem. Soc.* **2012**, *134*, 6309.

[189] X. Wang, D. Baiyila, X. Li, *RSC Adv.* **2016**, *6*, 107233.

[190] Z. W. Seh, S. Liu, M. Low, S. Y. Zhang, Z. Liu, A. Mlayah, M. Y. Han, *Adv. Mater.* **2012**, *24*, 2310.

[191] G. K. Mor, K. Shankar, M. Paulose, O. K. Varghese, C. A. Grimes, *Nano Lett.* **2006**, *6*, 215.

[192] J. Xiong, M. Z. Ghori, B. Henkel, T. Strunskus, U. Schürmann, M. Deng, L. Kienle, F. Faupel, *Appl. Phys. A* **2017**, *123*, 470.

[193] N. Sakai, Y. Fujiwara, Y. Takahashi, T. Tatsuma, *ChemPhysChem* **2009**, *10*, 766.

[194] S. Veziroglu, M. Z. Ghori, A. L. Obermann, K. Röder, O. Polonskyi, T. Strunskus, F. Faupel, O. C. Aktas, *Phys. Status Solidi Appl. Mater. Sci.* **2019**, 1800898.

[195] N. Li, X. Zhang, W. Zhou, Z. Liu, G. Xie, Y. Wang, Y. Du, **2014**, *1*, 521.

[196] S. Zhao, Z. Cheng, L. Kang, M. Li, Z. Gao, *RSC Adv.* **2017**, *7*, 50064.

[197] J. Cai, X. Wu, S. Li, F. Zheng, L. Zhu, Z. Lai, *ACS Appl. Mater. Interfaces* **2015**, *7*, 3764.

[198] R. Purbia, R. Borah, S. Paria, *Inorg. Chem.* **2017**, *56*, 10107.

[199] B. Zhu, P. Xia, Y. Li, W. Ho, J. Yu, *Appl. Surf. Sci.* **2017**, *391*, 175.

[200] Y.-F. Yang, P. Sangeetha, Y.-W. Chen, *Int. J. Hydrogen Energy* **2009**, *34*, 8912.

[201] T. Wang, J. Wei, H. Shi, M. Zhou, Y. Zhang, Q. Chen, Z. Zhang, *Phys. E Low-dimensional Syst. Nanostructures* **2017**, *86*, 103.

[202] H. Li, Z. Li, Y. Yu, Y. Ma, W. Yang, F. Wang, X. Yin, X. Wang, *J. Phys. Chem. C* **2017**, *121*, 12071.

[203] B. Li, B. Zhang, S. Nie, L. Shao, L. Hu, *J. Catal.* **2017**, *348*, 256.

[204] D. S. Warren, A. J. McQuillan, *J. Phys. Chem. B* **2004**, *108*, 19373.

[205] H. Zhang, P. Xu, G. Du, Z. Chen, K. Oh, D. Pan, Z. Jiao, *Nano Res.* **2011**, *4*, 274.

[206] K. Ishimaki, T. Uchiyama, M. Okazaki, D. Lu, Y. Uchimoto, K. Maeda, *Bull. Chem. Soc. Jpn.* **2017**, *91*, 486.

[207] H. G. Yang, C. H. Sun, S. Z. Qiao, J. Zou, G. Liu, S. C. Smith, H. M. Cheng, G. Q. Lu, *Nature* **2008**, *453*, 638.

[208] Y. Wen, H. Ding, Y. Shan, *Nanoscale* **2011**, *3*, 4411.

[209] S. U. M. Khan, M. Al-Shahry, W. B. Ingler, *Science (80-.).* **2002**, *297*, 2243.

[210] B. Ohtani, *Catalysts* **2013**, *3*, 942.

[211] R. Saravanan, D. Manoj, J. Qin, M. Naushad, F. Gracia, A. F. Lee, M. M. Khan, M. A. Gracia-Pinilla, *Process Saf. Environ. Prot.* **2018**, *120*, 339.

[212] E. Albiter, M. A. Valenzuela, S. Alfaro, G. Valverde-Aguilar, F. M. Martínez-Pallares, *J. Saudi Chem. Soc.* **2015**, *19*, 563.

[213] H. Zhang, C. Liang, J. Liu, Z. Tian, G. Wang, W. Cai, *Langmuir* **2012**, *28*, 3938.

[214] M. V. Liga, E. L. Bryant, V. L. Colvin, Q. Li, *Water Res.* **2011**, *45*, 535.

[215] D. Wodka, E. Bielańska, R. P. Socha, M. Elżbieciak - Wodka, J. Gurgul, P. Nowak, P. Warszyński, I. Kumakiri, *ACS Appl. Mater. Interfaces* **2010**, *2*, 1945.

[216] J. Low, S. Qiu, D. Xu, C. Jiang, B. Cheng, *Appl. Surf. Sci.* **2018**, *434*, 423.

[217] V. Iliev, D. Tomova, L. Bilyarska, A. Eliyas, L. Petrov, *Appl. Catal. B Environ.* **2006**, *63*, 266.

[218] Y. Zhang, T. Wang, M. Zhou, Y. Wang, Z. Zhang, *Ceram. Int.* **2017**, *43*, 3118.

[219] J. Zhou, Y. Cheng, J. Yu, *J. Photochem. Photobiol. A Chem.* **2011**, *223*, 82.

[220] C. Zhao, A. Krall, H. Zhao, Q. Zhang, Y. Li, *Int. J. Hydrogen Energy* **2012**, *37*, 9967.

[221] P. D. Cozzoli, E. Fanizza, R. Comparelli, M. L. Curri, A. Agostiano, D. Laub, *J. Phys. Chem. B* **2004**, *108*, 9623.

[222] J. Xiong, M. Z. Ghori, B. Henkel, T. Strunskus, U. Schürmann, L. Kienle, F. Faupel, *Acta Mater.* **2014**, *74*, 1.

[223] K. Kawahara, K. Suzuki, Y. Ohko, T. Tatsuma, *Phys. Chem. Chem. Phys.* **2005**, *7*, 3851.

[224] Y. Liu, J. Kong, J. Yuan, W. Zhao, X. Zhu, C. Sun, J. Xie, *Chem. Eng. J.* **2018**, *331*, 242.

[225] M. Sakamoto, M. Fujistuka, T. Majima, *J. Photochem. Photobiol. C Photochem. Rev.* **2009**, *10*, 33.

[226] I. Sopyan, M. Watanabe, S. Murasawa, K. Hashimoto, A. Fujishima, *J. Photochem. Photobiol. A Chem.* **1996**, *98*, 79.

[227] P. Ramasamy, D.-M. Seo, S.-H. Kim, J. Kim, *J. Mater. Chem.* **2012**, *22*, 11651.

[228] E. Stathatos, P. Lianos, P. Falaras, A. Siokou, *Langmuir* **2000**, *16*, 2398.

[229] Z. Cheng, S. Zhao, Z. Han, Y. Zhang, X. Zhao, L. Kang, *CrystEngComm* **2016**, *18*, 8756.

[230] H. Jensen, A. Soloviev, Z. Li, E. G. Søgaard, *Appl. Surf. Sci.* **2005**, *246*, 239.

[231] L. Xu, B. Wei, W. Liu, H. Zhang, C. Su, J. Che, *Nanoscale Res. Lett.* **2013**, *8*, 536.

[232] X. Wang, J. C. Yu, C. Ho, A. C. Mak, *Chem. Commun.* **2005**, *0*, 2262.

[233] H. C. Choi, Y. M. Jung, S. Bin Kim, *Vib. Spectrosc.* **2005**, *37*, 33.

[234] M. G. Méndez-Medrano, E. Kowalska, A. Lehoux, A. Herissan, B. Ohtani, D. Bahena, V. Briois, C. Colbeau-Justin, J. L. Rodríguez-López, H. Remita, *J. Phys. Chem. C* **2016**, *120*, 5143.

[235] J. Li, J. Xu, W.-L. Dai, K. Fan, *J. Phys. Chem. C* **2009**, *113*, 8343.

[236] J. Singh, B. Satpati, S. Mohapatra, *Plasmonics* **2017**, *12*, 877.

[237] Z. Li, V. Ravaine, S. Ravaine, P. Garrigue, A. Kuhn, *Adv. Funct. Mater.* **2007**, *17*, 618.

[238] A. Sclafani, J.-M. Herrmann, *J. Photochem. Photobiol. A Chem.* **1998**, *113*, 181.

[239] C. Clavero, *Nat. Photonics* **2014**, *8*, 95.

[240] R.-B. Wei, P.-Y. Kuang, H. Cheng, Y.-B. Chen, J.-Y. Long, M.-Y. Zhang, Z.-Q. Liu, *ACS Sustain. Chem. Eng.* **2017**, *5*, 4249.

[241] X. Wei, C. Shao, X. Li, N. Lu, K. Wang, Z. Zhang, Y. Liu, *Nanoscale* **2016**, *8*, 11034.

[242] P.-Y. Kuang, P.-X. Zheng, Z.-Q. Liu, J.-L. Lei, H. Wu, N. Li, T.-Y. Ma, *Small* **2016**, *12*, 6735.

[243] W. Hou, S. B. Cronin, *Adv. Funct. Mater.* **2013**, *23*, 1612.

[244] Y. Chen, X. Xin, N. Zhang, Y.-J. Xu, *Part. Part. Syst. Charact.* **2017**, *34*, 1600357.

[245] L. Zhou, C. Zhang, M. J. McClain, A. Manjavacas, C. M. Krauter, S. Tian, F. Berg, H. O. Everitt, E. A. Carter, P. Nordlander, N. J. Halas, *Nano Lett.* **2016**, *16*, 1478.

[246] M. J. McClain, A. E. Schlather, E. Ringe, N. S. King, L. Liu, A. Manjavacas, M. W. Knight, I. Kumar, K. H. Whitmire, H. O. Everitt, P. Nordlander, N. J. Halas, *Nano Lett.* **2015**, *15*, 2751.

[247] A. M. Ahadi, V. Zaporojtchenko, T. Peter, O. Polonskyi, T. Strunskus, F. Faupel, *J. Nanoparticle Res.* **2013**, *15*, 2125.

[248] T. Peter, O. Polonskyi, B. Gojdka, A. Mohammad Ahadi, T. Strunskus, V. Zaporojtchenko, H. Biederman, F. Faupel, *J. Appl. Phys.* **2012**, *112*, 114321.

[249] O. Polonskyi, O. Kylián, M. Drábik, J. Kousal, P. Solař, A. Artemenko, J. Čechvala, A. Choukourov, D. Slavínská, H. Biederman, *J. Mater. Sci.* **2014**, *49*, 3352.

[250] A. Shelemin, O. Kylián, J. Hanuš, A. Choukourov, I. Melnichuk, A. Serov, D. Slavínská, H. Biederman, *Vacuum* **2015**, *120*, 162.

[251] M. Veith, K. Andres, S. Faber, J. Blin, M. Zimmer, Y. Wolf, H. Schnockel, R. Koppe, R. de Masi, S. Hufner, *Eur. J. Inorg. Chem.* **2003**, 4387.

[252] M. Honda, Y. Kumamoto, a Taguchi, Y. Saito, S. Kawata, *J. Phys. D. Appl. Phys.* **2015**, *48*, 184006.

[253] M. Honda, Y. Kumamoto, A. Taguchi, Y. Saito, S. Kawata, *Appl. Phys. Lett.* **2014**, *104*, 061108.

[254] L.-B. Xiong, J.-L. Li, B. Yang, Y. Yu, *J. Nanomater.* **2012**, *2012*, 1.

[255] S. Veziroglu, J. Hwang, J. Drewes, I. Barg, J. Shondo, T. Strunskus, O. Polonskyi, F. Faupel, O. C. Aktas, *Mater. Today Chem.* **2020**, *16*, 100251.

[256] T. Berger, M. Sterrer, O. Diwald, E. Knözinger, D. Panayotov, T. L. Thompson, J. T. Yates, *J. Phys. Chem. B* **2005**, *109*, 6061.

[257] K. Rajeshwar, M. E. Osugi, W. Chanmanee, C. R. Chenthamarakshan, M. V. B. Zanoni, P. Kajitvichyanukul, R. Krishnan-Ayer, *J. Photochem. Photobiol. C Photochem. Rev.* **2008**, *9*, 171.

[258] M. Pelaez, N. T. Nolan, S. C. Pillai, M. K. Seery, P. Falaras, A. G. Kontos, P. S. M. Dunlop, J. W. J. Hamilton, J. A. Byrne, K. O'Shea, M. H. Entezari, D. D. Dionysiou, *Appl. Catal. B Environ.* **2012**, *125*, 331.

[259] A. Meng, L. Zhang, B. Cheng, J. Yu, *Adv. Mater.* **2019**, *1807660*, 1807660.

[260] T. Hisatomi, J. Kubota, K. Domen, *Chem. Soc. Rev.* **2014**, *43*, 7520.

[261] G. S. Das, J. P. Shim, A. Bhatnagar, K. M. Tripathi, T. Kim, *Sci. Rep.* **2019**, *9*, 15084.

[262] J. Tian, Y. Leng, Z. Zhao, Y. Xia, Y. Sang, P. Hao, J. Zhan, M. Li, H. Liu, *Nano Energy* **2015**, *11*, 419.

[263] M. N. Chong, B. Jin, C. W. K. Chow, C. Saint, *Water Res.* **2010**, *44*, 2997.

[264] R. Marschall, *Adv. Funct. Mater.* **2014**, *24*, 2421.

[265] K. K. Mandari, J. Y. Do, S. Pandey, S. V. P. Vattikuti, M. Kang, *Mater. Res. Bull.* **2020**, *122*, 110695.

[266] C. Karunakaran, P. Gomathisankar, *ACS Sustain. Chem. Eng.* **2013**, *1*, 1555.

[267] Q. Wang, X. Wang, M. Zhang, G. Li, S. Gao, M. Li, Y. Zhang, *J. Colloid Interface Sci.* **2016**, *463*, 308.

[268] C. Karunakaran, G. Abiramasundari, P. Gomathisankar, G. Manikandan, V. Anandi, *Mater. Res. Bull.* **2011**, *46*, 1586.

[269] A. Hadi, I. I. Yaacob, *Catal. Today* **2004**, *96*, 165.

[270] A. A. Ismail, *Appl. Catal. B Environ.* **2012**, *117–118*, 67.

[271] C.-J. Huang, F.-M. Pan, I.-C. Chang, *Appl. Surf. Sci.* **2012**, *263*, 345.

[272] G. E. Johnson, R. Colby, J. Laskin, *Nanoscale* **2015**, *7*, 3491.

[273] E. Palesch, A. Marek, P. Solar, O. Kylian, J. Vyskocil, H. Biederman, V. Cech, *Thin Solid Films* **2013**, *544*, 593.

[274] A. Vahl, J. Dittmann, J. Jetter, S. Veziroglu, S. Shree, N. Ababii, O. Lupan, O. C. Aktas, T. Strunskus, E. Quandt, R. Adelung, S. K. Sharma, F. Faupel, *Nanotechnology* **2019**, *30*, 235603.

[275] L. S. Kibis, A. I. Titkov, A. I. Stadnichenko, S. V. Koscheev, A. I. Boronin, *Appl. Surf. Sci.* **2009**, *255*, 9248.

[276] M. A. Ud Din, F. Saleem, M. Zulfiqar, X. Wang, *Nanoscale* **2018**, *10*, 17140.

[277] G. Yang, Y. Chen, Y. Zhou, Y. Tang, T. Lu, *Electrochem. commun.* **2010**, *12*, 492.

[278] Z. Wu, Z. Sheng, H. Wang, Y. Liu, *Chemosphere* **2009**, *77*, 264.

[279] O. Lupan, V. Postica, M. Hoppe, N. Wolff, O. Polonskyi, T. Pauporté, B. Viana, O. Majérus, L. Kienle, F. Faupel, R. Adelung, *Nanoscale* **2018**, *10*, 14107.

[280] D. Zhang, C. Jin, H. Tian, Y. Xiong, H. Zhang, P. Qiao, J. Fan, Z. Zhang, Z. Y. Li, J. Li, *Nanoscale* **2017**, *9*, 6327.

[281] L. M. Neal, M. L. Everett, G. B. Hoflund, H. E. Hagelin-Weaver, *J. Mol. Catal. A Chem.* **2011**, *335*, 210.

[282] P. Fu, P. Zhang, J. Li, *Appl. Catal. B Environ.* **2011**, *105*, 220.

[283] M. D. Hernández-Alonso, J. M. Coronado, A. Javier Maira, J. Soria, V. Loddo, V. Augugliaro, *Appl. Catal. B Environ.* **2002**, *39*, 257.

[284] M. Veith, E. Sow, U. Werner, C. Petersen, O. C. Aktas, *Eur. J. Inorg. Chem.* **2008**, *2008*, 5181.

[285] H. Hussain, G. Tocci, T. Woolcot, X. Torrelles, C. L. Pang, D. S. Humphrey, C. M. Yim, D. C. Grinter, G. Cabailh, O. Bikondoa, R. Lindsay, J. Zegenhagen, A. Michaelides, G. Thornton, *Nat. Mater.* **2017**, *16*, 461.

[286] A. Wold, *Chem. Mater.* **1993**, *5*, 280.

[287] H. Gerischer, H. Tributsch, *Ber. Bunsenges. Phys. Chem* **1968**, *72*, 437.

[288] W. Zhang, Y. Liu, D. Zhou, J. Wen, W. Liang, F. Yang, *RSC Adv.* **2015**, *5*, 57155.

[289] P. Salvador, *J. Appl. Phys.* **1984**, *55*, 2977.

[290] H. Li, Z. Bian, J. Zhu, Y. Huo, H. Li, Y. Lu, *J. AM. CHEM. SOC* **2007**, *129*, 33.

[291] A. B. Haugen, I. Kumakiri, C. Simon, M.-A. Einarsrud, *J. Eur. Ceram. Soc.* **2011**, *31*, 291.

[292] S. Luo, T. D. Nguyen-Phan, A. C. Johnston-Peck, L. Barrio, S. Sallis, D. A. Arena, S. Kundu, W. Xu, L. F. J. Piper, E. A. Stach, D. E. Polyansky, E. Fujita, J. A. Rodriguez, S. D. Senanayake, *J. Phys. Chem. C* **2015**, *119*, 2669.

[293] A. C. Johnston-Peck, S. D. Senanayake, J. J. Plata, S. Kundu, W. Xu, L. Barrio, J. Graciani, J. F. Sanz, R. M. Navarro, J. L. G. Fierro, E. A. Stach, J. A. Rodriguez, *J. Phys. Chem. C* **2013**, *117*, 14463.

[294] X. Gao, Y. Jiang, Y. Zhong, Z. Luo, K. Cen, *J. Hazard. Mater.* **2010**, *174*, 734.

[295] M. J. Muñoz-Batista, M. N. Gómez-Cerezo, A. Kubacka, D. Tudela, M. Fernández-García, *ACS Catal.* **2014**, *4*, 63.

[296] M. Ouzzine, J. A. Maciá-Agulló, M. A. Lillo-Ródenas, C. Quijada, A. Linares-Solano, *Appl. Catal. B Environ.* **2014**, *154–155*, 285.

[297] V. Swamy, D. Menzies, B. C. Muddle, A. Kuznetsov, L. S. Dubrovinsky, Q. Dai, V. Dmitriev, *Appl. Phys. Lett.* **2006**, *88*, 243103.

[298] G. Greczynski, L. Hultman, *ChemPhysChem* **2017**, *18*, 1507.

[299] H. Abdullah, M. R. Khan, M. Pudukudy, Z. Yaakob, N. A. Ismail, *J. Rare Earths* **2015**, *33*, 1155.

[300] B. Ullah, W. Lei, Q.-S. Cao, Z.-Y. Zou, X.-K. Lan, X.-H. Wang, W.-Z. Lu, *J. Am. Ceram. Soc.* **2016**, *99*, 3286.

[301] C. Gionco, M. C. Paganini, S. Agnoli, A. E. Reeder, E. Giamello, *J. Mater. Chem. A* **2013**, *1*, 10918.

[302] A. Migani, G. N. Vayssilov, S. T. Bromley, F. Illas, K. M. Neyman, *Chem. Commun.* **2010**, *46*, 5936.

[303] A. R. Puigdollers, P. Schlexer, S. Tosoni, G. Pacchioni, *ACS Catal.* **2017**, *7*, 6493.

[304] O. C. Aktas, S. Schröder, S. Veziroglu, M. Z. Ghori, A. Haidar, O. Polonskyi, T. Strunskus, K. Gleason, F. Faupel, *Adv. Mater. Interfaces* **2019**, *6*, 1801967.

[305] D. Öner, T. J. McCarthy, *Langmuir* **2000**, *16*, 7777.

[306] K. K. S. Lau, J. Bico, K. B. K. Teo, M. Chhowalla, G. A. J. Amaratunga, W. I. Milne, G. H. McKinley, K. K. Gleason, *Nano Lett.* **2003**, *3*, 1701.

[307] O. Kylián, M. Petr, A. Serov, P. Solař, O. Polonskyi, J. Hanuš, A. Choukourov, H. Biederman, *Vacuum* **2014**, *100*, 57.

[308] R. Enright, N. Miljkovic, A. Al-Obeidi, C. V. Thompson, E. N. Wang, *Langmuir* **2012**, *28*, 14424.

[309] D. Murakami, H. Jinnai, A. Takahara, *Langmuir* **2014**, *30*, 2061.

[310] A. Marmur, *Langmuir* **2003**, *19*, 8343.

[311] S. T. Yohe, J. D. Freedman, E. J. Falde, Y. L. Colson, M. W. Grinstaff, *Adv. Funct. Mater.* **2013**, *23*, 3628.

[312] U. Tuvshindorj, A. Yildirim, F. E. Ozturk, M. Bayindir, *ACS Appl. Mater. Interfaces* **2014**, *6*, 9680.

[313] M. Thieme, F. Streller, F. Simon, R. Frenzel, A. J. White, *Appl. Surf. Sci.* **2013**, *283*, 1041.

[314] Y.-W. Jang, Y.-K. Kim, H.-W. Park, D.-H. Won, S.-E. Cho, W.-P. Hwang, K.-S. Jung, M.-R. Kim, J.-K. Lee, *Mol. Cryst. Liq. Cryst.* **2011**, *538*, 240.

[315] M. Mintken, M. Schweichel, S. Schröder, S. Kaps, J. Carstensen, Y. K. Mishra, T. Strunskus, F. Faupel, R. Adelung, *Nano Energy* **2019**, *56*, 420.

[316] J. Hao, C. Liu, Y. Li, R. Liao, Q. Liao, C. Tang, *Materials (Basel).* **2018**, *11*, 851.

[317] A. Vesel, M. Mozetic, A. Zalar, *Surf. Interface Anal.* **2008**, *40*, 661.

[318] P. Žvátora, P. Řezanka, V. Prokopec, J. Siegel, V. Švorčík, V. Král, *Nanoscale Res. Lett.* **2011**, *6*, 1.

[319] Z. Wang, P. Jin, M. Wang, G. Wu, C. Dong, A. Wu, *ACS Appl. Mater. Interfaces* **2016**, *8*, 32862.

[320] M. Takeuchi, K. Sakamoto, G. Martra, S. Coluccia, M. Anpo, *J. Phys. Chem. B* **2005**, *109*, 15422.

[321] J.-L. Liu, X.-Q. Feng, G. Wang, S.-W. Yu, *J. Phys. Condens. Matter* **2007**, *19*, 356002.

[322] A. A. Ali, A. Haidar, O. Polonskyi, F. Faupel, H. Abdul-Khaliq, M. Veith, O. C. Aktas, *Nanoscale* **2017**, *9*, 14814.

[323] L. Gao, T. J. McCarthy, *Langmuir* **2007**, *23*, 9125.

[324] D. Kim, H. Im, M. J. Kwak, E. Byun, S. G. Im, Y. K. Choi, *Sci. Rep.* **2016**, *6*, 1.

Declaration of Authorship / Co-authorship

I, Salih Veziroglu, state here the nature of my involvement to the work in the following publications which form this cumulative dissertation.

Publication 1

S. Veziroglu, M. Kuru, M.Z. Ghori, F.K. Dokan, A.M. Hinz, T. Strunskus, F. Faupel, O.C. Aktas, Ultra-fast degradation of methylene blue by Au/ZnO-CeO_2 nano-hybrid catalyst, ***Mater. Lett.*** 209 (2017) 486–491.

Contribution:

Conceptualization	Methodology	Investigation	Visualization	Writing
High	High	High	High	Medium

Publication 2

S. Veziroglu, M.Z. Ghori, M. Kamp, L. Kienle, H.G. Rubahn, T. Strunskus, J. Fiutowski, J. Adam, F. Faupel, O.C. Aktas, Photocatalytic Growth of Hierarchical Au Needle Clusters on Highly Active TiO_2 Thin Film, ***Adv. Mater. Interfaces.*** 5 (2018) 1800465. **(FRONTISPIECE)**

Contribution:

Conceptualization	Methodology	Investigation	Visualization	Writing
High	High	Medium	High	Medium

Publication 3

S. Veziroglu, A.-L. Obermann, M. Ullrich, M. Hussein, M. Kamp, L. Kienle, T. Leißner, H.-G. Rubahn, O. Polonskyi, T. Strunskus, J. Fiutowski, M. Es-Sounid, J. Adam, F. Faupel, O. C. Aktas, Photo-deposition of Au Nanoclusters for Enhanced Photocatalytic Dye Degradation over TiO_2 Thin Film, ***ACS Applied Materials and Interfaces.*** 12, (2020) 14983.

Contribution:

Conceptualization	Methodology	Investigation	Visualization	Writing
High	High	Medium	High	Medium

Publication 4

S. Veziroglu, M. Ullrich, M. Hussain, J. Drewes, J. Shondo, T. Strunskus, J. Adam, F. Faupel, O. C. Aktas, Plasmonic and non-plasmonic contributions on photocatalytic activity of Au-TiO_2 thin film under mixed UV-Visible light, ***Surface & Coatings Tech.*** 389, (2020) 125613.

Contribution:

Conceptualization	Methodology	Investigation	Visualization	Writing
High	High	High	High	High

Publication 5

S. Veziroglu, M.Z. Ghori, A.L. Obermann, K. Röder, O. Polonskyi, T. Strunskus, F. Faupel, O.C. Aktas, Ag Nanoparticles Decorated TiO_2 Thin Films with Enhanced Photocatalytic Activity, ***Phys. Status Solidi Appl. Mater. Sci.*** (2019) 1800898. **(FRONT COVER)**

Contribution:

Conceptualization	Methodology	Investigation	Visualization	Writing
High	High	High	High	High

Publication 6

M.Z. Ghori, **S. Veziroglu,** A. Hinz, B.B. Shurtleff, O. Polonskyi, T. Strunskus, J. Adam, F. Faupel, O.C. Aktas, Role of UV Plasmonics in the Photocatalytic Performance of TiO_2 Decorated with Aluminum Nanoparticles, ***ACS Appl. Nano Mater.*** 1 (2018) 3760–3764. **(FRONT COVER)**

Contribution:

Conceptualization	Methodology	Investigation	Visualization	Writing
Medium	Medium	Medium	High	Medium

Publication 7

S. Veziroglu, J.Hwang, J. Drewes, J. Shondo, T. Strunskus, O. Polonskyi, F. Faupel, and O. C. Aktas, PdO Nanoparticles Decorated TiO_2 Film with Enhanced Photocatalytic and Self-Cleaning Properties, ***Materials Today Chemistry.*** 16 (2020) 100251.

Contribution:

Conceptualization	Methodology	Investigation	Visualization	Writing
High	Medium	Medium	High	High

Publication 8

__**S. Veziroglu,**__ K. Röder, O. Gronenberg, A. Vahl, O. Polonskyi, T. Strunskus, H.-G. Rubahn, L. Kienle, J. Adam, J. Fiutowski, F. Faupel, O.C. Aktas, Cauliflower-like CeO_2 –TiO_2 hybrid nanostructures with extreme photocatalytic and self-cleaning properties, ***Nanoscale.*** 11 (2019) 9840–9844. **(INSIDE BACK COVER)**

Contribution:

Conceptualization	**Methodology**	**Investigation**	**Visualization**	**Writing**
High	High	Medium	High	Medium

Publication 9

O.C. Aktas, S. Schröder, **S. Veziroglu,** M.Z. Ghori, A. Haidar, O. Polonskyi, T. Strunskus, K. Gleason, F. Faupel, Superhydrophobic 3D Porous PTFE/TiO_2 Hybrid Structures, ***Adv. Mater. Interfaces.*** 6 (2019) 1801967. **(INSIDE BACK COVER)**

Contribution:

Conceptualization	**Methodology**	**Investigation**	**Visualization**	**Writing**
Medium	Medium	Medium	High	Low

Kiel, 11.08.2020

M.Sc. Salih Veziroglu

Prof. Dr. Franz Faupel